ISSN 2074-272X

науково-практичний журнал 2024/1

Електротехніка і Електромеханіка

Electrical Engineering & Electromechanics

Електротехнічні комплекси та системи
Теоретична електротехніка
Інженерна електрофізика.
Техніка сильних електричних та магнітних полів
Електроізоляційна та кабельна техніка
Електричні станції, мережі і системи

Журнал включено до найвищої категорії «А»
Переліку фахових видань України

З 2019 р. журнал індексується у Scopus

З 2015 р. журнал індексується
у Web of Science Core Collection:
Emerging Sources Citation Index

Electrical Engineering & Electromechanics

Scientific Journal was founded in 2002
Founder – National Technical University «Kharkiv Polytechnic Institute» (Kharkiv, Ukraine)

From no. 1 2019 Journal «Electrical Engineering & Electromechanics» is indexing in **Scopus** and from no. 1 2015 Journal is indexing in **Web of Science Core Collection: Emerging Sources Citation Index (ESCI)**.

Also included in DOAJ (Directory of Open Access Journals), in EBSCO's database, in ProQuest's databases – Advanced Technologies & Aerospace Database and Materials Science & Engineering Database, in Gale/Cengage Learning databases.

Editorial office address:
National Technical University «Kharkiv Polytechnic Institute», Kyrpychova Str., 2, Kharkiv, 61002, Ukraine
phones: +380 57 7076281, +380 67 3594696, **e-mail:** a.m.grechko@gmail.com (**Grechko O.M.)**

ISSN (print) 2074-272X
ISSN (online) 2309-3404

Printed 29 December 2023. Format 60 × 90 ⅛. Paper – offset. Laser printing. Edition 200 copies.
Printed by Printing house «Madrid Ltd» (18, Gudanova Str., Kharkiv, 61024, Ukraine)

Electrical Engineering & Electromechanics
Scientific Journal

no. 1, 2024

Table of Contents

Electrotechnical Complexes and Systems

Latreche K., Taleb R., Bentaallah A., Toubal Maamar A.E., Helaimi M., Chabni F. Design and experimental implementation of voltage control scheme using the coefficient diagram method based PID controller for two-level boost converter with photovoltaic system..... **3**

Srinivas G., Durga Sukumar G., Subbarao M. Total harmonic distortion analysis of inverter fed induction motor drive using neuro fuzzy type-1 and neuro fuzzy type-2 controllers..... **10**

Themozhi G., Srinivasan K., Arun Srinivas T., Prabha A. Analysis of suitable converter for the implementation of drive system in solar photovoltaic panels..... **17**

Theoretical Electrical Engineering

Kuznetsov B.I., Nikitina T.B., Bovdui I.V., Chunikhin K.V., Kolomiets V.V., Kobylianskyi B.B. Method for prediction and control by uncertain microsatellite magnetic cleanliness based on calculation and compensation magnetic field spatial harmonics **23**

Engineering Electrophysics. High Electric and Magnetic Fields Engineering

Baranov M.I. A generalized physical principle of development of plasma channel of a high-voltage pulse spark discharge in a dielectric **34**

Boiko M.I., Tatkova K.S. Computer simulation of operation plant effective modes for water disinfection by electrical discharges in gas bubbles..... **43**

Shcherba A.A., Podoltsev O.D., Suprunovska N.I., Bilianin R.V., Antonets T.Yu., Masluchenko I.M. Modeling and analysis of electro-thermal processes in installations for induction heat treatment of aluminum cores of power cables..... **51**

Electrical Insulation and Cable Engineering

Bezprozvannych G.V., Grynyshyna M.V., Moskvitin Y.S. Requirements for cables as categories of construction products and thermal resistance of power cables..... **61**

Palchykov O.O. Determination of the maximum mechanical stresses in the insulating material around a defect with a high dielectric permittivity in an electrostatic field **69**

Power Stations, Grids and Systems

Paquianadin V., Navin Sam K., Koperundevi G. Maximizing solar photovoltaic system efficiency by multivariate linear regression based maximum power point tracking using machine learning..... **77**

UDC 621.3 https://doi.org/10.20998/2074-272X.2024.1.01

K. Latreche, R. Taleb, A. Bentaallah, A.E. Toubal Maamar, M. Helaimi, F. Chabni

Design and experimental implementation of voltage control scheme using the coefficient diagram method based PID controller for two-level boost converter with photovoltaic system

Introduction. *Currently, in the solar energy systems and a variety of electrical applications, the power converters are essential part. The main challenge for similar systems is controller design. In the literature, the PID controller has proved its effectiveness in many industrial applications, but determining its parameters remains one of the challenges in control theory field. The* ***novelty*** *of the work resides in the design and experimental implementation of a two-level boost DC-DC converter controlled by a PID controller for photovoltaic (PV) maximum power extraction.* ***Purpose.*** *Analysis and control of the two-level boost topology with renewable energy source and design of the PID controller parameters using simple and accurate method.* ***Methods.*** *PID coefficients are optimized using Coefficient Diagram Method (CDM) in the MATLAB environment.* ***Results.*** *A mathematical model of a two-level boost converter with PID controller and PV energy source was developed and analyzed. The model allows to design the controller parameters of the proposed system.* ***Practical value.*** *A prototype steered by the proposed CDM-PID controller was tested using an Arduino embedded board. A comparison between the simulation results and the experimental one is presented. The obtained results illustrate that the experimental results match the simulation closely, and the proposed CDM-PID controller provides a fast and precise results.* References 24, table 2, figures 16.

Key words: **power electronics, energy conversion, two-level boost converter, coefficient diagram method controller.**

Вступ. *В даний час перетворювачі потужності є невід'ємною частиною сонячних енергетичних систем та різних електричних пристроїв. Основною проблемою для таких систем є проектування контролера. У літературі ПІД-регулятор довів свою ефективність у багатьох промислових застосуваннях, але визначення його параметрів залишається однією з проблем у галузі теорії управління.* ***Новизна*** *роботи полягає у розробці та експериментальній реалізації дворівневого підвищувального перетворювача постійного струму, керованого ПІД-регулятором, для отримання максимальної потужності фотоелектричних пристроїв.* ***Мета***. *Аналіз та управління дворівневою топологією підвищення з використанням відновлюваного джерела енергії та розрахунок параметрів ПІД-регулятора простим та точним методом.* ***Методи***. *Коефіцієнти ПІД оптимізуються за допомогою методу діаграми коефіцієнтів (CDM) у середовищі MATLAB.* ***Отримані результати***. *Розроблено та проаналізовано математичну модель дворівневого підвищувального перетворювача з ПІД-регулятором та фотоелектричним джерелом енергії. Модель дозволяє спроєктувати параметри контролера пропонованої системи.* ***Практична цінність***. *Прототип, керований пропонованим контролером CDM-PID, протестували з використанням вбудованої плати Arduino. Наведено порівняння результатів моделювання з експериментальними даними. Отримані результати показують, що експериментальні результати близько відповідають моделюванню, а пропонований CDM-ПІД-регулятор забезпечує швидкі та точні результати.* Бібл. 24, табл. 2, рис. 16.

Ключові слова: **силова електроніка, перетворення енергії, дворівневий підвищувальний перетворювач, регулятор методу діаграми коефіцієнтів.**

Introduction. Nowadays, solar and wind energies are from the most contributor for power generation among different renewable energy resources. The use of solar energy because of their advantageous such as the free availability, solar energy systems on buildings have minimal impact on the environment, electricity produced by solar cells is clean (not produce air pollution or carbon dioxide) and silent [1-3].

In solar energy systems and a variety of electrical applications, the power converters are essential part. There is a several type of converters: AC to DC converters, DC to AC converters, AC to AC converters, and DC to DC converters. Also, the use of multilevel converters topologies in power circuits has many benefices, including the increase of the voltage level, the reduction of stress across static switches, the improvement of power factor with the reduction of power losses, the reduction of filter size [4-9]. DC to DC converters are widely used in many modern electronic systems. They convert a DC input voltage into a different DC output voltage, and are widely used in power supplies for all types of electronic devices, such as computers, cell phones, tablets and telecommunications equipment.

An overview of DC-DC converters allows us to conclude the importance of this type of converter. Authors in [10] have presented enhanced fuzzy logic controller using boost DC-DC converter topologies for a grid system. In the work [11] have proposed high step up boost converter for uninterrupted power supply using renewable energy resources (wind and photovoltaic (PV)). Authors in [12] have discussed switching DC step-up/step-down regulators voltage for maximum power transmission. In the work [13] have presented DC-DC converter topologies for energy management system. Authors in [14] have proposed five-level inverter alimented by DC-DC converter with artificial intelligence control. The control of DC-DC converters is an important topic in modern electronic circuit design. Precise regulation of the output voltage of a DC-DC converter is crucial to ensure the smooth operation of the overall electronic system. The intelligent control techniques and the PID control method are often used to control these converters [15, 16]. However, optimizing PID coefficients can be difficult, especially for converters with variable frequency switching.

The **goal** of the paper is design and experimental implementation of a two-level boost DC-DC converter controlled by a PID controller for PV maximum power extraction. The PID coefficients are optimized using Coefficient Diagram Method (CDM); hence the Maximum Power Point Tracking (MPPT)-PID controller adopting CDM is utilized for providing better accuracy. A two-level boost DC-DC converter is exploited which boosts the oscillating PV voltage. The two-level boost DC-DC topology, the design of MPPT-PID controller based on CDM, and the main findings are summarized in this article.

Theoretical background of the CDM. CDM is an algebraic approach, proposed by Prof. Manabe to design

the controller parameters [17]. The standard block scheme of CDM is shown in Fig. 1, on which $R(s)$ is the reference input signal; $Y(s)$ is the output signal; $d(s)$ is the disturbance; $N(s)$ is the numerator polynomial of the controlled system; $D(s)$ is the denominator polynomial of the controlled system; $A(s)$, $B(s)$, and $F(s)$ are the CDM controller polynomials.

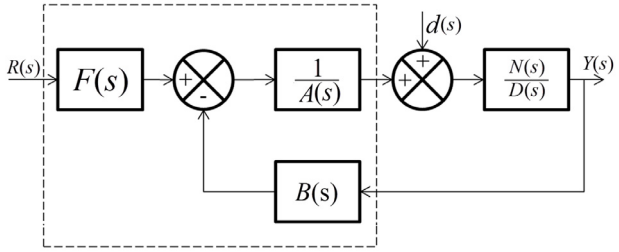

Fig. 1. The standard block diagram of CDM

The closed-loop transfer function of the system can be written as:

$$Y(s)=\frac{N(s)F(s)}{P(s)}R(s)+\frac{A(s)N(s)}{P(s)}d(s), \qquad (1)$$

where $P(s)$ is the characteristic polynomial of the closed-loop system presented as:

$$P(s)=A(s)D(s)+N(s)B(s). \qquad (2)$$

The polynomials $A(s)$ and $B(s)$ of the CDM controller structures are given as:

$$A(s)=\sum_{i=0}^{x} l_i s^i; \quad B(s)=\sum_{i=0}^{y} k_i s^i, \qquad (3)$$

where x and y are the degrees of CDM controller.

Next step of design consists of the calculation of the target polynomial $P_t(s)$ as follows:

$$P_t(s)=a_0\left[\left(\sum_{i=2}^{n}\left(\prod_{j=1}^{i-1}\frac{1}{\gamma_{i-j}^{j}}\right)(\tau s)^i\right)+\tau s+1\right], \qquad (4)$$

where n is the order of the characteristic polynomial $P(s)$; τ is the equivalent time constant; γ_i is the stability indices.

In design of CDM controller, the most important point is setting of key parameters (γ_i and τ), because the key parameters come into closely relation with the dynamic system performances (rapidity, robustness, stability). Value of equivalent time constant (τ) has relation with the system rapidity, because it has an impact on the rise time and settling time. Values of stability parameter (γ_i) have relation with the system stability and robustness, because have impact on the steady state error. According to [17] γ_i and τ values can be selected as follows: γ_i values can be written as: {2.5, 2, 2...2}. Usually (γ_i) is selecting from the range of (1.5 to 4) to have a good stability performance based on Routh-Hurwitz stability criterion and Lipatov's stability criterion. In other hand, the key parameters (γ_i and τ) can be adjusted to have good desired performances [17-19].

Last step of design is determination of the PID controller gains. Putting $P(s) = P_t(s)$, then presenting the equations system in matrix form ($AX = B$). Note that $X = [k_2; k_1; k_0; l_1]$ is the vector of gains for estimating the PID controller parameters; k_p is the proportional gain of PID controller; k_i is the integral gain of PID controller; k_d is the derivative gain of PID controller:

$$k_p = k_1/l_1; \quad k_i = k_0/l_1; \quad k_d = k_2/l_1.$$

Description of the proposed two-level boost connected PV system. Figure 2 displays the proposed boost-connected PV system. It includes a two-level boost converter linked to PV system.

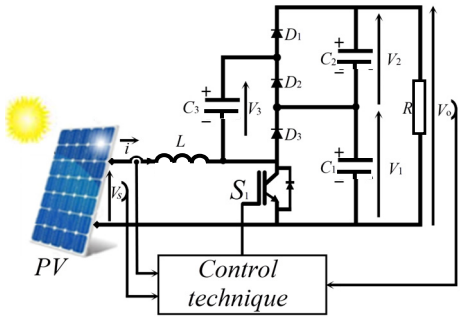

Fig. 2. The proposed boost-connected PV scheme

To study the control of the system, we must present briefly the principle and the mathematical model of each element of the system.

Model of the PV panel. In the literature several PV models have been discussed. The models differ from each other in the procedure and the number of parameters involved in the calculation of the current-voltage pair [20-22]. Figure 3 illustrates the most common equivalent electrical circuit of the PV module.

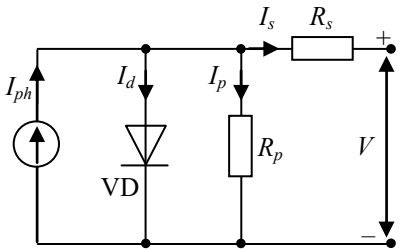

Fig. 3. Equivalent electrical circuit of a PV cell (one diode model)

From the electrical circuit, we can obtain the formula that allows us to obtain the *I-V* characteristic of the PV cell and panel. The law of nodes lets us to write the following relationship (5):

$$I = I_{ph} - I_d - I_p = \\ = I_{ph} - I_s\left(e^{\left(\frac{q(V+R_sI)}{nkT}\right)}-1\right)-\frac{V+R_sI}{R_p}, \qquad (5)$$

where I, V are the current and the voltage generated by the solar cell; I_d, I_p are the diode current and the parallel resistor current; R_s, R_p are the series and parallel resistors of the solar cell; k is the Boltzmann constant ($k = 1.38 \cdot 10^{-23}$ J/K); n is the ideality factor of the solar cell, varies between 1 and 2; T is the temperature of a diode; q is the charge of an electron ($q = 1{,}6 \cdot 10^{-19}$ C); I_{ph} is the photocurrent generated by the solar cell.

The photocurrent I_{ph} is proportional to the solar radiation E and is assumed to be linear as a function of the surface temperature T of the cell, it can be described as:

$$I_{ph}=\frac{E}{E_{ref}}\left(I_{phref}+\mu_{scc}\left(T-T_{ref}\right)\right), \qquad (6)$$

where E is the real solar irradiance, W/m²; E_{ref} is the standard test conditions (STC) irradiance, W/m²; T is the

operating temperature; T_{ref} is the STC temperature; μ_{scc} is the temperature coefficient of the short-circuit current; STC conditions are cell temperature of 25 °C and global solar irradiance of 1000 W/m².

The choice of the series and parallel resistance values for simulation is detailed in papers [23, 24]. The series and parallel resistance values can be calculated as:

$$R_p > \frac{10V_{co}}{I_{cc}};\quad R_s < \frac{0.1V_{co}}{I_{cc}}, \tag{7}$$

where:

$$I_{CC} \approx I_{ph};\quad V_{CO} = V_t \ln\left(\frac{I_{ph}}{I_S}+1\right);\quad V_t = \frac{nkT}{q},$$

where V_t is the thermal voltage of the diode; V_{co} is the open circuit voltage; I_{cc} is the short-circuit current.

For a solar panel with N cells, we can write the saturation current as:

$$I_S = \frac{I_{ph}}{e^{\left(\frac{V_{CO}}{N_{cell}\cdot V_t}\right)}-1}. \tag{8}$$

Model of the two-level boost converter. Figure 4 displays the topology of the two-level boost converter. A two-level boost converter is typically composed of one switch S_1, one inductance L, three capacitors C_1, C_2, C_3, three diode D_1, D_2, D_3, one DC power supply or renewable energy source (in our case the DC power supply is replaced by a PV), one resistor R as load. The output voltage V_0 is related to the voltage of the two capacitors V_1 and V_2. Thus, $V_0 = V_1 + V_2 = 2V_c$. The output voltage can be calculated as:

$$V_0 = \frac{2V_s}{1-\alpha}, \tag{9}$$

where α is the duty cycle; V_s is the input voltage.

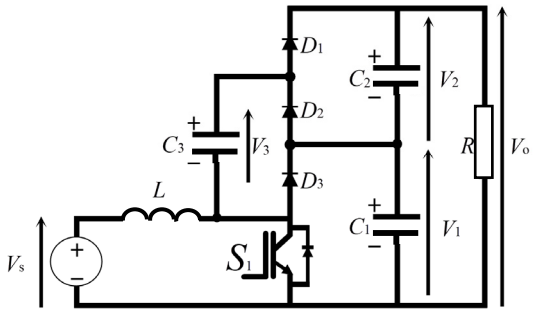

Fig. 4. Topology of the two-level boost converter

The state-space model of the two-level boost converter can be written with the following system of equations:

$$\begin{cases} \dfrac{dI_L}{dt} = -\dfrac{(1-\alpha)}{2\cdot L}\cdot v_0 + \dfrac{1}{L}\cdot v_s; \\ \dfrac{dv_0}{dt} = \dfrac{(1-\alpha)}{C}\cdot I_L + \dfrac{2}{R\cdot C}\cdot v_0. \end{cases} \tag{10}$$

In matrix form, the state space model of the system is given as:

$$\begin{cases} \dot{X} = A\cdot X + B\cdot U; \\ Y = C\cdot X, \end{cases} \tag{11}$$

where:

$$A = \begin{bmatrix} 0 & -\dfrac{(1-\alpha)}{2\cdot L} \\ \dfrac{(1-\alpha)}{C} & -\dfrac{2}{R\cdot C} \end{bmatrix};\quad B = \begin{bmatrix} 1/L \\ 0 \end{bmatrix};\quad C = \begin{bmatrix} 0 & 1 \end{bmatrix}.$$

Based on the state space model, the system transfer function can be expressed using the complement (com) and the determinant (det) of a matrix ($SI_2 - A$), as:

$$G(S) = \frac{C\cdot(\mathrm{com}(SI_2 - A))^T \cdot B}{\det(SI_2 - A)}. \tag{12}$$

By applying some mathematical manipulations, the transfer function of the system is given as:

$$G(S) = \frac{\dfrac{(1-\alpha)}{L\cdot C}}{S^2 + \left(\dfrac{2}{R\cdot C}\right)S + \dfrac{(1-\alpha)^2}{2\cdot L\cdot C}}. \tag{13}$$

CDM-PID controller design for the proposed system. To identify the parameters of the proposed controller used in this application by the CDM technique, the open-loop transfer function $G(s)$ of the system is used. First, the transfer function $G(s)$ of the system is given in polynomial forms as follow:

$$\begin{cases} N(s) = \dfrac{(1-\alpha)}{L\cdot C}; \\ D(s) = S^2 + \left(\dfrac{2}{R\cdot C}\right)S + \dfrac{(1-\alpha)^2}{2\cdot L\cdot C}. \end{cases} \tag{14}$$

In this work, we have chosen a second-order polynomial controller $C(s)$ given by the following structure:

$$\begin{cases} B(s) = k_2 s^2 + k_1 s^1 + k_0; \\ A(s) = l_2 s^2 + l_1 s^1 + l_0. \end{cases} \tag{15}$$

So, the transfer function $C(s)$ of the controller is given by:

$$C(s) = \frac{k_2 s^2 + k_1 s^1 + k_0}{l_2 s^2 + l_1 s^1 + l_0}. \tag{16}$$

The characteristic expression of the standard PID controller is written as:

$$C_{PID}(s) = k_p + \frac{k_i}{S} + k_d S = \frac{k_p S + k_i + k_d S^2}{S}. \tag{17}$$

By identification between (16) and (17), the second-order polynomial controller is written as:

$$C(s) = \frac{k_2 s^2 + k_1 s^1 + k_0}{l_1 s^1} = \frac{k_2}{l_1} S + \frac{k_1}{l_1} + \frac{k_0}{l_1 S}. \tag{18}$$

By identification between (17) and (18), the PID controller parameters can be estimated as:

$$k_p = k_1/l_1;\quad k_i = k_0/l_1;\quad k_d = k_2/l_1.$$

The characteristic polynomial $P(s)$ of the closed-loop system is given as:

$$P(s) = A(s)D(s) + N(s)B(s) = \begin{pmatrix} \left(l_1 s^1\right)\cdot\left(s^2 + \left(\dfrac{2}{R\cdot C}\right)s + \dfrac{(1-\alpha)^2}{2\cdot L\cdot C}\right) + \\ + \left(\dfrac{(1-\alpha)}{L\cdot C}\right)\cdot\left(k_2 s^2 + k_1 s^1 + k_0\right) \end{pmatrix}. \tag{19}$$

Applying some mathematical manipulations, the characteristic polynomial $P(s)$ can be written as:

$$P(s)=\begin{pmatrix} l_1\cdot s^3+\left(\frac{(1-\alpha)}{L\cdot C}\cdot k_2+\frac{2.l_1}{R\cdot C}\right)\cdot s^2+ \\ +\left(\frac{(1-\alpha)}{L\cdot C}\cdot k_1+\frac{(1-\alpha)^2}{2\cdot L\cdot C}\cdot l_1\right)\cdot s+ \\ +\frac{(1-\alpha)}{L\cdot C}\cdot k_0. \end{pmatrix} \quad (20)$$

The target characteristic polynomial $P_t(s)$ is given as:

$$P_t(s)=a_0\left[\left(\sum_{i=2}^{3}\left(\prod_{j=1}^{i-1}\frac{1}{\gamma_{i-j}^{j}}\right)(\tau\cdot s)^i\right)+\tau\cdot s+1\right]. \quad (21)$$

Applying some mathematical manipulations and simplifications, the target characteristic polynomial $P_t(s)$ can be written as:

$$P_t(s)=\begin{pmatrix} \left(\frac{1}{\gamma_2^1\gamma_1^2}a_0\tau^3\right)\cdot s^3+\left(\frac{1}{\gamma_1^1}a_0\tau^2\right)\cdot s^2+ \\ +(a_0\cdot\tau)\cdot s+a_0 \end{pmatrix}. \quad (22)$$

The time constant τ and a_0 are picked as follows for our application: $\tau = 0.001$ and $a_0 = 1$. The stability indices γ_1 and γ_2 are selected as $\gamma_i = [2.5, 2]$, $i = 1, 2$. In order to improve the system's performance, these parameters were picked from the Manabe's standard form.

Putting $P(s) = P_t(s)$, by identification between (20) and (22), the polynomials expressions can be written as:

$$\begin{cases} l_1=\frac{1}{\gamma_2^1\gamma_1^2}a_0\tau^3; \\ \frac{(1-\alpha)}{L\cdot C}k_2+\frac{2l_1}{R\cdot C}=\frac{1}{\gamma_1^1}a_0\tau^2; \\ \frac{(1-\alpha)}{L\cdot C}k_1+\frac{(1-\alpha)^2}{2\cdot L\cdot C}l_1=a_0\tau; \\ \frac{(1-\alpha)}{L\cdot C}k_0=a_0. \end{cases} \quad (23)$$

In matrix form ($AX = B$), the matrix equations of the polynomials expressions (23) are given as:

$$A=\begin{pmatrix} 0 & 0 & 0 & 1 \\ \frac{(1-\alpha)}{L\cdot C} & 0 & 0 & \frac{2}{R\cdot C} \\ 0 & \frac{(1-\alpha)}{L\cdot C} & 0 & \frac{(1-\alpha)^2}{2\cdot L\cdot C} \\ 0 & 0 & \frac{(1-\alpha)}{L\cdot C} & 0 \end{pmatrix};$$

$$X=\begin{pmatrix} k_2 \\ k_1 \\ k_0 \\ l_1 \end{pmatrix}; \quad B=\begin{pmatrix} \frac{a_0\tau^3}{\gamma_2^1\gamma_1^2} \\ \frac{a_0\tau^2}{\gamma_1^1} \\ a_0\tau \\ a_0 \end{pmatrix},$$

where X is the matrix of gains for estimating the PID controller parameters.

The previous design steps of the CDM-PID controller are programed in MATLAB editor. Achieved results are discussed in the following section.

Results and discussion. Simulation of the proposed two levels DC-DC boost-connected PV is validated through MATLAB environment. Table 1 displays the electrical parameters of the solar panel Solarex MSX-60.

Table 1

The electrical parameters of the solar panel Solarex MSX-60

Parameter	Value
Maximum power P_{max}, W	60
Number of cells	36
Voltage at maximum power V_{mpp}, V	17.1
Current at maximum power I_{mpp}, A	3.5
Minimum power guaranteed, W	58
Short-circuit current I_{cc}, A	3.8
Open circuit voltage V_{co}, V	21.1
Temperature coefficient at V_{co}, mV/°C	–(80±10)
Temperature coefficient at I_{cc}, %/°C	(0.065±0.015)
Approximate effect of power temperature, %/°C	–(0.5±0.05)

Figures 5,*a*,*b* illustrate the curves of PV panel characteristics, the current-voltage (*I-V*) characteristic and the power-voltage (*P-V*) characteristic, respectively.

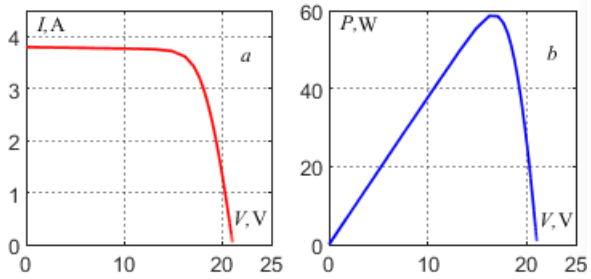

Fig. 5. Characteristics of a PV panel:
a – *I-V* characteristic; *b* – *P-V* characteristic

Figure 6 illustrates the impact of irradiance and temperature on the $I = f(V)$ and $P = f(V)$ characteristics.

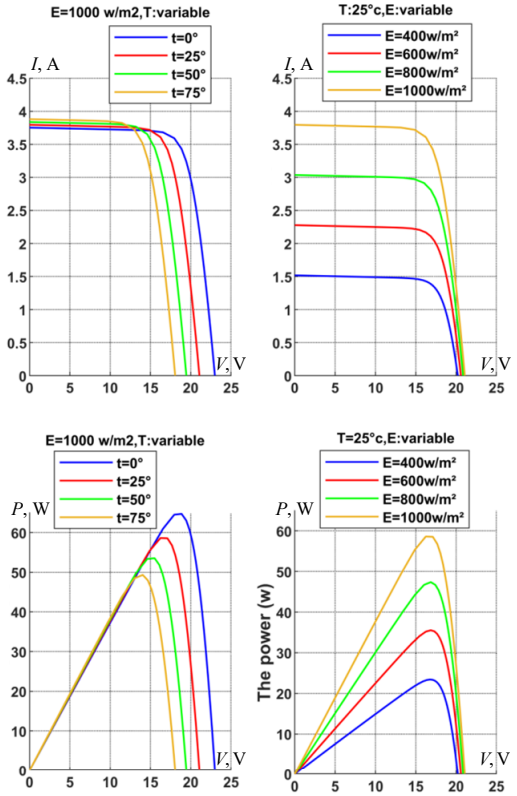

Fig. 6. *I-V* and *P-V* curves of the solar panel with various scenarios of temperature and irradiance values

To check the system through simulation, the parameters of the converter are given in Table 2.

Table 2
The electrical parameters of the converter

Parameter	Value
Input voltage V_s, V	30
Switching frequency, kHz	1
Inductance L, mH	800
Capacitances C_1, C_2, C_3, μF	220
Resistance R, Ω	1500
Duty cycle α	0.5

Figure 7 shows example of gate signal for the switch S_1 with f = 1 kHz and variable duty cycle α. Figure 8 shows the input and output voltages of the two-level boost converter with duty cycle α = 0.5. From Fig. 8 we note that the output voltage achieve a maximum value equal to 120 V with an input value equal to 30 V. Equation (9) confirm the obtained results.

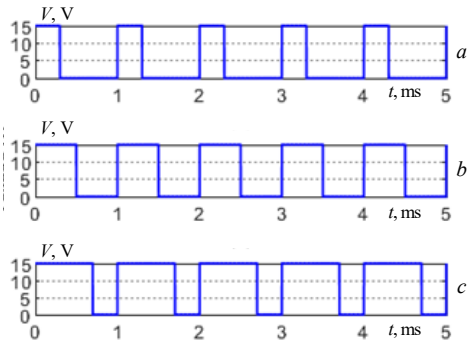

Fig. 7. Simulation example of gate signal for the switch S_1 with f = 1 kHz: a – α = 30 %; b – α = 50 %; c – α = 70 %.

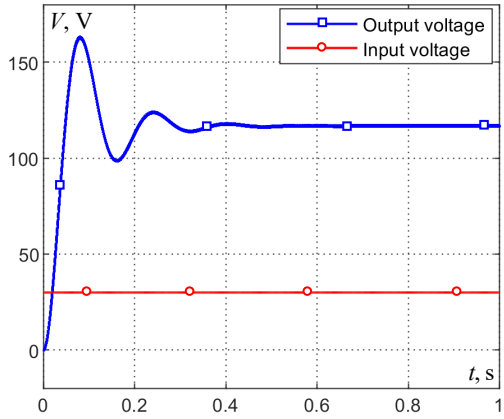

Fig. 8. Input and output voltages of the two-level boost converter with duty cycle α = 50 %

Now, we will execute the programmed CDM-PID code in MATLAB editor. Solving the system gives the coefficients of the PID controller as: $k_p = 4.3997 \cdot 10^3$; $k_i = 4.4 \cdot 10^6$; $k_d = 1.7579$.

After achieving the PID controller parameters using the CDM, the next step is testing the system responses. Figure 9 illustrates the system's output with the CDM-PID controller in the scenario of variable reference. The reference was changed from 5 V to 20 V, and then to 10 V.

According to the achieved simulation results, it can be seen that the system output tracks the variable reference with a good accuracy and quickly, where the system output follows the reference path after varying its value; therefore, the PID based on CDM controller provides a good dynamic response to the system.

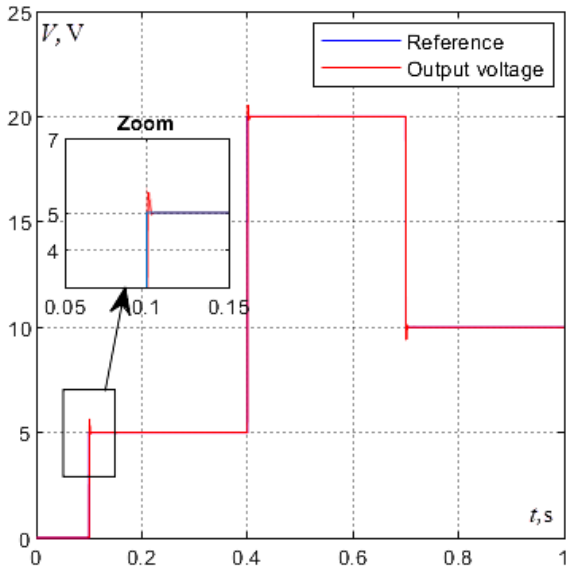

Fig. 9. System responses with the PID based on CDM controller in the case of variable reference

For testing the robustness of the PID-CDM controller, disturbance is injected in the closed-loop system. Figure 10 shows the block diagram of the closed-loop system when adding disturbance. The effects of the disturbances and their corresponding system responses are depicted in Fig. 11.

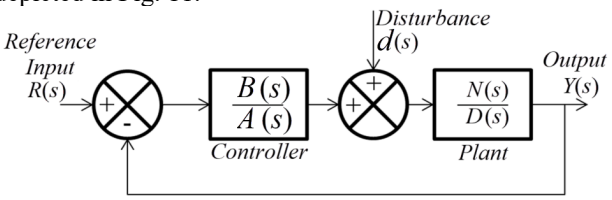

Fig. 10. Block diagram of the closed-loop system with disturbance

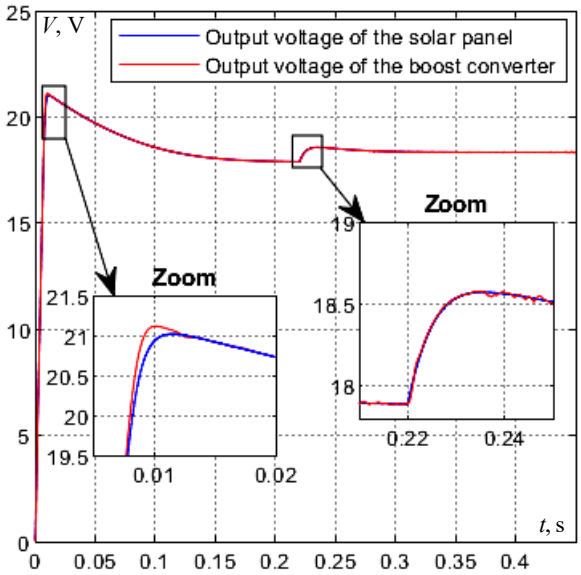

Fig. 11. System response with PID-CDM controller when adding disturbance

The curves in Fig. 11 demonstrate that the disturbances are rejected. The system responses return to the reference trajectory in the case of step disturbance.

According to the obtained simulation results, it can be seen that the PID-CDM controller provides good system responses and robust rejection of the disturbance.

Experimental results. To validate the achieved theoretical and simulation results, an experimental setup of the two-level boost converter with PV system has been constructed using one MOSFET switch, one inductance, three capacitors, three diode, one resistor as load, one DC power supply as PV panel, Arduino chip, oscilloscope, and PC with MATLAB/Simulink software. Figure 12 illustrates the experimental prototype of the proposed system.

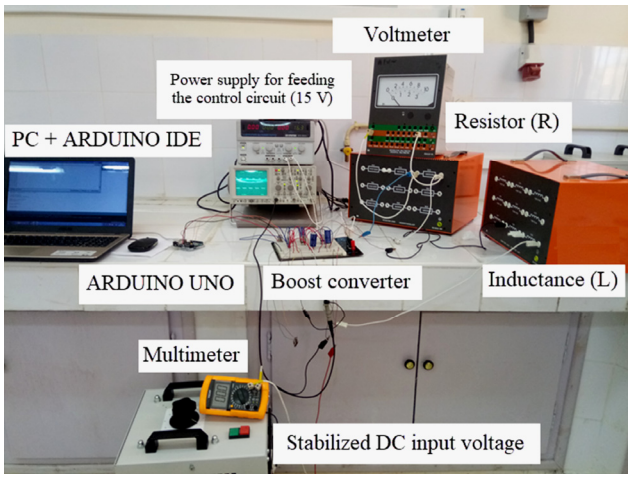

Fig. 12. Prototype of the two-level boost converter

Figure 13 demonstrates an experimental example of gate signal for the switch S_1 with switching frequency f = 1 kHz and variable duty cycle: a – α = 30 %, b – α = 50 %, c –α = 70 %, respectively.

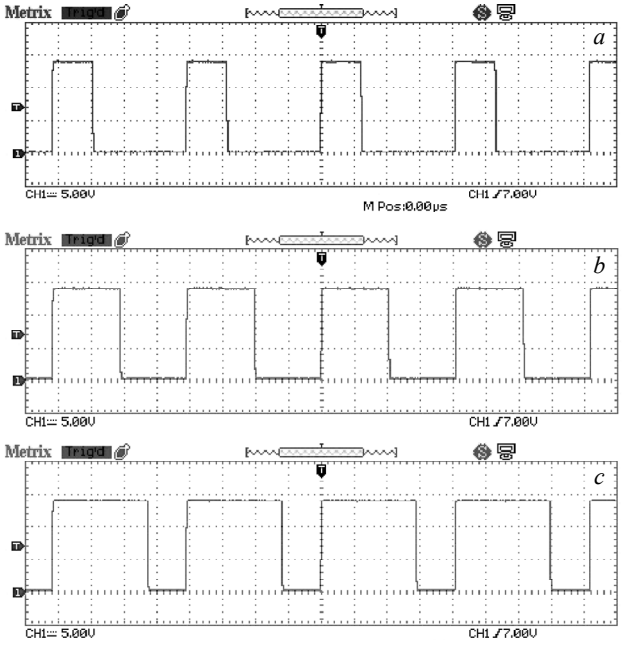

Fig. 13. Experimental example of gate signal for the switch S_1 with f = 1 kHz and duty cycle a – α = 30 %, b – α = 50 %, c – α = 70 %

Figure 14 shows the capacitors voltage and the output voltage of the two-level boost converter with duty cycle α = 0.5, and switching frequency f = 1 kHz. From Fig. 14 we note that the output voltage V_o achieve a maximum value equal to 120 V with an input value equal to 30 V.

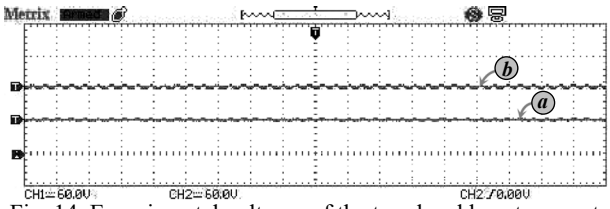

Fig. 14. Experimental voltages of the two-level boost converter with duty cycle α = 50 %: a – the capacitors voltages; b – the output voltage V_o

Figure 7 illustrates simulation example of gate signal for the switch S_1 with f = 1 kHz and variable duty cycle using MATLAB/Simulink. Figure 13 illustrates the experimental gate signal for the switch S_1 using the experimental prototype. By comparison, the simulation results are matching closely the experimental one. Also, the simulation analyses of the converter output voltage V_o is matching closely the experimental analyses as shown in Fig. 14. All the results were achieved using a simple and accurate design method.

Conclusions.

1. A mathematical model of a new system composed of coefficient diagram method based PID controller and two-level boost converter with photovoltaic system has been developed and investigated. The model allows to design the controller parameters based on the coefficient diagram method.

2. The two-level boost converter has been employed to extract the maximum power from the photovoltaic panel. coefficient diagram method based PID controller has been used to control the output voltage.

3. Simulation was done in MATLAB/Simulink software to verify the performance of the proposed system. In addition, an experimental evaluation was conducted using a low-cost Arduino board. The experimental results confirm that coefficient diagram method for controling multilevel boost converter is an effective and easy-to-apply technique.

4. As an extension to the work, it looks interesting to implement other methods to design the controller parameters, like the intelligent metaheuristic algorithms. Control the system with fuzzy logic controller, or neural network controller. Furthermore, other similar systems can be addressed, such as: feeding the multilevel boost converter with other renewable energies as the wind. The principal advantages of sustainable energies are to meet the increasing demand for electricity, particularly in the event of natural crises and international problems, to reduce air pollution and to limit global warming.

Conflict of interest. The authors declare that they have no conflicts of interest.

REFERENCES

1. Sai Thrinath B.V., Prabhu S., Meghya Nayak B. Power quality improvement by using photovoltaic based shunt active harmonic filter with Z-source inverter converter. *Electrical Engineering & Electromechanics*, 2022, no. 6, pp. 35-41. doi: https://doi.org/10.20998/2074-272X.2022.6.06.

2. Oumaymah E., Abdellah O., Omar B., Lhoussain E.B. NPC five level inverter using SVPWM for Grid-Connected Hybrid Wind-Photovoltaic Generation System. *Advances in Science, Technology and Engineering Systems Journal*, 2020, vol. 5, no. 6, pp. 981-987. doi: https://doi.org/10.25046/aj0506117.

3. Bekhoucha N., Mesbahi N., Bouchikha H., Heguig L., Chikha S. Model Predictive Control of Three-Level Shunt

Active Power Filter Connected to a Photovoltaic System. *2022 19th International Multi-Conference on Systems, Signals & Devices (SSD)*, 2022, pp. 128-133. doi: https://doi.org/10.1109/SSD54932.2022.9955660.
4. Maamar A.E.T., Helaimi M., Taleb R., Analysis, Simulation and Experimental Validation of High Frequency DC/AC Multilevel Inverter. *Przegląd Elektrotechniczny*, 2020, no. 8, pp. 16-19. doi: https://doi.org/10.15199/48.2020.08.03.
5. Nebti K., Lebied R. Fuzzy maximum power point tracking compared to sliding mode technique for photovoltaic systems based on DC-DC boost converter. *Electrical Engineering & Electromechanics*, 2021, no. 1, pp. 67-73. doi: https://doi.org/10.20998/2074-272X.2021.1.10.
6. Maamar A.E.T., Kermadi M., Helaimi M., Taleb R., Mekhilef S. An Improved Single-Phase Asymmetrical Multilevel Inverter Structure With Reduced Number of Switches and Higher Power Quality. *IEEE Transactions on Circuits and Systems II: Express Briefs*, 2021, vol. 68, no. 6, pp. 2092-2096. doi: https://doi.org/10.1109/TCSII.2020.3046186.
7. Benkahla M., Taleb R., Boudjema Z. A new robust control using adaptive fuzzy sliding mode control for a DFIG supplied by a 19-level inverter with less number of switches. *Electrical Engineering & Electromechanics*, 2018, no. 4, pp. 11-19. doi: https://doi.org/10.20998/2074-272X.2018.4.02.
8. Toubal Maamar A.E., Helaimi M., Taleb R., Kermadi M., Mekhilef S., Wahyudie A., Rawa M. Analysis and Small Signal Modeling of Five-Level Series Resonant Inverter. *IEEE Access*, 2021, no. 9, pp. 109384-109395. doi: https://doi.org/10.1109/ACCESS.2021.3102102.
9. Elamri O., Oukassi A., Toubal Maamar A.E., El Bahir L. Design and Simulation of a Power System Composed of Grid-tied Five-level Inverter with LCL Filter. *Electronics*, 2022, vol. 26, no. 1, pp. 17-25. doi: https://doi.org/10.53314/ELS2226017E.
10. Muthubalaji S., Devadasu G., Srinivasan S., Soundiraraj N. Development and validation of enhanced fuzzy logic controller and boost converter topologies for a single phase grid system. *Electrical Engineering & Electromechanics*, 2022, no. 5, pp. 60-66. doi: https://doi.org/10.20998/2074-272X.2022.5.10.
11. Chandramouli B., Vijayaprabhu A., Arun Prasad D., Kathiravan K., Udhayaraj N., Vijayasanthi M. Design of single switch-boosted voltage current suppressor converter for uninterrupted power supply using green resources integration. *Electrical Engineering & Electromechanics*, 2022, no. 5, pp. 31-35. doi: https://doi.org/10.20998/2074-272X.2022.5.05.
12. Romashko V.Y., Batrak L.M., Abakumova O.O. Step-up/step-down regulators in maximum power transmission mode. *Electrical Engineering & Electromechanics*, 2022, no. 2, pp. 18-22. doi: https://doi.org/10.20998/2074-272X.2022.2.03.
13. Ayat Y., Badoud A.E., Mekhilef S., Gassab S. Energy management based on a fuzzy controller of a photovoltaic/fuel cell/Li-ion battery/supercapacitor for unpredictable, fluctuating, high-dynamic three-phase AC load. *Electrical Engineering & Electromechanics*, 2023, no. 3, pp. 66-75. doi: https://doi.org/10.20998/2074-272X.2023.3.10.
14. Toubal Maamar A.E., Helaimi M., Taleb R., Kermadi M., Mekhilef S. A neural network-based selective harmonic elimination scheme for five-level inverter. *International Journal of Circuit Theory and Applications*, 2022, vol. 50, no. 1, pp. 298-316. doi: https://doi.org/10.1002/cta.3130.
15. Kumar R.S., Reddy C.S.R., Chandra B.M. Optimal performance assessment of intelligent controllers used in solar-powered electric vehicle. *Electrical Engineering & Electromechanics*, 2023, no. 2, pp. 20-26. doi: https://doi.org/10.20998/2074-272X.2023.2.04.
16. Anwar N., Hanif A., Ali M.U., Zafar A. Chaotic-based particle swarm optimization algorithm for optimal PID tuning in automatic voltage regulator systems. *Electrical Engineering & Electromechanics*, 2021, no. 1, pp. 50-59. doi: https://doi.org/10.20998/2074-272X.2021.1.08.
17. Manabe S. Coefficient Diagram Method. *IFAC Proceedings Volumes*, 1998, vol. 31, no. 21, pp. 211-222. doi: https://doi.org/10.1016/S1474-6670(17)41080-9.
18. Ikeda H. PID Controller Design Methods for Multi-Mass Resonance System. *PID Control for Industrial Processes*, 2018, pp. 187-207. doi: https://doi.org/10.5772/intechopen.74298.
19. Haouari F., Nourdine B., Boucherit M.S., Tadjine M. A Coefficient Diagram Method Controller with Backstepping Methodology for Robotic Manipulators. *Journal of Electrical Engineering*, 2015, vol. 66, no. 5, pp. 270-276. doi: https://doi.org/10.2478/jee-2015-0044.
20. Toubal Maamar A.E., Ladjouzi S., Taleb R., Kacimi Y. Détection et classification de défauts pour un GPV: Etude comparative entre la méthode de seuillage et réseaux de neurones. *Revue des Energies Renouvelables*, 2018, vol. 21, no. 1, pp. 45-53. (Fra).
21. Humada A.M., Hojabri M., Mekhilef S., Hamada H.M. Solar cell parameters extraction based on single and double-diode models: A review. *Renewable and Sustainable Energy Reviews*, 2016, vol. 56, pp. 494-509. doi: https://doi.org/10.1016/j.rser.2015.11.051.
22. Kermadi M., Berkouk E.M. Artificial intelligence-based maximum power point tracking controllers for Photovoltaic systems: Comparative study. *Renewable and Sustainable Energy Reviews*, 2017, vol. 69, pp. 369-386. doi: https://doi.org/10.1016/j.rser.2016.11.125.
23. Savitha P.B., Shashikala M.S., Puttabuddhi K.L. Modelling of Photovoltaic Cell/Module under Environmental Disturbances using MATLAB/Simulink. *International Journal of Engineering Trends and Technology*, 2014, vol. 9, no. 1, pp. 48-55. doi: https://doi.org/10.14445/22315381/IJETT-V9P210.
24. Tian H., Mancilla-david F., Ellis K., Jenkins P., Muljadi E. A Detailed Performance Model for Photovoltaic Systems. Preprint. *Solar Energy Journal*, 2012, 56 p.

Received 20.05.2023
Accepted 15.07.2023
Published 02.01.2024

Kamel Latreche[1]*, PhD Student,*
Rachid Taleb[2]*, Professor,*
Abderrahim Bentaallah[1]*, Professor,*
Alla Eddine Toubal Maamar[3]*, Assistant Professor,*
M'hamed Helaimi[2]*, Professor,*
Fayçal Chabni[4]*, Assistant Professor,*
[1] Electrical Engineering Department, Djillali Liabes University, Intelligent Control and Electrical Power Systems Laboratory (ICEPS), Sidi Bel Abbes, Algeria,
e-mail: ka.latreche02@gmail.com (Corresponding Author); bentaallah65@yahoo.fr
[2] Electrical Engineering Department,
Hassiba Benbouali University,
Laboratoire Génie Electrique et Energies Renouvelables (LGEER), Chlef, Algeria.
e-mail: rac.taleb@gmail.com; halimi1976@yahoo.fr
[3] Electrical Systems Engineering Department, Faculty of Technology, M'hamed Bougara University, Boumerdes, Algeria,
e-mail: allaeddine140dz@gmail.com
[4] Electronics Department,
Abdellah Morseli University Center, Tipaza, Algeria,
e-mail: fayssalc@gmail.com

How to cite this article:
Latreche K., Taleb R., Bentaallah A., Toubal Maamar A.E., Helaimi M., Chabni F. Design and experimental implementation of voltage control scheme using the coefficient diagram method based PID controller for two-level boost converter with photovoltaic system. *Electrical Engineering & Electromechanics*, 2024, no. 1, pp. 3-9. doi: https://doi.org/10.20998/2074-272X.2024.1.01

UDC 621.3 https://doi.org/10.20998/2074-272X.2024.1.02

G. Srinivas, G. Durga Sukumar, M. Subbarao

Total harmonic distortion analysis of inverter fed induction motor drive using neuro fuzzy type-1 and neuro fuzzy type-2 controllers

Introduction. *When the working point of the indirect vector control is constant, the conventional speed and current controllers operate effectively. The operating point, however, is always shifting. In a closed-system situation, the inverter measured reference voltages show higher harmonics. As a result, the provided pulse is uneven and contains more harmonics, which enables the inverter to create an output voltage that is higher.* ***Aim.*** *A space vector modulation (SVM) technique is presented in this paper for type-2 neuro fuzzy systems. The inverter's performance is compared to that of a neuro fuzzy type-1 system, a neuro fuzzy type-2 system, and classical SVM using MATLAB simulation and experimental validation.* ***Methodology.*** *It trains the input-output data pattern using a hybrid-learning algorithm that combines back-propagation and least squares techniques. Input and output data for the proposed technique include information on the rotation angle and change of rotation angle as input and output of produced duty ratios. A neuro fuzzy-controlled induction motor drive's dynamic and steady-state performance is compared to that of the conventional SVM when using neuro fuzzy type-2 SVM the induction motor, performance metrics for current, torque, and speed are compared to those of neuro fuzzy type-1 and conventional SVM.* ***Practical value.*** *The performance of an induction motor created by simulation results are examined using the experimental validation of a dSPACE DS-1104. For various switching frequencies, the total harmonic distortion of line-line voltage using neuro fuzzy type-2, neuro fuzzy type-1, and conventional based SVMs are provided. The 3 hp induction motor in the lab is taken into consideration in the experimental validations.* References 22, tables 3, figures 15.
Key words: **space vector modulation, neuro fuzzy type-1, neuro fuzzy type-2, induction motor, total harmonic distortion.**

Вступ. *Коли робоча точка непрямого векторного управління стала, традиційні регулятори швидкості та струму працюють ефективно. Проте робоча точка постійно змінюється. У ситуації закритої системи виміряна інвертором опорна напруга показує вищі гармоніки. В результаті імпульс, що подається, нерівномірний і містить більше гармонік, що дозволяє інвертору створювати більш високу вихідну напругу.* ***Мета***. *У цій статті представлена методика просторової векторної модуляції (SVM) для нейронечітких систем типу 2. Продуктивність інвертора порівнюється з продуктивністю нейронечіткої системи типу 1, нейронечіткої системи типу 2 та класичної SVM з використанням моделювання MATLAB та експериментальної перевірки.* ***Методологія***. *Навчається шаблон даних введення-виводу, використовуючи алгоритм гібридного навчання, який поєднує у собі методи зворотного поширення помилки та методу найменших квадратів. Вхідні та вихідні дані для запропонованої методики включають інформацію про кут повороту і зміну кута повороту як отримані вхідні і вихідні коефіцієнти заповнення. Динамічні характеристики приводу асинхронного двигуна з нейронечітким управлінням порівнюються з характеристиками звичайного SVM. При використанні нейронечіткого SVM типу 2 асинхронний двигун, показники продуктивності по струму обертаючого моменту і швидкості порівнюються з показниками приводу асинхронного двигуна з нейронечітким управлінням типу 1 та традиційного SVM.* ***Практична цінність***. *Продуктивність асинхронного двигуна, створеного за результатами моделювання, досліджується з використанням експериментальної перевірки dSPACE DS-1104. Для різних частот перемикання розраховуються загальні гармонічні спотворення лінійної напруги з використанням нейронечіткого управління типу 2, нейронечіткого управління типу 1 і традиційного SVM. Асинхронний двигун потужністю 3 л.с. у лабораторії враховується під час експериментальних перевірок.* Бібл. 22, табл. 3, рис. 15.
Ключові слова: **просторово-векторна модуляція, нейронечіткий тип 1, нейронечіткий тип 2, асинхронний двигун, повне гармонійне спотворення.**

1. Introduction. Space vector modulation (SVM) is a technique for managing the pulse width modulation method used to regulate the inverter-fed induction motor (IM). At the turning points, which are caused by space vector instants, the pulse width modulated voltage source inverter is used. In compared to the straightforward sinusoidal approach, switching times are reduced and current and torque ripple are decreased [1]. For both linear and non-linear modes of operation, the digital implementation is a technique utilized in transient simulation. SVM is a method for implementing optimum bus voltage utilization and support for the harmonic spectrum utilized in current applications is explained in [2]. To reduce ripple in torque and current, the adaptive neuro fuzzy interference system based on maximum power point tracking is presented for IM driving in MATLAB/Simulink and is confirmed using an experimental setup utilising the hardware D-space (1104) is discuss in [3]. The type-2 fuzzy logic direct torque control technique is implemented because of the replacement of proportional-integral controllers. Using the control technique, the reaction improved in both transient and steady state conditions. Under various operating conditions, it also reduces torque ripple and flux distortion in contrast to the regular direct torque control [4]. Instead of using filters to reduce torque ripple like standard propositional integral controllers, adaptive neuro fuzzy interference system current controllers are employed for an indirect vector of an inverter driven IM. The performance of the drive is simulated under various operating conditions [5].To reduce switching losses and output voltage distortion from the created SVM algorithm, the proposed method uses variable frequency modulation to voltage source inverter fed IM [6]. Instead of a proposal integral controller with no filter, a neuro fuzzy torque controller is employed to eliminate torque ripple. The SVM approach is also suggested, although information is required to calculate the sector and angle [7]. For the error inside the boundary, an *n*-level voltage source inverter fed with current error space vector hysteresis is used as the current controller. The advantage of the hysteresis controller is that it transitions from linear to over modulation smoothly. It has also been confirmed by experimental validation with steady and transient performances. [8]. For the voltage source inverter fed IM drive, type-2 fuzzy-based methodology has been used. The technique has been compared to traditional SVM for performance and is independent of switching frequency. [9]. The adaptive-

network-based fuzzy inference system based SVM is not required to predict the switching frequency or required training error when using the SVM method. This is the reason why, in contrast to other optimization strategies like genetic, neural and fuzzy [10]. The development of a technology known as constant switching frequency torque control can be used to manage torque in both steady state and dynamic conditions. For calculating the torque ripple and angular velocity, it employs flux error vector-based SVM [11]. Fast switching frequency is implemented using the artificial neural network SVM based fed voltage source inverter, which leads to dynamic operation of the IM drive under linear region to square wave. [12]. SVM based on neuro fuzzy and three-level inverter fed voltage source used to implement improved constant and dynamic performance of the IM drive. The suggested method generates an output with the proper duty ratios by changing the input space-vector angle. The neural network with a specific integrated circuit chip is used to easily implement the SVM algorithm. [13, 14].The recommended artificial neural network with SVM-based voltage source inverter fed IM drive estimate a variety of outputs without regard to switching frequency [15]. The five-layer network fed into the neuro fuzzy SVM-based inverter produces output that is trained duty ratios from input from V_{ds} and V_{qs}. Simulation and experimental validation can be used to estimate the total harmonic distortion (THD) computation for various switching frequencies [16]. For a wind turbine with a doubly fed induction generator, use SVM. The method is used for minimizing the harmonic distortion of stator currents under various wind speed [17].

2. Mathematical modelling of IM. Using direct-quadrature (*d-q*) stationary references, a mathematical model of a three-phase squirrel cage IM was developed [18].

$$\frac{\mathrm{d}i_{ds}}{\mathrm{d}t} = -\frac{1}{\sigma L_s}\left(R_s + \frac{L_m^2}{L_r^2}\right) i_{ds} + \frac{1}{\sigma L_s}\frac{L_m R_r}{L_r^2}\psi_{dr} + \\ + \frac{pL_m}{\sigma L_s L_r}\omega_r \psi_{dr} + \frac{V_{ds}}{\sigma L_s}; \quad (1)$$

$$\frac{\mathrm{d}i_{qs}}{\mathrm{d}t} = -\frac{1}{\sigma L_s}\left(R_s + \frac{L_m^2}{L_r^2}R_r\right) i_{qs} + \frac{1}{\sigma L_s}\frac{L_m R_r}{L_r^2}\psi_{qr} - \\ - \frac{pL_m}{\sigma L_s L_r}\omega_r \psi_{dr} + \frac{V_{qs}}{\sigma L_s}; \quad (2)$$

$$\frac{\mathrm{d}\psi_{dr}}{\mathrm{d}t} = -\frac{R_r}{L_r}\psi_{dr} - p\omega_r \psi_{qr} + \frac{L_m R_r}{L_r} i_{ds}; \quad (3)$$

$$\frac{\mathrm{d}\psi_{qr}}{\mathrm{d}t} = -\frac{R_r}{L_r}\psi_{qr} + p\omega_r \psi_{dr} + \frac{L_m R_r}{L_r} i_{qs}; \quad (4)$$

$$\frac{\mathrm{d}\omega_r}{\mathrm{d}t} = -\frac{B}{J}\omega_r + \frac{1}{J}(T_e - T_l), \quad (5)$$

where $\sigma = (1 - L_m^2/L_s L_r)$ is the leakage coefficient; i_{ds}, i_{dr} are the stator currents of *d-q* axis; R_s, R_r are the stator and rotor resistances; V_{ds}, V_{dr} are the stator voltage of *d-q* axis; L_s, L_r are the stator and rotor inductances; ψ_{ds}, ψ_{dr} are the rotor fluxes of *d-q* axis; L_m, ω_r, p are the magnetizing inductance, rotor speed and number of poles; B is the damping coefficient; J is the moment of inertia; T_e, T_l are the electromagnetic and load torques.

3. Mathematically modulated two level inverter. Variable speed drives use pulse width modulation, which is regulated using a method known as space vector. The states of a two-level inverter are flipped using these various vectors. The connection diagram of two level inverter and space vector diagram is presented in Fig. 1. Choosing the V_0 and V_7 vectors results in a voltage that is zero. The remaining vectors V_1 to V_6 are chosen to provide the induction machine with the necessary voltage.

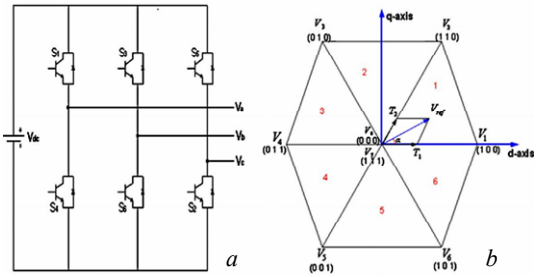

Fig. 1 Two level inverter (*a*) and space vector diagram with active vectors (*b*)

The reference voltage V_{ref}, which has a constant value, is created by combining the nearest two active vectors V_n and V_{n+1}, with zero vectors (V_0 and V_7). By merging two active vectors, effective vectors can be employed to achieve the desired results. The block diagram of proposed SVM based inverter control using neuro fuzzy type-2 (NFT2) is shown in Fig. 2.

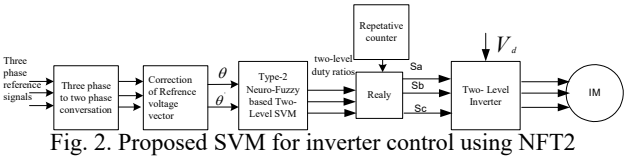

Fig. 2. Proposed SVM for inverter control using NFT2

The following can be inferred from mentioned concept of the necessary mean voltage and unit sample time for the reference vector:

$$V_{ref} = (T_1 V_n + T_2 V_{n+1})/T_s, \quad (7)$$

where T_1, T_2 represent the V_1-V_6 sector's active times.

While the equation are being equated, along the direct axis is

$$V_{ref}\cos\alpha T_s = V_{dc}T_1 + (V_{dc}\cos(\pi/3))T_2. \quad (8)$$

As the equation are being equated along the quadrature axis:

$$V_{ref}\sin\alpha T_s = V_{dc}T_1 + (V_{dc}\sin(\pi/3))T_2, \quad (9)$$

where V_{dc} is the magnitude of each active vector; V_{ref} is the angle of 60° sector with respect to the sector's beginning V_1-V_6;

$$T_1 = M\frac{\sin(\pi/3 - \alpha)}{\sin(\pi/3)}T_s; \quad (10)$$

$$T_2 = M\frac{\sin\alpha}{\sin(\pi/3)}T_s; \quad (11)$$

$$T_0 = T_s - T_1 - T_2, \quad (12)$$

where T_s is the sampling period; T_0 is the duration of zero vector and M is the modulation index and is given by V_{ref}/V_{dc}. The ripple value decreases to zero when time is divided uniformly.

4. Modified NFT2 based SVM. In order to develop a NFT2 system, the IF-THEN rules are used which have antecedent and consequent sections with type-2 fuzzy values. Uncertainties in fuzzy sets of Gaussian type-2 can be connected to the mean and standard deviation.

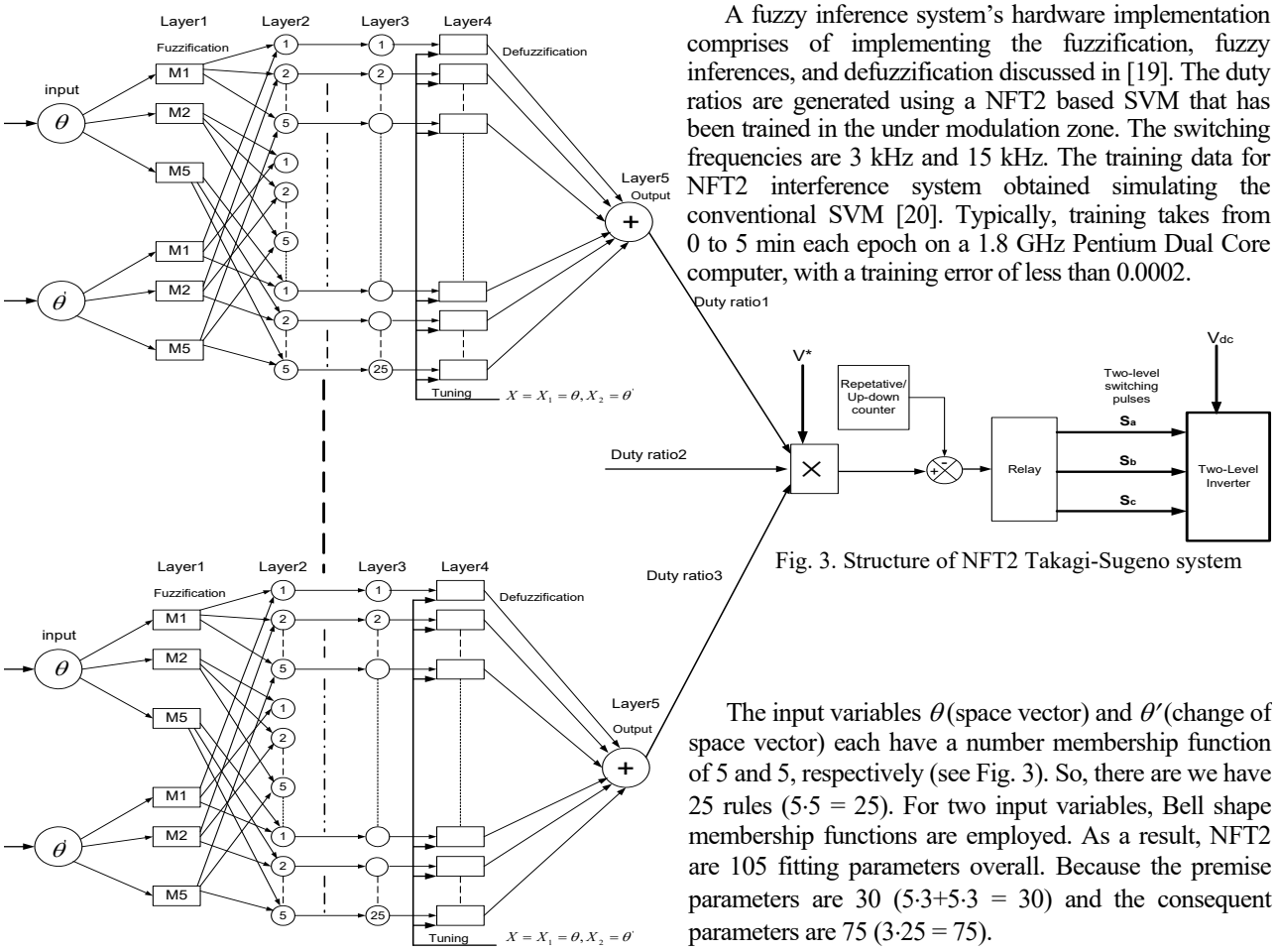

Fig. 3. Structure of NFT2 Takagi-Sugeno system

A fuzzy inference system's hardware implementation comprises of implementing the fuzzification, fuzzy inferences, and defuzzification discussed in [19]. The duty ratios are generated using a NFT2 based SVM that has been trained in the under modulation zone. The switching frequencies are 3 kHz and 15 kHz. The training data for NFT2 interference system obtained simulating the conventional SVM [20]. Typically, training takes from 0 to 5 min each epoch on a 1.8 GHz Pentium Dual Core computer, with a training error of less than 0.0002.

The input variables θ (space vector) and θ' (change of space vector) each have a number membership function of 5 and 5, respectively (see Fig. 3). So, there are we have 25 rules (5·5 = 25). For two input variables, Bell shape membership functions are employed. As a result, NFT2 are 105 fitting parameters overall. Because the premise parameters are 30 (5·3+5·3 = 30) and the consequent parameters are 75 (3·25 = 75).

5. Results and discussions. In the direct torque control concept, using a proportional integral speed controller causes a loss of decoupling with respect to parameter fluctuations [21]. The performance characteristics of an IM have been studied using proportional integral, neuro fuzzy type-1 (NFT1), and NFT2 SVM-based controllers in a different operating condition, i.e. steady state and step change. The command speed of the 3 hp IM is 157 rad/s (1500 rpm). The parameters of the IM are shown in Table 1.

Table 1

Parameters of the IM

Motor power	2.2 kW (3 hp), 400 V
Number of the poles p	4
Inverter switching frequencies, kHz	3 and 15
DC link voltage, V	150
Modulation index	0.86
Stator resistance R_s, Ω	0.55
Stator inductance L_s, mH	93.38
Rotor resistance R_r, Ω	0.78
Rotor inductance L_r, mH	93.36
Magnetizing inductance L_m, mH	90.5
Moment of inertia J, kg·m^2	0.019
Damping coefficient B	5·10^{-5}

5.1 Inverter line-to-line voltage and harmonic spectrum switching frequency of 3 kHz.

For DC link voltage 150 V the fundamental line voltage increased by 0.56 % in NFT2 as compared with conventional based SVM (see Fig. 4,*a*,*c*) and 0.44 % increased as compared NFT1 based SVM (see Fig. 4,*b*,*c*).

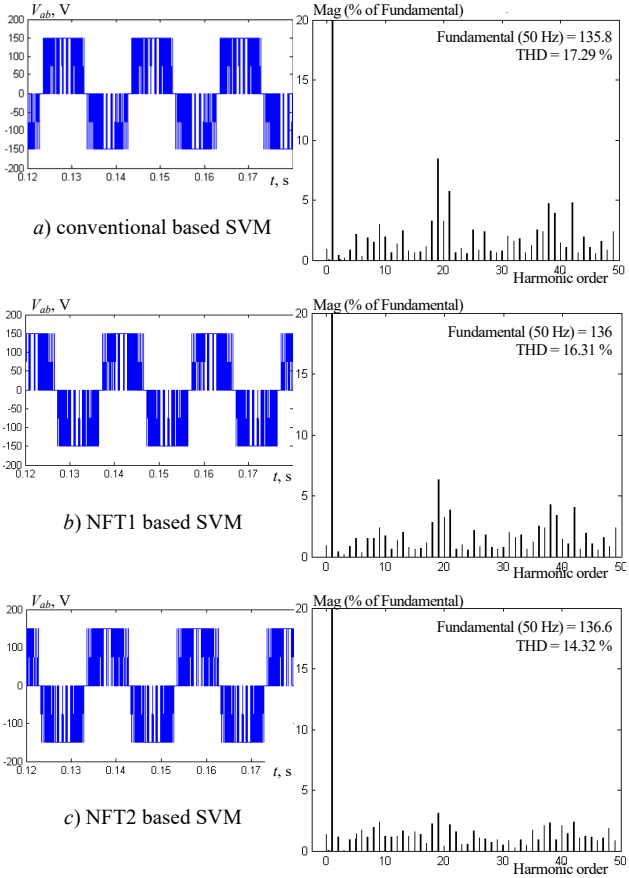

a) conventional based SVM

b) NFT1 based SVM

c) NFT2 based SVM

Fig. 4. Inverter line to-line voltage and harmonic spectrum at switching frequency of 3 kHz

In comparison to NFT1 SVM and conventional SVM, the 5th and 7th harmonics are decreased in NFT2 SVM. Comparing NFT2 based SVM to NFT1 based SVM and conventional SVM, the THD was also lowered (see Table 2)

Table 2

THD comparison at 3 kHz

No	Parameter	Conventional SVM	NFT1 based SVM	NFT2 based SVM
1	Fundamental line voltage (peak), V	135.8	136	136.6
2	5th harmonic, %	2.13	1.98	1.87
3	7th harmonic, %	1.86	1.55	1.1
4	THD, %	17.29	16.31	14.32

5.2 Performance of IM (switching frequency 3 kHz).

1. Operation during steady state. IM steady state torque ripple decreased from 2.2 N·m to 1 N·m in NFT2 based SVM as compared to conventional based SVM (see Fig. 5,*a*,*c*). Similarly, torque ripple reduced from 2.2 N·m to 2 N·m in NFT2 as compared with NFT1 based SVM (see Fig. 5,*b*,*c*). The speed response reaches early in NFT2 based SVM compared with NFT1 and conventional based SVM (see Fig. 5,*c*). SVM technique and fuzzy logic control are used in two distinct direct torque control methods, which are described in [22].

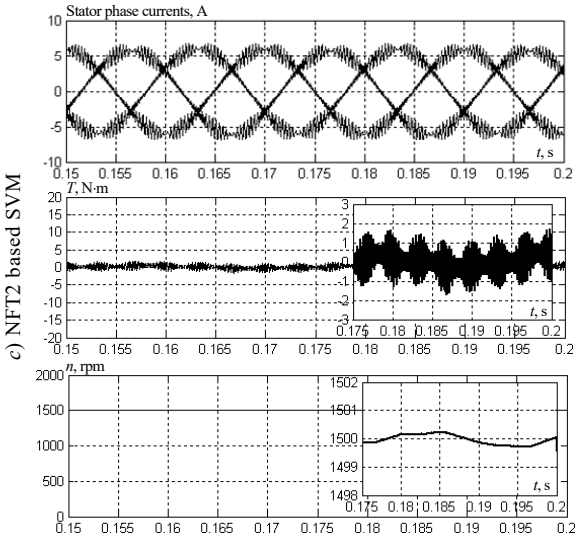

Fig. 5. IM performance at 3 kHz during steady state operation

2. During step change operation. When compared to conventional SVM, an IM is operating during a step change, the torque ripple is reduced from 17.5 N·m to 15 N·m in NFT2 based SVM (see Fig. 6,*a*,*c*). Similarly as compared to NFT1 based SVM, torque ripple reduced from 17 N·m to 15 N·m (see Fig. 6,*b*,*c*).

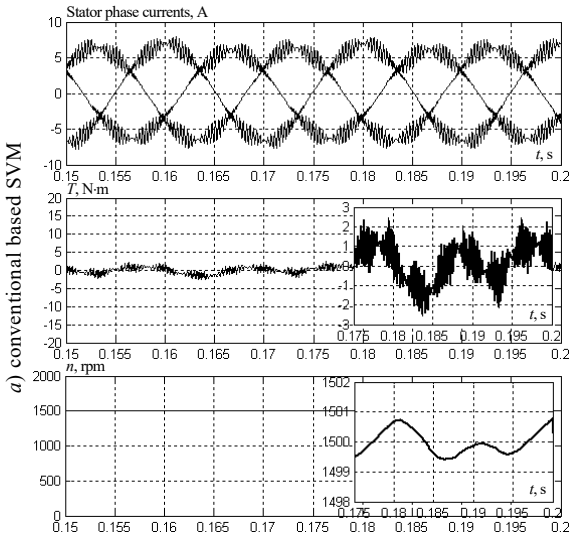

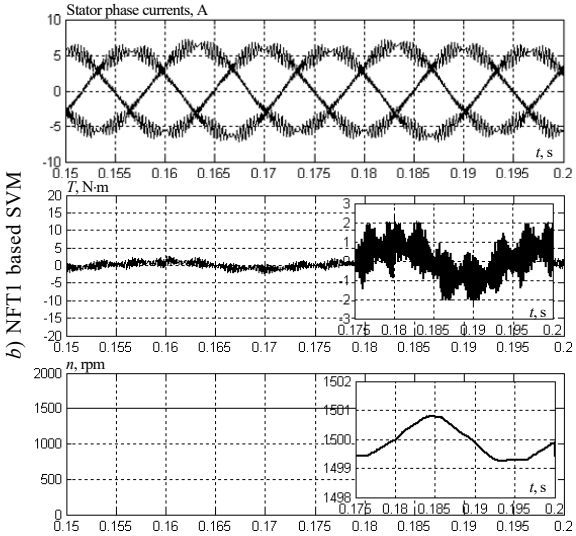

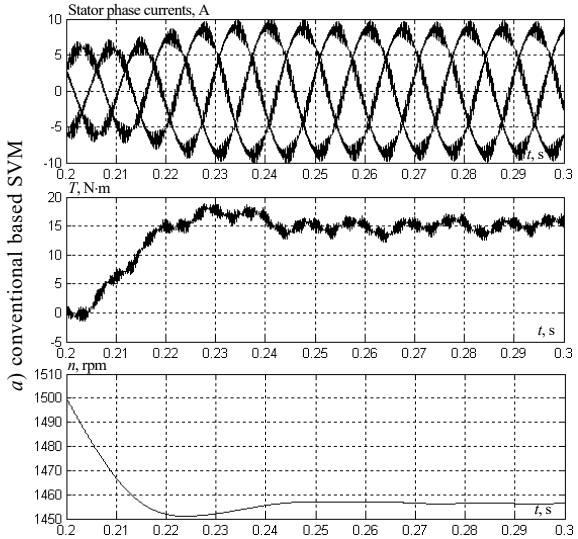

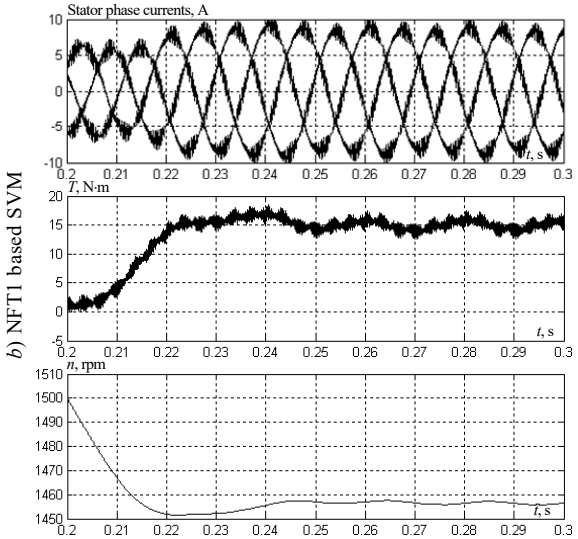

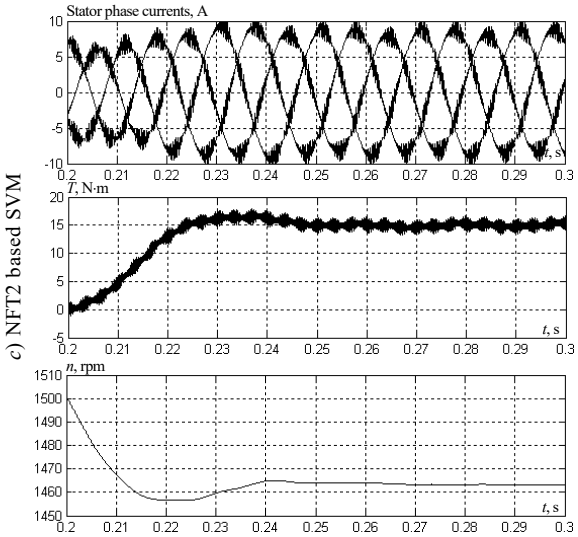

Fig. 6. Performance of a step change IM running at 3 kHz

The torque ripple reduced by 16.66 % in NFT2 based SVM. When compared to NFT1 and conventional SVM, the stator current increased by 33.33 % in NFT2 based SVM (Fig. 6,*c*). The quick response arrives before time (see Fig. 6,*c*).

5.3 Inverter line-to-line voltage and harmonic spectrum at switching frequency of 15 kHz.

The fundamental line voltage increased by 0.87 % in NFT2 as compared with conventional SVM (see Fig. 7,*a*,*c*).

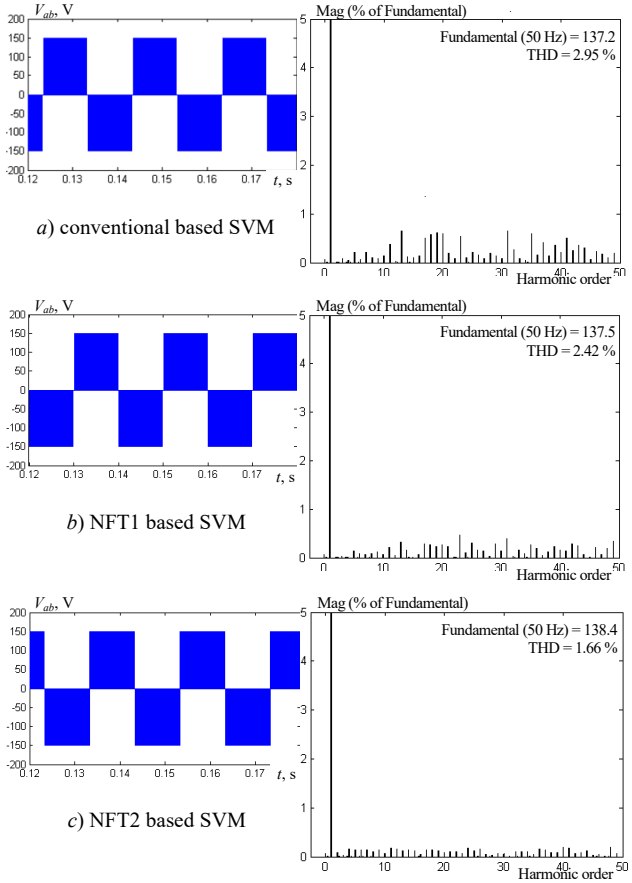

Fig. 7. Inverter line-to-line voltage and harmonic spectrum at switching frequency of 15 kHz

Similarly, in NFT2 based SVM the fundamental line voltage increased by 0.65 % as compared with NFT1 based SVM (see Fig. 7,*b*,*c*). For a 150 V DC inverter, NFT2 based SVM reduces the 5th and 7th harmonic as comparing with conventional and NFT1 based SVM, the overall THD was similarly lower (see Table 3).

Table 3

Comparison of THD at 15 kHz

No	Parameter	Conventional SVM	NFT1 based SVM	NFT2 based SVM
1	Fundamental line voltage (peak), V	137.2	137.5	138.4
2	5th harmonic, %	1.2	0.2	0.14
3	7th harmonic, %	0.47	0.31	0.06
4	THD, %	2.95	2.42	1.66

5.4 Performance of IM (switching frequency 15 kHz). Operation during steady state. When compared to conventional SVM, the torque ripple caused by an IM operating in steady state is reduced (1.5 N·m to 0.5 N·m) by 66.665 % in NFT2 (see Fig. 8,*a*,*c*). Similarly, in NFT2 based SVM, the ripple in torque reduced (0.8 N·m to 0.5 N·m) by 0.375 % as compared with NFT1 based SVM (see Fig. 8,*b*,*c*). The ripple in the stator current was also reduced by 0.37 %, and the speed response arrived earlier (see Fig. 8,*c*).

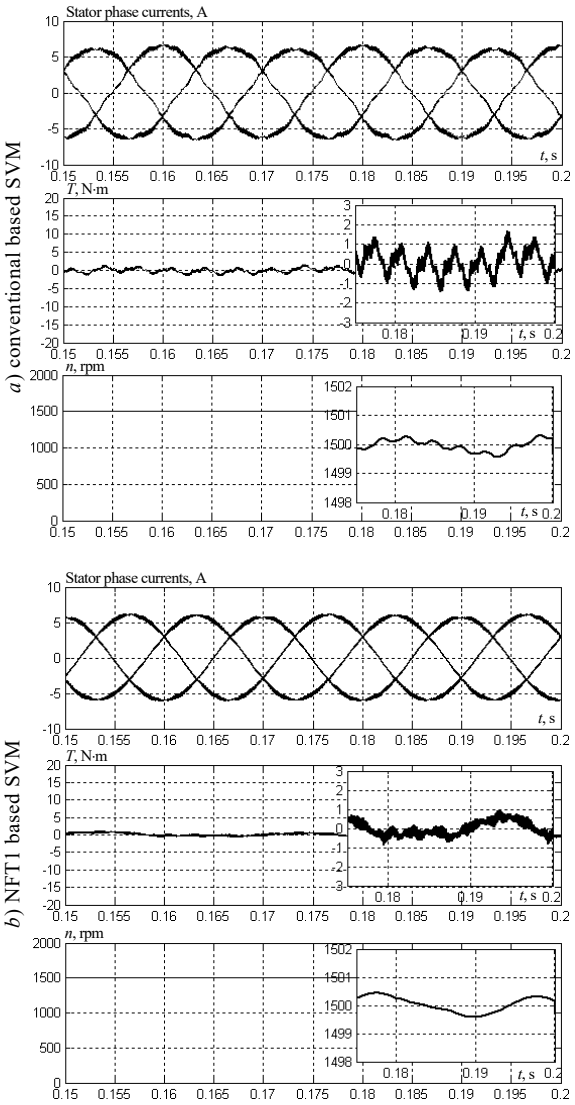

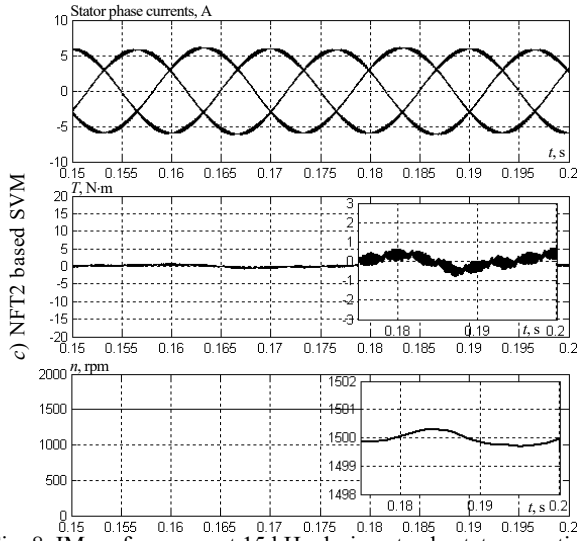

Fig. 8. IM performance at 15 kHz during steady state operation

6. Experimental validation. A dSPACE DS-1104 is employed to carry out the NFT2 based SVM algorithm in real time. The initial development of the control algorithm takes place in MATLAB/Simulink. By using MATLAB's real time workshop, automatic *C* code generation for real time implementation is accomplished. The experimental setup is shown in Fig. 9.

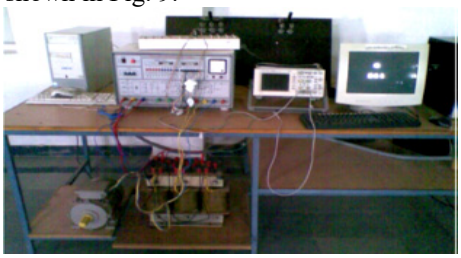
Fig. 9. Experimental setup

6.1 Line–to-line voltage at 3 kHz. The THD value also reduced in NFT2 based SVM as compared with NFT1 based SVM and conventional SVM (Fig. 10-12, where 1 div is 50 V).

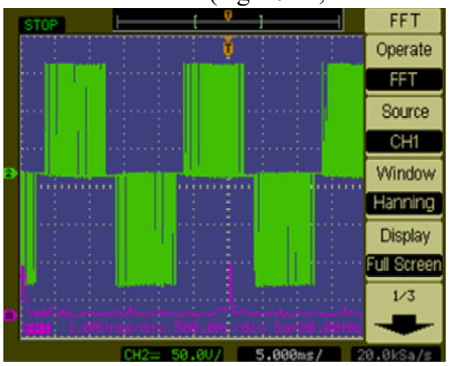

Fig. 10. Conventional SVM

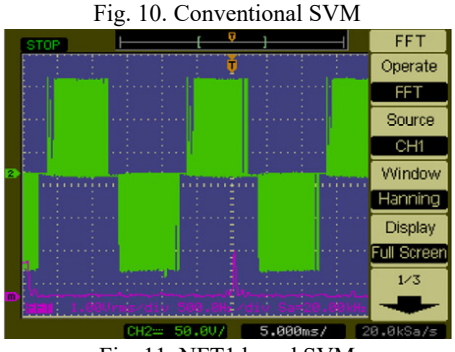

Fig. 11. NFT1 based SVM

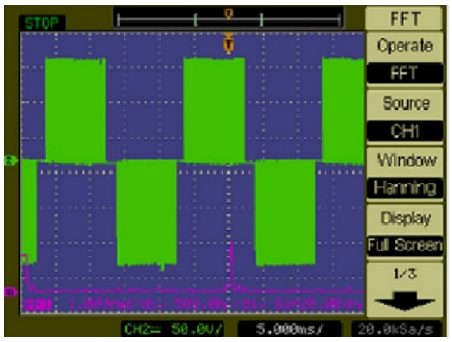

Fig. 12. NFT2 based SVM

6.2 Speed response of IM drive. Finally, Fig. 13-15 present the speed response reaches early in NFT2 based SVM as compared with NFT1 based SVM and conventional based SVM. The performance of IM drive improved under steady state operation and step change operation.

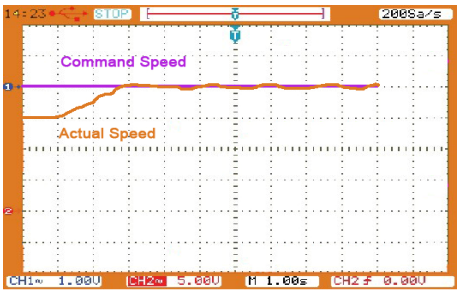

Fig. 13. Conventional based SVM

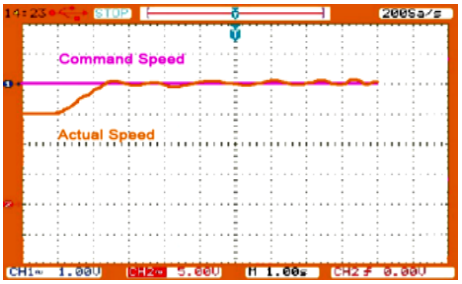

Fig. 14. NFT1 based SVM

Fig. 15. NFT2 based SVM

7. Conclusions. A dynamic response of the induction motor (IM) has been seen while comparing the recommended neuro fuzzy type-2 (NFT2) space vector modulation (SVM) based controller to the conventional based SVM and neuro fuzzy type-1 (NFT1) based SVM controllers.

The performance of NFT1 controllers based SVM IM drive under various operating conditions with switching frequency at 3 and 15 kHz examined. The fundamental line voltage is 0.14 % increase in NFT1 based SVM as compared with conventional SVM. The 5^{th}, 7^{th} harmonic components are reduced by 7.04 %, 16.66 % respectively in NFT1 based SVM as compared with conventional SVM. The total harmonic distortion (THD) in NFT1 based SVM reduced by 5.66 % as compared with conventional SVM.

Similarly, IM drive operates under 15 kHz operation the fundamental line voltage is increased by 0.21 % as compared with conventional SVM. The 5^{th} , 7^{th} harmonic components are reduced by 83.33 %, 34.04 % respectively in NFT1 based SVM as compared with conventional SVM. The THD in NFT1 based SVM reduced by 17.96 % as compared with conventional SVM.

The experimental implementation of the IM drive with conventional SVM, NFT1 and NFT2 controllers based SVM examine at switching frequency 3 kHz using dSPACE DS-1104. The inverter line voltage V_{ab} THD value reduced by 23.1 %, 9.65 % in NFT2 SVM by as compared with conventional SVM, NFT1 SVM respectively. The inverter line voltage V_{bc} THD value is reduced by 18.9 % in NFT2 SVM by as compared with conventional SVM. The inverter line voltage V_{ca} THD value is reduced by 23.1 %, 9.65 % in NFT2 SVM by as compared with conventional SVM, NFT1 SVM respectively.

The dynamic performance of IM drive improved with NFT2 based SVM as compared with NFT1 and conventional based SVM.

Conflict of interest: The authors declare that they have no conflicts of interest.

REFERENCES

1. Van der Broeck H.W., Skudelny H.-C., Stanke G.V. Analysis and realization of a pulsewidth modulator based on voltage space vectors. *IEEE Transactions on Industry Applications*, 1988, vol. 24, no. 1, pp. 142-150. doi: https://doi.org/10.1109/28.87265.

2. Mehrizi-Sani A., Filizadeh S. Digital implementation and transient simulation of space-vector modulated converters. *2006 IEEE Power Engineering Society General Meeting*, 2006, pp. 1-7. doi: https://doi.org/10.1109/PES.2006.1709108.

3. Pakkiraiah B., Durga Sukumar G. Enhanced Performance of an Asynchronous Motor Drive with a New Modified Adaptive Neuro-Fuzzy Inference System-Based MPPT Controller in Interfacing with dSPACE DS-1104. *International Journal of Fuzzy Systems*, 2017, vol. 19, no. 6, pp. 1950-1965. doi: https://doi.org/10.1007/s40815-016-0287-5.

4. Venkataramana Naik N., Singh S.P. Improved Torque and Flux Performance of Type-2 Fuzzy-based Direct Torque Control Induction Motor Using Space Vector Pulse-width Modulation. *Electric Power Components and Systems*, 2014, vol. 42, no. 6, pp. 658-669. doi: https://doi.org/10.1080/15325008.2013.871608.

5. Durgasukumar G., Pathak M.K. Neuro-fuzzy-based torque ripple reduction and performance improvement of VSI fed induction motor drive. *International Journal of Bio-Inspired Computation*, 2012, vol. 4, no. 2, pp. 63-72. doi: https://doi.org/10.1504/IJBIC.2012.047174.

6. Attaianese C., Nardi V., Tomasso G. Space Vector Modulation Algorithm for Power Losses and THD Reduction in VSI Based Drives. *Electric Power Components and Systems*, 2007, vol. 35, no. 11, pp. 1271-1283. doi: https://doi.org/10.1080/15325000701351724.

7. Durgasukumar G., Pathak M.K. Neuro-fuzzy-based space vector modulation for THD reduction in VSI fed induction motor drive. *International Journal of Power Electronics*, 2012, vol. 4, no. 2, pp. 160-180. doi: https://doi.org/10.1504/IJPELEC.2012.045629.

8. Dey A., Rajeevan P.P., Ramchand R., Mathew K., Gopakumar K. A Space-Vector-Based Hysteresis Current Controller for a General n-Level Inverter-Fed Drive With Nearly Constant Switching Frequency Control. *IEEE Transactions on Industrial Electronics*, 2013, vol. 60, no. 5, pp. 1989-1998. doi: https://doi.org/10.1109/TIE.2012.2200217.

9. Durgasukumar G., Abhiram T., Pathak M.K. TYPE-2 Fuzzy based SVM for two-level inverter fed induction motor drive. *2012 IEEE 5th India International Conference on Power Electronics (IICPE)*, 2012, pp. 1-6. doi: https://doi.org/10.1109/IICPE.2012.6450468.

10. Durgasukumar G., Ramanjan Prasad R. Torque ripple minimization of vector controlled VSI Induction Motor Drive using Neuro-Fuzzy Controller. *International Journal of Advances in Engineering Sciences*, 2011, vol. 1, no. 1, pp. 40-43.

11. Tripathi A., Khambadkone A.M., Panda S.K. Torque Ripple Analysis and Dynamic Performance of a Space Vector Modulation Based Control Method for AC-Drives. *IEEE Transactions on Power Electronics*, 2005, vol. 20, no. 2, pp. 485-492. doi: https://doi.org/10.1109/TPEL.2004.842956.

12. Kazmierkowski M.P., Da Silva L.E.B., Bose B.K., Pinto J.O.P. A neural-network-based space-vector PWM controller for voltage-fed inverter induction motor drive. *IEEE Transactions on Industry Applications*, 2000, vol. 36, no. 6, pp. 1628-1636. doi: https://doi.org/10.1109/28.887215.

13. Sukumar D., Jithendranath J., Saranu S. Three-level Inverter-fed Induction Motor Drive Performance Improvement with Neuro-fuzzy Space Vector Modulation. *Electric Power Components and Systems*, 2014, vol. 42, no. 15, pp. 1633-1646. doi: https://doi.org/10.1080/15325008.2014.927022.

14. Mondal S.K., Pinto J.O.P., Bose B.K. A neural-network-based space-vector PWM controller for a three-level voltage-fed inverter induction motor drive. *IEEE Transactions on Industry Applications*, 2002, vol. 38, no. 3, pp. 660-669. doi: https://doi.org/10.1109/TIA.2002.1003415.

15. Muthuramalingam A., Sivaranjani D., Himavathi S. Space Vector Modulation of a Voltage fed Inverter Using Artificial Neural Networks. *2005 Annual IEEE India Conference - Indicon*, 2005, pp. 487-491. doi: https://doi.org/10.1109/INDCON.2005.1590218.

16. Durgasukumar G., Pathak M.K. Comparison of adaptive Neuro-Fuzzy-based space-vector modulation for two-level inverter. *International Journal of Electrical Power & Energy Systems*, 2012, vol. 38, no. 1, pp. 9-19. doi: https://doi.org/10.1016/j.ijepes.2011.10.017.

17. Boukadoum A., Bouguerne A., Bahi T. Direct power control using space vector modulation strategy control for wind energy conversion system using three-phase matrix converter. *Electrical Engineering & Electromechanics*, 2023, no. 3, pp. 40-46. doi: https://doi.org/10.20998/2074-272X.2023.3.06.

18. Diab A.A.Z., Elsawy M.A., Denis K.A., Alkhalaf S., Ali Z.M. Artificial Neural Based Speed and Flux Estimators for Induction Machine Drives with Matlab/Simulink. *Mathematics*, 2022, vol. 10, no. 8, art. no. 1348. doi: https://doi.org/10.3390/math10081348.

19. Aib A., Khodja D.E., Chakroune S. Field programmable gate array hardware in the loop validation of fuzzy direct torque control for induction machine drive. *Electrical Engineering & Electromechanics*, 2023, no. 3, pp. 28-35. doi: https://doi.org/10.20998/2074-272X.2023.3.04.

20. Srinivas G., Sukumar G.D. A modified type-2 neuro-fuzzy SVM-based inverter fed IM drive. International *Journal of Power Electronics*, 2022, vol. 15, no. 3/4, pp. 267-289. doi: https://doi.org/10.1504/IJPELEC.2022.122406.

21. Guezi A., Bendaikha A., Dendouga A. Direct torque control based on second order sliding mode controller for three-level inverter-fed permanent magnet synchronous motor: comparative study. *Electrical Engineering & Electromechanics*, 2022, no. 5, pp. 10-13. doi: https://doi.org/10.20998/2074-272X.2022.5.02.

22. Moussaoui L. Performance enhancement of direct torque control induction motor drive using space vector modulation strategy. *Electrical Engineering & Electromechanics*, 2022, no. 1, pp. 29-37. doi: https://doi.org/10.20998/2074-272X.2022.1.04.

Received 03.06.2023
Accepted 30.08.2023
Published 02.01.2024

G. Srinivas[1], *Research Scholar*,
G. Durga Sukumar[2], *Professor*,
M. Subbarao[1], *Associative Professor*,
[1] Electrical and Electronics Engineering Department,
Vignan's Foundation for Science, Technology and Research University, Vadlamudi, Guntur 522213, India,
e-mail: gadde.cnu@gmail.com (Corresponding Author);
msr_eee@vignan.ac.in
[2] Vignan Institute of Technology and Science, Deshmukhi, 508284 Telangana, India,
e-mail: durgasukumar@gmail.com

How to cite this article:
Srinivas G., Durga Sukumar G., Subbarao M. Total harmonic distortion analysis of inverter fed induction motor drive using neuro fuzzy type-1 and neuro fuzzy type-2 controllers. *Electrical Engineering & Electromechanics*, 2024, no. 1, pp. 10-16. doi: https://doi.org/10.20998/2074-272X.2024.1.02

UDC 621.3 https://doi.org/10.20998/2074-272X.2024.1.03

G. Themozhi, K. Srinivasan, T. Arun Srinivas, A. Prabha

Analysis of suitable converter for the implementation of drive system in solar photovoltaic panels

Introduction. *Photovoltaic (PV) systems gained immense attraction in the recent years since it produces electricity without causing environmental pollution through direct conversion of solar irradiance into electricity. Solar PV panels produce DC power. The magnitude of this DC power varies with temperature and irradiance of the sun rays. The DC supply from solar panels can be regulated using DC-DC converter and then can further be converted into the desired AC voltage by means of a voltage source inverter before being fed to an induction motor (IM). The speed and torque of an IM, fed from PV arrays, can vary due to the variation in the output power of the panels.* ***Goal*** *of this work is to improve the dynamic performance and reduce the torque ripple of Cuk converter-inverter fed IM drive system. The* ***novelty*** *of the current work proposes interleaved Cuk converter between solar PV DC source and the inverter.* ***Purpose.*** *To provide continuous current using an interleaved Cuk converter to the IM drive and in turn to reduce the torque ripple in IM.* ***Methodology****. Introduced an interleaved Cuk converter which is a blend of Cuk converters connected in parallel with each other between solar PV arrays and IM drive system.* ***Originality.*** *Simulation results are obtained for Cuk converter and interleaved Cuk converter fed IM drive by means of MATLAB. The hardware setup for the same IM systems is developed.* ***Practical value.*** *Simulation and hardware results are coincided with each other and it is subject from the simulation and hardware results that the interleaved Cuk converter-inverter fed IM system produced results superior than the Cuk converter inverter fed IM drive system.* References 25, table 2, figures 22.
Key words: **induction motor drive, interleaved Cuk converter, voltage source inverter.**

Вступ*. Фотоелектричні (ФЕ) системи набули величезної привабливості в останні роки, оскільки вони виробляють електроенергію, не викликаючи забруднення навколишнього середовища, за рахунок прямого перетворення сонячного випромінювання на електрику. Сонячні ФЕ панелі виробляють енергію постійного струму. Значення цієї потужності постійного струму залежить від температури та освітленості сонячних променів. Подача постійного струму від сонячних панелей може регулюватися за допомогою DC-DC перетворювача, а потім може бути перетворена в бажану змінну напругу за допомогою інвертора джерела напруги перед подачею на асинхронний двигун. Швидкість та обертаючий момент асинхронного двигуна, що живиться від ФЕ батарей, можуть змінюватися через зміну вихідної потужності панелей.* ***Метою*** *даної роботи є покращення динамічних характеристик та зменшення пульсацій обертаючого моменту системи приводу асинхронного двигуна з живленням від Cuk перетворювача-інвертора.* ***Новизна*** *цієї роботи пропонує Cuk перетворювач, що чергується, між сонячним ФЕ джерелом постійного струму та інвертором.* ***Мета****. Забезпечення безперервності струму за допомогою Cuk перетворювача, що чергується, для приводу асинхронного двигуна і, у свою чергу, зменшення пульсації обертаючого моменту в асинхронному двигуні.* ***Методологія****. Представлений Cuk перетворювач, що чергується, який являє собою суміш Cuk перетворювачів, підключених паралельно один до одного між сонячними ФЕ батареями і системою приводу асинхронного двигуна.* ***Оригінальність****. Результати моделювання отримані для Cuk перетворювача і приводу асинхронного двигуна з живленням Cuk перетворювача, що чергується, за допомогою MATLAB. Розроблено апаратну частину цих же асинхронних двигунів.* ***Практична цінність****. Результати моделювання та апаратного забезпечення збігаються один з одним, і з результатів моделювання та апаратного забезпечення випливає, що система асинхронного двигуна з живленням від Cuk перетворювача-інвертора, що чергується, дає результати, які перевищують результати, ніж система приводу асинхронного двигуна з живленням від Cuk перетворювача.* Бібл. 25, табл. 2, рис. 22.
Ключові слова: **привід асинхронного двигуна, Cuk перетворювач, що чергується, інвертор джерела напруги.**

1. Introduction. Photovoltaic (PV) systems gained immense attraction in the recent years since it produces electricity without causing environmental pollution through direct conversion of solar irradiance into electricity. This reality, together with constant decline in the cost incurred for PV arrays and increased efficiency which makes the next generation PV systems a preferable one. The capacity of PV cells relies upon a number of elements, for example, temperature, solar irradiance, daylight timings, soil condition, shadow timings and types of PV panels etc. The magnitude of this DC power varies with temperature and irradiance of the sun rays. DC supply from solar panels can be regulated using DC-DC converter and then can further be converted into the desired AC using a Voltage Source Inverter (VSI) before being feed to an induction motor (IM) for controlling its velocity and modes of operation.

The output from the PV system gets increased when utilizing a Cuk converter. With the help of a 3-phase VSI, the Cuk converter's output is upturned and pragmatically feed into a 3-phase IM. PV fed Cuk converter is permitted to make DC voltage as the input of inverter. In this way, the PV system's output is improved by using a Cuk converter. In general, the yield of the Cuk converter is reversed in an inverter-fed 3-phase IM.

By presenting a novel active clamper circuit, a converter circuit for electric vehicles (EVs) that achieves high efficiency and constant input current is demonstrated [1]. A modular multilevel inverter was designed using fuzzy logic technique for marine water pumping applications. A systematic method to attain Maximum Power Point Tracking (MPPT) for a PV fed IM support water pumping system was proposed [2]. Cuk converters were not employed in PV array-based water pumping systems prior to this study, despite the fact that they have various advantages and are a viable choice for utilisation when compared to other DC-DC converters. This study also proposed low-esteemed DC interface capacitor of VSI [3].

In order to eliminate the input current ripple at the selected duty cycle, two Cuk converters with positive and negative output voltage polarity are interleaved to create a buck-boost converter [4]. By calculating the quantity of inductors on the input side of both converters, the selective duty ratio can be calculated. The buck-boost converter uses output inductors to achieve low output current ripple and zero input current ripple. The converter's maximum voltage gain is straightforward and easy controlled [5].

A novel MPPT procedure for solar panels utilizing a SEPIC or Cuk converter was proposed. This study

proposed a novel method to leverage the highest result power from solar panels under differing environmental conditions. The study followed a methodology in which a pulse-width-modulated DC-DC SEPIC or Cuk converter was connected with a solar panel along with load or the battery bus [6]. The converter functions in a manner under discontinuous capacitor voltage mode, whereas the input current-fed switched inverter having single-stage, high boost inverter with buck-boost capability is reported for better electromagnetic interference noise immunity, wide input and output voltage range of operation, etc. A hybrid converter has been also developed to suit both AC and DC loads [7]. To enhance the robustness of a robotic system, a fractional PID control system is identified and analyzed. Control system parameters are obtained by employing recursive least-squares method [8]. Given attention on a 5 horse power, 110 V, 80 Hz IM that is appropriate for EV applications. High base frequency is utilised for uphill driving in order to maintain steady torque over a wider range. When developing the IM for an EV application, efficiency, power factor, and breakdown torque are taken into account [9]. It is said that an IM with four active and reactive power quadrants, a variable speed operation range, excellent energy efficiency, and better power quality. Because of its unique functions, this IM was specifically created for high-power wind energy conversion systems. Additionally, a three phase matrix converter is offered to lower the big harmonics [10].

Bridgeless Power Factor Correction (PFC), SEPIC and Cuk rectifiers were introduced that resulted in fewer amounts of conduction and switching losses). The study proposed novel bridgeless single-stage AC-DC PFC rectifiers in line with SEPIC and Cuk topologies. Due to the lack of input diode connect and since the two semiconductor switches are close proximity to the current streaming way, during each switching cycle, it ensures that the conduction losses get reduced while the thermal management is also increased in comparison with general SEPIC converter and Cuk PFC converter. The recommended topologies were proposed to exertion in DC motor to finish a next solitary control aspect in a flourishing method [11]. Model predictive control based field weakening algorithm is insisted to eliminate the DC-link disturbance in traction EV using a low-voltage IM [12]. A dynamic snubber zero voltage exchanging Cuk converter was planned, designed and executed [13]. The primary windings seemed to be series-connected in two transformers of the converter proposed in the study, while parallel connection was established between two half-wave rectifiers at output end in order to diminish the power stretches that occur in the transformer's secondary winding. The design and control of a single stage power controller used in a solar fed standalone application is given in [14]. A DC synchronous reference frame based controller is designed for the converter to normalize the yield voltage as per the requirement of the load [15]. Robust analysis on a non-linear system controlled by PID controller and FOPID controller were performed and compared their performance based on their ability to reject external disturbance. The performance of the controllers was done on the system based on their response for a step input [16-18]. There is a requirement to normalize the speed of IM while the guidelines for open loop Interleaved Cuk Converter-Inverter fed IM (ILCCIIM) seem impressive.

The review of literature is evident that the works conducted earlier missed to deal with ILCCIIM [19-25]. There is a requirement to regulate the speed of ILCCIIM system.

The goal of the article. The current work proposes interleaved Cuk converter between solar PV DC source and the inverter to regulate the speed and torque of the IM.

2. Selection of Cuk converter for IM drive system.

DC-DC Cuk converter. In general, DC-DC Cuk converter can work in both boost and buck modes. It further ensures the energy is flown in both directions i.e., between source and the load. Based on input voltage, the output voltage from Cuk converter remains negative. The converter can handle nonstop input voltage and persistent output current. The inductor, on the output side, is used for better output current. Likewise, on input side, it is used to support the voltage level. It is possible to make the Cuk converter function in either continuous conduction mode or in discontinuous conduction mode based on load requirements. Since the output current of the converter is discontinuous, in order to make it continuous and to meet the load current requirement of the IM, the Cuk converter can be interleaved. Here the *interleaving* means the parallel connection of Cuk converters by retaining the rating of the components like inductors and capacitors. This work concentrated on two stages of interleaved Cuk converter. If the number of stages is increased that will lead to increase in complexity and more switching loss. Hence two stages of interleaved Cuk converter are preferred here for the decide speed control of IM drive.

3. Proposed interleaved Cuk converter.

Output of Cuk converter. The production of all the Cuk converters is available as output for the load. The course of action of two converters makes the output in such a way that an interleaved Cuk converter turns into a single controlled device topology. The benefit of the proposed interleaved Cuk converter is the mitigation of torque ripples in the output.

The turn-around stream of current that emerges from load side to input side gets inhibited by the input side inductor. Figure 1 shows the proposed interleaved Cuk converter in which two Cuk converters are connected in parallel. Figure 2 shows the circuit diagram of converter-inverter fed IM system.

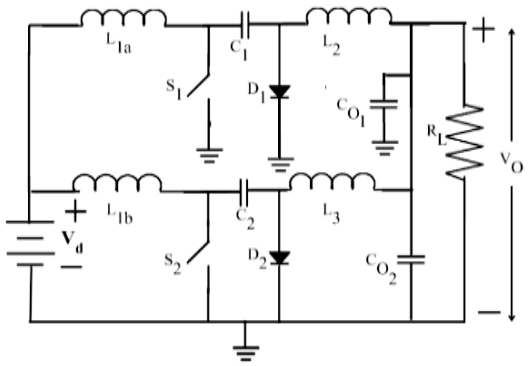

Fig. 1. Proposed interleaved Cuk converter

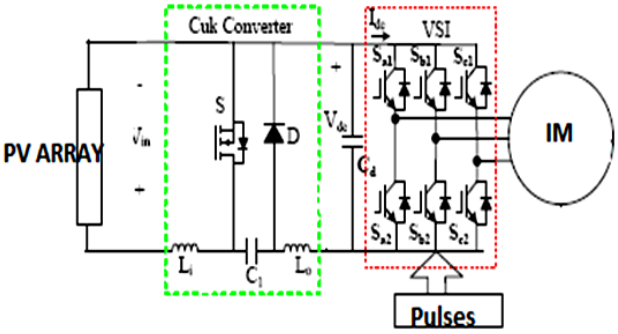

Fig. 2.Circuit diagram of Cuk converter-inverter fed IM

4. Simulation results of Cuk converter-inverter fed IM. The MATLAB/Simulink model is used to investigate the performance of the Cuk converter and interleaved converter circuit. The high gain interleaved Cuk converter has a 100 V input voltage and a 400 V output voltage. The switching frequency is held constant at 10 kHz.

The Cuk converter fed IM system created in MATLAB/Simulink is shown in Fig. 3. Figures 4, 5 illustrate the applied input voltage and the voltage across the Cuk converter, respectively. The applied input voltage is 150 V DC. The voltage across the Cuk converter is shown in Fig. 6. The Cuk converter's output voltage is 60 V. Figure 7 depicts the Cuk converter's voltage ripple.

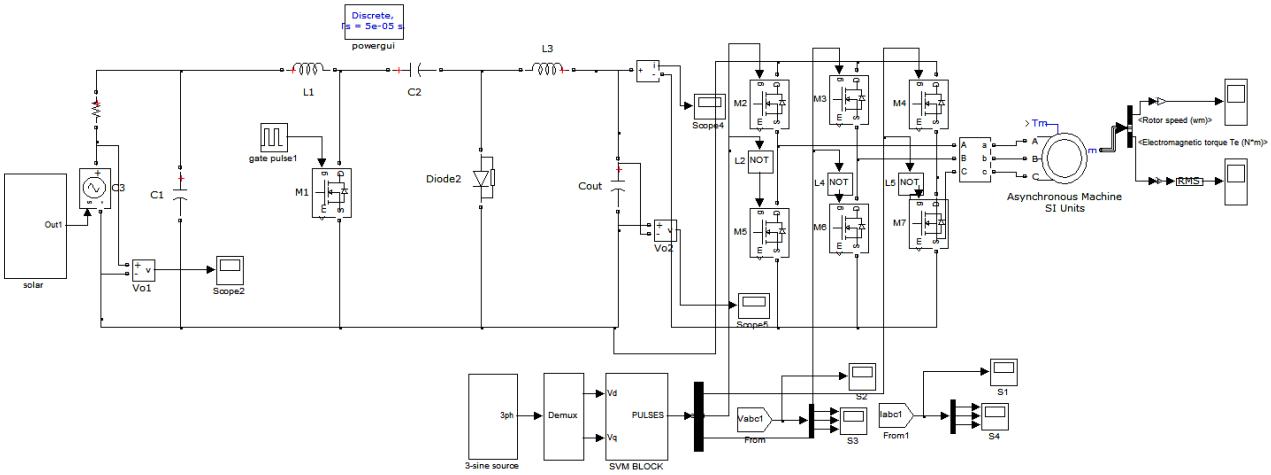

Fig. 3. Cuk converter fed IM system

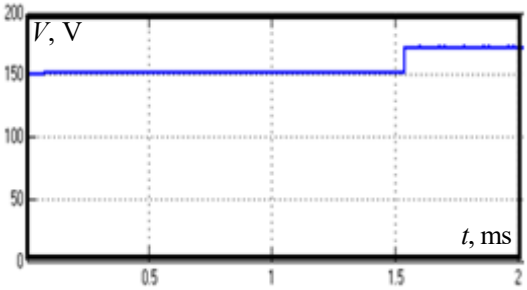

Fig. 4. Input voltage applied to the Cuk converter in open loop ILCCIIM

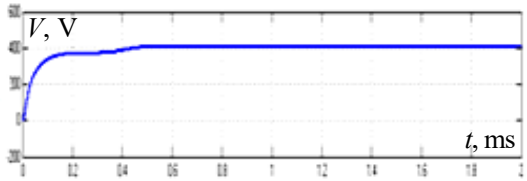

Fig. 5. Voltage across Cuk converter

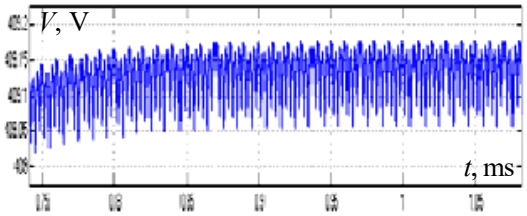

Fig. 6. Voltage ripple of CUK converter

Figures 7, 8 show the inverter's output voltage and current, respectively. The output current (peak to peak) is 50 A, and the output voltage is 500 V.

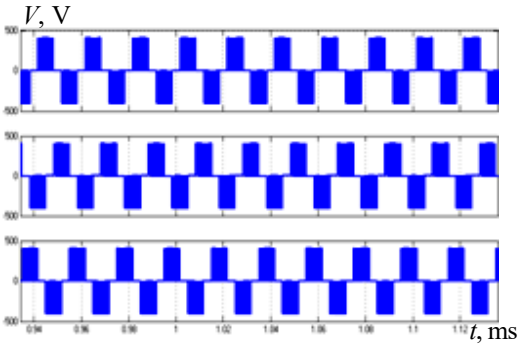

Fig. 7. Output voltage of the inverter

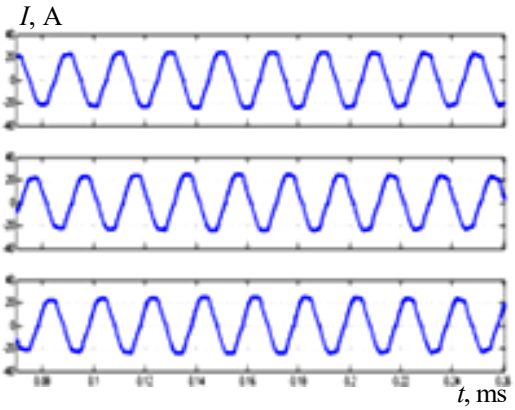

Fig. 8. Output current of the inverter

Figures 9, 10, respectively, display the motor speed and motor wave forms. According to the findings, the motor torque stabilizes about 0.5 s.

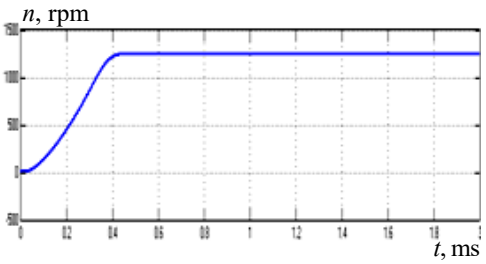

Fig. 9. Motor speed

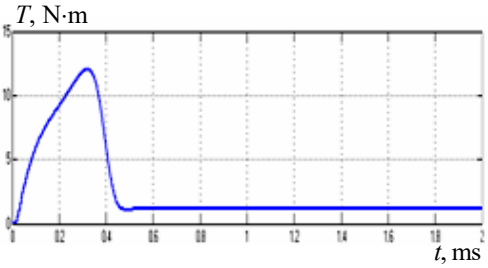

Fig. 10. Motor torque

5. Simulation of ILCCIIM system. The MATLAB Simulink is used to build the ILCCIIM system. Similar outcomes are also attained with this system. ILCCIIM system circuit is depicted in Fig. 11. Figure 12 depicts the output torque ripple of a single Cuk converter as well as the superimposed waveform of a two-stage interleaved Cuk converter.

In order to lessen the input current ripple, two Cuk converters were assigned in tandem. The speed response established by ILCCIIM is depicted in Fig. 13, and it had a value of 0.48 N·m. Due to improved insulation, the ILCCIIM's torque and speed were both stabilized at higher values.

6. Implementation results of ILCCIIM. A hardware setup for an inverted-fed, interleaved Cuk converter motor was created and put into practice in a lab environment (Table 1). Figure 14 shows the hardware setup of ILCCIIM system. Figure 15 shows the output voltage of solar panel whereas. Figure 16 shows the Cuk converter's output voltage.

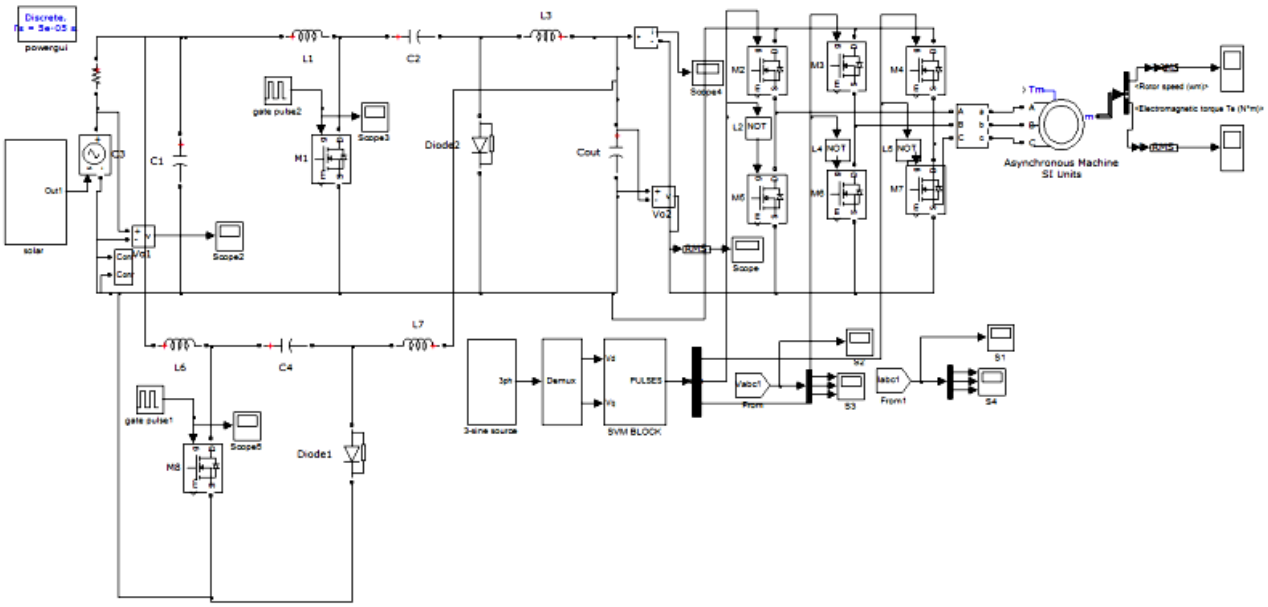

Fig. 11. Interleaved Cuk converter-inverter fed IM

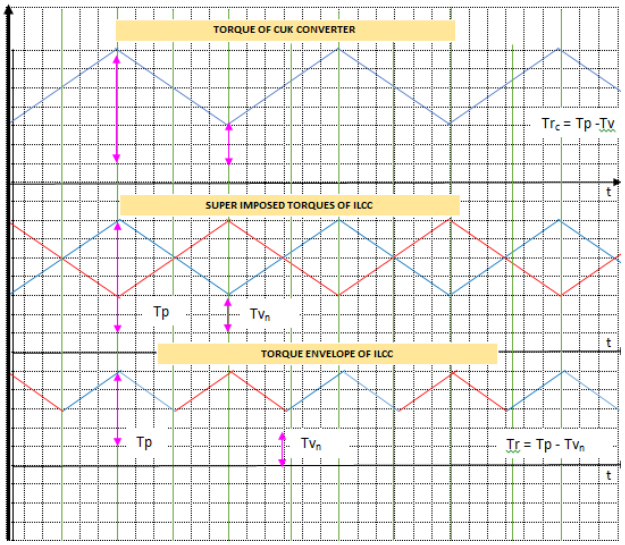

Fig. 12. Torque wave form of the interleaved CUK converter

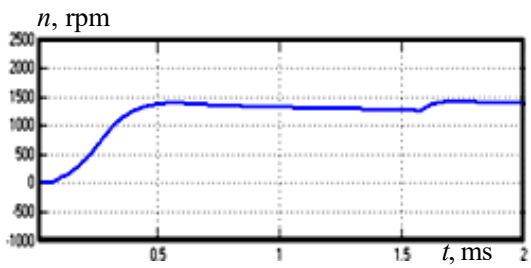

Fig. 13. Motor speed

Table 1

Hardware parameters of Cuk converter-inverter fed IM

Parameter	Value
L_1,L_3	0.5 mH
C_2,C_4	1000 μF
MOSFET(IRF840)	500 V / 8 A
Diode	230 V / 1 A
Controller	PIC16F84A
Driver IC	IR2110

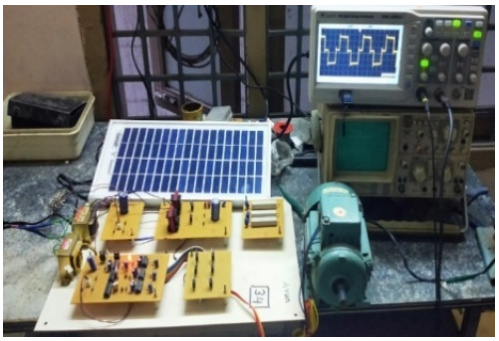

Fig. 14. Hardware setup of solar based IRCCIIM

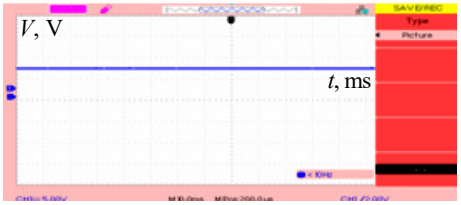

Fig. 15. Output voltage of the solar panel

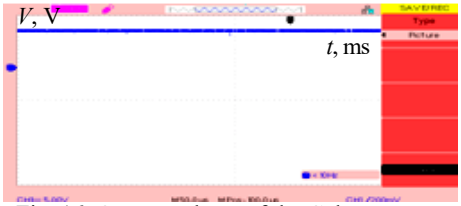

Fig. 16. Output voltage of the Cuk converter

Figure 17 shows the switching pulses for M1, M4 and Fig. 18 shows the switching pulses for M5, M2. Figure 19 shows the voltage across the motor load. The inverter's output spiked because the switching order was changed at intervals of 600.

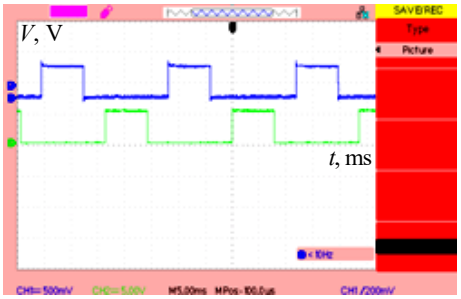

Fig. 17. Switching pulse for M1, M4

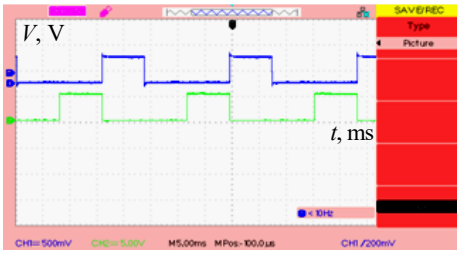

Fig. 18 Switching pulses for M5, M2

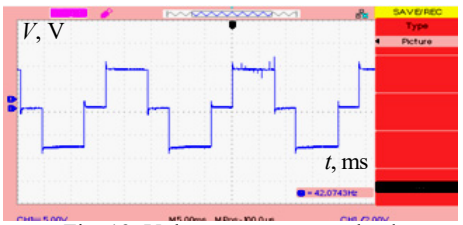

Fig. 19. Voltage across motor load

The output voltage contains reverse polarity nature in case if it is attached with input voltage. Cuk converter's output is then applied on to 3-phase inverter. The balanced voltage, which is actually developed with the help of 3-phase inverter, is then applied onto IM.

The hardware setup for ILCCIIM is checked and verified. The structure suggested in this study is shown in Fig. 20 in terms of hardware setup and it is composed of PV panel, inverter board, Cuk converter board, control board and transformer board.

Figure 21 shows the input voltage from solar PV system further. Figure 22 shows the voltage across Cuk converter.

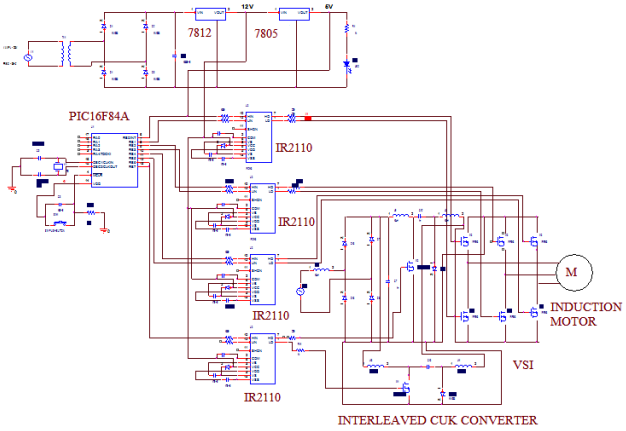

Fig. 20. Hardware circuit of IRCCIIM

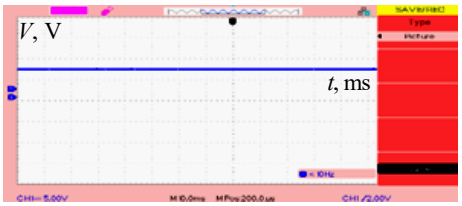

Fig. 21. Input voltage from solar panel to Cuk converter

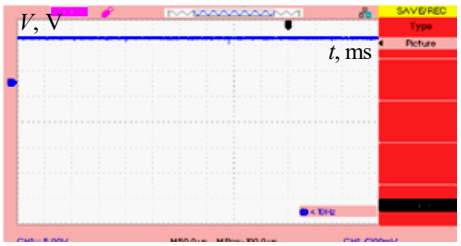

Fig. 22. Voltage across Cuk converter

The comparison between Cuk converter based system and interleaved Cuk converter based system is given in Table 2.

Table 2

Comparison between CCIM and ILCCIIM

Parameters	CCIM	ILCCIIM
Input voltage V_{in}, V	150	150
Output voltage V_o, V	400	475
Frequency, kHz	5	5
Speed n, rpm	1200	1250

7. Conclusions.

1. An interleaved Cuk converter compared to other conventional converters, inverter-fed induction motor systems offer greater voltage transformation and a reduction in input and output current ripple.

2. In continuous conduction mode, a traditional Cuk converter creates enormous input side current ripples, which then inject harmonics into the source. The interleaved Cuk converter is used to reduce the undesired input current ripple.

3. The output voltage of an interleaved Cuk converter is 75 V higher than that of a regular Cuk converter,

according to simulation data. Cuk converter with interleave inverter designed is also suitable for high power applications, such as electric car systems.

Conflict of interest. The authors declare that they have no conflicts of interest.

REFERENCES

1. Lahooti Eshkevari A., Ghaffarpour Sadighi H., Salemnia A., Mosallanejad A. A new high-efficiency interleaved step-up converter with zero-voltage switching, zero-current switching, and common-ground features for stand-alone electric vehicle charging stations. *International Journal of Circuit Theory and Applications*, 2021, vol. 49, no. 6, pp. 1613-1632. doi: https://doi.org/10.1002/cta.2979.

2. Shukla S., Singh B., Shaw P., Al-Durra A., El-Fouly T.H.M., El-Saadany E.F. A New Analytical MPPT-Based Induction Motor Drive for Solar PV Water Pumping System With Battery Backup. *IEEE Transactions on Industrial Electronics*, 2022, vol. 69, no. 6, pp. 5768-5781. doi: https://doi.org/10.1109/TIE.2021.3091929.

3. Joseph K.D, Asha Elizabeth Daniel, Unnikrishnan A. Interleaved Cuk converter with improved transient performance and reduced current ripple. *The Journal of Engineering*, 2017, vol. 2017, no. 7, pp. 362-369. doi: https://doi.org/10.1049/joe.2017.0153.

4. Taghizadegan Kalantari N., Ghabeli Sani S., Sarsabahi Y. Implementation and design of an interleaved Cuk converter with selective input current ripple elimination capability. *International Journal of Circuit Theory and Applications*, 2021, vol. 49, no. 6, pp. 1743-1756. doi: https://doi.org/10.1002/cta.2940.

5. Sravya T., Aswini K. Analysis and Comparison of Conventional and Interleaved DC/DC CUK Converter using Fuzzy Logic Controller. *International Journal for Research in Applied Science and Engineering Technology*, 2020, vol. 8, no. 5, pp. 2738-2744. doi: https://doi.org/10.22214/ijraset.2020.5460.

6. Chung H.S.-H., Tse K.K., Hui S.Y.R., Mok C.M., Ho M.T. A novel maximum power point tracking technique for solar panels using a SEPIC or Cuk converter. *IEEE Transactions on Power Electronics*, 2003, vol. 18, no. 3, pp. 717-724. doi: https://doi.org/10.1109/TPEL.2003.810841.

7. Nag S.S., Adda R., Ray O., Mishra S.K. Current-Fed Switched Inverter based hybrid topology for DC Nanogrid application. *IECON 2013 - 39th Annual Conference of the IEEE Industrial Electronics Society*, 2013, pp. 7146-7151. doi: https://doi.org/10.1109/IECON.2013.6700320.

8. Viola J., Angel L. Fractional control and robustness analysis of an inverted pendulum system. *2015 IEEE 2nd Colombian Conference on Automatic Control (CCAC)*, 2015, pp. 1-6. doi: https://doi.org/10.1109/CCAC.2015.7345223.

9. Akhtar M.J., Behera R.K. Optimal design of stator and rotor slot of induction motor for electric vehicle applications. *IET Electrical Systems in Transportation*, 2019, vol. 9, no. 1, pp. 35-43. doi: https://doi.org/10.1049/iet-est.2018.5050.

10. Boukadoum A., Bouguerne A., Bahi T. Direct power control using space vector modulation strategy control for wind energy conversion system using three-phase matrix converter. *Electrical Engineering & Electromechanics*, 2023, no. 3, pp. 40-46. doi: https://doi.org/10.20998/2074-272X.2023.3.06.

11. Singh S., Singh B. PFC buck converter fed PMBLDCM drive for low power applications. *2012 IEEE Fifth Power India Conference*, 2012, pp. 1-5. doi: https://doi.org/10.1109/PowerI.2012.6479551.

12. Su J., Gao R., Husain I. Model Predictive Control Based Field-Weakening Strategy for Traction EV Used Induction Motor. *IEEE Transactions on Industry Applications*, 2018, vol. 54, no. 3, pp. 2295-2305. doi: https://doi.org/10.1109/TIA.2017.2787994.

13. Lin B.-R., Huang C.-L., Chiang, H.-K. Analysis, design and implementation of an active snubber zero-voltage switching Cuk converter. *IET Power Electronics*, 2008, vol. 1, no. 1, pp. 50-51. doi: https://doi.org/10.1049/iet-pel:20070107.

14. Sobhan S., Hoque M.A., Sarowar G., Ahmad T., Farhan A.M. Dual Mode-Multiple Output SEPIC Converter Integrated with Passive Ripple Cancelling Circuit for Standalone PV Energy Harvesting System. *Journal of Power and Energy Engineering*, 2016, vol. 4, no. 11, pp 1-18. doi: https://doi.org/10.4236/jpee.2016.411001.

15. Anand A., Singh B. Modified Dual Output Cuk Converter-Fed Switched Reluctance Motor Drive With Power Factor Correction. *IEEE Transactions on Power Electronics*, 2019, vol. 34, no. 1, pp. 624-635. doi: https://doi.org/10.1109/TPEL.2018.2827048.

16. Hsu C.-H. Fractional Order PID Control for Reduction of Vibration and Noise on Induction Motor. *IEEE Transactions on Magnetics*, 2019, vol. 55, no. 11, pp. 1-7. doi: https://doi.org/10.1109/TMAG.2019.2933176.

17. Seo S.-W., Choi H.H. Digital Implementation of Fractional Order PID-Type Controller for Boost DC–DC Converter. *IEEE Access*, 2019, vol. 7, pp. 142652-142662. doi: https://doi.org/10.1109/ACCESS.2019.2945065.

18. Umadevi D., Shivakumar E.G. Fractional order PID controlled Quadratic-Boost-Converter - Multilevel inverter fed Induction Motor System. *2019 IEEE International Conference on Electrical, Computer and Communication Technologies (ICECCT)*, 2019, pp. 1-6. doi: https://doi.org/10.1109/ICECCT.2019.8869346.

19. Karkkainen H., Aarniovuori L., Niemela M., Pyrhonen J. Converter-Fed Induction Motor Efficiency: Practical Applicability of IEC Methods. *IEEE Industrial Electronics Magazine*, 2017, vol. 11, no. 2, pp. 45-57. doi: https://doi.org/10.1109/MIE.2017.2693421.

20. Rekha Y., Christopher I.W., Jamuna V. Fuel Cell Based Sl Quasi Z-Source Inverter for Motor Drive. *2019 Fifth International Conference on Electrical Energy Systems (ICEES)*, 2019, pp. 1-6. doi: https://doi.org/10.1109/ICEES.2019.8719296.

21. Wang H., Tang Y., Khaligh A. A Bridgeless Boost Rectifier for Low-Voltage Energy Harvesting Applications. *IEEE Transactions on Power Electronics*, 2013, vol. 28, no. 11, pp. 5206-5214. doi: https://doi.org/10.1109/TPEL.2013.2242903.

22. Kumar R., Singh B. Solar PV array fed Cuk converter-VSI controlled BLDC motor drive for water pumping. *2014 6th IEEE Power India International Conference (PIICON)*, 2014, pp. 1-7. doi: https://doi.org/10.1109/POWERI.2014.7117669.

23. Lekhchine S., Bahi T., Abadlia I., Layate Z., Bouzeria H. Speed Control of Doubly Fed Induction Motor. *Energy Procedia*, 2015, vol. 74, pp. 575-586. doi: https://doi.org/10.1016/j.egypro.2015.07.758.

24. Shurub Y.V., Vasilenkov V.Y., Tsitsyurskiy Y.L. Method of calculation of electromagnetic torque and energy losses of three-phase induction motors when powered by a regulated single-phase voltage. *Electrical Engineering & Electromechanics*, 2022, no. 6, pp. 8-14. doi: https://doi.org/10.20998/2074-272X.2022.6.02.

25. Sher H.A., Addoweesh K.E., Khalid Z., Khan Y. Theoretical and experimental analysis of inverter fed induction motor system under DC link capacitor failure. *Journal of King Saud University - Engineering Sciences*, 2017, vol. 29, no. 2, pp. 103-111. doi: https://doi.org/10.1016/j.jksues.2015.06.001.

Received 26.05.2023
Accepted 01.09.2023
Published 02.01.2024

G. Themozhi[1], *Professor*,
K. Srinivasan[2], *Professor*,
T. Arun Srinivas[3], *Assistant Professor*,
A. Prabha[4], *Assistant Professor*,
[1] Department of Electrical and Electronics Engineering,
AMET Deemed to be University,
Chennai, India,
e-mail: gthemozhivijayakumar@gmail.com (Corresponding Author)
[2] Department of Electrical and Electronics Engineering,
Tagore Engineering College, Chennai, India,
e-mail: omsrivas@yahoo.co.in
[3] Department of Electrical and Electronics Engineering,
JP College of Engineering, Tenkasi, India,
e-mail: arunsrinivas1984@gmail.com
[4] Department of Electrical and Electronics Engineering,
Kings College of Engineering, Pudukottai, India,
e-mail: sriprabha823@gmail.com

How to cite this article:
Themozhi G., Srinivasan K., Arun Srinivas T., Prabha A. Analysis of suitable converter for the implementation of drive system in solar photovoltaic panels. *Electrical Engineering & Electromechanics*, 2024, no. 1, pp. 17-22. doi: https://doi.org/10.20998/2074-272X.2024.1.03

UDC 621.3.013 https://doi.org/10.20998/2074-272X.2024.1.04

B.I. Kuznetsov, T.B. Nikitina, I.V. Bovdui, K.V. Chunikhin, V.V. Kolomiets, B.B. Kobylianskyi

Method for prediction and control by uncertain microsatellite magnetic cleanliness based on calculation and compensation magnetic field spatial harmonics

Aim. *Development of method for prediction and control the microsatellite magnetic cleanliness taking into account the uncertainties of the magnetic characteristics of the microsatellite, based on calculation the magnetic field spatial spherical harmonics in the area of the onboard magnetometer installation and using compensating multipoles.* ***Methodology.*** *Spatial spherical harmonics of microsatellite magnetic field in the area of the onboard magnetometer installation calculated as solution of nonlinear minimax optimization problem based on near field measurements for prediction far spacecraft magnetic field magnitude. Nonlinear objective function calculated as the weighted sum of squared residuals between the measured and predicted magnetic field. Values of the compensating dipoles, quadrupoles and octupoles and coordinates of them placement inside the spaceship for compensation of the dipoles, quadrupoles and octupoles components of the microsatellite initial magnetic field also calculated as solution of nonlinear minimax optimization problem. Both solutions of this nonlinear minimax optimization problems calculated based on particle swarm nonlinear optimization algorithms.* ***Results.*** *Results of prediction spacecraft far magnetic field magnitude based on spacecraft spatial spherical harmonics of the magnetic field using near field measurements and compensation of the dipoles, quadrupoles and octupoles components of the initial magnetic field with consideration of spacecraft magnetic characteristics uncertainty for ensuring the microsatellite magnetic cleanliness.* ***Originality.*** *The method for prediction and control by spacecraft magnetic cleanliness based on calculation spatial spherical harmonics of the magnetic field in the area of the onboard magnetometer installation using compensation of the dipoles, quadrupoles and octupoles components of the initial magnetic field with consideration of magnetic characteristics uncertainty is developed.* ***Practical value.*** *The important practical problem of ensuring the magnetic cleanliness of the «Sich-2» microsatellite family based on the spatial spherical harmonics of the magnetic field model using the compensation of the dipole, quadrupole and octupole components of the output magnetic field of the sensor for the kinetic parameters of the neutral component of the space plasma at the point of installation of the on-board magnetometer LEMI-016 by setting the compensating dipole, quadrupole and octupole with consideration of spacecraft magnetic characteristics uncertainty solved.* References 59, figures 2.

Key words: **microsatellite, magnetic cleanliness, magnetic field spatial spherical harmonics, prediction, control, measurements, uncertainty.**

Мета. *Розробка методу прогнозування та управління магнітною чистотою мікросупутника на основі обчислення просторових сферичних гармонік магнітного поля в зоні встановлення бортового магнітометру з використанням компенсації сферичних гармонік вихідного магнітного поля та з урахуванням невизначеності магнітних характеристик.* ***Методологія***. *Просторові сферичні гармоніки магнітного поля мікросупутника розраховані як рішення задачі нелінійної мінімаксної оптимізації на основі вимірювань ближнього магнітного поля для прогнозування величини дальнього магнітного поля. Нелінійна цільова функція обчислена в вигляді зваженої суми квадратів залишків між виміряним і прогнозованим магнітним полем. Величини компенсуючих диполів, квадруполів та октуполів та координати їх розташування в просторі мікросупутника для компенсації вихідного магнітного поля космічного апарату розраховані як рішення нелінійної задачі мінімаксної оптимізації. Рішення обох задач нелінійної мінімаксної оптимізації розраховані на основі алгоритмів нелінійної оптимізації роєм частинок.* ***Результати.*** *Результати прогнозування величини дальнього магнітного поля мікросупутника на основі обчислення просторових сферичних гармонік моделі магнітного поля в зоні встановлення бортового магнітометру з використанням вимірювань ближнього поля та компенсації дипольних, квадрупольних та октупольних компонент вихідного магнітного поля з урахуванням невизначеності магнітних характеристик для забезпечення магнітної чистоти мікросупутника.* ***Оригінальність***. *Розроблено метод прогнозування та управління магнітною чистотою мікросупутника на основі обчислення просторових сферичних гармонік магнітного поля з використанням компенсації дипольних, квадрупольних та октупольних компонент вихідного магнітного поля та з урахуванням невизначеності магнітних характеристик.* ***Практична цінність.*** *Вирішено важливу практичну задачу забезпечення магнітної чистоти орбітального космічного апарату сімейства «Січ-2» на основі обчислення просторових сферичних гармонік моделі магнітного поля з використанням компенсації дипольних, квадрупольних та октупольних компонент вихідного магнітного поля датчика кінетичних параметрів нейтрального компонента космічної плазми в точці розташування бортового магнітометру LEMI-016 шляхом установки компенсуючих диполів, квадруполів та октуполів та з урахуванням невизначеності магнітних характеристик.* Бібл. 59, рис. 2.

Ключові слова: **космічний апарат, магнітна чистота, просторові сферичні гармоніки магнітного поля, прогнозування, керування, вимірювання, невизначеність.**

Introduction. To model the satellites magnetic field the multi-dipole model is currently the most widely used [1 – 14]. On the basis of such a model, the magnetic moment satellite calculated and the magnetic field satellite calculated with sufficient accuracy for practice at a distance greater than three satellites dimensions. Such a model is quite adequate for satellites in which the onboard magnetometer is mounted on a sufficiently long rod. In particular, the length of the rod of the onboard magnetometer of the Danish «Oersted» satellite is 8 m [15]. On «MicroSAT» spacecraft with the «IonoSAT-Micro» instrumentation on-board magnetometer and three wave probes are fixed on the rods lengths are 2 m [16]. However, spacecraft designers are constantly striving to reduce the length of this rod. In particular, on the «Sich-2» family, «CubeSAT» spacecraft onboard magnetometer located inside the spacecraft [17, 18].

Figure 1 shows the location of the sensor of the kinetic parameters of the neutral component of the space plasma (KPNCSP) of the «Potential» scientific equipment complex and onboard magnetometer LEMI-016 on the «Sich-2» spacecraft [18].

In particular, on the «Sich-2» spacecraft family onboard magnetometer LEMI-016 is located at a distance of 0.35 m from the sensor KPNCSP [18]. The principle of operation of this sensor is based on the use of the force effect of a magnetic field on an electrically neutral component of space plasma. In this case, permanent magnets are used to create an internal magnetic field in the sensor.

Therefore, the standard of the European Space Agency ECSS-E-20A limits the value of the magnetic field spacecraft units at a distance of 0.1 m from their surface [19]. Therefore, to model the magnetic field of

such satellites, it is necessary to use a multipole model based on spatial harmonics [20 – 26].

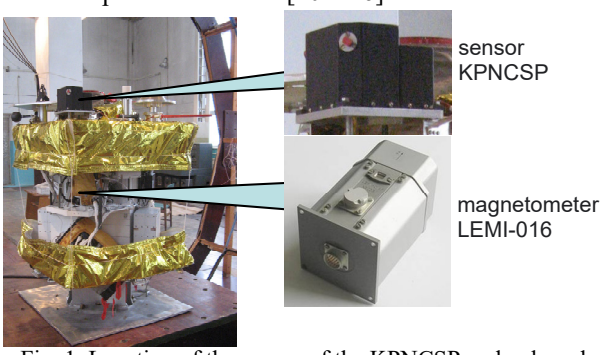

Fig. 1. Location of the sensor of the KPNCSP and onboard magnetometer LEMI-016 on the «Sich-2» spacecraft

In addition, in the course of spacecraft assembly, to compensate for the satellite units magnetic moments, such a spatial arrangement of these units is often used so that the total magnetic moment would be equal to zero. To compensate for the spacecraft units magnetic moments, as well as to compensate for the residual magnetic moments of the entire spacecraft, compensating magnetic units are used. As a result of such measures, it is possible to reduce the magnitudes of the units magnetic moments and the entire spacecraft to sufficiently small values. However, as a result of these measures, quadrupole, octupole and harmonics of a higher order appear, so that the level of the magnetic field near the satellite surface determined mainly by quadrupole, octupole, etc. harmonics.

In particular, in the practice of spacecraft designing to compensate for the dipole magnetic moments of electromagnetic relays, they are often installed in pairs next to each other, so that such a design becomes a quadrupole magnetic field source. To compensate for the dipole magnetic moments of high-frequency gate switch, they are often installed side by side in fours, six or even eight elements. This design becomes a quadrupole, octopole, and even higher order magnetic field source.

To reduce the magnetic moment of the sensor of the neutral component of the plasma, which is part of the scientific equipment of the «Sich-2» spacecraft, an antisymmetric orientation of permanent magnets and a ferromagnetic screen are used. In this case [18], the magnetic moment of the sensor of the neutral component of the plasma generates only 20 % of the induction at the installation point of the onboard magnetometer LEMI-016, and the remaining 80 % of the induction generates by the a quadrupole and octupole – second and third spatial harmonics of the magnetic field of the sensor of the neutral component of the plasma.

Therefore, for an adequate description of the magnetic field in the satellite near zone it is necessary to use a multipole model, including a quadrupole, octopole, and, possibly, a higher order model of the satellite's magnetic field. The European Space Agency ECSS-E-HB-20-07A also recommends using spherical harmonics as integral characteristics of the magnetic field to improve the satellites magnetic cleanliness [19].

In addition, the characteristics of the magnetic cleanliness of the spacecraft units change when their operating modes change and during the flight. Therefore, the European Space Agency recommends testing the units and the entire spacecraft in various modes of operation [19].

The aim of the work is to develop a method for prediction and control the microsatellite magnetic cleanliness taking into account the uncertainties of the magnetic characteristics of the microsatellite, based on calculation the magnetic field spatial spherical harmonics in the area of the onboard magnetometer installation and using compensating multipole.

Model of spatial spherical harmonics microsatellite magnetic field. When design a mathematical model of the microsatellite magnetic field the Gauss equation for the scalar magnetic potential of the source in the surrounding space written in spherical coordinates r, φ and θ in the following form [2]:

$$U = \frac{1}{4\pi}\cdot\sum_{n=1}^{\infty}\left(\frac{1}{r}\right)^{n+1}\cdot\sum_{m=0}^{n}(g_n^m\cdot\cos m\varphi+\ldots \\ \ldots+h_n^m\cdot\sin m\varphi)\cdot P_n^m(\cos\theta), \quad (1)$$

where r is the radius of the sphere on which the potential is determined; g_n^m, h_n^m – constant coefficients.

Then from (1) the components B_r, B_φ, B_θ of the magnetic field in the spherical coordinate system r, φ and θ associated with the geometric center of the microsatellite calculated (2).

To ensure the microsatellite magnetic field cleanliness the European Space Agency ECSS-E-HB-20-07A recommends [19] used spatial harmonics up to octupole harmonics as characteristics of the microsatellite magnetic field cleanliness. In addition to the microsatellite magnetic moment, which is characterized by three components g_1^0, g_1^1, h_1^1 in (1), it is necessary to determine five more coefficients g_2^0, g_2^1, g_2^2, h_2^1, h_2^2 for the quadruple component and seven coefficients g_3^0, g_3^1, g_3^2, g_3^3, h_3^1, h_3^2, h_3^3 octupole component of the magnetic field spherical harmonics:

$$B_r = \frac{\mu_0}{4\pi}\cdot\sum_{n=1}^{\infty}(n+1)\cdot\frac{1}{r^{n+2}}\cdot\sum_{m=0}^{n}(g_n^m\times\ldots \\ \ldots\times\cos m\varphi+h_n^m\cdot\sin m\varphi)\cdot P_n^m(\cos\theta);$$

$$B_\varphi = \frac{\mu_0}{4\pi}\cdot\sum_{n=1}^{\infty}\frac{1}{r^{n+2}}\cdot\sum_{m=0}^{n}(g_n^m\cdot\sin m\varphi-\ldots \\ \ldots-h_n^m\cdot\cos m\varphi)\cdot\frac{P_n^m(\cos\theta)}{\sin\theta}; \quad (2)$$

$$B_\theta = \frac{\mu_0}{4\pi}\cdot\sum_{n=1}^{\infty}\frac{1}{r^{n+2}}\cdot\sum_{m=0}^{n}(g_n^m\cdot\cos m\varphi+\ldots\cdot\cdot \\ \ldots+h_n^m\cdot\sin m\varphi)\cdot\frac{1}{\sin\theta}\cdot\left[(n-m+1)\times\ldots \\ \ldots\times\overline{P}_{n+1}^m(\cos\theta)-(n+1)\cdot\cos\theta\cdot P_n^m(\cos\theta)\right]$$

Let us first consider the case when for all N units of the microsatellite at the preliminary testing stage of magnetic cleanliness, three quantities g_{n1}^0, g_{n1}^1, h_{n1}^1 of the dipole component, five quantities g_{n2}^0, g_{n2}^1, g_{n2}^2, h_{n2}^1, h_{n2}^2 of the quadrupole component and seven quantities g_{n3}^0, g_{n3}^1, g_{n3}^2, g_{n3}^3, h_{n3}^1, h_{n3}^2, h_{n3}^3 of the

octupole component of spherical harmonics determined. Let us set the spherical coordinates r_n, φ_n and θ_n the location of all N units of the microsatellite in the spherical coordinate system associated with the magnetic center of the microsatellite.

Then the components B_{kr}, $B_{k\varphi}$, $B_{k\theta}$ of the magnetic field generated by all N units of the microsatellite at the point with coordinates r_k, φ_k and θ_k in the spherical coordinate system associated with the geometric center of the microsatellite calculated taking into account the expression for Legendre polynomials up to the third term of series based on (2) [25].

Here the coordinates r_{kn} and two angles φ_{kn} and θ_{kn} of points of calculation of the magnetic field generated by n microsatellite units in the spherical coordinate system associated with the geometric center of that N microsatellite units.

Transferred coordinates r_k, φ_k and θ_k of calculated point of components B_{kr}, $B_{k\varphi}$, $B_{k\theta}$ of the magnetic field in the spherical coordinate system associated with the geometric center of the microsatellite from the spherical coordinate system to the orthogonal system (6):

$$B_{kr}=\frac{\mu_0}{4\pi}\sum_{n=1}^{N}\left(\begin{array}{l} g_{n1}^0\frac{2}{r_{kn}^3}\cos\theta_{kn}+\left[g_{n1}^1\cos\varphi_{kn}+h_{n1}^1\sin\varphi_{kn}\right]\frac{2}{r_{kn}^3}\sin\theta_{kn}+g_{n2}^0\frac{3/2}{r_{kn}^4}\left(3\cos^2\theta_{kn}-1\right)+\ldots \\ \ldots+\left[g_{n2}^1\cos\varphi_{kn}+h_{k2}^1\sin\varphi_{kn}\right]\frac{9}{r_{kn}^4}\cos\theta_{kn}\sin\theta_{kn}+\left[g_{n2}^2\cos(2\varphi_{kn})+h_{n2}^2\sin(2\varphi_{kn})\right]*\ldots \\ \ldots*\frac{9}{r_{kn}^4}\sin^2\theta_{kn}+g_{n3}^0\frac{2}{r_{kn}^5}\left(5\cos^3\theta_{kn}-3\cos\theta_{kn}\right)+\left[g_{n3}^1\cos\varphi_{kn}+h_{n3}^1\sin\varphi_{kn}\right]*\ldots \\ \ldots*\frac{2}{r_{kn}^5}\sin\theta_{kn}\left(15\cos^2\theta_{kn}-3\right)+\left[g_{n3}^2\cos(2\varphi_{kn})+h_{n3}^2\sin(2\varphi_{kn})\right]\frac{60}{r_{kn}^5}\cos\theta_{kn}\sin^2\theta_{kn}+\ldots \\ \ldots+\left[g_{n3}^3\cos(3\varphi_{kn})+h_{n3}^3\sin(3\varphi_{kn})\right]\frac{60}{r_{kn}^5}\sin^3\theta_{kn} \end{array}\right); \quad (3)$$

$$B_{k\varphi}=\frac{\mu_0}{4\pi}\sum_{n=1}^{N}\left(\begin{array}{l} \left[g_{n1}^1\sin\varphi_{kn}-h_{n1}^1\cos\varphi_{kn}\right]\frac{1}{r_{kn}^3}\sin\theta_{kn}+\left[g_{n2}^1\sin\varphi_{kn}-h_{n2}^1\cos\varphi_{kn}\right]\frac{3}{r_{kn}^4}\cos\theta_{kn}+\ldots \\ \ldots+\left[g_{n2}^2\sin(2\varphi_{kn})-h_{n2}^2\cos(2\varphi_{kn})\right]\frac{6}{r_{kn}^4}\sin\theta_{kn}+\left[g_{n3}^1\sin\varphi_{kn}-h_{n3}^1\cos\varphi_{kn}\right]\frac{1/2}{r_{kn}^5}*\ldots \\ \ldots*\left(15\cos^2\theta_{kn}-3\right)+\left[g_{n3}^2\sin(2\varphi_{kn})-h_{n3}^2\cos(2\varphi_{kn})\right]\frac{30}{r_{kn}^5}\cos\theta_{kn}\sin\theta_{kn}+\ldots \\ +\left[g_{n3}^3\sin(3\varphi_{kn})-h_{n3}^3\cos(3\varphi_{kn})\right]\frac{45}{r_{kn}^5}\sin^2\theta_{kn} \end{array}\right); \quad (4)$$

$$B_{k\theta}=\frac{\mu_0}{4\pi}\sum_{n=1}^{N}\left(\begin{array}{l} g_{n1}^0\frac{1}{r_{kn}^3}\sin\theta_{kn}+\left[-g_{n1}^1\cos\varphi_{kn}-h_{n1}^1\sin\varphi_{kn}\right]\frac{1}{r_{kn}^3}\cos\theta_{kn}+\ldots \\ \ldots+g_{n2}^0\frac{3}{r_{kn}^4}\cos\theta_{kn}\sin\theta_{kn}+\left[-g_{n2}^1\cos\varphi_{kn}-h_{n2}^1\sin\varphi_{kn}\right]\frac{3}{r_{kn}^4}\cos(2\theta_{kn})+\ldots \\ \ldots+\left[-g_{n2}^2\cos(2\varphi_{kn})+h_{n2}^2\sin(2\varphi_{kn})\right]\frac{-6}{r_{kn}^4}\cos\theta_{kn}\sin\theta_{kn}+\ldots \\ \ldots+g_{n3}^0\frac{1/2}{r_{kn}^5}\left(15\cos^2\theta_{kn}-3\right)\sin\theta_{kn}+\ldots \\ \ldots+\left\{\begin{array}{l} g_{n3}^1\cos\varphi_{kn} \\ h_{n3}^1\sin\varphi_{kn} \end{array}\right\}\frac{3/2}{r_{kn}^5}\left(11\sin^2\theta_{kn}-4\cos^2\theta_{kn}\right)\cos\theta_{kn}+\ldots \\ \ldots+\left\{\begin{array}{l} g_{n3}^2\cos(2\varphi_{kn}) \\ h_{n3}^2\sin(2\varphi_{kn}) \end{array}\right\}\frac{15}{r_{kn}^5}\left(\sin^2\theta_{kn}-2\cos^2\theta_{kn}\right)\sin\theta_{kn}+\ldots \\ \ldots+\left\{\begin{array}{l} g_{n3}^3\cos(3\varphi_{kn}) \\ h_{n3}^3\sin(3\varphi_{kn}) \end{array}\right\}\frac{-45}{r_{kn}^5}\cos\theta_{kn}\sin^2\theta_{kn} \end{array}\right) \quad (5)$$

$$z_k=r_k\cos(\theta_k),\quad x_k=r_k\cos(\varphi_k)\sin(\theta_k),\quad y_k=r_k\sin(\theta_k)\sin(\varphi_k) \quad (6)$$

Transferred coordinates r_n and two angles φ_n and θ_n location of all N units of the microsatellite from the spherical coordinate system in the orthogonal system for the orthogonal

$$z_n = r_n \cos(\theta_n), \quad x_n = r_n \cos(\varphi_n)\sin(\theta_n), \quad y_n = r_n \sin(\theta_n)\sin(\varphi_n). \tag{7}$$

Then the coordinates r_{kn}, φ_{kn} and θ_{kn} of calculated point of components B_{kr}, $B_{k\varphi}$, $B_{k\theta}$ of the magnetic field in spherical coordinate system associated with the geometric center n unit of the microsatellite calculate

$$r_{kn} = \sqrt{((x_k - x_n)^2 + (y_k - y_n)^2 + (z_k - z_n)^2)}; \quad \cos(\theta_{kn}) = (z_k - z_n)/r_{kn}; \quad \mathrm{tg}(\varphi_{kn}) = (y_k - y_n)/(x_k - x_n). \tag{8}$$

Microsatellite magnetic characteristics uncertain. The microsatellite has completed units in its composition, which must meet the magnetic cleanliness requirements. The solar cell is potentially one of the main sources of the microsatellite magnetic field currents. To reduce the magnetic field of solar batteries, the so-called «backwiring» technique of mounting their circuits with current is used, in which the return wire from each module of the battery elements is returned under the same module along its axis line, which allows you to effectively reduce the magnetic field of the solar battery in all modes of its work [1].

The characteristics of the magnetic field of the microsatellite units do not remain constant and change depending on the microsatellite operation mode and operating time. In particular, the initial magnetic moment of the 8S3P MPS battery «SICH-2-1»spacecraft with a change in the charge current from minus 8 A to the discharge current 8 A almost linearly changed from –0.17 A·m^2 to 0.17 A·m^2. Besides, antennas and components use latch springs, control valves and other moving parts magnetic characteristics of which change under different operating modes of the microsatellite.

All units with a magnetic drive (motors, linear motion converters and all other mechanisms) require independent development in terms of ensuring their magnetic cleanliness. In conclusion, we note that all spacecraft units undergo testing regarding the characteristics of their magnetic cleanliness, which must be within certain limits [19].

Let us introduce the vector $\vec{G}$ of uncertainties of the parameters of microsatellite units magnetic cleanliness [27 – 32]. It should be noted that the values of three quantities g_{n1}^0, g_{n1}^1, h_{n1}^1 of the dipole component, five quantities g_{n2}^0, g_{n2}^1, g_{n2}^2, h_{n2}^1, h_{n2}^2 of the quadrupole component and seven quantities g_{n3}^0, g_{n3}^1, g_{n3}^2, g_{n3}^3, h_{n3}^1, h_{n3}^2, h_{n3}^3 of the octupole component of spherical harmonics for all N units of the microsatellite determined in the course of testing the magnetic purity of all microsatellite units depend on the operating modes of the microsatellite and, therefore, are functions of the components of the vector $\vec{G}$ of uncertainties of the parameters of the magnetic purity of the microsatellite units.

Then for a given value of the vector $\vec{G}$ of uncertainties of the parameters of the magnetic cleanliness of microsatellite units, given coordinates r_n, φ_n and θ_n of spatial arrangement of N microsatellite units with given values of three quantities $g_{n1}^0(\vec{G})$, $g_{n1}^1(\vec{G})$, $h_{n1}^1(\vec{G})$ of the dipole component, five quantities $g_{n2}^0(\vec{G})$, $g_{n2}^1(\vec{G})$, $g_{n2}^2(\vec{G})$, $h_{n2}^1(\vec{G})$, $h_{n2}^2(\vec{G})$ of the quadrupole component and seven quantities $g_{n3}^0(\vec{G})$, $g_{n3}^1(\vec{G})$, $g_{n3}^2(\vec{G})$, $g_{n3}^3(\vec{G})$, $h_{n3}^1(\vec{G})$, $h_{n3}^2(\vec{G})$, $h_{n3}^3(\vec{G})$ of the octupole component of spherical harmonics three components $\vec{B}_{kr}(\vec{G})$, $\vec{B}_{k\varphi}(\vec{G})$, $\vec{B}_{k\theta}(\vec{G})$ of the magnetic field generated by all N units of the microsatellite at the point with coordinates r_k, φ_k and θ_k calculated based on (3) – (5). Since the results of measuring the magnetic field depend on the operating modes of the spacecraft, the components of the measurement vector $\vec{B}_{kr}(\vec{G})$, $\vec{B}_{k\varphi}(\vec{G})$, $\vec{B}_{k\theta}(\vec{G})$ also are functions of the vector $\vec{G}$.

Statement of the prediction problem. For design of the spatial spherical harmonics magnetic field model the methods for experimental determination of the coefficients of spatial harmonics based on the signatures of the magnetic characteristics of the tested objects during their movement or rotation relative to the measuring windings have been developed in the works [17 – 25]. With the help of such measuring windings, it is also possible to selectively measure spatial harmonics of various orders. However, this approach involves the use of measuring windings of a rather complex spatial shape, and the dimensions of such selective windings must exceed the test object when it moves through these measuring windings.

However, at present, the most common approach to building a magnetic field model is the use of many point sensors to measure the magnetic field induction generated by the test object. This approach is most widely used in the construction of a multi dipole model of the magnetic field of the test object [3 – 14]. In the ship magnetism laboratory (France), to determine the spherical harmonics of the magnetic field, when modeling the ships magnetization, a system of 39 stationary sensors is used, relative to which the test object is moved [26].

Note that today systems with point measurement of the magnetic field induction using many sensors and precision systems for moving the object under test make it possible to realize the highest accuracy in calculating the parameters of the multipole model of the magnetic field of the object under test.

Let us now consider the inverse problem of design the spatial spherical harmonics magnetic field model (3) – (5) based on the results of measurements $\vec{B}_{kr}(\vec{G})$, $\vec{B}_{k\varphi}(\vec{G})$, $\vec{B}_{k\theta}(\vec{G})$ of the microsatellite magnetic field at the K point with coordinates r_k, φ_k and θ_k by analogy with the design of a multidipole model of the magnetic field [3 – 14].

Let us introduce the vector $\vec{Y}_M(\vec{G})$, components of which are the measured values $\vec{B}_{kr}(\vec{G})$, $\vec{B}_{k\varphi}(\vec{G})$, $\vec{B}_{k\theta}(\vec{G})$ of the magnetic field at the K measurement points with the coordinates r_k, φ_k and θ_k.

Let us introduce the vector $\vec{X}$ of the desired parameters of the mathematical model of the spacecraft magnetic field, the components of which are the desired coordinates r_n, φ_n and θ_n of spatial arrangement of N microsatellite units as well as the desired values of three quantities $g_{n1}^0(\vec{G})$, $g_{n1}^1(\vec{G})$, $h_{n1}^1(\vec{G})$ of the dipole component, five quantities $g_{n2}^0(\vec{G})$, $g_{n2}^1(\vec{G})$, $g_{n2}^2(\vec{G})$,

$h^1_{n2}(\vec{G})$, $h^2_{n2}(\vec{G})$ of the quadrupole component and seven quantities $g^0_{n3}(\vec{G})$, $g^1_{n3}(\vec{G})$, $g^2_{n3}(\vec{G})$, $g^3_{n3}(\vec{G})$, $h^1_{n3}(\vec{G})$, $h^2_{n3}(\vec{G})$, $h^3_{n3}(\vec{G})$ of the octupole component of spherical harmonics of the magnetic field generated by n units of the microsatellite at the point with coordinates r_k, φ_k and θ_k.

Let us introduce the vector $\vec{Y}_C(\vec{X},\vec{G})$, components of which are the calculated values $\vec{B}_{kr}(\vec{G})$, $\vec{B}_{k\varphi}(\vec{G})$, $\vec{B}_{k\theta}(\vec{G})$ of the magnetic field at the K measurement points with the coordinates r_k, φ_k and θ_k.

For vector $\vec{X}$ of the desired parameters of the mathematical model of the spacecraft magnetic field, then, based on (3) – (8) the initial nonlinear equation $\vec{Y}_C(\vec{X},\vec{G})$ for the spacecraft multipole magnetic dipole model calculated

$$\vec{Y}_C(\vec{X},\vec{G}) = \vec{F}(\vec{X},\vec{G}), \qquad (9)$$

where the vector nonlinear function $\vec{F}(\vec{X},\vec{G})$ obtained on the basis of expression (3) – (8) with respect to the vector $\vec{X}$ of unknown variables, whose components are desired coordinates r_n, φ_n and θ_n of spatial arrangement of N microsatellite units as well as the desired values of three quantities $g^0_{n1}(\vec{G})$, $g^1_{n1}(\vec{G})$, $h^1_{n1}(\vec{G})$ of the dipole component, five quantities $g^2_{n2}(\vec{G})$, $h^1_{n2}(\vec{G})$, $h^2_{n2}(\vec{G})$ of the quadrupole component and seven quantities $g^0_{n3}(\vec{G})$, $g^1_{n3}(\vec{G})$, $g^2_{n3}(\vec{G})$, $g^3_{n3}(\vec{G})$, $h^1_{n3}(\vec{G})$, $h^2_{n3}(\vec{G})$, $h^3_{n3}(\vec{G})$ of the octupole component of spherical harmonics of the magnetic field generated by n units of the microsatellite at the point with coordinates r_k, φ_k and θ_k.

Naturally that the vector nonlinear function $\vec{F}(\vec{X},\vec{G})$ also is a function of the vector $\vec{G}$ of uncertainties of the parameters of microsatellite units magnetic cleanliness.

Let us introduce the $\vec{E}(\vec{X},\vec{G})$ vector of the discrepancy between the vector $\vec{Y}_M(\vec{G})$ of the measured magnetic field and the vector $\vec{Y}_C(\vec{X},\vec{G})$ of the predicted by model (18) magnetic field

$$\vec{E}(\vec{X},\vec{G}) = \vec{Y}_M(\vec{G}) - \vec{Y}_C(\vec{X},\vec{G}) = \vec{Y}_M(\vec{G}) - \vec{F}(\vec{X},\vec{G}). \qquad (10)$$

We write the objective nonlinear function as the weighted sum of squared residuals between the measured and predicted by the model (23) values of the magnetic field

$$f(\vec{X},\vec{G}) = (\vec{E}(\vec{X},\vec{G}))^T \, W \, \vec{E}(\vec{X},\vec{G}), \qquad (11)$$

where the weight matrix W takes into account different «weights» of magnetic field measurement errors depending on the distance to the minisatellite surface.

The nonlinear objective function (11) is obtained on the basis of expression (9) with respect to the vector $\vec{X}$ of unknown variables, whose components are the values coordinates r_n, φ_n and θ_n of spatial arrangement of N microsatellite units as well as the desired values of three quantities $g^0_{n1}(\vec{G})$, $g^1_{n1}(\vec{G})$, $h^1_{n1}(\vec{G})$ of the dipole component, five quantities $g^0_{n2}(\vec{G})$, $g^1_{n2}(\vec{G})$, $g^2_{n2}(\vec{G})$, $h^1_{n2}(\vec{G})$, $h^2_{n2}(\vec{G})$ of the quadrupole component and seven quantities $g^0_{n3}(\vec{G})$, $g^1_{n3}(\vec{G})$, $g^2_{n3}(\vec{G})$, $g^3_{n3}(\vec{G})$, $h^1_{n3}(\vec{G})$, $h^2_{n3}(\vec{G})$, $h^3_{n3}(\vec{G})$ of the octupole component of spherical harmonics of the magnetic field generated by n units of the microsatellite at the point with coordinates r_k, φ_k and θ_k and the vector $\vec{G}$ of uncertainties of the parameters of the magnetic cleanliness of microsatellite units.

This approach is standard when designing robust mathematical model of the spacecraft magnetic field, when the coordinates of the spatial arrangement and the magnitudes of the magnetic moments of the dipoles are found from the conditions for minimizing the vector of the discrepancy between the vector of the measured magnetic field and the vector of the predicted by model magnetic field, but for the «worst» the vector of uncertainty parameters of the spacecraft magnetic moments are found from the conditions for maximizing the same vector of the discrepancy between the vector of the measured magnetic field and the vector of the predicted by model magnetic field.

As a rule, when optimizing the nonlinear objective function (11), it is necessary to take into account restrictions on the values of coordinates r_n, φ_n and θ_n of spatial arrangement of N microsatellite units C as well as the desired values of three quantities $g^0_{n1}(\vec{G})$, $g^1_{n1}(\vec{G})$, $h^1_{n1}(\vec{G})$ of the dipole component, five quantities $g^0_{n2}(\vec{G})$, $g^1_{n2}(\vec{G})$, $g^2_{n2}(\vec{G})$, $h^1_{n2}(\vec{G})$, $h^2_{n2}(\vec{G})$ of the quadrupole component and seven quantities $g^0_{n3}(\vec{G})$, $g^1_{n3}(\vec{G})$, $g^2_{n3}(\vec{G})$, $g^3_{n3}(\vec{G})$, $h^1_{n3}(\vec{G})$, $h^2_{n3}(\vec{G})$, $h^3_{n3}(\vec{G})$ of the octupole component of spherical harmonics of the magnetic field generated by n units of the microsatellite at the point with coordinates r_k, φ_k and θ_k. These restrictions usually written as vector inequalities [31 – 36].

$$\vec{G}(\vec{X},\vec{G}) \le \vec{G}_{\max}. \qquad (12)$$

Statement of the control problem. Consider the statement of the problem of controlling by microsatellite magnetic cleanliness based on spherical harmonics magnetic field model (3) – (5) based on the results of measurements. To ensure microsatellite magnetic cleanliness, it is necessary to install in the microsatellite space not only compensating dipoles, but also compensating quadrupole and compensating octupole to compensate for the quadrupole and octupole components of the initial magnetic field of the microsatellite. Usually, the microsatellite magnetic cleanliness requirements are presented in the form of restrictions on the total magnetic moment of the microsatellite and the magnetic field magnitude at the onboard magnetometer installation point [2, 10]. To compensate the initial microsatellite magnetic field at the onboard magnetometer installation point we introduce C magnetic units with unknown values of three quantities g^0_{C1}, g^1_{C1}, h^1_{C1} of the compensating dipole component, five quantities g^0_{C2}, g^1_{C2}, g^2_{C2}, h^1_{C2}, h^2_{C2} of the compensating quadrupole component and seven quantities g^0_{C3}, g^1_{C3}, g^2_{C3}, g^3_{C3}, h^1_{C3}, h^2_{C3}, h^3_{C3} of the compensating octupole component of spherical harmonics of the magnetic field generated by C magnetic units with located at C points P_C with unknown coordinates r_c, φ_c and θ_c at the onboard magnetometer installation point.

Let us introduce the vector $\vec{X}$ of the desired parameters for solving the problem of compensating the microsatellite initial magnetic field, whose components are the oblique values of the unknown values of three quantities g_{C1}^0, g_{C1}^1, h_{C1}^1 of the compensating dipole component, five quantities g_{C2}^0, g_{C2}^1, g_{C2}^2, h_{C2}^1 of the compensating quadrupole component and seven quantities g_{C3}^0, g_{C3}^1, g_{C3}^2, g_{C3}^3, h_{C3}^1, h_{C3}^2, h_{C3}^3 of the compensating octupole component of spherical harmonics of the magnetic field generated by C magnetic units with located at C points P_C with unknown coordinates r_c, φ_c and θ_c at the onboard magnetometer installation point.

Then, for a given value of the vector $\vec{X}$ of the desired parameters of the compensating dipoles, based on (14), the vector $\vec{B}_C(\vec{X})$ of the compensating magnetic field generated by all compensating dipoles at the installation point of the onboard magnetometer generated by all compensating dipoles can be calculated [21 – 23].

Then we calculated the vector $\vec{B}_R(\vec{X},\vec{G})$ of resulting magnetic field generated at the installation point of the onboard magnetometer by the all microsatellite units and all compensating elements

$$\vec{B}_R(\vec{X},\vec{G}) = \vec{B}(\vec{G}) + \vec{B}_C(\vec{X}). \qquad (13)$$

Then we also calculated the vector $\vec{M}_R(\vec{X},\vec{G})$ of resulting magnetic moment

$$\vec{M}_R(\vec{X},\vec{G}) = \vec{M}(\vec{G}) + \vec{M}_C(\vec{X}) \qquad (14)$$

of all microsatellite units and all compensating elements.

Then the problem of calculated unknown values of three quantities g_{C1}^0, g_{C1}^1, h_{C1}^1 of the dipole component, five quantities g_{C2}^0, g_{C2}^1, g_{C2}^2, h_{C2}^1 of the anti-quadrupole component and seven quantities g_{C3}^0, g_{C3}^1, g_{C3}^2, g_{C3}^3, h_{C3}^1, h_{C3}^2, h_{C3}^3 of the anti-octupole component of spherical harmonics of the magnetic field generated by C magnetic units with located at C points P_C with unknown coordinates at the onboard magnetometer installation point of the compensating anti-quadrupole and anti-octupole can be reduced to solving the problem of minimax optimization of resulting magnetic field (13) at the onboard magnetometer installation point and resulting magnetic moment (14) of all microsatellite units and all compensating elements.

This approach is standard when designing of robust control by microsatellite magnetic cleanliness, when the coordinates of the spatial arrangement and the magnitudes of the compensating dipole, quadrupole and octupole are found from the conditions for minimizing modulus of spacecraft resulting magnetic field (13) at the magnetometer installation point and resulting magnetic moment (14) of all microsatellite units and all compensating elements for the «worst» values of the vector of uncertainty parameters of the microsatellite magnetic characteristics.

Naturally, that in this case it is necessary to take into account the restriction on the coordinates r_c, φ_c and θ_c of the spatial arrangement and quantities on anti-dipole, anti-quadrupole and on anti-octupole components in the form of inequalities (12).

In conclusion, we note that the measurement of the components of the magnetic field of the units and the entire microsatellite assembly is usually performed in the orthogonal coordinate system. To calculate the magnetic field components B_r, B_φ, B_θ in spherical coordinates R, φ and θ according to the measured values of the magnetic field components B_X, B_Y, B_Z in an orthogonal coordinate system X, Y, Z we obtain the following expression

$$\begin{aligned} B_r &= B_x \sin(\theta)\cos(\varphi) + \dots \\ &\dots + B_y \sin(\theta)\sin(\varphi) + B_z \cos(\theta); \\ B_\theta &= B_x \cos(\theta)\cos(\varphi) + \dots \\ &\dots + B_y \cos(\theta)\sin(\varphi) - B_z \sin(\theta); \\ B_\varphi &= -B_x \sin(\varphi) + B_y \cos(\varphi). \end{aligned} \qquad (15)$$

To calculate the magnetic field components B_X, B_Y, B_Z in a orthogonal coordinate system X, Y, Z according to the values of the magnetic field components B_r, B_φ, B_θ in spherical coordinates R, φ and θ we obtain the following expression

$$\begin{aligned} B_x &= B_r \sin\theta_0 \cos\varphi_0 + B_\theta \cos\theta_0 \cos\varphi_0 - \dots \\ &\dots - B_\varphi \sin\varphi_0; \\ B_y &= B_r \sin\theta_0 \sin\varphi_0 + B_\theta \cos\theta_0 \sin\varphi_0 + \dots \\ &\dots + B_\varphi \cos\varphi_0; \\ B_z &= B_r \cos\theta_0 - B_0 \sin\theta_0. \end{aligned} \qquad (16)$$

In conclusion, we note that since the strength of the magnetic field and its induction are determined from (1) by the known formulas

$$\vec{H} = -grad\,\vec{U},\ \ \vec{B} = \mu_0 \cdot \vec{H}, \qquad (17)$$

then the magnetic field components R, φ and θ in spherical coordinates R, φ and θ, as well as the magnetic field components B_X, B_Y, B_Z in a orthogonal coordinate system X, Y, Z can be calculated based on the numerical differentiation of the original expression (1) for a scalar magnetic potential.

The scalar magnetic potential in the form of expression (1) is a function $U(R, \theta, \varphi)$ of three variables – spherical coordinates R, φ and θ. Therefore, the calculation of derivatives in numerical form with respect to these variables is connected with the calculation of derivatives directly from expression (1), for example, for the magnetic field components B_r, in the form

$$\frac{\partial(U(R,\theta,\varphi))}{\partial R} = \frac{U(R+\delta R,\theta,\varphi) - U(R-\delta R,\theta,\varphi)}{2\delta R}. \qquad (18)$$

To calculate the magnetic field components B_X, B_Y, B_Z in an orthogonal coordinate system X, Y, Z first, based on the transformation of spherical coordinates R, φ and θ into orthogonal coordinate system X, Y, Z on the basis of expression (8), we represent the expression for the scalar magnetic potential (1) as a function $U(X, Y, Z)$ of three independent variables X, Y, Z, which are the orthogonal coordinate system. Then the calculation of magnetic field components B_X, B_Y, B_Z in an orthogonal coordinate system X, Y, Z in numerical derivatives calculation form with respect to these variables with is connected with the calculation of derivatives directly by expression (1) by analogy (18), for example, for magnetic field components B_X, in the form

$$\frac{\partial(U(X,Y,Z))}{\partial X} = \frac{U(X+\delta X,\theta,\varphi) - U(X-\delta X,\theta,\varphi)}{2\delta X}. \qquad (19)$$

Note that when calculating the magnetic field components using expressions (3) – (5), it is required to perform 3 calculations, and when calculating the same

magnetic field components using expressions (18), (19), it is necessary to perform a calculation at 12 points, however, this uses the same expression (1) for the scalar magnetic potential.

Algorithm for solving the minimax optimization problem. To solve the problems of robust prediction and control by microsatellite magnetic cleanliness, it is necessary to solve minimax optimization problems (11), (13) and (14) with constraints (12). Consider algorithms for solving these problems. Algorithms for solving global minimax optimization problems are not trivial [37 – 42]. It is especially difficult to solve such problems, due to the need to search for a global optimum; complex landscape of the search surface, associated, among other things, with the presence of ravines; multidimensionality, multiextremality, multicriteria of problems with restrictions; lack of analytical expressions for objective functions, and, consequently, their algorithmic representation and high computational complexity, which involves the use of cumbersome numerical methods and is often a difficult independent task; non-differentiability and non-linearity; the presence of discrete and continuous variables in the goal function.

When using deterministic local search methods, a multi-start strategy is often used, which does not guarantee that the global optimum will eventually be found. Stochastic search methods are more promising for these purposes, since they explore the entire search space much more efficiently with subsequent localization in areas of local optima of the greatest interest [43 – 46].

Metaheuristic algorithms include ant colony and bee colony optimization algorithms, bacterial algorithms, particle swarm optimizations, evolutionary computations including genetic algorithms, simulated annealing method, and many others. Swarm optimization algorithms, as a kind of stochastic search method, due to their bionic features, are well suited for solving such problems [47 – 52].

The Particle Swarm Optimization (PSO) algorithm is a bionic multiagent global optimization method that models the social behavior of interacting agents [53 – 57]. The idea of the PSO method corresponds to the simulation of the movement of living beings in a flock of birds or a school of fish. Behavioral metaheuristic optimization methods are based on the bionic idea of collective adaptation, collective intelligence, i.e. the mechanism of dissemination of information in the «flock», «swarm», «school», which is due to the superiority of group intelligence over the mental abilities of one individual The social sharing of information provides evolutionary benefits to all members of the population, and the dominance of collective intelligence is the basis for the development of PSO algorithms.

In terms of the theory of artificial intelligence, each element of the system is called an agent. In the process of finding the optimum in such methods, not one agent is involved, but their whole system, called a population. This means that the solution to the problem is sought using a multi-agent system consisting of several intelligent agents with simple rules of interaction and autonomous behavior.

The characteristic properties of objects are: communicativeness, i.e. the ability to communicate with other agents, the ability to cooperate; adaptability, i.e. adaptability to environmental conditions and the ability to learn; decentralization, simplicity of individual behavior.

These properties of agents allow the phenomenon of self-organization to manifest itself in the system when performing the task of finding an extremum. In bionic methods of metaheuristic optimization, the goal function is more often called the fitness function, which is its synonym, but at the same time reflects the specifics of the approach used to solve the problem. Metaheuristic behavioral algorithms use a population of agents to find solutions close to optimal, checking the suitability of the current solution using a fitness function.

Agents, as a result of competition and cooperation with each other, look for a potential solution in the search space, using the value of the fitness function to improve the solution. Such methods operate on a set of potential solutions rather than a single possible solution. Each solution is incrementally improved and evaluated, with a single potential solution affecting how other solutions are improved.

Consider the PSO algorithm. In this method a swarm of particles is a set of decision points moving in space in search of a global optimum. During their movement, the particles try to improve the solution they found earlier and exchange information with their neighbors. At the initial stage of the PSO algorithm, a random initialization of a swarm of particles is performed. When performing optimization, 10–30 particles are usually sufficient. The swarm makes it possible to find the global optimum even when the number of particles in it is less than the dimension of the search space.

In the standard PSO algorithm for optimizing a swarm of particles, the speed of a swarm j particle i changes according to linear laws, in which the motion of a swarm of particles is described by the following expressions [57, 58]

$$v_{ij}(t+1) = c_{1j} r_{1j}(t) \ldots \times \left[y_{ij}(t) - x_{ij}(t) \right] + c_{2j} r_{2j}(t) \ldots \times \left[y_j^*(t) - x_{ij}(t) \right]; \quad (20)$$

$$x_{ij}(t+1) = x_{ij}(t) + v_{ij}(t+1), \quad (21)$$

where position $x_{ij}(t)$ and speed $v_{ij}(t)$ of the swarm j particle i; positive constants c_1 and c_2 determine the weights of the cognitive and social components of the particle's velocity; random numbers $r_{1j}(t)$ and $r_{2j}(t)$ from the range [0; 1] determine the stochastic component of the particle velocity component. Here $y_{ij}(t)$ and y_j^* are the best local-lbest and global-gbest positions of this particle, respectively, only one particle i and all particles i of this swarm j find.

The value of the cognitive coefficient c_1 characterizes the degree of individual behavior of the particle and its desire to return to the best solution found by it earlier, while the value of the social coefficient c_2 specifies the degree of collective behavior and the desire to move towards the best solution of its neighbors.

The inertial coefficient w_j determines the influence of the particle's previous velocity on its new value. The use of the inertia coefficient makes it possible to improve the quality of the optimization process.

If, during the optimization process, the particle goes beyond the search space specified by constraints (12), then the corresponding components of its velocity are set to zero, and the particle itself returns to the nearest boundary.

The algorithm for searching for a global solution to an optimization problem can be represented as an iterative process that generates a sequence of points in accordance with a prescribed set of rules, including the termination criterion. The search for a global solution to the optimization problem occurs by enumeration of local

solutions. In the general case, it is impossible to guarantee the exact solution of the global optimization problem for multiextremely function in a finite number of steps.

To prove that the found solution is the global optimum, it is necessary to perform a complete enumeration of all possible values of the parameter vector. In most cases, this is not possible, therefore, in global optimization, it is usually not about finding the optimal one, but about finding something close to it, i.e. suboptimal solution. The preference of stochastic methods of global optimization over deterministic ones is caused by their universality, which is explained by the estimation of the values of the goal function at random points of the admissible set, followed by analysis of the results at trial points of the search space.

To increase the speed of finding a global solution, special nonlinear algorithms for stochastic multi-agent optimization have recently become widespread [58].

The PSO method, as well as its various modifications, which have shown high efficiency in single-criteria optimization, can also be used to solve optimization problems in a multi-criteria formulation. In this case, the optimization problem is formulated and solved as a vector optimization problem. When solving a vector optimization problem (13), (14), it is necessary to take into account the priority of criteria, normalize them, choose a trade-off scheme, and determine the set of Pareto optimal solutions. To solve multicriteria optimization problems, the vector criterion scalarization method can be used by aggregating particular criteria, and an acceptable solution can be searched from the set of Pareto-optimal solutions by introducing additional information about the priority of particular criteria.

One of the simplest ways to solve an optimization problem in a multicriteria setting is the method of scalar convolution of a vector optimality criterion. This approach to solving a multicriteria optimization problem allows us to reduce it to solving a single-criteria problem by aggregating particular criteria. For these purposes, in practice, linear (additive) convolution is most often used:

$$\vec{X}^* = \underset{\vec{X}}{\operatorname{argmin}} \sum_{i=1}^{J} \alpha_i \left[f_i(\vec{x}) \right], \qquad (22)$$

where α_i are weight coefficients that characterize the importance of particular criteria f_i and determine the preference for individual criteria by the decision maker.

To solve the problem of multicriteria optimization, the simplest nonlinear trade-off scheme is also often used, in which the original multicriteria problem is reduced to a single criterion

$$\vec{X}^* = \underset{\vec{X}}{\operatorname{argmin}} \sum_{i=1}^{J} \alpha_i \left[1 - y_i(\vec{x}) \right]^{-1}, \qquad (23)$$

where y_i are normalized local criteria f_i, the value of which is in the range [0; 1]. Naturally, such a formalization of the solution of the multiobjective optimization problem by reducing it to a single-objective problem allows one to reasonably choose one single point from the area of compromises – the Pareto area. However, this «single» point can be further tested in order to further improve the trade-off scheme from the point of view of the decision maker.

An alternative approach to multiobjective optimization is to search for the Pareto set, which includes all solutions that are not dominated by other solutions. To find non-dominated solutions, it is convenient to use specially calculated ranks. However, this raises the problem of comparing several solutions that have the same rank values. To adapt the PSO method in relation to the problem of finding Pareto-optimal solutions on the set of possible values of a vector criterion, it is most simple to use binary preference relations that determine the Pareto dominance of individual solutions.

In conclusion, we note that when designing a multidipole model in the form of N dipoles, it is necessary to calculate $3N$ spherical coordinates r_k, φ_k and θ_k of the location of dipoles in microsatellite space and $3N$ values $g_{n1}^0(\vec{G})$, $g_{n1}^1(\vec{G})$, $h_{n1}^1(\vec{G})$ of the components of the magnetic moments of the N dipoles. As a result, it is necessary to calculate $6N$ unknown coordinates

When designing a multipole model in the form of N multipoles with dipole, quadrupole and octupole components, it is necessary, in addition to solving the problem of designing a multidipole model, to calculate another $5N$ values $g_{n2}^0(\vec{G})$, $g_{n2}^1(\vec{G})$, $g_{n2}^2(\vec{G})$, $h_{n2}^1(\vec{G})$, $h_{n2}^2(\vec{G})$ of the components of the quadrupole components, and also calculate $7N$ values $g_{n3}^0(\vec{G})$, $g_{n3}^1(\vec{G})$, $g_{n3}^2(\vec{G})$, $g_{n3}^3(\vec{G})$, $h_{n3}^1(\vec{G})$, $h_{n3}^2(\vec{G})$, $h_{n3}^3(\vec{G})$ of the components of the orthorupole components. As a result when designing a multipole model $18N$ unknown variables need calculated compared to $6N$ unknown variables in the design of the multi-dipole model.

Simulation results. Let us consider the use of the developed method for prediction and control by spacecraft magnetic cleanliness based on spatial harmonic analysis at the point of installation of the LEMI-016 magnetometer generated by the sensor of the KPNCSP, which is part of the «Potential» scientific equipment of the «Sich-2» spacecraft family to ensure the spacecraft magnetic cleanliness.

The layout of the onboard magnetometer LEMI-016 and the sensor for the KPNCSP on the «Sich-2» spacecraft family [18] shown in Fig. 2.

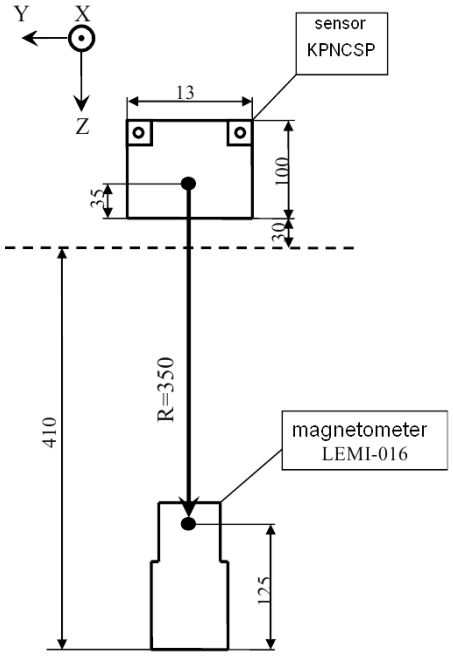

Fig. 2. The layout of the onboard magnetometer LEMI-016 and the sensor for the KPNCSP on the «Sich-2» spacecraft

To compensate the magnetic moment of the sensor, its permanent magnets are oriented antisymmetrically to

each other and a ferromagnetic screen is used. As a result, the magnetic moment of the sensor was reduced to the following values [18] of magnetic moment components in orthogonal coordinate system:

$M_x = 0.087$ A·m^2; $M_y = -0.084$ A·m^2; $M_z = 0.042$ A·m^2.

When using only the dipole model, the magnetic field components in a orthogonal coordinate system created by the residual magnetic moment of the sensor in the zone of the onboard magnetometer, calculated by formula (2), have the values:

$B_X = -203$ nT; $B_Y = 196$ nT; $B_Z = 196$ nT.

The paper [18] presents the values of harmonics calculated on the basis of the experimentally measured signatures of the magnetic flux of the sensor at the at the magnetic measuring stand of the Anatolii Pidhornyi Institute of Mechanical Engineering Problems of the National Academy of Sciences of Ukraine [59] when it moves through the measuring circuit

$$g_1^0 = 4.1\ 10^{-3},\ g_1^1 = -8.4\ 10^{-2},\ h_1^1 = 4.2\ 10^{-2},$$
$$g_2^0 = 1.411\ 10^{-3},\ g_3^0 = 2.5\ 10^{-4}.$$

In this case, the value of the magnetic field component B_Z in a orthogonal coordinate system along the axis Z at the installation point of the onboard magnetometer, taking into account only the first harmonic $B_Z = 237$ nT, taking into account only the second harmonic $B_Z = 352$ nT, and taking into account only the third harmonic $B_Z = 247$ nT. The magnitude of the resulting magnetic field when three spatial harmonics are taken into account $B_Z = 836$ nT [18]. The relative contribution of the dipole harmonic (field of the magnetic moment) to the magnetic induction created by the sensor in the area of the onboard magnetometer is only about 20 %. The contribution of quadrupole and octupole spherical harmonics to the magnetic induction of disturbance to the on-board magnetometer is about 80 % [18].

Let us consider the solution of the problem of compensation of spatial harmonics of the initial magnetic field. As a result of solving the optimization problem, the values of the harmonics of the compensating quadrupole are calculated

$$g_2^0 = 0.0249959,\ g_2^1 = 0.981453,\ g_2^2 = 0.271729,$$
$$h_2^1 = 0.62818,\ h_2^2 = 0.620474.$$

The values of the harmonics of the compensating octupole are calculated

$$g_3^0 = 0.00160516,\ g_3^1 = 0.0282545,\ g_3^2 = 0.651052,$$
$$g_3^3 = -0.704719,\ h_3^1 = 0.0031692,$$
$$h_3^2 = 0.175824,\ h_3^3 = -1.11672.$$

And also the spherical coordinates of the spatial arrangement of the compensating quadrupole and octupole are calculated

$r_k = 0.0768617$; $\varphi_k = 0.163995$; $\theta_k = 3.90015$.

In this case, the following values of magnetic induction were obtained in the probe of the location of the onboard magnetometer. Initial magnetic field

$B_X = -202{,}86$ nT; $B_Y = 195{,}935$ nT; $B_Z = 243{,}115$ nT.

Compensating magnetic field

$B_{KX} = 202.913$ nT; $B_{KY} = -195.669$ nT; $B_{KZ} = -243.13$ nT.

The resulting magnetic field

$B_{RX} = 0.0527476$ nT; $B_{RY} = 0.26579$ nT; $B_{RZ} = -0.0153575$ nT.

Thus, due to the installation of compensating quadropoles and octupoles, it was possible to reduce the level of magnetic field induction at the point of installation of the «Sich-2» spacecraft family onboard magnetometer by a factor of more than two orders.

In conclusion, we note that the implementation of compensating quadrupoles and octupoles can be performed both with the help of permanent magnets and with the help of electromagnets [21, 24]. Naturally, the technical implementation of compensating elements with the help of permanent magnets is simpler, however, when implementing compensating elements with the help of electromagnets, an additional possibility appears to increase the magnetic purity of the microsatellite when it operates in various operating modes by controlling the parameters of the compensating elements in real time.

Conclusions.

1. The method for prediction and control the microsatellite magnetic cleanliness taking into account the uncertainties of the magnetic characteristics of the microsatellite, based on calculation the magnetic field spatial spherical harmonics in the area of the onboard magnetometer installation and using compensating multipole has been developed.

2. The spatial spherical harmonics of the microsatellite magnetic field is calculated based on the solution of the nonlinear minimax optimization problem. The nonlinear objective function of this nonlinear minimax optimization problem is calculated as a weighted sum of squared residuals between the measured and predicted magnetic field levels at the measurement points. The values of the spatial spherical harmonics of compensating dipole, quadrupole and octupole, as well as the coordinates of their spatial placement inside the microsatellite to compensate the dipole, quadrupole, and octupole components of the initial magnetic field of the microsatellite, are also calculated as a solution to the nonlinear minimax optimization problem. Solutions to both nonlinear minimax optimization problems are computed based on particle swarm nonlinear optimization algorithms.

3. The developed method was used to improve the magnetic cleanliness of the «Sich-2» microsatellite. Based on calculation of spatial spherical harmonics of the magnetic field generated by the kinetic parameters sensor of the neutral component of the space plasma at the installation point of the onboard magnetometer LEMI-016 of the «Sich-2» microsatellite family, the spatial harmonics of the compensating dipole, quadrupole and octupole, as well as the coordinates of the spatial location of these compensating elements in the space of a microsatellite are calculated to compensate for quadrupole and octupole harmonics of the initial magnetic field. The use of compensating quadrupole and octupole made it possible to reduce the level of magnetic field induction of the microsatellite at the point of installation of the magnetometer by more than two orders of magnitude, which will increase its controllability in orbit.

Acknowledgments. The authors express their gratitude to the researcher Anatoliy Erisov of the Department of Magnetism of Technical Objects of Anatolii Pidhornyi Institute of Mechanical Engineering Problems of the National Academy of Sciences of Ukraine for the kindly provided materials on the results of experimental measured magnetic field generated by elements and «Sich-2» spacecraft family and also for numerous discussions that allowed the authors to improve the article manuscript.

Conflict of interest. The authors declare that they have no conflicts of interest.

REFERENCES

1. Rozov V.Yu., Getman A.V., Petrov S.V. Spacecraft magnetism. *Technical Electrodynamics. Thematic issue «Problems of modern electrical engineering»*, 2010, part 2, pp. 144-147. (Rus).

2. Rozov V.Yu. Methods for reducing external magnetic fields of energy-saturated objects. *Technical Electrodynamics*, 2001, no. 1, pp. 16-20.

3. Birsan M., Holtham P., Carmen. Using global optimisation techniques to solve the inverse problem for the computation of the static magnetic signature of ships. *Defense Research Establishment Atlantic*, 9 Grove St., PO Box 1012, Dartmouth, Nova Scotia, B2Y 3Z7, Canada.

4. Acuña M.H. *The design, construction and test of magnetically clean spacecraft – a practical guide*. NASA/GSFC internal report. 2004.

5. Junge A., Marliani F. Prediction of DC magnetic fields for magnetic cleanliness on spacecraft. *2011 IEEE International Symposium on Electromagnetic Compatibility*, 2011, pp. 834-839. doi: https://doi.org/10.1109/ISEMC.2011.6038424.

6. Lynn G.E., Hurt J.G., Harriger K.A. Magnetic control of satellite attitude. *IEEE Transactions on Communication and Electronics*, 1964, vol. 83, no. 74, pp. 570-575. doi: https://doi.org/10.1109/TCOME.1964.6539511.

7. Junge A., Trougnou L., Carrubba E. Measurement of Induced Equivalent Magnetic Dipole Moments for Spacecraft Units and Components. *Proceedings ESA Workshop Aerospace EMC 2009 ESA WPP-299*, 2009, vol. 4, no. 2, pp. 131-140.

8. Mehlem K., Wiegand A. Magnetostatic cleanliness of spacecraft. *2010 Asia-Pacific International Symposium on Electromagnetic Compatibility*, 2010, pp. 936-944. doi: https://doi.org/10.1109/APEMC.2010.5475692.

9. Messidoro P., Braghin M., Grande M. Magnetic cleanliness verification approach on tethered satellite. *16th Space Simulation Conference: Confirming Spaceworthiness into the Next Millennium*, 1991, pp. 415-434.

10. Mehlem K., Narvaez P. Magnetostatic cleanliness of the radioisotope thermoelectric generators (RTGs) of Cassini. *1999 IEEE International Symposium on Electromagnetic Compatability*, 1999, vol. 2, pp. 899-904. doi: https://doi.org/10.1109/ISEMC.1999.810175.

11. Eichhorn W.L. *Magnetic dipole moment determination by near-field analysis*. Goddard Space Flight Center. Washington, D.C., National Aeronautics and Space Administration, 1972. NASA technical note, D 6685. 87 p.

12. Matsushima M., Tsunakawa H., Iijima Y., Nakazawa S., Matsuoka A., Ikegami S., Ishikawa T., Shibuya H., Shimizu H., Takahashi F. Magnetic Cleanliness Program Under Control of Electromagnetic Compatibility for the SELENE (Kaguya) Spacecraft. *Space Science Reviews*, 2010, vol. 154, no. 1-4, pp. 253-264. doi: https://doi.org/10.1007/s11214-010-9655-x.

13. Boghosian M., Narvaez P., Herman R. Magnetic testing, and modeling, simulation and analysis for space applications. *2013 IEEE International Symposium on Electromagnetic Compatibility*, 2013, pp. 265-270. doi: https://doi.org/10.1109/ISEMC.2013.6670421.

14. Mehlem K. Multiple magnetic dipole modeling and field prediction of satellites. *IEEE Transactions on Magnetics*, 1978, vol. 14, no. 5, pp. 1064-1071. doi: https://doi.org/10.1109/TMAG.1978.1059983.

15. Thomsen P.L., Hansen F. Danish Ørsted Mission In-Orbit Experiences and Status of The Danish Small Satellite Programme. *Annual AIAA/USU Conference on Small Satellites*, 1999, pp. SSC99-I–8.

16. Droughts S.A., Fedorov O.P. Space project Ionosat-Micro. Monograph. Kyiv, Akademperiodika Publ., 2013. 218 p. (Rus).

17. Getman A.V. *Analysis and synthesis of the magnetic field structure of technical objects on the basis of spatial harmonics*. Dissertation thesis for the degree of Doctor of Technical Sciences. Kharkiv, 2018. 43 p. (Ukr).

18. Getman A.V. Spatial harmonic analysis of the magnetic field of the sensor of the neutral plasma component. *Eastern European Journal of Advanced Technologies*, 2010, vol. 6, no. 5(48), pp. 35-38. doi: https://doi.org/10.15587/1729-4061.2010.3326.

19. *ECSS-E-HB-20-07A. Space engineering: Electromagnetic compatibility hand-book. ESA-ESTEC. Requirements & Standards Division*. Noordwijk, Netherlands, 2012. 228 p.

20. Rozov V.Yu. Mathematical model of electrical equipment as a source of external magnetic field. *Technical Electrodynamics*, 1995, no. 2, pp. 3-7. (Rus).

21. Rozov V.Yu., Dobrodeev P.N., Volokhov S.A. Multipole model of a technical object and its magnetic center. *Technical Electrodynamics*, 2008, no. 2, pp. 3-8. (Rus).

22. Rozov V.Yu. Selective compensation of spatial harmonics of the magnetic field of energy-saturated objects. *Technical Electrodynamics*, 2002, no. 1, pp. 8-13. (Rus).

23. Rozov V.Y., Reutskyi S.Y., Pelevin D.Y., Yakovenko V.N. The research of magnetic field of high-voltage AC transmissions lines. *Technical Electrodynamics*, 2012, no. 1, pp. 3-9. (Rus).

24. Volokhov S.A., Dobrodeev P.N., Ivleva L.F. Spatial harmonic analysis of the external magnetic field of a technical object. *Technical Electrodynamics*, 1996, no. 2, pp. 3-8. (Rus).

25. Getman A. Ensuring the Magnetic Compatibility of Electronic Components of Small Spacecraft. *2022 IEEE 3rd KhPI Week on Advanced Technology (KhPIWeek)*, 2022, no. 1-4. doi: https://doi.org/10.1109/KhPIWeek57572.2022.9916339.

26. Chadebec O., Rouve L.-L., Coulomb J.-L. New methods for a fast and easy computation of stray fields created by wound rods. *IEEE Transactions on Magnetics*, 2002, vol. 38, no. 2, pp. 517-520. doi: https://doi.org/10.1109/20.996136.

27. Rozov V.Y., Pelevin D.Y., Kundius K.D. Simulation of the magnetic field in residential buildings with built-in substations based on a two-phase multi-dipole model of a three-phase current conductor. *Electrical Engineering & Electromechanics*, 2023, no. 5, pp. 87-93. doi: https://doi.org/10.20998/2074-272X.2023.5.13.

28. Rozov V.Yu., Kundius K.D., Pelevin D.Ye. Active shielding of external magnetic field of built-in transformer substations. *Electrical Engineering & Electromechanics*, 2020, no. 3, pp. 24-30. doi: https://doi.org/10.20998/2074-272x.2020.3.04.

29. Martynenko G. Analytical Method of the Analysis of Electromagnetic Circuits of Active Magnetic Bearings for Searching Energy and Forces Taking into Account Control Law. *2020 IEEE KhPI Week on Advanced Technology (KhPIWeek)*, 2020, pp. 86-91. doi: https://doi.org/10.1109/KhPIWeek51551.2020.9250138.

30. Martynenko G., Martynenko V. Rotor Dynamics Modeling for Compressor and Generator of the Energy Gas Turbine Unit with Active Magnetic Bearings in Operating Modes. *2020 IEEE Problems of Automated Electrodrive. Theory and Practice (PAEP)*, 2020, pp. 1-4. doi: https://doi.org/10.1109/PAEP49887.2020.9240781.

31. Ostroverkhov M., Trinchuk D. Increasing the Efficiency of Electric Vehicle Drives with Supercapacitors in Power Supply. *2020 IEEE 7th International Conference on Energy Smart Systems (ESS)*, 2020, pp. 258-261. doi: https://doi.org/10.1109/ESS50319.2020.9160291.

32. Ostroverkhov N., Buryk N. Control System with Field Weakening of Synchronous Motor Drive. *2020 IEEE Problems of Automated Electrodrive. Theory and Practice (PAEP)*, 2020, pp. 1-5. doi: https://doi.org/10.1109/PAEP49887.2020.9240903.

33. Chen C.S., Reutskiy S.Y., Rozov V.Y. The method of the fundamental solutions and its modifications for electromagnetic field problems. *Computer Assisted Mechanics and Engineering Sciences*, 2009, vol. 16, no. 1, pp. 21-33.

34. Tytiuk V., Chornyi O., Baranovskaya M., Serhiienko S., Zachepa I., Tsvirkun L., Kuznetsov V., Tryputen N. Synthesis of a fractional-order $PI^{\lambda}D^{\mu}$-controller for a closed system of switched reluctance motor control. *Eastern-European Journal of Enterprise Technologies*, 2019, no. 2 (98), pp. 35-42. doi: https://doi.org/10.15587/1729-4061.2019.160946.

35. Zagirnyak M., Serhiienko S., Chornyi O. Innovative technologies in laboratory workshop for students of technical specialties. *2017 IEEE First Ukraine Conference on Electrical and Computer Engineering (UKRCON)*, 2017, pp. 1216-1220. doi: https://doi.org/10.1109/UKRCON.2017.8100446.

36. Chornyi O., Serhiienko S. A virtual complex with the parametric adjustment to electromechanical system parameters. *Technical Electrodynamics*, 2019, pp. 38-41. doi: https://doi.org/10.15407/techned2019.01.038.

37. Shchur I., Kasha L., Bukavyn M. Efficiency Evaluation of Single and Modular Cascade Machines Operation in Electric Vehicle. *2020 IEEE 15th International Conference on Advanced Trends in Radioelectronics, Telecommunications and Computer Engineering (TCSET)*, Lviv-Slavske, Ukraine, 2020, pp. 156-161. doi: https://doi.org/10.1109/tcset49122.2020.235413.

38. Shchur I., Turkovskyi V. Comparative Study of Brushless DC Motor Drives with Different Configurations of Modular Multilevel Cascaded Converters. *2020 IEEE 15th International Conference on Advanced Trends in Radioelectronics, Telecommunications and Computer Engineering (TCSET)*, Lviv-Slavske, Ukraine, 2020, pp. 447-451. doi: https://doi.org/10.1109/tcset49122.2020.235473.

39. Solomentsev O., Zaliskyi M., Averyanova Y., Ostroumov I., Kuzmenko N., Sushchenko O., Kuznetsov B., Nikitina T., Tserne E., Pavlikov V., Zhyla S., Dergachov K., Havrylenko O., Popov A., Volosyuk V., Ruzhentsev N., Shmatko O. Method of Optimal Threshold Calculation in Case of Radio Equipment Maintenance. *Data Science and Security. Lecture Notes in Networks and Systems*, 2022, vol. 462, pp. 69-79. doi: https://doi.org/10.1007/978-981-19-2211-4_6.
40. Ruzhentsev N., Zhyla S., Pavlikov V., Volosyuk V., Tserne E., Popov A., Shmatko O., Ostroumov I., Kuzmenko N., Dergachov K., Sushchenko O., Averyanova Y., Zaliskyi M., Solomentsev O., Havrylenko O., Kuznetsov B., Nikitina T. Radio-Heat Contrasts of UAVs and Their Weather Variability at 12 GHz, 20 GHz, 34 GHz, and 94 GHz Frequencies. *ECTI Transactions on Electrical Engineering, Electronics, and Communications*, 2022, vol. 20, no. 2, pp. 163-173. doi: https://doi.org/10.37936/ecti-eec.2022202.246878.
41. Havrylenko O., Dergachov K., Pavlikov V., Zhyla S., Shmatko O., Ruzhentsev N., Popov A., Volosyuk V., Tserne E., Zaliskyi M., Solomentsev O., Ostroumov I., Sushchenko O., Averyanova Y., Kuzmenko N., Nikitina T., Kuznetsov B. Decision Support System Based on the ELECTRE Method. *Data Science and Security. Lecture Notes in Networks and Systems*, 2022, vol. 462, pp. 295-304. doi: https://doi.org/10.1007/978-981-19-2211-4_26.
42. Shmatko O., Volosyuk V., Zhyla S., Pavlikov V., Ruzhentsev N., Tserne E., Popov A., Ostroumov I., Kuzmenko N., Dergachov K., Sushchenko O., Averyanova Y., Zaliskyi M., Solomentsev O., Havrylenko O., Kuznetsov B., Nikitina T. Synthesis of the optimal algorithm and structure of contactless optical device for estimating the parameters of statistically uneven surfaces. *Radioelectronic and Computer Systems*, 2021, no. 4, pp. 199-213. doi: https://doi.org/10.32620/reks.2021.4.16.
43. Volosyuk V., Zhyla S., Pavlikov V., Ruzhentsev N., Tserne E., Popov A., Shmatko O., Dergachov K., Havrylenko O., Ostroumov I., Kuzmenko N., Sushchenko O., Averyanova Yu., Zaliskyi M., Solomentsev O., Kuznetsov B., Nikitina T. Optimal Method for Polarization Selection of Stationary Objects Against the Background of the Earth's Surface. *International Journal of Electronics and Telecommunications*, 2022, vol. 68, no. 1, pp. 83-89. doi: https://doi.org/10.24425/ijet.2022.139852.
44. Halchenko V., Trembovetska R., Tychkov V., Storchak A. Nonlinear surrogate synthesis of the surface circular eddy current probes. *Przegląd Elektrotechniczny*, 2019, vol. 95, no. 9, pp. 76-82. doi: https://doi.org/10.15199/48.2019.09.15.
45. Halchenko V.Ya., Storchak A.V., Trembovetska R.V., Tychkov V.V. The creation of a surrogate model for restoring surface profiles of the electrophysical characteristics of cylindrical objects. *Ukrainian Metrological Journal*, 2020, no. 3, pp. 27-35. doi: https://doi.org/10.24027/2306-7039.3.2020.216824.
46. Zhyla S., Volosyuk V., Pavlikov V., Ruzhentsev N., Tserne E., Popov A., Shmatko O., Havrylenko O., Kuzmenko N., Dergachov K., Averyanova Y., Sushchenko O., Zaliskyi M., Solomentsev O., Ostroumov I., Kuznetsov B., Nikitina T. Practical imaging algorithms in ultra-wideband radar systems using active aperture synthesis and stochastic probing signals. *Radioelectronic and Computer Systems*, 2023, no. 1, pp. 55-76. doi: https://doi.org/10.32620/reks.2023.1.05.
47. Chystiakov P., Chornyi O., Zhautikov B., Sivyakova G. Remote control of electromechanical systems based on computer simulators. *2017 International Conference on Modern Electrical and Energy Systems (MEES)*, Kremenchuk, Ukraine, 2017, pp. 364-367. doi: https://doi.org/10.1109/mees.2017.8248934.
48. Zagirnyak M., Bisikalo O., Chorna O., Chornyi O. A Model of the Assessment of an Induction Motor Condition and Operation Life, Based on the Measurement of the External Magnetic Field. *2018 IEEE 3rd International Conference on Intelligent Energy and Power Systems (IEPS)*, Kharkiv, 2018, pp. 316-321. doi: https://doi.org/10.1109/ieps.2018.8559564.
49. Maksymenko-Sheiko K.V., Sheiko T.I., Lisin D.O., Petrenko N.D. Mathematical and Computer Modeling of the Forms of Multi-Zone Fuel Elements with Plates. *Journal of Mechanical Engineering*, 2022, vol. 25, no. 4, pp. 32-38. doi: https://doi.org/10.15407/pmach2022.04.032.
50. Hontarovskyi P.P., Smetankina N.V., Ugrimov S.V., Garmash N.H., Melezhyk I.I. Computational Studies of the Thermal Stress State of Multilayer Glazing with Electric Heating. *Journal of Mechanical Engineering*, 2022, vol. 25, no. 1, pp. 14-21. doi: https://doi.org/10.15407/pmach2022.02.014.
51. Kostikov A.O., Zevin L.I., Krol H.H., Vorontsova A.L. The Optimal Correcting the Power Value of a Nuclear Power Plant Power Unit Reactor in the Event of Equipment Failures. *Journal of Mechanical Engineering*, 2022, vol. 25, no. 3, pp. 40-45. doi: https://doi.org/10.15407/pmach2022.03.040.
52. Rusanov A.V., Subotin V.H., Khoryev O.M., Bykov Y.A., Korotaiev P.O., Ahibalov Y.S. Effect of 3D Shape of Pump-Turbine Runner Blade on Flow Characteristics in Turbine Mode. *Journal of Mechanical Engineering*, 2022, vol. 25, no. 4, pp. 6-14. doi: https://doi.org/10.15407/pmach2022.04.006.
53. Ummels M. *Stochastic Multiplayer Games Theory and Algorithms*. Amsterdam University Press, 2010. 174 p.
54. Shoham Y., Leyton-Brown K. *Multiagent Systems: Algorithmic, Game-Theoretic, and Logical Foundations.* Cambridge University Press, 2009. 504 p.
55. Sushchenko O., Averyanova Y., Ostroumov I., Kuzmenko N., Zaliskyi M., Solomentsev O., Kuznetsov B., Nikitina T., Havrylenko O., Popov A., Volosyuk V., Shmatko O., Ruzhentsev N., Zhyla S., Pavlikov V., Dergachov K., Tserne E. Algorithms for Design of Robust Stabilization Systems. *Computational Science and Its Applications – ICCSA 2022. ICCSA 2022. Lecture Notes in Computer Science*, 2022, vol. 13375, pp. 198-213. doi: https://doi.org/10.1007/978-3-031-10522-7_15.
56. Zhyla S., Volosyuk V., Pavlikov V., Ruzhentsev N., Tserne E., Popov A., Shmatko O., Havrylenko O., Kuzmenko N., Dergachov K., Averyanova Y., Sushchenko O., Zaliskyi M., Solomentsev O., Ostroumov I., Kuznetsov B., Nikitina T. Statistical synthesis of aerospace radars structure with optimal spatio-temporal signal processing, extended observation area and high spatial resolution. *Radioelectronic and Computer Systems*, 2022, no. 1, pp. 178-194. doi: https://doi.org/10.32620/reks.2022.1.14.
57. Xin-She Yang, Zhihua Cui, Renbin Xiao, Amir Hossein Gandomi, Mehmet Karamanoglu. *Swarm Intelligence and Bio-Inspired Computation: Theory and Applications*, Elsevier Inc., 2013. 450 p.
58. Hashim F.A., Hussain K., Houssein E.H., Mabrouk M.S., Al-Atabany W. Archimedes optimization algorithm: a new metaheuristic algorithm for solving optimization problems. *Applied Intelligence*, 2021, vol. 51, no. 3, pp. 1531-1551. doi: https://doi.org/10.1007/s10489-020-01893-z.
59. Baranov M.I., Rozov V.Y., Sokol Y.I. To the 100th anniversary of the National Academy of Sciences of Ukraine – the cradle of domestic science and technology. *Electrical Engineering & Electromechanics*, 2018, no. 5, pp. 3-11. doi: https://doi.org/10.20998/2074-272X.2018.5.01.

Received 30.08.2023
Accepted 28.10.2023
Published 02.01.2024

B.I. Kuznetsov[1], *Doctor of Technical Science, Professor,*
T.B. Nikitina[2], *Doctor of Technical Science, Professor,*
I.V. Bovdui[1], *PhD, Senior Research Scientist,*
K.V. Chunikhin[1], *PhD, Research Scientist,*
V.V. Kolomiets[2], *PhD, Assistant Professor,*
B.B. Kobylianskyi[2], *PhD, Associate Professor,*
[1] Anatolii Pidhornyi Institute of Mechanical Engineering Problems of the National Academy of Sciences of Ukraine,
2/10, Pozharskogo Str., Kharkiv, 61046, Ukraine,
e-mail: kuznetsov.boris.i@gmail.com (Corresponding Author)
[2] Educational scientific professional pedagogical Institute of Ukrainian Engineering Pedagogical Academy,
9a, Nosakov Str., Bakhmut, Donetsk Region, 84511, Ukraine,
e-mail: nnppiuipa@ukr.net

How to cite this article:
Kuznetsov B.I., Nikitina T.B., Bovdui I.V., Chunikhin K.V., Kolomiets V.V., Kobylianskyi B.B. Method for prediction and control by uncertain microsatellite magnetic cleanliness based on calculation and compensation magnetic field spatial harmonics. *Electrical Engineering & Electromechanics*, 2024, no. 1, pp. 23-33. doi: https://doi.org/10.20998/2074-272X.2024.1.04

UDC 621.3.015.52: 621.3.022: 621.319.53 https://doi.org/10.20998/2074-272X.2024.1.05

M.I. Baranov

A generalized physical principle of development of plasma channel of a high-voltage pulse spark discharge in a dielectric

Goal. *Development of the generalized physical principle of development of plasma channel of a high-voltage electrical pulse spark discharge in the homogeneous dielectric of the different aggregate state.* ***Methodology.*** *Basis of physical optics, theoretical electrical engineering, electrophysics bases of technique of high-voltage and large pulse currents, bases of high-voltage pulse technique and measuring technique.* ***Results.*** *Development of physical principle of development of plasma channel of an electric pulse spark discharge is executed in a homogeneous gas dielectric on the applied example of the use in calculations and experiments of the double-electrode discharge system (DEDS) with a long air interval, testing action of standard interconnect aperiodic pulse of high-voltage of temporal shape of T_m/T_d≈200 μs/1990 μs of positive polarity. The generalized formula is got for the calculation of total length of l_c of the real way of development of an pulse spark discharge in an air dielectric, which allowed to formulate the offered physical principle in the following kind: «The plasma channel of an pulse spark discharge in a gas dielectric spreads from one of its points to other after a way length of l_c, providing the least falling on it of electric voltage of U_c». It is shown that this principle in the first approaching can be applied and to the homogeneous liquid and hard dielectrics. Comparison of the developed physical principle of distribution of plasma channel of an electrical spark discharge is executed in a dielectrical environment with fundamental Fermat physical principle (a law) for distribution of light in an optically transparent environment, which specifies on mathematical likeness and closeness on destiny of these physical principles. Calculation estimations of falling of electric voltage of U_c on total length of l_c of the real zigzag way of development in the air dielectric of DEDS a «edge-plane» with the least length of its discharge interval of l_{min}=1,5 m is presented, that a value U_c does not exceed 9 % from the experimental level of aggressive voltage of U_{md}≈611,6 κV in this DEDS for the aperiodic pulse of voltage of T_m/T_d≈200 μs/1990 μs. It is set that the estimated time of t_d advancement of leader channel of electric pulse discharge in air DEDS (l_{min}=1,5 m) on its real way total length of l_c≈1,53 m makes t_d≈15,3 μs, and experimental duration of cut of T_{dc} of the indicated aperiodic impulse of voltage utilized in experiments, characterizing time of short circuit by the plasma channel of discharge of air interval in DEDS, appears equal T_{dc}≈t_d≈17 μs.* ***Originality.*** *The generalized physical principle of development of plasma channel of a high-voltage electrical pulse spark discharge is first developed in the homogeneous dielectric of the different aggregate state.* ***Practical value.*** *Application in electrical engineering practice and high-voltage pulse technique of the offered principle of distribution in the dielectrics of plasma channel of an pulse spark discharge will allow to develop both new and to perfect the existent methods of computer design of electro-discharge processes in the gas, liquid and hard insulation of different high-voltage electrical power engineering and electrophysics devices, directed on the increase of reliability of their operation.* References 25, figures 5.

Key words: **plasma channel, spark discharge, dielectric environment, physical principle of development of plasma channel, calculation, experiment.**

Надані результати розробки узагальненого фізичного принципу розвитку в гомогенному діелектричному середовищі плазмового каналу високовольтного електричного імпульсного іскрового розряду. Показано, що канал даного виду електричного розряду в газовому діелектрику розповсюджується по зигзагоподібному шляху завдовжки l_c, який забезпечує найменше падіння на ньому електричної напруги U_c. Для обґрунтування прийнятих початкових фізичних положень і верифікації отриманих розрахункових електрофізичних даних представлені результати високовольтних сильнострумових експериментів по електричному пробою довгого повітряного проміжку в двоелектродній розрядній системі «вістря-площина» (l_{min}=1,5 м) із застосуванням стандартного комутаційного аперіодичного імпульсу високої напруги часової форми T_m/T_d≈200 мкс/1990 мкс позитивної полярності. Виконано порівняння розробленого фізичного принципу розповсюдження плазмового каналу високовольтного електричного імпульсного іскрового розряду в діелектричному середовищі з фундаментальним фізичним принципом (законом) Ферма для розповсюдження світла в оптично прозорому середовищі, яке вказує на схожість за формою математичного запису і близькість за змістовним призначенням даних фізичних принципів. Бібл. 25, рис. 5.

Ключові слова: **плазмовий канал, іскровий розряд, діелектричне середовище, фізичний принцип розвитку плазмового каналу**, **розрахунок, експеримент.**

State-of-the-art and relevance of the problem. Electric pulse spark discharge in vacuum, gas, liquid and solid dielectric media, which is carried out with the help of high-voltage low- and high-current electrical equipment, has found quite wide practical application for both scientific and technological purposes [1-5]. Let us point out that this type of high-voltage electric discharge belongs to one of the known and well-studied classical types of self-discharge in a dielectric today in electrophysics [6-8]. Electric discharge technologies based on the transformation of electrical energy stored, as a rule, in powerful high-voltage capacitor batteries into the energy of phase transitions, chemical reactions, explosion of solid substances, shock waves, into mechanical work, heat and other types of energy [3, 9-11], have one fundamental difference from other technologies: they are capable of providing a large energy density in the pulse mode of its action to the substance under investigation or the processed product (object). At the same time, the time of this action can vary in a wide range: from hundreds of milliseconds to units of nanoseconds. Taking into account the prospects of electrical discharge technologies based on pulse spark discharge, in recent decades the following important scientific results were obtained by domestic and foreign electrical engineering scientists and electrophysicists in this area of high-voltage pulsed technology (HPT) [1, 3-12]: data on the dependence of the electrical strength of many dielectrics from the length of the interelectrode

gaps, the geometry of the electrodes used in these gaps of different metals and conductive compositions, the amplitude-time parameters (ATPs) of the electric voltage (current) acting on the dielectric, and the electrophysical parameters of the surrounding dielectric insulating medium; volt-second characteristics of electrical breakdown of many types of dielectrics; found distributions of the strength of high pulse electric field in linear and heterogeneous dielectrics placed in interelectrode spaces with electrodes of different configurations; determined main types of electric discharge structures and the parameters of discharge plasma channels in the main types of dielectrics at different ATPs of voltage (current); obtained the first adequate calculation data for computer modeling of complex electrophysical processes of the development of the plasma channel of an electrical pulse spark discharge in some types of dielectrics.

Despite the above-mentioned scientific results, in the field of modern HPT, in the study of pulse spark discharge in dielectrics, those related to the development of mechanisms and the description of analytical models of the development of the plasma channel of this discharge in them remain poorly studied issues. The presence of similar mechanisms and analytical models will contribute to the further improvement of computer modeling methods of the development of the plasma channel of electric spark discharge in dielectrics of various natures [13-18], which have important applied value in the field of high-voltage electrical engineering, industrial electric power engineering, HPT, high-current electronics, nuclear engineering and protection of aircraft and ground infrastructure objects from the impact of atmospheric electricity (lightning).

The goal of the article is to obtain a generalized physical principle of the development of a plasma channel of a high-voltage pulse spark discharge in a homogeneous dielectric of a different aggregate state.

1. Problem definition. For the certainty of solving this applied electrophysical problem, consider a high-voltage double-electrode discharge system (DEDS), which contains a potential electrode in the form of a metal rod 1 of finite geometric dimensions pointed at the edge and a grounded electrode in the form of a metal plane 2 of unlimited geometric dimensions (Fig. 1). Let the electric potentials of these electrodes 1 and 2 be equal to φ_1 and φ_2=0, respectively, and between them in the interelectrode air gap of minimum length $l_{\min}$, equal to the length of the straight line drawn from the tip of the potential electrode 1 along the normal to the flat surface of the grounded electrode 2, a homogeneous gas is placed by the following atmospheric conditions [19]: gas pressure $P_a \approx (1.013 \pm 0.003) \cdot 10^5$ Pa; absolute gas temperature $T_a \approx (293.15 \pm 5)$ K; relative humidity of gas (45±15) %. Let us assume that the electrical strength of the interelectrode air gap in the DEDS in relation to the average level of its breakdown voltage of high pulse electric field for the electric voltage pulse applied to the DEDS is equal to E_d. Here, the potential φ_1 acquires a value equal to φ_{1d}.

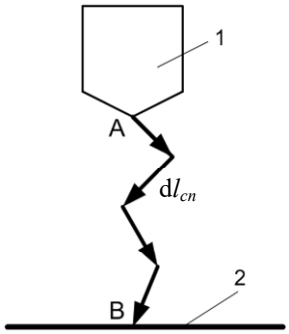

Fig. 1. Schematic representation of the aerial DEDS, on the example of which the process of the development of a plasma channel of a high-voltage electric pulse spark discharge in a gas dielectric is considered (1, 2 − respectively, the metal rod with potential φ_1 and the metal plane with potential φ_2; A, B − the starting and ending points of the path of the spatial development of the pulse plasma channel spark discharge in a gas dielectric)

We will limit ourselves to the consideration of the applied case, when the ATPs of high electrical pulse voltage $U_{12}(t)=(\varphi_1-\varphi_2)$ in the interelectrode air gap of the DEDS changes in time t according to the law of the standard switching aperiodic voltage pulse of the time shape $T_m/T_d \approx (250\pm50)$ μs/(2500±750) μs of positive polarity with appropriate tolerances on its parameters [20, 21]. It is this type of high pulse voltage that is most often used in industrial electric power and HPT when determining the electrical strength of the internal and external insulation of various high-voltage electrical equipment and powerful high-voltage electrophysical test equipment. Taking into account the leading stage of the development of the plasma channel of an electric discharge in a gas dielectric, when the discharge channel can branch out and have a zigzag character [8], we will limit ourselves to considering the processes at the stage of the formation of a conductive pulse spark channel in an air DEDS after passing through the leader channel of the return wave of the pulse current, which causes its bright glow [5]. Based on the analysis of calculated and experimental data relating to the flow of the main electrophysical processes in the studied discharge air gap of the DEDS (see Fig. 1), it is necessary to develop the physical principle of the development of the plasma channel of a high-voltage pulse spark discharge in the gas dielectric adopted for the study and further generalize it to homogeneous dielectrics of a different aggregate state, the physical properties of which change in space continuously without jumps.

2. Basic physical conditions and calculation relationships. Taking into account the electromagnetic nature of light and the plasma channel of a brightly glowing high-voltage electrical pulse spark discharge in the studied gas dielectric [8, 19], for a better understanding of the complex electrophysical processes in the air DEDS under consideration, let us first dwell on the well-known Fermat physical principle from the field of geometric optics, which for the optical length L_0 of a real light beam in an optically transparent medium is written in the following classical analytical form [22]:

$$L_0 = \int_A^B n_0 \mathrm{d}s\,, \qquad (1)$$

where n_0 is the dimensionless index of refraction of the light beam, which is minimal for a real beam in an optically transparent medium; ds is the length of the elementary section of the propagation of a light beam in an optically transparent medium from the starting point A to the ending point B of the real path of propagation of light in it.

In the case when the index of refraction n_0 of the medium spatially changes continuously in it, then according to (1) the optical length L_0 of the path traveled in it by a real light ray from point A to point B will be less than the optical length of any other path or the length of any other geometric curve connecting these extreme points of the light ray propagation path. Therefore, the time t_0 of passing through this or that medium with the index of refraction n_0 of the light beam of this path with the optical length L_0 will be the smallest. At the same time, it should be noted that the indicated time t_0 of the beam passage will have the following calculated analytical form: $t_0=L_0/c$, where $c \approx 3\cdot10^8$ m/s is the speed of light propagation in a vacuum [19]. Note that according to Maxwell law, there is a valid formula for the value of the index of refraction n_0 of the medium [22]:

$$n_0 = \sqrt{\varepsilon_r \mu_r}\,, \qquad (2)$$

where ε_r, μ_r are, respectively, the relative dielectric and magnetic permeability of the medium in which the light beam propagates.

Formula (2) clearly indicates the electromagnetic nature of light. It follows from (2) for an air medium (ε_r=1; μ_r=1) that the physical parameter n_0 in this case is numerically close to n_0=1 [19].

In this regard, Fermat physical principle, which is a general law of geometric optics, according to (1) and the accepted principle in the field of modern optics, is formulated as follows [22]: «*Light propagates from one point of the medium to another along a path for which the least amount of time is spent*». From Fermat principle the physical statement follows that light in an optically transparent medium propagates in a straight line [22]. Taking into account the above-mentioned electromagnetic nature of light and the plasma channel of the electric discharge, it is quite reasonable to accept the physical provision that the development of the plasma leader channel of the electric discharge and then the plasma spark channel of this pulse discharge in the air discharge gap (n_0=1) of the investigated DEDS on its short elementary sections of length $\mathrm{d}l_{cn} \ll l_{\min}$ occurs along rectilinear directions of one or another spatial orientation. Moreover, given rectilinear directions on elementary sections of length dl_{cn}, both at the stage of development of the plasma leader channel of the discharge in air, and at the stage of development of its spark channel in it, will satisfy the condition of the maximum value of the specific electrical conductivity γ_{cn} of the conductive path in the gas dielectric at the specified elementary sections of length dl_{cn} of the plasma leader (spark) discharge channel.

We believe that this conductive path is initiated by its main part (the head of the discharge leader) growing in space, which glows brightly and moves quickly in this dielectric (at the average velocity v_L of the forward front of the discharge leader in the air $v_L \approx 10^5$ m/s [8]) from the potential to the grounded electrodes of the DEDS. Spatial distributions in the discharge interval of the investigated DEDS of values of γ_{cn} on the elementary sections with the length dl_{cn} of the germinating leading channel of the pulse discharge are, as a rule, probabilistic in nature. These spatial probability distributions of γ_{cn} values in one or another dielectric are determined both by the technology of their manufacture (this applies more to solid and liquid insulation), and by the physical state and composition of the gas dielectric, as well as the properties of the gas or liquid insulating medium surrounding the solid dielectric [1 , 5]. Therefore, in the case of an electrical breakdown of the air discharge gap in the investigated DEDS with a conducting plasma channel of a pulse discharge with a total length $l_c = \sum_{n=1}^{m} \mathrm{d}l_{cn} = \int_A^B \mathrm{d}l_{cn}$ the indicated rectilinear elementary sections of the length dl_{cn} of the plasma leader channel of a pulse electrical discharge, which quickly grows in the air, will form a broken zigzag curve of the real path ($l_c > l_{\min}$) of the studied pulse spark discharge in the DEDS between the starting point A and the ending point B of the development of the plasma channel of this type of electric discharge (see Fig. 1).

Based on Ohm law in the differential form [22], for a rectilinear elementary section with a length dl_{cn} (see Fig. 1) of a conducting plasma channel of a high-voltage electric pulse spark discharge in the studied air DEDS, which corresponds to the specific electrical conductivity γ_{cn} of the gas dielectric, the following relation can be written:

$$\mathrm{d}l_{cn} = \gamma_{cn}\delta_{cn}^{-1}\mathrm{d}U_{cn}\,, \qquad (3)$$

where δ_{cn} is the density of the discharge current in the channel of the high-voltage air electric spark discharge in its elementary section of the length dl_{cn}; dU_{cn} is the electric voltage drop in the elementary section with the length dl_{cn} of the plasma channel of the high-voltage pulse spark discharge in the air DEDS.

Then, from (3), for the total length l_c of the plasma channel of the high-voltage electrical pulse spark discharge in the studied air DEDS, in general form, we obtain:

$$l_c = \int_A^B \mathrm{d}l_{cn} = \int_A^B \gamma_{cn}\delta_{cn}^{-1}\mathrm{d}U_{cn}\,. \qquad (4)$$

In the case of a continuous change in the plasma channel of an air pulse spark discharge, the value of the specific electrical conductivity γ_{cn} of its rectilinear elementary sections with length dl_{cn} and the invariance of the density $\delta_{cn} \approx \delta_c$ of the discharge current along the plasma spark channel, expression (4) has the following form:

$$l_c = \delta_c^{-1} \int_A^B \gamma_{cn}\mathrm{d}U_{cn}\,. \qquad (5)$$

The maximum values of the specific electrical conductivity γ_{cn} of the low-temperature plasma, both from

the beginning of the leader channel and further of the spark channel of the air discharge in the DEDS on its rectilinear elementary sections with length of dl_{cn}, will correspond to their minimum electrical resistances. In this regard, the plasma leader (spark) channel of the pulse discharge in the air DEDS will spatially germinate (develop) to the place where it and the dielectric, which is under the action of the external high electric field of the discharge leader, will ensure the minimum value of the electric voltage drop $U_c=\int_A^B dU_{cn}$. As an approximation of the fulfillment of the equality $\gamma_{cn}\approx\gamma_c$, which satisfies the largest current value of γ_{cn} on the path of propagation in the gas of the leader (spark) channel of the discharge, formula (5) for the real path of development of a high-voltage electrical pulse spark discharge in an air dielectric takes the form:

$$l_c = \gamma_c \delta_c^{-1} \int_A^B dU_{cn} . \quad (6)$$

In the well-known formula (1), the integral $\int_A^B n_0 ds$ determines the minimum value of the optical length L_0 of a real light beam in an optically transparent medium. In the obtained formula (6), the minimum value of the integral $\int_A^B dU_{cn} = l_c\delta_c/\gamma_c$, which corresponds to the maximum value of γ_c, determines the minimum value of the total length $l_c=\int_A^B dl_{cn}$ of the real plasma channel of the spark discharge in its specific conditions of spatial development in the gas dielectric. Therefore, when considering an electric discharge in a gas, we can say that for the electrophysical process of the development of a high-voltage electric pulse spark discharge in a gas dielectric, the physical laws of minimizing its main characteristics are also fulfilled, which lead to the minimization of energy consumption to support the flow of such a process in it.

We see that the proposed formula (6) for the development of a plasma channel of a high-voltage electric pulse spark discharge in a gas dielectric is close to the classical formula (1) for the propagation of light in an optically transparent medium in terms of its mathematical form and purpose. From the comparison of the obtained formula (6) for the total length l_c of the real path of the development of the plasma channel of a high-voltage electrical pulse spark discharge in the air DEDS during an electrical breakdown of its gap and formula (1), which corresponds to the Fermat physical principle, which determines the minimum optical length L_0 during the propagation of a real light beam in an optically transparent medium, it can be concluded that the total length l_c of a real plasma channel of a high-voltage electrical pulse spark discharge in an air dielectric between the points of its beginning A and ending B corresponds to the minimum drop of electric voltage on it $U_c=\int_A^B dU_{cn}$.

Taking into account the above, the proposed physical principle of the development of the plasma channel of a high-voltage electric pulse spark discharge in relation to the studied air DEDS can be formulated as follows: «*The plasma channel of a pulse spark discharge in a gas dielectric spreads from one point to another along the path of length l_c, which provides the smallest drop in it of electric voltage U_c*». For the calculated quantitative assessment, taking into account the proposed formula (6), the drop in electric voltage $U_c=\int_A^B dU_{cn}$ on the total length l_c of the real path of development in the homogeneous gas dielectric of the studied DEDS of a plasma channel of a high-voltage pulse spark discharge, we use the following approximate relationship from the field of HPT [5]:

$$l_c \approx (\varphi_{1d} - \varphi_2)/E_d . \quad (7)$$

When φ_2=0, from (6) and (7), for the drop in electric voltage U_c over the total length l_c of the real path of development in the gas dielectric of the plasma channel of a high-voltage electrical pulse spark discharge, in the accepted approximation, we obtain the expression:

$$U_c \approx \int_A^B dU_{cn} \approx \delta_c \varphi_{1d}/(\gamma_c E_d) . \quad (8)$$

By substituting into formula (8) calculated and experimental numerical data for a high-current plasma channel of a pulse spark discharge in atmospheric air ($\delta_c\approx5.8\cdot10^7$ A/m^2; $\gamma_c\approx1625$ (Ω·m)$^{-1}$; $\varphi_{1d}\approx611.6$ kV; $E_d\approx400$ kV/m), obtained by the author in the electric circuit of a powerful high-voltage test electrical equipment [23-25] containing the investigated DEDS ($l_{\min}$ =1.5 m), we find that the desired value of the electric voltage drop U_c on the total length $l_c>l_{\min}$ of the real path of development in the accepted air environment of the plasma channel of the high-voltage pulse spark discharge is numerically approximately $U_c\approx54.6$ kV. As we can see, $U_c=\int_A^B dU_{cn} << (\varphi_{1d} - \varphi_2)$. The calculated numerical value of the electric voltage drop $U_c\approx54.6$ kV obtained from (8) on the high-current plasma channel of an air pulse spark discharge does not exceed 9 % of the level of the breakdown electric voltage $U_{12d}(t)\approx\varphi_{1d}\approx611.6$ kV (φ_2=0) in this DEDS. This calculated value of $U_c\approx54.6$ kV correlates well with the experimental result for $U_c\approx I_{mc}R_{c0}l_{\min}\approx53.6$ kV given by the author in [24] regarding a high-voltage, high-current pulse spark discharge in a tip-plane DEDS with a long air gap ($l_{\min}$= 1.5 m; the amplitude of the pulse discharge current $I_{mc}\approx213.9$ kA, which corresponds to the time $t_{mc}\approx38$ μs, during the electrical breakdown of the air gap in this DEDS; the running active resistance $R_{c0}\approx0.167$ Ω/m of the plasma channel of the air spark discharge in the DEDS). The reliability of these experimental results is indicated by the author's calculated estimates of some

parameters for this applied electrophysical case (for example, the maximum radius r_{mc}≈34.27 mm of the plasma channel of the spark discharge in atmospheric air; the amplitude of the current density δ_{mc} in the discharge channel $\delta_{mc}\approx I_{mc}/(\pi r_{mc}^2)\approx 5.79\cdot 10^7$ A/m^2; the value of the specific electrical conductivity γ_c of its low-temperature plasma $\gamma_c\approx(\pi r_{mc}^2 R_{c0})^{-1}\approx 1624$ $(\Omega\cdot\text{m})^{-1}$) of electric discharge processes in the studied high-current plasma channel of pulse spark discharge in air DEDS using the Brahinsky formula for the radius r_{mc} of the plasma channel [6, 8].

The results of mathematical modeling of electric discharge processes in homogeneous liquid and solid dielectrics using the investigated DEDS and the existing mechanisms of their electrical breakdown [5, 7] will fundamentally not differ in anything (except for the numerical values of the parameters l_c, γ_c, δ_c, φ_{1d}, E_d and U_c) from those given above calculation results for the development of a plasma channel of a pulse spark discharge in a homogeneous air dielectric DEDS (see Fig. 1). Therefore, in the first approximation, the calculated relation (6) and the physical principle of the development of the plasma channel of a high-voltage electrical pulse spark discharge in a gas, based on it, proposed by the author, can be applied also for homogeneous liquid and solid dielectrics.

3. Results of an experimental study of the development of a plasma channel of a pulse spark discharge in an air DEDS. In order to verify some obtained approximate calculation results for electric discharge processes in air DEDS, appropriate experiments were performed using powerful high-voltage high-current test equipment of the Research and Design Institute «Molniya» of NTU «KhPI» [25]. Figure 2 shows the general view of the studied tip-plane DEDS with a discharge air gap of length $l_{\min}$=1.5 m.

Fig. 2. The general view of the tip-plane air DEDS with a discharge gap of length $l_{\min}$=1.5 m (the tip on a vertically placed steel electrode-rod with a diameter of 30 mm has a radius of rounding of its edge ~1 mm; the horizontal plane of the electrode is 5 m × 5 m made of thin galvanized steel sheets)

Figure 3 shows an experimental oscillogram of a complete standard switching aperiodic high-voltage pulse of the time shape T_m/T_d≈200 μs/1990 μs of positive polarity, which acts in the discharge circuit of the high-voltage, high-current test electrical equipment based on the GIN-4 generator [25] on the investigated tip-plane DEDS without electrical breakdown of its air gap of length $l_{\min}$=2 m, and Figure 4 shows an oscillogram of a truncated similar high-voltage voltage pulse with an electrical breakdown of the air discharge gap in the tip-plane DEDS of length $l_{\min}$=1,5 m.

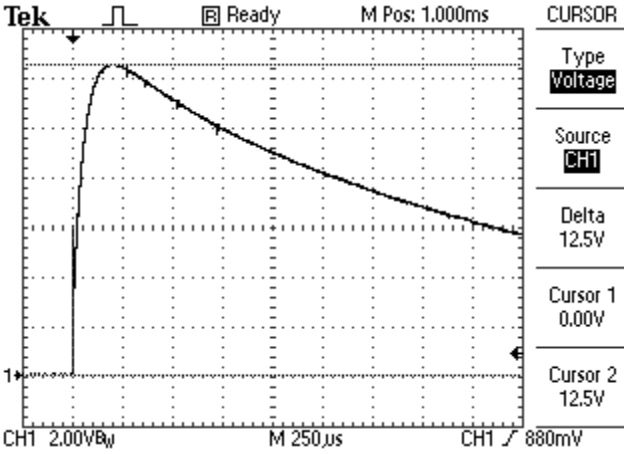

Fig. 3. Oscillogram of a complete standard switching aperiodic voltage pulse of the time shape T_m/T_d≈200 μs/1990 μs of positive polarity without electrical breakdown of the air gap of length $l_{\min}$=2 m in the tip-plane DEDS ($U_m\approx\varphi_{1m}$≈12.5 V × 53650≈670.6 kV – amplitude of the voltage pulse; T_m≈200 μs – time of rise of the pulse to the voltage amplitude U_m; T_d≈1990 μs – voltage pulse duration at the level of 0.5 U_m; vertical scale – 107.3 kV/div; horizontal scale – 250 μs/div)

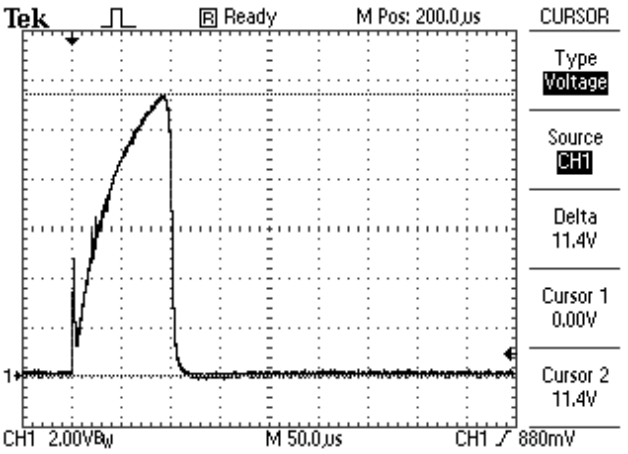

Fig. 4. Oscillogram of a truncated standard switching aperiodic voltage pulse of the time shape T_m/T_d≈200 μs/1990 μs of positive polarity during electrical breakdown of an air gap of length $l_{\min}$=1.5 m in a tip-plane DEDS ($U_{md}\approx\varphi_{1d}$≈11.4 V × 53650≈611.6 kV – voltage pulse cut-off level; T_c ≈95 μs – voltage pulse cut-off time; T_{dc}≈17 μs – duration of the cut-off of the voltage pulse, which corresponds to the time t_d of the propagation of the conductive channel of the leader of the electric pulse discharge in the air gap of the DEDS of length l_c between its potential and grounded metal electrodes; vertical scale − 107.3 kV/div; horizontal scale – 50 μs/div)

Let us point out that when measuring the ATPs shown in Fig. 3, 4 of high-voltage test switching aperiodic voltage pulses, which are intended for the experimental study of the development of the plasma channel of the electric pulse spark discharge in the air tip-plane DEDS (see Fig. 2), an ohmic voltage divider of the OPN-2.5 type was used (for a maximum voltage of up to 2.5 MV with a division factor of K_d≈53650 [25]) and a Tektronix TDS 1012 digital oscilloscope.

Figure 5 shows the general view of a high-current plasma channel of a high-voltage electric pulse spark discharge, which glows brightly in the atmospheric air, in the investigated tip-plane DEDS with the length of the air discharge gap l_{min}=1.5 m, obtained in the summer of 2023 during the experimental determination of electrical strength of air insulation more than 1 m long with the use of ultra-high-voltage equipment of the experimental range of the Research and Design Institute «Molniya» of NTU «KhPI» [25].

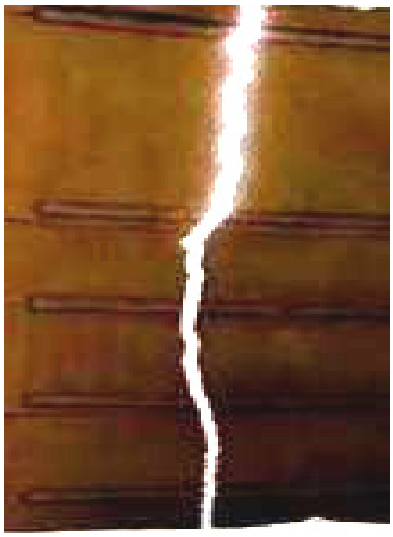

Fig. 5. General view of a high-current plasma channel of a high-voltage electric pulse spark discharge in a tip-plane DEDS with atmospheric air during electrical breakdown of its air gap of length l l_{min}=1.5 m by a standard switching aperiodic voltage pulse of the time shape T_m/T_d≈200 μs/1990 μs of positive polarity (U_{md}≈φ_{1d}≈611.6 kV; T_c≈95 μs – voltage pulse cut-off time; T_{dc}≈17 μs – duration of voltage pulse cut-off, which characterizes the time of rapid shortening by the conductive plasma leader channel of a pulsed discharge of a long air gap in the DEDS)

From the experimental data (Fig. 5), we can see that in the used tip-plane DEDS (l_{min}=1.5 m; φ_2=0) a real high-current plasma channel of a high-voltage pulse spark discharge in air under normal atmospheric conditions [19] is characterized by a zigzag geometric shape (l_c>l_{min}). This is indicated also by the calculated numerical estimates according to (6) taking into account (8) at φ_{1d}≈611.6 kV and E_d≈400 kV/m of the total length l_c of the spark discharge channel in the studied air DEDS (l_{min}=1.5 m): l_c≈φ_{1d}/E_d≈1.53 m. This unequivocally indicates that during the electrical breakdown of the gas (air) dielectric, the main part of the plasma leader channel of the pulse discharge, which glows brightly, spatially grows into those areas of the specified dielectric located between the potential 1 and grounded 2 electrodes (Fig. 1) of the investigated DEDS, which have the highest specific electrical conductivity γ_{cn} and, accordingly, the lowest electrical resistance in the specific conditions of such an electrical breakdown of this insulation. In this regard, this experimental result from the field of HPT indicates the reliability of the basic physical provision associated with the orientation of the main part of the leader channel of the discharge during its germination, adopted by the author in the development of the proposed physical principle of the development of the high-voltage plasma channel of a pulse spark discharge in the studied gas dielectric to those sections of it that are characterized by the highest specific electrical conductivity γ_{cn} at the given moment of time.

And if this is so, then the physical principle of the development of a plasma channel of a pulse spark discharge in it, formulated in this work in relation to a gas dielectric, which indicates the spread in this type of dielectric first of the leader and then of the spark channels of the discharge along the path with the smallest drop in the electric voltage U_c, is also confirmed the results of these high-voltage, high-current experiments performed with the author's participation. In addition, the experimental data obtained according to Fig. 4 at U_{md}≈(φ_{1d}–φ_2)≈611.6 kV testify to the fact that when using in the investigated air tip-plane DEDS (l_{min}=1,5 m; φ_2=0) of a standard switching aperiodic pulse of high voltage of the time shape T_m/T_d ≈200 μs/1990 μs of positive polarity, the average breakdown voltage of the high electric field E_d≈φ_{1d}/l_c for atmospheric air in this DEDS at U_{md}≈φ_{1d}≈611.6 kV and l_c≈1.53 m is numerically approximately E_d≈400 kV/m with a tolerance of ±3 %, which is mainly determined by the minimum measurement error of the test high pulse voltage from powerful ultra-high-voltage electrical equipment using an ohmic voltage divider of the OPN-2.5 type (K_d≈53650 [25]) and the applied digital Tektronix TDS 1012 oscilloscope.

Experimental data according to Fig. 4 also indicate that the plasma leader channel of the electric discharge in the studied air DEDS (l_{min}=1.5 m) has a total path length of l_{cm}≥l_c≥1.53 m, where l_{cm} is the maximum length of the actual path of the gas discharge in the DEDS, from the potential electrode to the grounded electrode of this DEDS passes through the air during the time t_d, which is numerically equal to about t_d≈T_{dc}≈17 μs. It is during the time T_{dc}≈17 μs that the conductive plasma leader channel of the pulse discharge shortens the air gap in the investigated DEDS (l_{min}=1.5 m) and equalizes the electric potentials (φ_1≈φ_2≈0) on its metal electrodes (see Fig. 4). According to the developed physical principle of the development of the plasma channel of an electric pulse spark discharge in a gas dielectric at the average speed v_L of the advance in the air of the leading edge of the leader in the channel of this electric discharge, quantitatively

equal to $v_L \approx 10^5$ m/s [8], the calculated numerical value for the specified time t_d relative to of atmospheric air in this DEDS is found at $l_c \approx 1.53$ m equal to $t_d \approx l_c / v_L \approx 15.3$ μs. As we can see, the calculated numerical value obtained for the time parameter $t_d \approx 15.3$ μs differs from its corresponding experimental value $t_d \approx T_{dc} \approx 17$ μs according to the oscillogram in Fig. 4 for a truncated standard switching aperiodic high-voltage pulse of the time shape $T_m/T_d \approx 200$ μs/1990 μs of positive polarity during electrical breakdown of the air gap of length l_c in the tip-plane DEDS ($l_{\min}$ =1.5 m) within 11 %. Note that at $T_{dc} \approx 17$ μs, the maximum length l_{cm} of the real path of the plasma channel of the gas discharge in the studied DERS will be approximately equal to $l_{cm} \approx v_L T_{dc} \approx 1.7$ m. The calculated numerical value of $l_c \approx 1.53$ m obtained above differs from this experimental value of l_{cm} by more than 11 %. These computational and experimental data also indicate the reliability of the basic initial physical assumptions adopted in the work and the calculated results obtained on their basis, which relate to the physics of the development of electric discharge processes in a homogeneous gas dielectric of the investigated DEDS and the quantitative selection according to formulas (6), (7) of the total the length l_c of the real path of the development of the plasma channel of the high-voltage electric pulse spark discharge in the atmospheric air of this DEDS.

It is important to note that the minimum value of the voltage drop U_c along the length l_c of the real path of development in the air of the plasma channel of the pulse spark discharge will be conditioned by (6) and the minimum value of l_c. At a constant average speed v_L of propagation in the atmospheric air of the leading front of the leader in the plasma channel of the gas discharge ($v_L \approx 10^5$ m/s [8]), the minimization of the length l_c will also lead to the minimization of the time t_d of the advancement of both the plasma leader and the spark channel of the pulse discharge in the investigated air DEDS ($l_{\min}$=1.5 m).

Conclusions.

1. A generalized physical principle of the development of a plasma channel of a high-voltage electrical pulse spark discharge in a homogeneous dielectric of a different aggregate state, mathematically written for the total length $l_c = \int_A^B \mathrm{d}l_{cn}$ of the real path of the development of this type of electric discharge along rectilinear elementary sections of the plasma channel with a length of $\mathrm{d}l_{cn}$ of different spatial orientation in the gas dielectric of the accepted double-electrode discharge system (DEDS) with the smallest length $l_{\min}$ of its discharge gap is proposed. This principle (physical law) indicates that in DEDS the plasma channel of a high-voltage electric pulse spark discharge in gas, liquid and solid dielectrics spreads from its starting point A on the potential electrode of DERS to the ending point B on the grounded electrode of DEDS along a path that provides the smallest drop of electric voltage on it $U_c = \int_A^B \mathrm{d}U_{cn}$, where $\mathrm{d}U_{cn}$ is the drop of electric voltage on the rectilinear elemental section of the plasma discharge channel of length $\mathrm{d}l_{cn} \ll l_{\min}$.

2. It is shown that the proposed physical principle of the development of the plasma channel of an electric pulse spark discharge in the studied gas dielectric of the DEDS is by mathematical form and purpose close to the Fermat fundamental physical principle, which is a general law of geometric optics and which determines the minimum optical length $L_0 = \int_A^B n_0 \mathrm{d}s$ when propagating a real light beam in an optically transparent medium with the index of refraction of light n_0 between the starting point A and the ending point B of its propagation in this medium, where $\mathrm{d}s$ is the length of the elementary section of the propagation of the light beam in an optically transparent medium.

3. By calculation, it was established that the drop in electric voltage U_c on the total length l_c of the real zigzag path of development in the air dielectric of the investigated tip-plane DEDS ($l_{\min}$=1.5 m) of the plasma channel of the high-voltage electric pulse spark discharge for a standard switching aperiodic pulse of high voltage of time shape $T_m/T_d \approx \approx 200$ μs/1990 μs of positive polarity satisfies the inequality of the form $U_c << (\varphi_{1d} - \varphi_2)$ and at $\varphi_{1d} \approx 611.6$ kV (φ_2 =0) it numerically amounts to $U_c \approx 54.6$ kV, which does not exceed 9 % of the experimental level of breakdown electric voltage $U_{12d}(t) \approx (\varphi_{1d} - \varphi_2) \approx 611.6$ kV in this DEDS with atmospheric air. Here, the indicated calculated level of electric voltage drop $U_c \approx 54.6$ kV on this plasma channel of the spark discharge practically corresponds to the previously obtained experimental numerical level of electric voltage drop $U_c \approx 53.6$ kV on it in a similar air DEDS.

4. High-voltage, high-current experiments carried out on the powerful electrophysical equipment of the Research and Design Institute «Molniya» of NTU «KhPI» for the tip-plane aerial DEDS under investigation ($l_{\min}$=1.5 m; φ_2=0), which tests the effect of a standard switching aperiodic high-voltage pulse of the time shape $T_m/T_d \approx 200$ μs/1990 μs of positive polarity, confirm the validity of the basic physical conditions underlying the developed generalized principle of the development of a plasma channel of a pulse spark discharge in a dielectric (on the example of atmospheric air in the DEDS), and some calculated results obtained for it (in particular, for the numerical values of the electric voltage drop U_c on the total length l_c of the real path of development in the atmospheric air of the plasma channel of the pulse spark discharge and the average breakdown voltage E_d for the atmospheric air of the high electric field $E_d \approx \varphi_{1d}/l_c \approx 400$ kV/m under the conditions of action on the air DEDS of the specified a microsecond voltage pulse, as

well as for quantitative data of the total length l_c of the real path of the development of the plasma discharge channel l_c≈1.53 m, which confirm the fulfillment of the inequality of the form $l_c > l_{min}$, which determines the zigzag shape of the development in atmospheric air of both the plasma leader discharge channel and further a similar shape of development of a high-voltage electric pulse spark discharge channel in this dielectric).

5. It is shown that the calculated time t_d of the advancement of the plasma leader channel of an electric pulse spark discharge in the investigated air DEDS (l_{min}=1.5 m) along its real path in atmospheric air with a total length of l_c≈1.53 m at the average speed of propagation in this air of the front of the leader in the discharge plasma channel v_L≈10^5 m/s is numerically about t_d≈l_c/v_L≈15.3 μs. This calculated result for the time t_d differs by no more than 11 % from the experimental duration of the cut-off T_{dc}≈t_d≈17 μs, which characterizes the time of shortening by the electrically conductive plasma leader channel of the discharge of the air gap of length l_c in the DEDS, for a standard switching aperiodic pulse of high voltage of the time shape T_m/T_d≈200 μs/1990 μs of positive polarity (φ_{1d}≈611.6 kV) in the investigated DEDS with the minimum length of its discharge air gap equal to l_{min}=1.5 m.

Acknowledgment. The work was carried out with the support of the Ministry of Education and Science of Ukraine (project DB No. 0123U101704).

Conflict of interest. The author declares no conflict of interest.

REFERENCES

1. Dashuk P.N., Zayents S.L., Komel'kov V.S., Kuchinskiy G.S., Nikolayevskaya N.N., Shkuropat P.I., Shneerson G.A. *The technique of large pulsed currents and magnetic fields*. Moscow, Atomizdat Publ., 1970. 472 p. (Rus).

2. Knopfel' G. *Ultra strong pulsed magnetic fields*. Moscow, Mir Publ., 1972. 391 p. (Rus).

3. Gulyy G.A. *Scientific basis of the discharge-pulse technologies*. Kyiv, Naukova Dumka Publ., 1990. 208 p. (Rus).

4. Mesiats G.A. *Generation of power nanosecond pulses.* Moscow, Soviet Radio Publ., 1974. 256 p. (Rus).

5. Brzhezitsky V.O., Biliy I.V., Boiko M.I., Gul' V.I., Gurin A.G., Il'enko O.S., Isakova A.V., Kondra B.M., Kopshin V.O., Kravchenko V.I., Naboka B.G., Protsenko O.R., Rudakov V.V., Khymenko L.T., Khominich V.I., Shostak V.O., Yanishevsky V.I. *Technique and Electrophysics of High Voltages*. Kharkiv, NTU «KhPI», Tornado Publ., 2005. 930 p. (Ukr).

6. Lozanskyi E.D., Firsov O.B. *Theory of spark*. Moscow, Atomizdat Publ., 1975. 272 p. (Rus).

7. Ushakov V.Ja. *Pulse electrical breakdown of liquids*. Tomsk, TSU Publ., 1975. 255 p. (Rus).

8. Rayzer Yu.P. *Physics of gas discharge*. Moscow, Nauka Publ., 1987. 592 p. (Rus).

9. Vovchenko A.I., Bohuslavsky L.Z., Myroshnychenko L.N. Trends in development of high-powered high-voltage pulse current generators in the Institute of Pulse Processes and Technology of Ukraine (review). *Technical electrodynamics*, 2010, no. 5, pp. 69-74. (Rus).

10. Baranov M.I., Buriakovskyi S.G., Kniaziev V.V. A calculation of basic thermophysical, gasodynamic and electropower parameters of electric explosion is in the gas environment of metallic explorer. *Electrical Engineering & Electromechanics*, 2023, no. 1, pp. 40-50. doi: https://doi.org/10.20998/2074-272X.2023.1.06.

11. Boyko N.I., Evdoshenko L.S., Zarochentsev A.I., Ivanov V.M., Tour A.N. High-Voltage Spark Gaps for Technological Purposes. *Instruments and Experimental Techniques*, 2001, vol. 44, no. 2, pp. 204-212. doi: https://doi.org/10.1023/A:1017515003483.

12. Podoltsev A.D., Kucheryavaya I.N. *Multiphysics Modeling in Electrical Engineering*. Kyiv, Institute of Electrodynamics of the NASU of Ukraine, 2015. 305 p. (Rus).

13. Niemeyer L., Pietronero L., Wiesmann H.J. Fractal Dimension of Dielectric Breakdown. *Physical Review Letters*, 1984, vol. 52, no. 12, pp. 1033-1036. doi: https://doi.org/10.1103/PhysRevLett.52.1033.

14. Wiesmann H.J., Zeller H.R. A fractal model of dielectric breakdown and prebreakdown in solid dielectrics. *Journal of Applied Physics*, 1986, vol. 60, no. 5, pp. 1770-1773. doi: https://doi.org/10.1063/1.337219.

15. Kebbabi L., Beroual A. Fractal analysis of creeping discharge patterns propagating at solid/liquid interfaces: influence of the nature and geometry of solid insulators. *Journal of Physics D: Applied Physics*, 2006, vol. 39, no. 1, pp. 177-183. doi: https://doi.org/10.1088/0022-3727/39/1/026.

16. Hu H.M., Yang Y., Lu W., Zhao G.P. Electrical Tree Simulation Based on the Self-Organization Criticality. *Energy and Power Engineering*, 2013, vol. 5, no. 4, pp. 1273-1276. doi: https://doi.org/10.4236/epe.2013.54B241.

17. Pashchenko A.V., Maslov V.I., Naugolnij I.N. Fractal phenomenological theory of impulse breakdown of liquid and solid dielectrics. *Digest of Technical Papers. Tenth IEEE International Pulsed Power Conference*, 1995, vol. 2, pp. 863-868. doi: https://doi.org/10.1109/PPC.1995.599720.

18. Gladkov V.S., Maslov V.I., Naugolniy I.N., Pashchenko A.V. To the Problem of the Physical Model of the Fractal Discharge in Liquid and solid Dielectric. *Bulletin of National Technical University «Kharkiv Polytechnic Institute»*, 2002, vol. 1, no. 7, pp. 81-85.

19. Kuhling H. *Handbook of Physics*. Moscow, Mir Publ., 1982. 520 p. (Rus).

20. *Standard GOST 1516.2-97. Electrical equipment and installations for a.c. voltages 3 kV and higher. General methods of dielectric tests*. Minsk, Intergovernmental Council of Standardization, Measuring and Certification Publ., 1997. 31 p. (Rus).

21. Baranov M.I., Koliushko G.M., Kravchenko V.I. A switching aperiodic superhigh-voltage pulse generator for testing the electric strength of insulation of technical objects. *Instruments and Experimental Techniques*, 2013, vol. 56, no. 6, pp. 653-658. doi: https://doi.org/10.1134/S0020441213050126.

22. Kuz'michev V.E. *Laws and formulas of physics*. Kyiv, Naukova Dumka Publ., 1989. 864 p. (Rus).

23. Baranov M.I., Koliushko G.M., Lysenko V.O. Experimental determination of active resistance and conductivity of heavy-current plasma channel in the discharge chain of generator impulsive components of current of artificial lightning. *Electrical Engineering & Electromechanics*, 2011, no. 3, pp. 51-55. (Rus).
24. Baranov M.I. *Selected topics of Electrophysics. Monograph in 4 Vols. Vol. 3. Theory and practice of electrophysics tasks*. Kharkiv, Tochka Publ., 2014. 400 p. (Rus).
25. Baranov M.I., Buriakovskyi S.G., Kniaziev V.V., Rudenko S.S. Analysis of characteristics and possibilities of high-voltage electrical engineering complex Scientific-&-Research Planning-&-Design Institute «Molniya» of NTU «KhPI» for the tests of objects of energy, armament, aviation and space-rocket technique on electric safety and electromagnetic compatibility. *Electrical Engineering & Electromechanics*, 2020, no. 4, pp. 37-53. doi: https://doi.org/10.20998/2074-272X.2020.4.06.

Received 17.08.2023
Accepted 12.10.2023
Published 02.01.2024

M.I. Baranov[1], *Doctor of Technical Science*, *Chief Researcher,*
[1] Research and Design Institute «Molniya»
of National Technical University «Kharkiv Polytechnic Institute»,
47, Shevchenko Str., Kharkiv, 61013, Ukraine,
e-mail: baranovmi49@gmail.com (Corresponding Author)

How to cite this article:
Baranov M.I. A generalized physical principle of development of plasma channel of a high-voltage pulse spark discharge in a dielectric. *Electrical Engineering & Electromechanics*, 2024, no. 1, pp. 34-42. doi: https://doi.org/10.20998/2074-272X.2024.1.05

UDC 621.373 https://doi.org/10.20998/2074-272X.2024.1.06

M.I. Boiko, K.S. Tatkova

Computer simulation of operation plant effective modes for water disinfection by electrical discharges in gas bubbles

Purpose. *Determination by means of computer simulation of the most efficient modes of operation of the installation for water disinfection using discharges in gas bubbles, in which (modes) the amplitude of voltage pulses at the processing unit and on the layer of treated water is not less than the voltage amplitude immediately after the switching discharger.* ***Methodology.*** *To achieve this goal, we used computer simulation using Micro-Cap 10. We used two different electrical circuits that simulate the operation of the experimental setup in two different modes: in a mode with a restoring electrical strength of the discharge gap in the gas bubble between two adjacent voltage pulses on the discharge node and in the mode without restoring this dielectric strength. In computer simulation, we varied the following factors: the maximum simulation step, inductances, capacitances, active resistances, wave resistance of a long line, and the delay time for the operation of a spark gap simulating a discharge gap in a gas bubble.* ***Results.*** *Computer modeling has shown that in order to increase the voltage amplitude at the treatment unit and on the layer of treated water, it is necessary to reduce the load capacitance – the capacitance of the water layer in the treatment unit to 10 pF or less, to increase the active resistance of the water layer to 500 Ω or more. An important factor for increasing the voltage and electric field strength in the discharge unit and, consequently, for increasing the efficiency of treated water disinfection is the discharge delay time in gas bubbles. The most rational delay time for the operation of the arrester, which is the gap in the gas bubble inside the water, under the conditions considered by us is 4–5 ns. It is with this delay time that the amplitude of voltage pulses at the node of disinfecting water treatment and on the layer of treated water is maximum, all other things being equal. Furthermore, with such a delay time this amplitude of voltage pulses significantly exceeds the voltage amplitude directly after the main high-voltage discharger, switching energy from the high-voltage capacitive storage to the processing unit through a long line filled with water.* ***Originality.*** *Using computer simulation, we have shown the possibility of increasing the voltage at the discharge unit of the experimental setup by 35 % without increasing the voltage of the power source. This provides a higher efficiency of microbiological disinfection of water by nanosecond discharges in gas bubbles and lower specific energy consumption.* ***Practical value.*** *The obtained results of computer simulation confirm the prospect of industrial application of installations using nanosecond discharges for disinfection and purification of wastewater, swimming pools and post-treatment of tap water.* References 15, figures 10.

Key words: **high-voltage water disinfection unit, discharge unit, sharpening spark gap, discharge in gas bubbles in water, discharge delay time, long electric line.**

Мета. *Визначення за допомогою комп'ютерного моделювання найбільш ефективних режимів роботи установки для знезараження води за допомогою розрядів у газових бульках, при яких (режимах) амплітуда імпульсів напруги на вузлі обробки та на шарі води, що обробляється, не менше амплітуди напруги безпосередньо після комутуючого розрядника.* ***Методика.*** *Для досягнення поставленої мети ми використовували комп'ютерне моделювання за допомогою Micro-Cap 10. Ми використовували дві різні електричні схеми, що моделюють роботу експериментальної установки в двох різних режимах: в режимі з електричною міцністю, що відновлюється, розрядного проміжку в газовій бульці між двома сусідніми імпульсами напруги на розрядному вузлі та у режимі без відновлення цієї електричної міцності. При комп'ютерному моделюванні варіювалися такі фактори: максимальний крок при моделюванні, індуктивності, ємності, активні опори, хвильовий опір довгої лінії, час затримки спрацьовування розрядника, що моделює розрядний проміжок у газовому міхурі.* ***Результати.*** *Комп'ютерне моделювання показало, що для збільшення амплітуди напруги на вузлі обробки і на шарі води, що обробляється, слід зменшувати навантажувальну ємність – ємність шару води у вузлі обробки до 10 пФ і менше, збільшувати активний опір шару води до 500 Ом і більше. Важливим чинником збільшення напруги і напруженості електричного поля в розрядному вузлі і, отже, збільшення ефективності знезараження оброблюваної води є час затримки розряду в газових бульбашках. Найбільш раціональний час затримки спрацьовування розрядника, яким є зазор у газовій бульці всередині води, у розглянутих умовах становить 4-5 нс. Саме при такому часі затримки амплітуда імпульсів напруги на вузлі знезаражувальної обробки води і на шарі оброблюваної води є максимальною за інших рівних умов і істотно перевищує амплітуду напруги безпосередньо після основного високовольтного розрядника, що комутує енергію з високовольтного ємнісного нагромаджувача у вузол обробки.* ***Наукова новизна.*** *За допомогою комп'ютерного моделювання показана можливість підвищення напруги на розрядному вузлі експериментальної установки на 35 % без збільшення напруги джерела живлення, що забезпечує більш ефективне мікробіологічне знезараження води за допомогою наносекундних розрядів у газових бульбашках за малих питомих витрат енергії.* ***Практична значущість.*** *Отримані результати комп'ютерного моделювання підтверджують перспективу промислового застосування установок з використанням наносекундних розрядів для знезараження та очищення стічних вод, басейнів та доочищення водопровідної води.* Бібл. 15, рис. 10.

Ключові слова: **високовольтна установка для знезараження води, розрядний вузол, розрядник, що загострює, розряд у газових бульбашках у воді, час запізнення розряду, довга електрична лінія.**

Introduction. In recent years, various scientists have carried out intensive researches of the characteristics and considered prospects for the technological use of nanosecond discharges in gas bubbles inside liquids in various high-voltage installations [1–3]. These studies use both experimental methods and computer simulations. The latter is widely used in various fields of electrical engineering [4, 5].

Authors of [6] have shown microbubbles are very fine bubbles that shrink and collapse underwater within several minutes, leading to the generation of free radicals.

The characteristics of a multiple argon bubble jet in which a streamer is generated by a dc pulsed discharge have been experimentally clarified through discharge

visualization in a bubble and decolorization of a methylene blue solution [7].

In [8] authors have investigated experimentally a water treatment, which introduces a vaporized solution into a coaxial dielectric barrier discharge tube using Ar.

Authors of [9] provided a concise review of the state-of-art for research on plasma-bubble interactions and a perspective for future research.

The objective of the thesis [10] was to utilize plasma discharges to treat a large volume of produced water for recycling it for subsequent fracking. To recycle produced water, both bacterial inactivation and water softening are required, which are the two main objectives of the present study of plasma water treatment.

Authors of [11] achieved the next results. The discharge propagates into the bubble from the tip of the wire in the glass tube. Then, the discharge propagates along the bubble surface. The propagation velocity is almost independent of water conductivity and is $(2.7–3.6)\cdot10^5$ m/s. The average maximum length of the discharge propagation decreases from approximately 8.9 to 5.4 mm with increasing water conductivity from 7 to 1000 μS/cm. Indigo carmine, a commonly used organic dye, was used as the chemical probe of the active species produced by the discharge inside the bubble. The amounts of indigo carmine decomposition with 120 min of treatment is 0.24–0.26 μmol and independent of water conductivity. Meanwhile, the energy efficiency for the indigo carmine decomposition in water decreases from 18 to 7.3 μmol/Wh with increasing water conductivity from 7 to 1000 μS/cm. The amount of hydrogen peroxide production by the treatment increases from 2.0 to 3.1 μmol with increasing the conductivity.

In article [12] authors start by describing our experimental methodology addressing bubble geometry and timing methods. For the first time, we present an original method of bubble positioning with control of statistical information of the bubble shape, size, and position between the electrodes. A unique timing scheme is introduced that allows the application of the voltage pulses when a bubble is in the desired position between the electrodes. Finally, the experimental results and discussion section present our evidence for the discharge initiation for two electrode configurations by order of timescale.

In our work [13], we have shown that when using nanosecond discharge pulses in gas bubbles, one should take into account the presence of long lines during the transmission of generated voltage pulses from sharpening spark gaps to units of water disinfection treatment. At the same time, we indicated that for all considered processing modes, the voltage amplitude at the processing nodes (at the output of a long line) is less than after the sharpening spark gap at the input of a long line. The question arises: are there modes in which the voltage amplitude at the nodes (node) of processing (load) is greater than at the input to long lines?

It is very important to answer the question of the possibility of obtaining the amplitudes of nanosecond voltage pulses directly on the load greater than the amplitudes of voltage pulses obtained because of switching the sharpening spark gap immediately after it. The load is a serial connection of a gas bubble with a discharge inside it and a layer of water. The magnitude of the voltage amplitude of these pulses determines the efficiency of the production of active particles and radiation in the node (or nodes) of water treatment and, consequently, the efficiency of disinfecting water treatment. Experimentally, using direct measurements of voltage pulses at the processing unit is extremely difficult. Therefore, we use the computer simulation method for this.

In this work, we consider the following two modes of operation of the installation. The first mode is one in which the electric strength of the gas in the bubble is restored after each discharge. The second regime is one in which the electric strength of the gas in the bubble is not restored after each discharge, i.e. the plasma channel(s) burns (burn) continuously. Let us also consider the effect on the voltage amplitude at the processing node of the discharge delay time in the gas bubble of the node, as well as the effect of the inductance, capacitance and active resistance of the processing node on the amplitude of this voltage, all other things being equal.

An increase in the amplitude of nanosecond voltage pulses at the processing unit (a series connection of a gas bubble with a discharge and a water layer) at a given voltage amplitude at the input of a long line filled with water and located in front of the discharge unit is an important task. Such an increase in amplitude makes it possible to increase the production of active particles in the processing unit and the intensity of broadband radiation from plasma channels.

The **purpose** of the work is to determine, using computer simulation, the most efficient modes of operation of the installation for water disinfection using discharges in gas bubbles, in which (modes) the amplitude of voltage pulses at the processing unit and on the layer of treated water is not less than the voltage amplitude immediately after the switching spark gap.

Electrical circuits for computer simulation and the influence of the maximum step size in computer simulation. A diagram with a discharge gap in a gas bubble that restores its electrical strength after each discharge is shown in Fig. 1.

Figure 2 shows a diagram with a discharge gap in a gas bubble in which, once ignited, the discharge does not go out (with a discharge gap that does not restore its electrical strength after each discharge).

Figure 3 demonstrates a schematic drawing of three discharge units of the experimental setup is presented, in each of which an electric discharge occurs in gas bubbles [14].

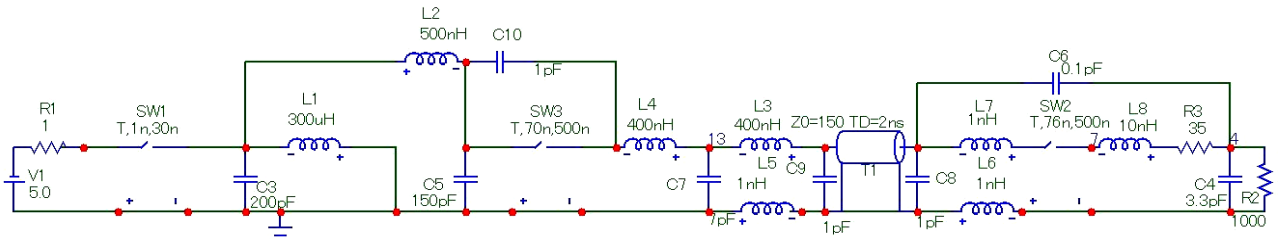

Fig. 1. Scheme with a discharge gap in a gas bubble, restoring its dielectric strength after each discharge

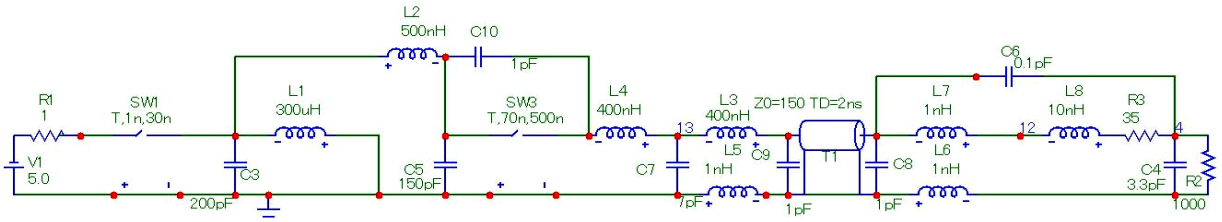

Fig. 2. Scheme with a discharge gap in a gas bubble that does not restore its dielectric strength after each discharge

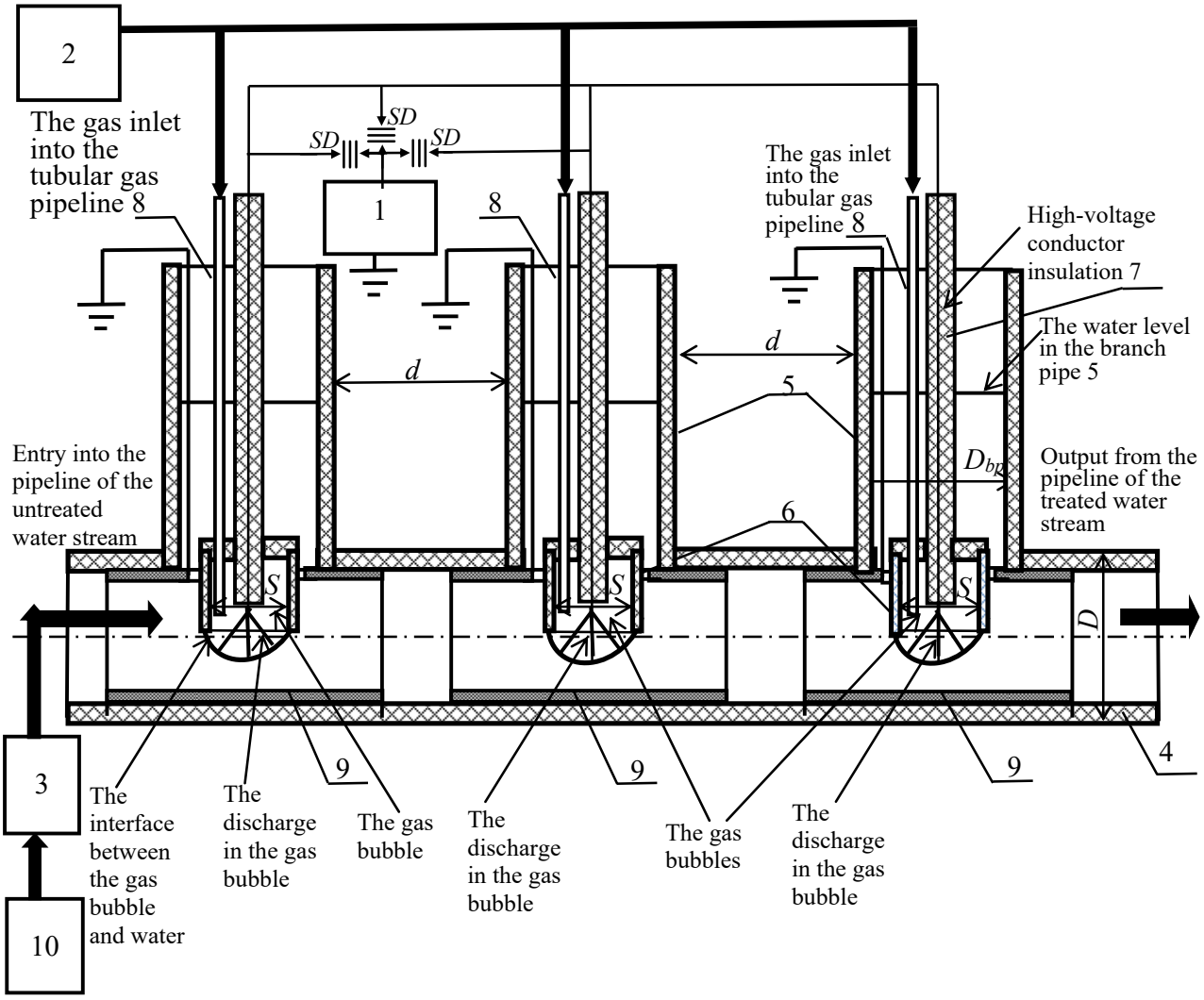

Fig. 3. A block diagram of the plant, which illustrates disinfecting method of treatment water with gas bubbles

Figure 4 shows a photograph of a tubular system with these three electric discharge nodes [14].

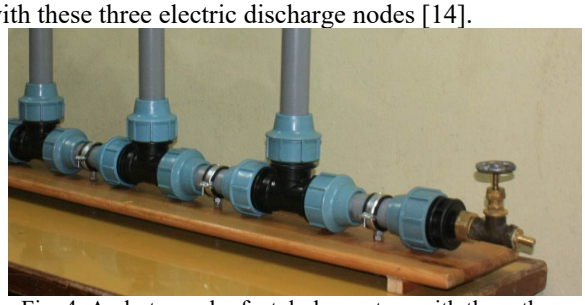

Fig. 4. A photograph of a tubular system with these three electric discharge nodes

The plant [14] consists of a low-impedance generator 1 of high voltage pulses, compressor 2, pump 3, pipeline 4 with a diameter of D = 40 mm with running water, made of insulating material. The experimental plant includes also three branch pipes 5 with a diameter of D_{bp} = 40 mm, through which insulation hollow cases 6 without a bottom are inserted and fixed there. Cases 6 are made combined with high-voltage conductors – pointed electrodes 7 in isolation and with tubular gas pipelines 8. The plant contains also a grounded electrode 9 in each of the three discharge units. This electrode is made in the form of a metal cylindrical ring with a hole in its side surface for the location of the case 6 in the pipeline 4. Each discharge unit consists of an electrode 7 in solid insulation, the tip of which is not insulated, a case 6 with a characteristic internal linear size S = 2,8 cm, a gas-pipe 8, an electrode 9 and a water layer inside the pipe 4 under and around the branch pipe 5. The branch pipes 5 may have caps (Fig. 3 not shows caps) with the possibility of gas outlet after discharges in gas bubbles. Wherein, the outflow of water through the caps on the branch pipes 5 is impossible. A pump 3 pumps water into a pipe 4 from a water source 10. The distance between adjacent branch

pipes is d≈300 mm. The flow rate of water and gas from the compressor is adjustable. The composition of the gas may be different. The flow of water can be carried out by gravity from a source of water 10.

Let us consider the influence on the results of computer simulation of the maximum step size in computer simulation, the delay time of operation of the terminal sharpening spark gap SW2, which is the gap in the gas bubble between the tip of the high-voltage electrode and the interface between the gas bubble and water. Besides let us consider the influence the capacitance C4 of the water layer and the operating modes of the spark gap SW2: with restoration of its electrical strength between two adjacent discharges and without such restoration of electrical strength.

We used two different steps for the simulation of the transient process: 0.2 ns and 0.01 ns.

Figure 5 shows the results when using the maximum step of 0.01 ns in a computer simulation. Figure 5 illustrates the results of simulation of voltage pulses V(4), V(7), V(13) as functions of time t according to the circuit in Fig. 1. This is under the following conditions: the moment T of the operation of the spark gap SW2 after the start of the transient process in the circuit T = 76 ns (the delay time of the operation of the spark gap SW2 after the arrival of the voltage wave front at the end of the long line TD is 4 ns). The long line TD is filled with water. Wherein, the final active resistance R3 of the discharge channels in gas bubble R3 = 35Ω, capacitance C4 of the water layer C4 = 3.3 pF, active resistance R2 of the water layer R2 = 1000 Ω, inductance L8 of the discharge channels in the gas bubble L8 = 10 nH.

These are the parameters for the variant with one processing node. Voltages V(4), V(7), V(13) – voltages respectively between points 4, 7, 13 and the grounded point.

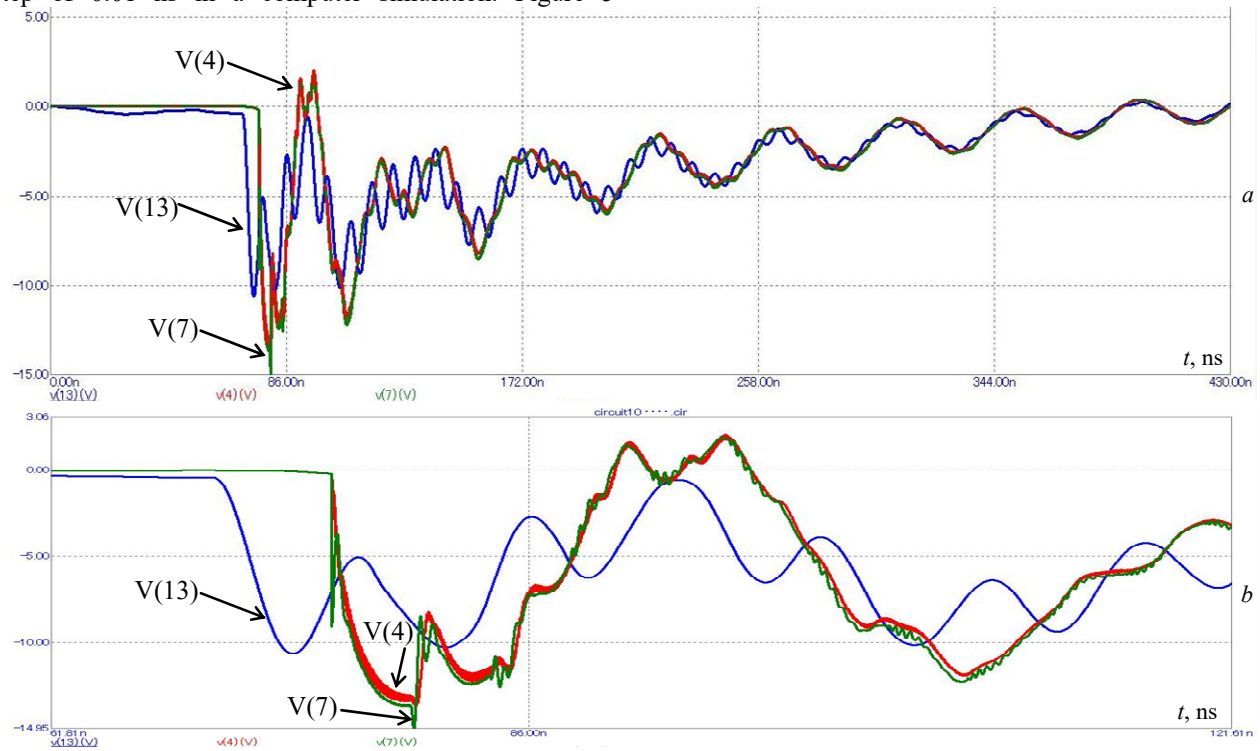

Fig. 5. Dependence of pulse voltages V(4), V(7), V(13) on time with a maximum simulation step of 0.01 ns: *a* – pulses in general ;*b* – initial sections of these pulses (T = 76 ns, R3 = 35 Ω, C4 = 3.3 pF, Z0 = 150 Ω – wave resistance, L8 = 10 nH, R2 = 1000 Ω, t_{step} = 0.01 ns)

Under the conditions considered in this work, the main transient process occurs in the experimental setup in the first approximately 120 ns. Therefore, voltage pulses as a whole, with their characteristic duration up to 200–300 ns, are shown only in Fig. 5. It follows from simulation that the steepest parts of the model waveforms are better reproduced when using a finer maximum step of 0.01 ns. Therefore, we carried out further simulations in Micro-Cap 10 using a maximum step of 0.01 ns.

Influence of the discharge delay time in a gas bubble on the transient process in the discharge unit. We took into account that, at nanosecond fronts and pulse durations, the electrical strength of the discharge gaps increases significantly. Fig. 6 illustrates this circumstance.

Computer simulation makes it possible to check which voltage pulses are formed on the discharge node in the case when the electrical strength of the discharge gap has time to recover between two adjacent discharges, and also in the case when the electrical strength does not have time to recover, and the plasma channel (channels) burns (burn) continuously.

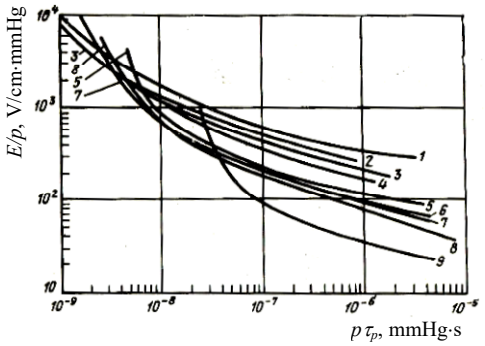

Fig. 6. [15, p. 22]. Dependence of E/p on $p\tau_p$ for various gases: *1-3* – freon of various grades; *4* – SF_6; *5* – O_2; *6* – air; *7* – N_2; *8* – Ar; *9* – Ne

The discharge node is both a node for disinfecting treatment and water purification, on the one hand, and a source of all factors for such treatment, on the other hand.

Figure 7 (the delay time of the discharge in the gas bubble is not taken into account) and Figure 5 (the delay time of the discharge in the gas bubble is 4 ns) present the results of computer simulation of the influence of the delay time of the discharge in the gas bubble. We keep in mind the influence of the delay time of such discharge on the amplitude of the voltage pulses at the discharge node (according to the scheme in Fig. 1).

Computer simulation in Micro-Cap 10 shows that there is the most rational time delay of the discharge in the gas bubble with respect to the moment. At this moment, the front of the falling voltage pulse arrives at the discharge unit with a gas bubble at the output of a long transmission line with water. This most rational time is approximately 4-5 ns.

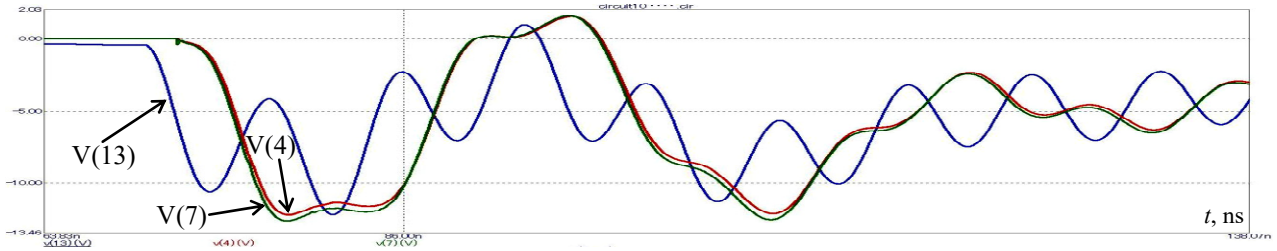

Fig. 7. Dependence of pulsed voltages V(4), V(7), V(13) on time without taking into account the delay time of the discharge in the gas bubble: initial sections of these pulses (T = 72 ns, other values – as for Fig. 5)

Let us estimate the capacitance C of the treated water layer as the capacitance of the flat capacitor with the effective square S of capacitor plates that is equal $S = 10^{-4}$ m^2 and the thickness d of water layer $d = 10^{-2}$ m:

$$C = \varepsilon\varepsilon_0 S/d = 81\cdot 8.85\cdot 10^{-12}\cdot 10^{-4}/10^{-2} \approx 6.9\cdot 10^{-12} \text{ F}.$$

In [4], we did not take into account the delay time of the discharge in the discharge node of the disinfection treatment, i.e. it was assumed that the discharge in the gas bubble begins at the instant of arrival of the voltage pulse at the discharge unit after a long line (with an electrical length of 2 ns). The discharge delay time is the sum of the statistical delay time during which an effective electron appears in the discharge gap (effective electrons appear) and the discharge formation time.

Let us estimate the discharge formation time using the formula [15, p. 21]

$$\tau_p = [1/(\alpha v_-)]\ln[i_{cr}d/(eN_0v_-)],$$

where τ_p is the discharge formation time; α is the impact ionization coefficient, which determines the number of electrons created by the primary electron when passing a distance of 1 cm in an electric field; v_- is the drift velocity of the electron avalanche; i_{cr} is the critical value of the current in the discharge circuit, which is reached by the current in the discharge circuit at the end of the discharge formation time; d is the length of the discharge gap; e is the electron charge; N_0 is the initial number of electrons (initiating electrons) that initiate the development of electron avalanches.

According to [15, p. 10] for air, the relation $\alpha/p = A(E/p–B)^2$ is valid, where $A = 1.17\cdot 10^{-4}$ cm·mmHg/V^2, B = 32.2 V/(cm·mmHg). So $\alpha = A(E/p–B)^2p$. In the nanosecond range of characteristic pulse durations, one can take E = 100 kV/cm = 10^5 V/cm. Then, at p = 760 mmHg

$$\alpha = A(E/p–B)^2p = 1.17\cdot 10^{-4}(10^5/760–32.2)^2\cdot 760 \approx 878 \text{ 1/cm}.$$

In addition, according to [15, p. 20-21] it is possible to accept $v = 10^7$ cm/s, and at i_{cr}, which is much smaller than the current in the discharge circuit, the value $[i_{cr}d/(eN_0v_-)]\sim 10^8$. From here we get $\ln[i_{cr}d/(eN_0v_-)] \approx \approx \ln 10^8 \approx 18.42$:

$$\tau_p = [1/(\alpha v_-)]\ln[i_{cr}d/(eN_0v_-)] \approx [1/(878\cdot 10^7)]\cdot 18.42 \approx 2\cdot 10^{-9} \text{ s}.$$

Thus, the estimated calculated value of the discharge formation time was $\tau_p = 2\cdot 10^{-9}$ s, i.e. 2 ns. The statistical delay time when voltage pulses with a steep edge (with a rise rate of $\geq 10^{12}$ V/s) are applied to the discharge gap does not exceed the value of the formation time.

To increase the voltage amplitude at the processing node and on the water layer in this node, it is necessary to reduce the load capacitance (capacity of the water layer in the processing node) to 10 pF or less, increase the active resistance of the water layer to 500 Ω or more.

It is important to estimate the ratio of the voltage across the entire discharge node (the voltage across the discharge channels in the gas bubble plus the voltage across the water layer) and the voltage directly across the water layer. The gap in the gas bubble between the tip of the high-voltage electrode and the interface with the water layer is the terminal sharpening gas discharger in the discharge channel(s) of which broadband radiation is formed and active micro-particles are formed that disinfect water.

Computer simulation showed that for the one shown in Fig. 1 of the circuit, close to the most rational delay time T for the operation of the spark gap SW2 relative to the moment of arrival of the front of the incident voltage wave along the long line is equal $T \approx 4$ ns. In this close to optimal mode, the spark gap SW3 operates 70 ns after the start of the transient process in the circuit in Fig. 1, and the arrester SW2 fires 76 ns after the start of this transient process. Taking into account the fact that between these arresters there is a long line T1 with an electrical length of 2 ns, from the moment 72 ns of the arrival of the front of the incident wave traveling along the long line T1, another 4 ns passes to the arrester SW2 until the moment of 76 ns of its operation. These four ns is the delay time operation of the spark gap SW2, close to most rational. With a smaller and longer delay time for the operation of the spark gap SW2, the voltage amplitude V(7) at the processing unit and at the water layer V(4) in the treatment unit decreases with a practically unchanged voltage amplitude V(13) immediately after the spark gap SW3. In a mode close to optimal (see Fig. 4), the voltage amplitude V(7) at the processing node exceeds the voltage amplitude V(13) by 1.35 times, and the source voltage V(1) is more than 2.7 times. At the same time, the voltage amplitude V(7) on the entire processing unit slightly

exceeds the voltage amplitude V(4) on the water layer. This excess is the smaller, the lower the final resistance R3 of the plasma channels (because of discharges) in the gas bubble. Figure 5 illustrates the voltage versus time dependences at three different points in the circuit (see Fig. 1) for the case when we are considering one multi-gap spark gap SW3, one long line T1, and one water treatment unit. This unit comprises one discharge gap SW2, and is electrically connected in series with it a layer of water having a capacitance C4 = 3.3 pF and an active resistance R2 = 1000 Ω.

Voltage versus time for the case when three identical multi-gap spark gaps connected in parallel are used. Figure 8 illustrates the voltage versus time dependences at the same three points [V(4), V(7), V(13)] of the circuit (see Fig. 1), for which some results have already been discussed above, for the case when three identical multi-gap arresters connected in parallel in the experimental setup. In the diagram (Fig. 1), these arresters are represented as one resulting spark gap SW3, three identical long lines with an electrical length of 2 ns, connected in parallel, and are represented by the resulting long line T1 with a threefold reduced wave resistance Z0 = 50 Ω. In this case, three water treatment units are also used, each consisting of one discharge gap and a layer of water electrically connected to it in series. These three identical processing nodes during modeling are combined into one node with the resulting discharge gap SW2 and the resulting water layer electrically connected to it in series, having a capacitance C4 = 10 pF and active resistance R2 = 333 Ω. At the same time, some other elements of the circuit have values that differ from those shown in Fig. 1, namely, C8 = C9 = 3 pF, L6 = L7 = 0.33 nH, L8 = 3.3 nH, R3 = 12 Ω. L8 and R3 are, respectively, the inductance and the calculated final active resistance of the resulting discharge gap SW2.

Both Fig. 5 and Fig. 8 show that the front of the pulses at points 4 and 7 is associated with the processes of reflection from the discharge gap SW2 at the end of the long line T1 and the path of voltage waves along the long line T1. The time interval between adjacent voltage surges caused by the reflection of voltage waves from the discharge gap SW2 is 4 ns, i.e. is equal to the double time of the wave travel along the line T1. On the oscillograms in Fig. 5, the voltage front for pulses V(4) and V(7) is much steeper than in Fig. 8, and is approximately 4 ns. In both of these figures, the voltage amplitude at the discharge nodes as a whole V(7) and at the water layer V(4) is greater than the voltage amplitude immediately after the multi-gap spark gap SW3. This was achieved by reducing the calculated capacitance of the water layer C4 to a value of 10 pF or less and choosing a delay time of 4 ns (close to optimal) for the operation of the spark gap SW2.

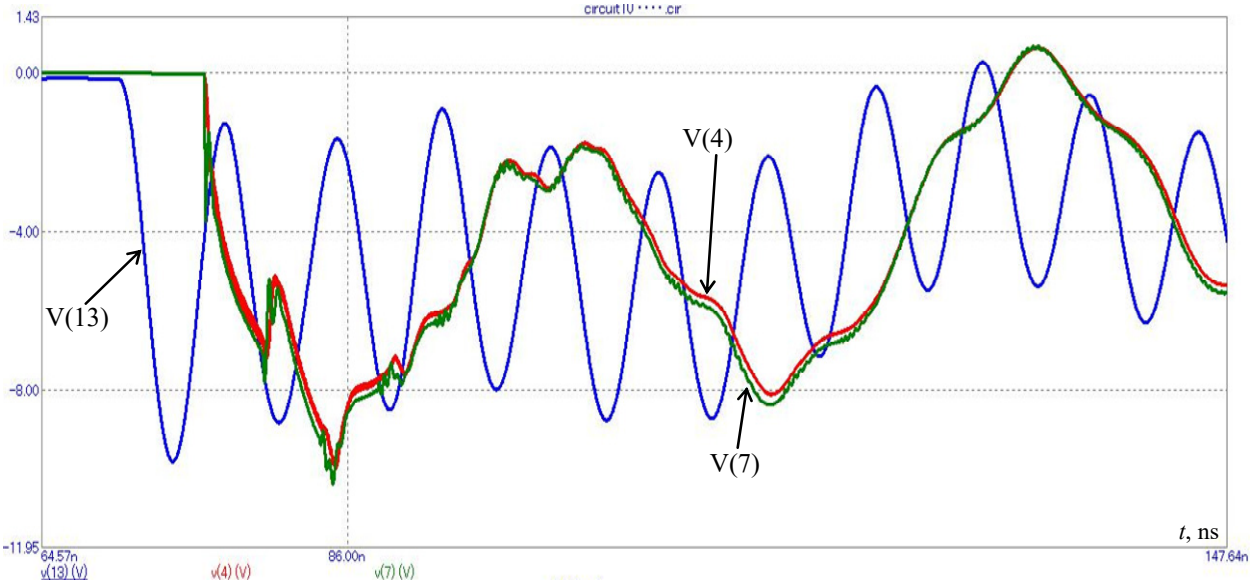

Fig. 8. Dependences of voltages V(4), V(7), V(13) on time according to the diagram in Fig. 1 for the case with three processing units. In this case three identical multi-gap spark gaps (their common designation SW3) connected in parallel are used: initial sections these pulses (T = 76 ns, R3 = 12 Ω, C4 = 10 pF, Z0 = 50 Ω – wave resistance, L8 = 3.3 nH, R2 = 333 Ω, t_{step} = 0.01 ns)

The mode without taking into account the restoration of the electrical strength of the discharge gap in the gas bubble in comparison with the mode in which the electrical strength of the gap is restored. Figure 9 shows the results of computer simulation for the operating mode of the experimental setup, when the plasma channels after discharges do not disappear until the next high-voltage pulse arrives, that is, the electric strength of the gas gap in the gas bubble does not have time to recover between two voltage pulses adjacent in time. This mode corresponds to the operation of an experimental setup with one processing unit, in which the plasma channels in the gas bubble burn continuously, and one sharpening multi-gap spark gap SW3, the electrical circuit of which is shown in Fig. 2. In this figure, the spark gap SW2 is absent, since the plasma channels (plasma channel) are well conducting, do not play the role of a switch, the impedance of which varies from a value much greater than the impedance of the discharge circuit to a value much less than the impedance of the discharge circuit. On Fig. 2 point number 7 in Fig. 1 has the number 12. As an estimate, we took both for the mode with the restoration of the electric strength of the discharge gap in the gas bubble, and for the mode without restoring its electric strength, when using one processing unit. The final (after the end of the transient) active resistance of the

plasma channels (plasma channel) R3 = 35 Ω, inductance L8 = 10 nH (see Fig. 2) in both these modes.

Comparison of the results of simulation of the regime taking into account the restoration of the electrical strength of the discharge gap in the gas bubble after each discharge (the main mode) and the regime without taking into account the restoration of the electrical strength of this discharge gap (without the arrester SW2) shows the following. The presence of the spark gap SW2, considering the delay time of its operation, which is close to most rational, takes place in the main mode. The amplitude of voltage pulses, when taking into account the restoration of electric strength, is greater by about 20 % (see Fig. 5 and Fig. 9). The conditions for the reflection of a voltage wave, taking into account the delay time of operation SW2 and the restoration of the electric strength of the discharge gap in the gas bubble, are closer to the conditions reflections from the end of a long line (in our case, the T1 line) that is open at the end. In addition, in the regime without taking into account the restoration of the electrical strength of the discharge gap in the gas bubble after each discharge, the curves of the voltage pulses V(4), V(12), V(13) are very similar to each other with a somewhat lower amplitude of the voltage V(4) on the layer water. A feature of the regime without taking into account the restoration of the electrical strength of the discharge gap in the gas bubble is that the plasma channels in the gas bubble burn continuously, providing broadband continuous radiation, including ultraviolet and even shorter wavelength. In this case, energy is supplied to the discharge unit by nanosecond pulses with a certain repetition rate. The energy supply to the discharge unit by nanosecond pulses is provided by a high-voltage capacitive storage with a capacity of C5 = 150 pF and a multi-gap spark gap SW3, the dielectric strength of which is restored much faster than that of SW2. The maximum repetition rate of pulses to the processing unit is determined by the minimum possible recovery time for the electrical strength of the spark gap SW3. If the pulse repetition rate exceeds the maximum, the electrical strength of the spark gap SW3 will not be restored, and the real experimental setup will go into emergency short circuit mode, which is unacceptable.

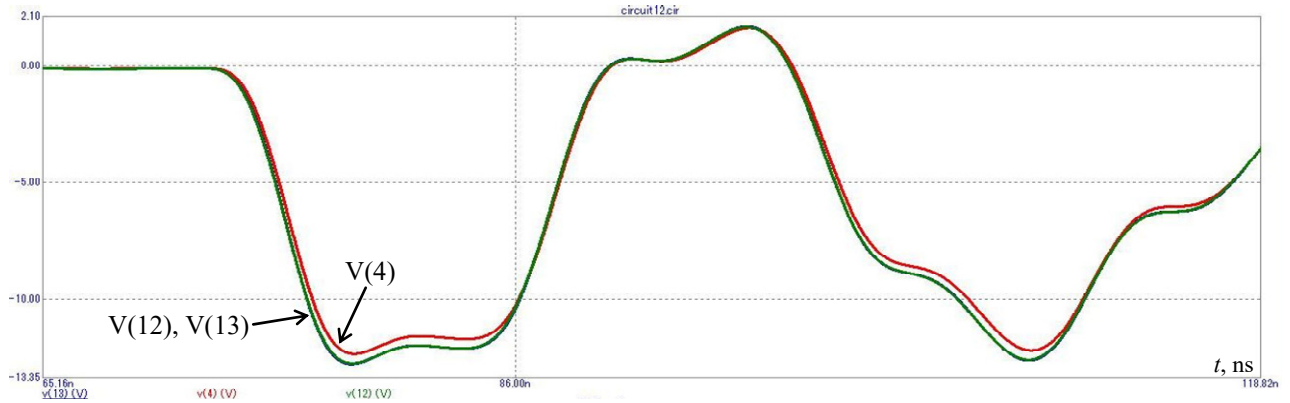

Fig. 9. Dependences of voltages V(4), V(12), V(13) on time in the mode without taking into account the restoration of the electrical strength of the discharge gap in the gas bubble (according to the scheme in Fig. 2). This is the case with one processing unit: the initial sections of these pulses (the arrester SW2 is replaced by a segment of the conductor, so the parameter *T* is absent. The remaining values correspond to the values in Fig. 4)

Influence of the capacitance value of the water layer on the voltage amplitude at the processing unit. Figure 7 and Fig. 10 show that with an increase in the capacitance of the C4 water layer from C4 = 3.3 pF (Fig. 7) to C4 = 50 pF (Fig. 10) the voltage amplitude at the processing unit V(7) and at the water layer V(4) becomes significantly less than the voltage amplitude V(13) after the spark gap SW3. In this case, the voltage amplitude V(13) practically does not change. Our calculations show the next thing. When we are using an experimental setup, in order for the amplitude of the voltage pulses at the processing unit and on the water layer to be no less than the amplitude of the voltage pulses directly after the spark gap SW3, the capacitance of the water layer C4 should not exceed 20 pF. Figure 1 demonstrates the electrical circuit of this setup for computer simulation in Micro-Cap 10.

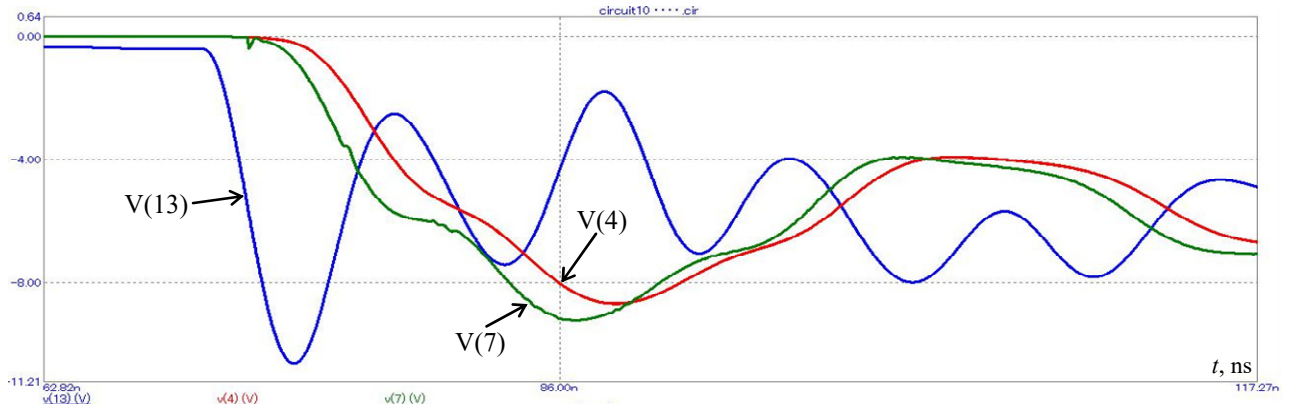

Fig. 10. Dependences of voltages V(4), V(7), V(13) on time according to the scheme in Fig. 1. This is the case with one processing unit and increased capacity C4 of the water layer C4 = 50 pF: initial segments of these pulses (*T* = 72 ns , C4 = 50 pF, other values as in Fig. 5.)

To illustrate the effect of the capacitance C4 of the water layer on the voltage amplitude at the processing unit, the results of simulation were taken without taking into account the delay time of the discharge in the spark gap SW2, since it is this simulation option that was considered in our work [13]. When taking into account the delay time of the discharge in the spark gap SW2 (delay in the operation of the spark gap SW2), an increase in the capacitance C4 of the water layer also leads to a decrease in the voltage amplitude at the processing unit, although the effect of this increase is reduced.

Conclusions. To increase the voltage amplitude at the processing node and on the water layer in this node, it is necessary to reduce the load capacitance (capacity of the water layer in the processing node) to 10 pF or less, increase the active resistance of the water layer to 500 Ω or more. The maximum step in computer simulation of the process of discharging a generator of high-voltage nanosecond pulses to an RLC load with a discharge gap should not exceed 0.01 ns. The most rational delay time for the operation of the discharger, which is the gap in the gas bubble inside the water, under the conditions considered by us is 4–5 ns. It is at this delay time that the amplitude of voltage pulses at the node of disinfecting water treatment and at the layer of treated water is maximum, other things being equal. This amplitude of voltage pulses exceeds by about 1.35 times the voltage amplitude immediately after the main high-voltage discharger, which commutates energy from the high-voltage capacitive storage to the processing node through long line filled with water.

Conflict of interest. The authors declare that they have no conflicts of interest.

REFERENCES

1. Ning W., Lai J., Kruszelnicki J., Foster J.E., Dai D., Kushner M.J. Propagation of positive discharges in an air bubble having an embedded water droplet. *Plasma Sources Science and Technology*, 2021, vol. 30, no. 1, art. no. 015005. doi: https://doi.org/10.1088/1361-6595/abc830.

2. Ghernaout D., Elboughdiri N. Disinfecting Water: Plasma Discharge for Removing Coronaviruses. *OALib*, 2020, vol. 7, no. 4, pp. 1-29. doi: https://doi.org/10.4236/oalib.1106314.

3. Gershman S. *Pulsed electrical discharge in gas bubbles in water*. Dissertation submitted for the Degree of Doctor of Philosophy, New Brunswick, New Jersey, 2008. 186 p. doi: https://doi.org/doi:10.7282/T30Z73K8.

4. Akkouchi K., Rahmani L., Lebied R. New application of artificial neural network-based direct power control for permanent magnet synchronous generator. *Electrical Engineering & Electromechanics*, 2021, no. 6, pp. 18-24. doi: https://doi.org/10.20998/2074-272X.2021.6.03.

5. Kuznetsov B.I., Nikitina T.B., Bovdui I.V., Kolomiets V.V., Kobylianskiy B.B. Overhead power lines magnetic field reducing in multi-story building by active shielding means. *Electrical Engineering & Electromechanics*, 2021, no. 2, pp. 23-29. doi: https://doi.org/10.20998/2074-272X.2021.2.04.

6. Takahashi M., Shirai Y., Sugawa S. Free-Radical Generation from Bulk Nanobubbles in Aqueous Electrolyte Solutions: ESR Spin-Trap Observation of Microbubble-Treated Water. *Langmuir*, 2021, vol. 37, no. 16, pp. 5005-5011. doi: https://doi.org/10.1021/acs.langmuir.1c00469.

7. Nishiyama H., Nagai R., Takana H. Characterization of a Multiple Bubble Jet With a Streamer Discharge. *IEEE Transactions on Plasma Science*, 2011, vol. 39, no. 11, pp. 2660-2661. doi: https://doi.org/10.1109/TPS.2011.2160367.

8. Shibata T., Nishiyama H. Water Treatment by Dielectric Barrier Discharge Tube with Vapor Flow. *International Journal of Plasma Environmental Science and Technology*. 2017, vol. 11, no. 1, pp. 112-117. doi: https://doi.org/10.34343/ijpest.2017.11.01.112.

9. Hong J., Zhang T., Zhou R., Zhou R., Ostikov K., Rezaeimotlagh A., Cullen P.J. Plasma bubbles: a route to sustainable chemistry. *AAPPS Bulletin*, 2021, vol. 31, no. 1, art. no. 26. doi: https://doi.org/10.1007/s43673-021-00027-y.

10. HyoungSup K. *Plasma Discharges in Produced Water and Its Applications to Large Scale Flow*. A Thesis Submitted to the Faculty of Drexel University for the degree of Doctor of Philosophy, March 2016. 205 p.

11. Takahashi K., Takayama H., Kobayashi S., Takeda M., Nagata Y., Karashima K., Takaki K., Namihira T. Observation of the development of pulsed discharge inside a bubble under water using ICCD cameras. *Vacuum*, 2020, vol. 182, art. no. 109690. doi: https://doi.org/10.1016/j.vacuum.2020.109690.

12. Sponsel N.L., Gershman S., Herrera Quesada M.J., Mast J.T., Stapelmann K. Electric discharge initiation in water with gas bubbles: A time scale approach. *Journal of Vacuum Science & Technology A*, 2022, vol. 40, no. 6, art. no. 063002. doi: https://doi.org/10.1116/6.0001990.

13. Boyko M.I., Makogon A.V. Discharge in gas bubbles in water as a source of an intensive factors' complex for water disinfection: comparison experimental and computer modelling results. *Technical Electrodynamics*, 2022, no. 3, pp. 56-61. doi: https://doi.org/10.15407/techned2022.03.056.

14. Boyko N.I., Makogon A.V. High voltage plant with 3 MW pulse power for disinfection flow of water by nanosecond discharges in gas bubbles. *Technical Electrodynamics*, 2020, no. 5, pp. 80-83. doi: https://doi.org/10.15407/techned2020.05.080.

15. Mesiats G.A. *Generation of power nanosecond pulses*. Moscow, Soviet Radio Publ., 1974. 256 p. (Rus).

Received 23.03.2023
Accepted 30.05.2023
Published 02.01.2024

M.I. Boiko[1], *Doctor of Technical Sciences, Professor,*
K.S. Tatkova[1], *Master Student,*
[1] National Technical University «Kharkiv Polytechnic Institute», 2, Kyrpychova Str., Kharkiv, 61002, Ukraine,
e-mail: qnaboyg@gmail.com (Corresponding Author)

How to cite this article:
Boiko M.I., Tatkova K.S. Computer simulation of operation plant effective modes for water disinfection by electrical discharges in gas bubbles. *Electrical Engineering & Electromechanics*, 2024, no. 1, pp. 43-50. doi: https://doi.org/10.20998/2074-272X.2024.1.06

UDC 621.365.51 https://doi.org/10.20998/2074-272X.2024.1.07

A.A. Shcherba, O.D. Podoltsev, N.I. Suprunovska, R.V. Bilianin, T.Yu. Antonets, I.M. Masluchenko

Modeling and analysis of electro-thermal processes in installations for induction heat treatment of aluminum cores of power cables

Introduction. *The development of the electric power industry is directly related to the improvement of cable lines. Cable lines meet modern requirements for reliability, they are increasingly used.* ***Problem***. *Currently, power cables with an aluminum multi-conductor core, which requires heat treatment - an annealing process at the stage of the technological manufacturing process, are widespread. This process makes it possible to desirably reduce the electrical resistance of the wire and increase its flexibility. For effective use of induction heating during annealing of an aluminum core, it is necessary to determine the optimal frequency of the power source of the inductor. Considering the long length of the inductor and the large number of its turns, the numerical calculation of the electromagnetic field, which is necessary for calculating the equivalent electrical parameters of the turns of the inductor and its efficiency, requires significant computer resources. The* ***goal*** *is to develop a computer model for calculating electro-thermal processes in an induction plant for heating (up to the annealing temperature) an aluminum core of a power cable moving in the magnetic field of a long multi-turn inductor, as well as obtaining frequency dependences of the equivalent R, L parameters of such an inductor and determining the optimal the value of the frequency of the power source, which corresponds to the maximum value of the electrical efficiency of the inductor.* ***Methodology***. *The mathematical model was developed to analyze the coupled electromagnetic and thermal processes occurring in a core moving in a time-harmonic magnetic field of an inductor at a constant speed. The differential equations for the electromagnetic and temperature fields, taking into account the boundary conditions, represent a coupled electro-thermal problem that was solved numerically by the finite element method using the Comsol software package. For a detailed analysis of the electromagnetic processes in the inductor, an additional problem was considered at the level of the elementary cell, which includes one turn of the inductor and a fragment of the core located near this turn.* ***Results***. *According to the results of the calculation of the electromagnetic field in the area of the elementary cell, the equivalent electrical parameters of one turn of the inductor and the entire multi-turn inductor were calculated depending on the frequency of the electric current. The frequency dependences of the electrical efficiency of the inductor were calculated.* ***Originality***. *Taking into account the design features of the inductor (its long length and large number of turns), the method of multiscale modeling was used. Electro-thermal processes in the core were studied at the macro level, and the distribution of the electromagnetic field and electric current density in the cross-section of the massive copper turn of the inductor was calculated at the micro level – at the level of an elementary cell containing only one turn of the inductor. The frequency dependences of the equivalent R, L parameters of the inductor, taking into account the skin effect, the proximity effect, and the geometric effect, were obtained, and the quantitative influence of the electric current frequency on these effects was studied.* ***Practical value***. *The dependence of the electrical efficiency of the inductor on the frequency of the power source was obtained and it was shown that for effective heating of an aluminum core with a diameter of 28 mm, the optimal value of the frequency is in the range of 1–2 kHz, and at the same time the electrical efficiency reaches values of* η_{ind} *= 0.3–0.33, respectively.* References 31, figures 10, table 1.

Key words: **electromagnetic processes, induction heat treatment, aluminum conductive core, power cables, multiscale modeling, current frequency, inductor efficiency**.

У роботі досліджено електромагнітні та теплові процеси в установках індукційного нагрівання алюмінієвої жили силових кабелів та умови реалізації технологій її відпалювання. При математичному моделюванні вказаних процесів ураховано такі конструктивні особливості індуктора, як його значна довжина і відповідно велика кількість його витків, що викликало необхідність використати метод мультимасштабного моделювання. При цьому на макрорівні розраховувались електротеплові процеси в жилі, що рухалась у магнітному полі індуктора, а на мікрорівні (тобто на рівні елементарної комірки, що має лише один виток індуктора) визначався розподіл електромагнітного поля та густини електричного струму в перерізі масивного мідного витка індуктора з урахуванням особливостей його конструкції. На обох рівнях у роботі використовувався чисельний метод скінченних елементів, реалізований в пакеті програм Comsol. За результатами розрахунку електромагнітного поля на рівні елементарної комірки, отримано частотні залежності еквівалентних R, L параметрів індуктора із урахуванням скін-ефекту, ефекту близькості та геометричного ефекту. Досліджено кількісний вплив частоти електричного струму на ці ефекти та отримано залежність електричного ККД індуктора від частоти джерела електроживлення. Показано, що для ефективного нагрівання алюмінієвої жили діаметром 28 мм оптимальне значення частоти знаходиться в діапазоні 1–2 кГц, в якому електричний ККД може досягати значень η_{ind} *= 0,3–0,33.* Бібл. 31, рис. 10, табл. 1.

Ключові слова: **електромагнітні процеси, індукційна термообробка, алюмінієва струмопровідна жила, силові кабелі, мультимасштабне моделювання, частота струму, ККД індуктора.**

Introduction. For a long time, innovative research and development in the domestic electric power industry was aimed at the development of decentralized local Microgrid electrical systems [1–4], which use dynamic regulation of the power balance of distributed sources of electricity in conditions of non-stationary consumption by industrial and residential complexes and objects without taking into account electrophysical features of structural elements of cable and conductor products of overhead [5] and cable power transmission lines (PTLs) [6–8].

In the 21st century, the industrialized countries of the world began to use self-supporting insulated wires (SIWs) with a reinforced current-conducting core made of electrotechnical alloys of the «TA» brand (hard aluminum) and nanomodified («cross-linked») polyethylene (LPE) insulation in overhead power lines. In Ukraine, YUZHCABLE WORKS, PJSC, Kharkiv, Ukraine was the first to master the industrial production of SIWs [5]. Their implementation in single-phase and three-phase PTLs with voltage of up to 1 kV made it possible to twist phase and neutral wires into one bundle, which reduced the running inductance and voltage drop several times. The land acquisition area for the construction of PTLs has significantly decreased, and

their repair and maintenance has been simplified. In such PTLs, short circuits do not occur during bad weather and other external influences, which increased the safety and reliability of power supply systems of responsible energy consumers [5]. A significant reduction in the inductance of overhead PTLs with SIWs even led to the appearance of studies on the feasibility of using capacitive reactive power compensators in them [9].

YUZHCABLE WORKS, PJSC also mastered the serial production of innovative domestic power cables with three-layer LPE insulation and mainly aluminum core, which ensured the intensive development of the construction and use of underground cable PTLs in Ukraine with voltage of up to 330 kV and power of hundreds to thousands MVA, which are more reliable and protected from any external influences [7] than overhead PTLs even with SIWs [5]. Moreover, in the production of current-conducting cores of cables, alloys of the «TA» brand are also mostly used.

However, the problem of speeding up work on restoration of power supply of critical infrastructure objects using undamaged cable channels and trays is currently intensifying in Ukraine, for the solution of which it is desirable to use cables with a core of increased plasticity and current conductivity.

Modern power cables with LPE insulation and multi-wire copper core have the highest plasticity and specific electrical conductivity [10–12]. Such cables are used in power systems of many countries of the world. But the lack of own copper deposits in Ukraine and the high price of its import limit the possibility of its wide use in the domestic electric power industry.

In our country, power cables with a copper current-conducting core are mainly used in pulse electrical engineering, in particular in the discharge circuits of linear [13] and nonlinear [14] capacitive electricity storage devices of electric discharge units for the implementation of pulse spark plasma processes of obtaining micro- and nanopowders with unique properties [15, 16]. To reduce the inductance of such circuits and obtain high dynamic parameters in them, the reverse pulse current can flow through the copper screen of the cables, that is, ordinary power cables can be used as coaxial.

In the electric power industry of Ukraine, modern power cables with LPE insulation and twisted and compacted aluminum multi-wire core are mostly used [7, 17]. To improve the plasticity and specific conductivity of such a wire, it must be «annealed», that is, subjected to a special heat treatment at temperature of about 420 °C for certain time, and then slowly cooled to bring the structure of aluminum products closer to an equilibrium state [18].

The practical and economic efficiency of using the «annealing» technology to improve the operational characteristics of aluminum conductive cores has already been confirmed by the authors of the article earlier when implementing the technology of passive heating of an aluminum core wound on a metal drum. Its passive heating was carried out from electric heaters located together with the core in a common thermal chamber. Currently, this technology of «annealing» of the aluminum core is used at YUZHCABLE WORKS, PJSC in the technological lines of serial production of modern low-voltage cables with aluminum core of increased plasticity and electrical conductivity.

However, in the technological lines of industrial production of modern domestic power cables for medium and high voltages, induction heating to 60–95 °C of the surface of the moving aluminum core of the cables with high-frequency current is already used to improve the quality of applying three-layer LPE insulation to it [7]. Therefore, it was important to evaluate the effectiveness of using induction units in such lines not only for relatively low-temperature heat treatment of the surface of aluminum cores, but also for increasing their plasticity and specific current conductivity.

In this work, a multi-turn inductor of small diameter (comparable to the diameter of the cable core) and relatively long (≥ 2 m) was investigated, in the harmonic magnetic field of which the cable core was moving. The electrical parameters of the inductor and the high-frequency power source were chosen in such a way that the core temperature at the output reached 420 °C.

Various modes of induction heat treatment of conductive materials and products were studied in numerous scientific publications [19-27]. In particular, in the publication of scientists of the world manufacturer of modern cable and wire heating systems Inductotherm Group Company [22], innovative inductor systems for simultaneous effective heating of single-conductor and multi-conductor cores of cables with justification for choosing the optimal frequency were investigated. The possibility of induction heating of conductors with diameter of 1.27 to 15.75 mm at power source frequency of 10 to 800 kHz is considered.

The article [23] shows ways to optimize induction heating using two types of inductors – flat and solenoid based on litz conductors. The optimal frequency for obtaining the maximum electrical efficiency was determined. It is shown that with fixed geometry and other system parameters, the efficiency of induction heating depends on the volume of copper in the windings. Experimental verification of the obtained results was carried out.

In [24], a transient electromagnetic-thermal model of induction heating of ferromagnetic materials was solved, taking into account their nonlinear dependencies (in particular, $B(H, T)$) and using the Finite Element Method. The multiphysics modeling strategy consisted in the fact that the electromagnetic problem was solved for fixed isothermal temperature fields, and the thermal problem was solved for the fixed heat of the heating source. The results of computer modeling of a ferromagnetic sample in a cylindrical inductor (with internal diameter of 50 mm and 5 turns) were confirmed by experimental studies of induction heating of material samples at three heating rates.

In the publication [25], the authors, using the Finite Element Method, conducted multiphysics modeling and experimental verification of the temperature distribution depending on the current frequency of the induction heater. A feature of the work is the manufacture of an inductor from a wire of the Litzendrat type and the use of relatively high frequencies from 15 to 25 kHz.

In [26], a study was conducted on the influence of the power of the induction heater, the feed rate, and the

diameter of the AISI 4140 steel sample on the temperature distribution in the samples depending on the diameter (7 mm, 14 mm, 21 mm, and 28 mm). An inductor in the form of a spiral coil with internal diameter of 5.8 cm was used, which heats the test sample in the temperature range from 492 °C to 746 °C. Two stages of heating are implemented – the first stage with ferromagnetic properties of the sample, and the second stage, when due to exceeding the Curie temperature, the sample becomes paramagnetic.

In the publication [27], the authors experimentally investigated the temperature distribution, heating rate, overheating, and temperature fluctuations of a commercial rod made of aluminum alloy 6061 with diameter of 10 mm and length of 1.5 m, with an analysis of the influence of heat treatment modes on the mechanical properties of the alloy. It is shown that the sample after induction heating to temperature of 560 °C has better mechanical properties compared to the sample heated in a conventional electric furnace.

One of the most important parameters of the efficiency of induction heating is the frequency of the power supply current of the inductor, at which its electrical efficiency reaches its maximum value. This frequency depends on many factors – the cross-sectional dimensions of the inductor turns, its overall dimensions and the air gap between the inductor and the core, as well as the material of the current-conducting core of the cables, its dimensions and other characteristic parameters. Considering the long length of such an inductor and, accordingly, the large number of turns (~ 100), the numerical calculation of the electromagnetic field and efficiency based on it, taking into account the geometric dimensions of the massive turns of the inductor in such a structure and the inhomogeneity of the electric current distribution in their volume, requires significant computer resources.

Features of simplifying computer calculations of the electromagnetic field and determining the efficiency in such systems were not considered in the above publications. In this article, to simplify calculations, the method of multiscale modeling [28–30] is used, which is based on the concept of an elementary cell containing only one inductor turn and a small core fragment located near this turn. At the same time, the action of the end effects in the inductor was not taken into account, because with its long length, they have a weak effect on the integral electromagnetic characteristics and the final value of the core temperature at the output of the inductor.

Thus, according to the multiscale modeling approach, the field problem was considered in the area of an elementary cell containing only one massive inductor turn and a core fragment. The equivalent R, L parameters of this cell were calculated as a function of the frequency of the power source, and then these results, by periodically repeating this cell, were transferred to the entire design of the inductor of the electro-induction heating installation.

The goal of the article is to develop, based on the method of multiscale modeling, a computer model for the analysis of electro-thermal processes in an induction plant for heating a moving aluminum core of a power cable to quantitatively assess the effectiveness of using such plants in existing industrial technological lines for the production of modern cables to increase the plasticity and specific conductivity of their aluminum cores.

One of the most important tasks was to obtain the frequency dependencies of the equivalent R, L parameters of such an inductor, taking into account the irregular distribution of electric current across its cross-section, and using them to determine the optimal frequency of the power source, which corresponds to the maximum value of the electrical efficiency of the inductor.

Research is aimed at assessing the possibility of achieving the goal in the industrial technological line of continuous application of modern three-layer cross-linked polyethylene insulation on the moving aluminum core of cables with voltage of up to 110 kV, which is serially manufactured by YUZHCABLE WORKS, PJSC.

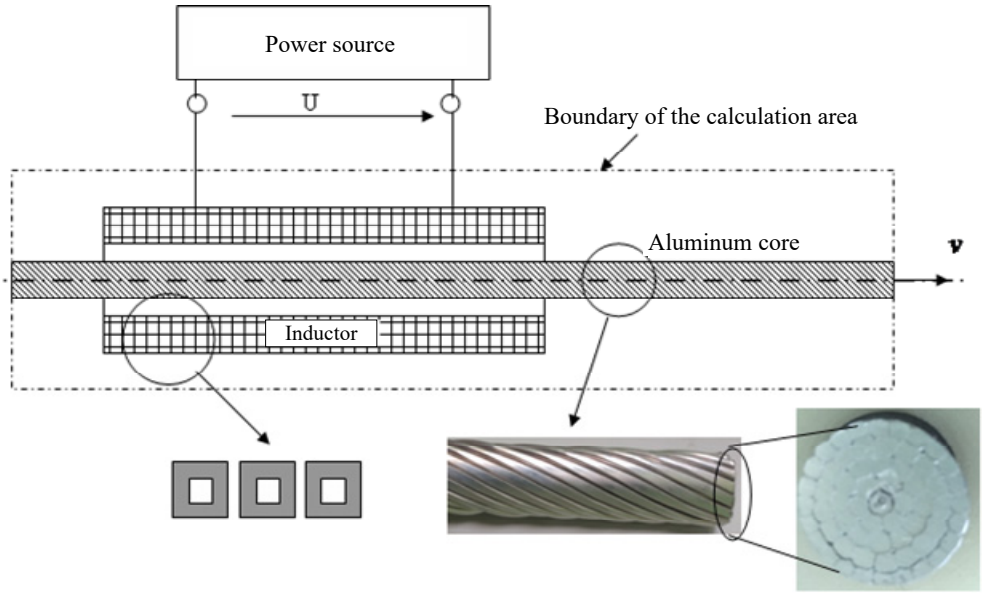

Fig. 1. Scheme of the physical model of the investigated installation for induction heating of the aluminum core of a power cable moving at constant speed v

Mathematical model of analysis of coupled electromagnetic and thermal processes. Figure 1 schematically shows the physical model of the investigated installation, which includes a relatively long water-cooled multi-turn inductor and an aluminum core of a power cable moving at constant speed v in the harmonic magnetic field of the inductor. When the inductor is connected to a power or high-frequency power source, induced electric currents arise in the core, and as a result of Joule heat release, it is heated.

A mathematical model for the analysis of coupled electromagnetic and thermal processes was constructed in the following approximation:

1. The consideration of the electromagnetic process was carried out in a steady state in the frequency domain, when all field characteristics are complex quantities. The thermal process was considered in the stationary mode.

2. In practice, the inductor is made of a copper tube and has a complex structure, which is conventionally shown in Fig. 1. However, at the first stage, when the main attention is paid to the thermal process in the core, the inductor can be considered as a multi-turn coil with given average electric current density $\dot{J}_i = \dot{I}_i N_i / S_i$, where $\dot{I}_i N_i$ is the MMF of the inductor, and S_i is its cross-sectional area. In this expression and below, complex quantities are indicated by a dot above.

3. The heated core is made of aluminum, is multi-wire and sealed. Its appearance and cross-section are shown in Fig. 1. The compaction coefficient reaches 0.96 and, as a result, it was considered solid in the calculations. Here, nonlinear dependencies of electrical conductivity, thermal conductivity, and specific heat capacity of its material on temperature were taken into account.

4. Taking into account the approximately cylindrical shape of the inductor and the core located symmetrically relative to the inductor, the problem was considered as axisymmetric, in a 2D formulation in the cylindrical coordinate system $r0z$ relative to the complex variable – the magnetic vector potential $\dot{A}(r, z)$, as well as the temperature $T(r, z)$ in the calculation area shown in Fig. 1.

This area contains three subareas – the inductor, the aluminum core, and the air surrounding these elements. The mathematical model that described the coupled electromagnetic and thermal processes included the formulation of electromagnetic and thermal problems, which are presented below.

The electromagnetic process was described by a system of differential equations for the complex value of the magnetic vector potential $\dot{A}$:

$$j\omega\sigma(T)\dot{A}_\varphi + \mu_0^{-1}\nabla\times(\nabla\times\dot{A}_\varphi) = 0\,, \text{ in the area of the core,} \quad (1)$$

$$\mu_0^{-1}\nabla\times(\nabla\times\dot{A}_\varphi) = \begin{cases} \dot{I}_i N_i / S_i, \text{ in the area of the inductor,} \\ 0, \text{ in air,} \end{cases} \quad (2)$$

where $\sigma(T)$ is the electrical conductivity of the core, which depends on the temperature, ω is the angular frequency of the current in the inductor, μ_0 is the magnetic constant.

As boundary conditions for the electromagnetic problem, the condition of symmetry with respect to the axis $r = 0$ and the condition of magnetic insulation on the outer boundary were set:

$$\dot{A}_\varphi|_C = 0\,. \quad (3)$$

The coupling between the electromagnetic problem and the thermal problem was carried out with the help of two quantities – he Joule heat release in the core q and the nonlinear dependence of the electrical conductivity of the core $\sigma(T)$.

The thermal problem for the unknown temperature distribution T included the following differential equation of heat transfer due to the mechanisms of heat conduction and convection:

$$\rho C_p(T)\boldsymbol{u}\cdot\nabla T - \nabla\cdot(\lambda(T)\nabla T) = \begin{cases} q, \text{ in the area} \\ \text{of the core,} \\ 0, \text{in other elements} \\ \text{of the area,} \end{cases} \quad (4)$$

where ρ, C_p, λ are the temperature-dependent density, specific heat capacity, and thermal conductivity of the material of the corresponding environment; $\boldsymbol{u} = (0, v)$ is the speed of movement of the core; q is the specific power of the heat source due to the induction heating of the core by the induced currents. It was defined as

$$q = \frac{\dot{J}\dot{J}^*}{\sigma} = \omega^2\sigma(\dot{A}_\varphi\cdot\dot{A}_\varphi^*)\,, \quad (5)$$

where $\dot{J} = -j\omega\sigma\dot{A}_\varphi$ is the effective value of the induced current density; $\dot{A}_\varphi^*$ is the complex-conjugate magnitude of the magnetic vector potential.

The following were taken as boundary conditions for the thermal problem:

- on the axis of symmetry $r = 0$ – symmetry condition;
- on the outer boundary of the calculation area, as well as on the inlet (in the direction of movement) boundary of the core, the temperature is equal to the ambient temperature $T = T_0$;
- only convective heat transfer was set at the outlet boundary of the core;
- at the boundaries of the inductor, the temperature was assumed to be constant and equal to 70 °C, which is due to the presence of water cooling of the inductor turns.

The differential equations for the electromagnetic field (1), (2) and the temperature field (4) taking into account the specified boundary conditions represented a coupled electro-thermal problem that was solved numerically by the Finite Element Method using the Comsol software package [31]. The temperature dependencies of the values $\rho(T)$, $C_p(T)$, $\lambda(T)$ for the aluminum core was set according to the data of the material library of this code.

Analysis of the results of the calculation of the electro-thermal problem. The following parameter values were used in the calculations. The dimensions of the calculation area are 4.5 × 0.2 m. The length of the inductor is 2 m, the inner diameter is 40 mm, the number of turns $N_i = 50$. The current in the inductor was chosen on the condition that the core temperature at the exit from the inductor is approximately equal to the annealing temperature for aluminum T_{an} = 400–430 °C, the current frequency in the inductor varied from 50 to 5000 Hz. The diameter of the core is 28 mm, the speed of its movement is $v = 0.5$ m/min. Ambient air temperature $T_0 = 20$ °C.

Isolines of the magnetic vector potential $\dot{A}(r, z)$ and the distribution of magnetic flux density $|\dot{\boldsymbol{B}}|$ in the calculation area at current frequency of 50 Hz are shown in Fig. 2,*a*. The magnetic field is concentrated in the skin layer,

which at frequency of 50 Hz is $\delta = \sqrt{1/(\pi f \mu_0 \sigma)} = 15$ mm. Hence, Joule losses were allocated almost throughout the entire volume of the core, which led to its uniform heating throughout the thickness.

The temperature distribution in the calculation area is shown in Fig. 2,*b*, and in Fig. 2,*c* – temperature distribution along the *z* axis on the axis of symmetry (lower curve) and on the surface of the core (upper curve) at current frequency of 50 Hz.

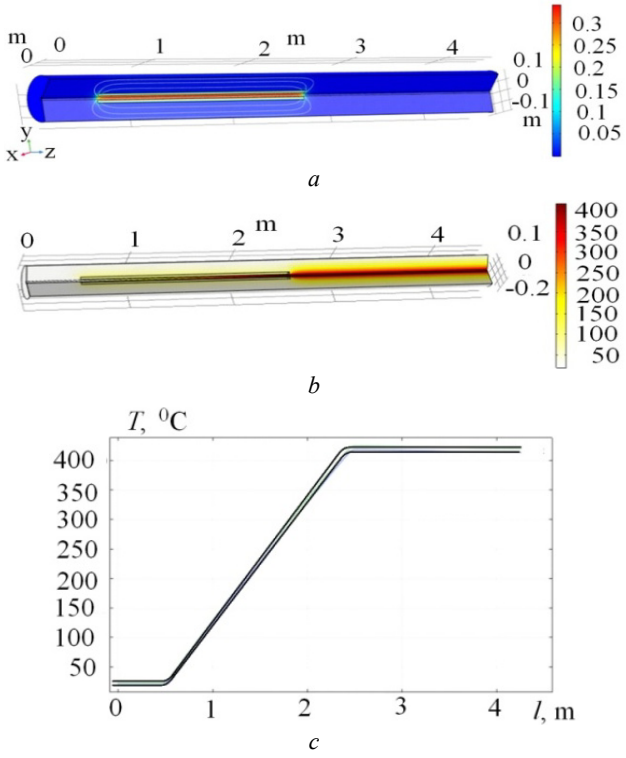

Fig. 2. Isolines of magnetic vector potential and distribution of magnetic flux density in the calculation area at current frequency of 50 Hz (*a*); temperature distribution in the calculation area (*b*); temperature distribution along the *z* axis on the axis of symmetry (lower curve) and on the surface of the core (upper curve) at current frequency of 50 Hz (*c*)

As can be seen from the results of the calculation, the temperature is regularly distributed along the depth of the core due to the small diameter of the core. Also, the temperature increases in the section «input – output from the inductor» according to a linear law, reaching the required annealing temperature 420 °C at the output.

The spatial distribution of the temperature at the output of the inductor is shown on a larger scale in Fig. 3. It should be noted that after leaving the inductor zone, the temperature distribution along the depth of the core does not become more uniform due to the cooling of the surface areas of the core.

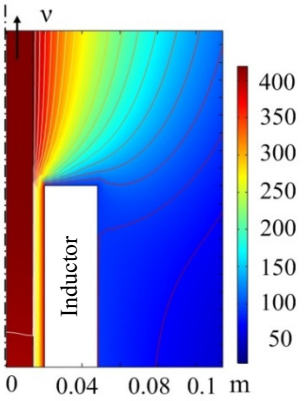

Fig. 3. Temperature distribution at the output from the inductor

To quantify the degree of irregular heating of the core along its depth, we can use the coefficient of temperature irregularity:

$$k_T = \frac{(T_{\max} - T_{\min})}{0{,}5(T_{\max} + T_{\min})} 100 \,, \qquad (6)$$

where $T_{\max}$, $T_{\min}$ are, respectively, the maximum and minimum temperature in the radial section of the core at the exit from the inductor. For the studied case according to Fig. 2,*c*, the value of $k_T = 1.6$ %.

Electromagnetic problem at the level of an elementary cell – at the micro level. The electro-thermal problem discussed above does not allow for a detailed analysis of electromagnetic processes in the inductor due to its relatively large length – the length/diameter ratio is 50. For such an analysis, an additional problem at the level of the elementary cell was further considered.

Figure 4 shows the structure of the inductor, which consists of massive copper coils made of a copper tube, which are cooled by a liquid pumped in this tube. Due to the long length of the inductor and the presence of a significant number of turns in its structure, an elementary cell was isolated, which included one turn of the inductor and a fragment of a core located near this turn (it is shown in Fig. 4 by a dotted line).

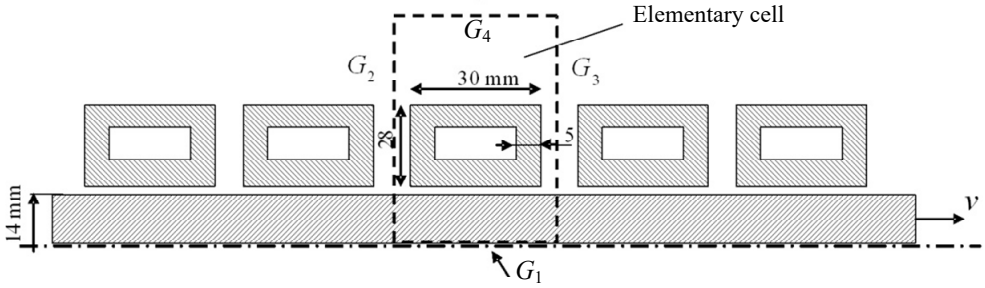

Fig. 4. Structure of a multi-turn inductor with a selected elementary cell

At the same time, it was assumed that the entire structure of the problem can be obtained by periodically repeating this cell along the *z* axis, and the total number of such cells is equal to the number of turns of the inductor N_i. Here, the action of the end effects in the inductor was not taken into account, however, with its long length,

these effects have a weak influence on the integral characteristics, and accordingly on the final value of the core temperature at the output of the inductor.

The dimensions of the inductor turns adopted in the calculations are shown in Fig. 4. It was assumed that all turns of the inductor are connected in series, and also that the core temperature in the cell region was equal to the average core temperature along its length of 220 °C.

Mathematical model of the electromagnetic problem in the area of the elementary cell in the approximation that the wire is stationary (the approximation of a small value of the magnetic Reynolds number) and assuming the validity of the axisymmetrical formulation has the following form:

- in the are of the core –

$$j\omega\sigma(T)\dot{A}_\varphi + \mu_0^{-1}\nabla\times(\nabla\times\dot{A}_\varphi) = 0\,; \tag{7}$$

- in the area of the inductor turn –

$$\begin{cases} j\omega\sigma\dot{A}_\varphi + \mu_0^{-1}\nabla\times(\nabla\times\dot{A}_\varphi) = \sigma\dfrac{\dot{U}_{turn}}{2\pi r}; \\ \displaystyle\int_{S_{\text{turn}}}\dot{J}dS = \dot{I}_{\text{turn}}, \quad \dot{J} = \sigma\left(\frac{\dot{U}_{turn}}{2\pi r} - j\omega\dot{A}_\varphi\right); \end{cases} \tag{8}$$

- in air –

$$\mu_0^{-1}\nabla\times(\nabla\times\dot{A}_\varphi) = 0\,, \tag{9}$$

where $\dot{U}_{turn}$ is the unknown voltage in the cross-section of the coil, which is calculated together with the magnetic vector potential $\dot{A}$ at given value of the electric current in the coil $\dot{I}_{turn}$. Since all turns of the inductor are connected in series, this current is equal to the current of the inductor $\dot{I}_i$, which is considered set.

The following boundary conditions were set for the electromagnetic problem (7)–(9): the symmetry condition with respect to the axis $r = 0$ at the boundary G_1 (see Fig. 4), the condition of even symmetry at the lateral boundaries G_2, G_3, and the condition of magnetic insulation at the outer boundary $G_4 - \dot{A}_\varphi|_{G_4} = 0$.

Figure 5 shows the distribution of the magnetic field $|\boldsymbol{B}|$, T (left) and the electric current density $|\boldsymbol{J}|$, A/m^2 (right) calculated in the Comsol code, in the cross-section of the elementary cell at different electric current frequency *f*. The current in the inductor coil was assumed to be 1 A.

The following effects can be seen from the presented figures:

- skin effect, when the magnetic field and electric current are displaced onto the surface of the conductor;
- proximity effect, when the presence of neighboring turns reduces the current on the side faces of the turn belonging to the cell;
- geometric effect, when due to the cylindrical structure of the coil, the electric current increases on its inner surface and decreases on its outer surface. Figure 5 shows how the manifestation of these effects increases with increasing frequency.

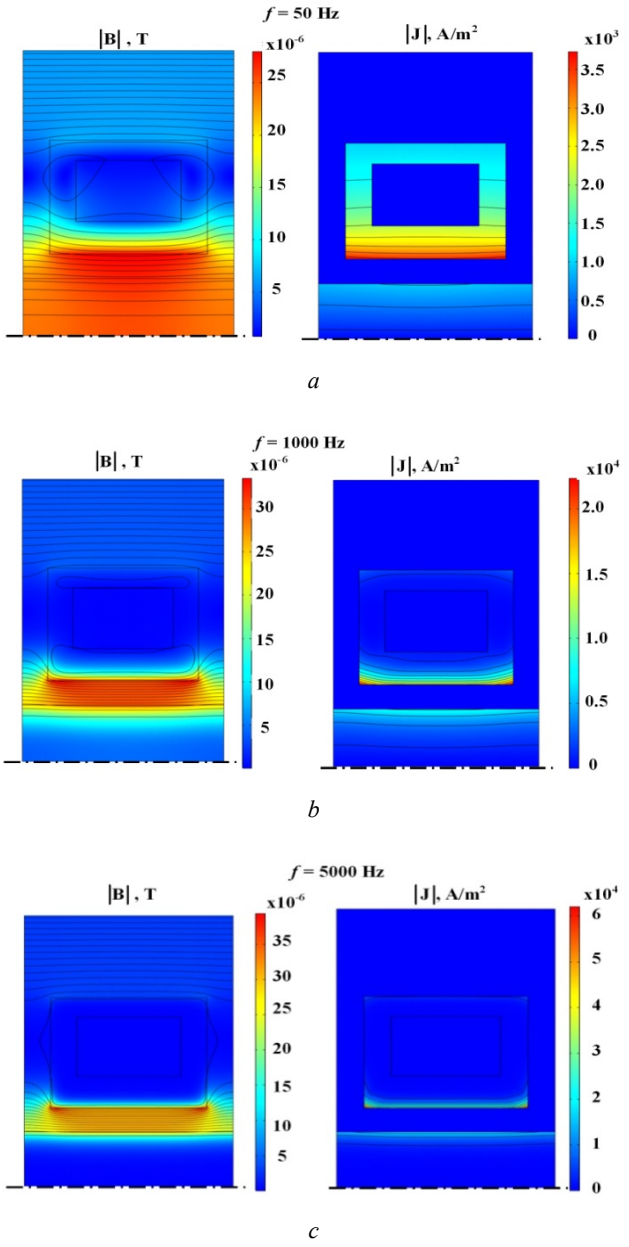

Fig. 5. Distributions of magnetic field (left) and density of electric current (right) in a cross-section of an elementary cells at the frequency of electric current: 50 Hz (*a*); 1000 Hz (*b*); 5000 Hz (*c*)

The distribution of the magnetic field in the inductor of a long length, which is studied in this problem, can be obtained by periodically repeating the pattern of the magnetic field for the cell – such patterns are shown in Fig. 6 for three values of the frequency of the power source. Note that this distribution will be valid for the internal areas of the inductor and will differ from the distribution in its end zones. But the use of such an approach, based on the calculation of the elementary cell field, allows to significantly simplify the problem of calculating the electromagnetic processes of long inductors, which is used in the task of induction heating of a power cable core.

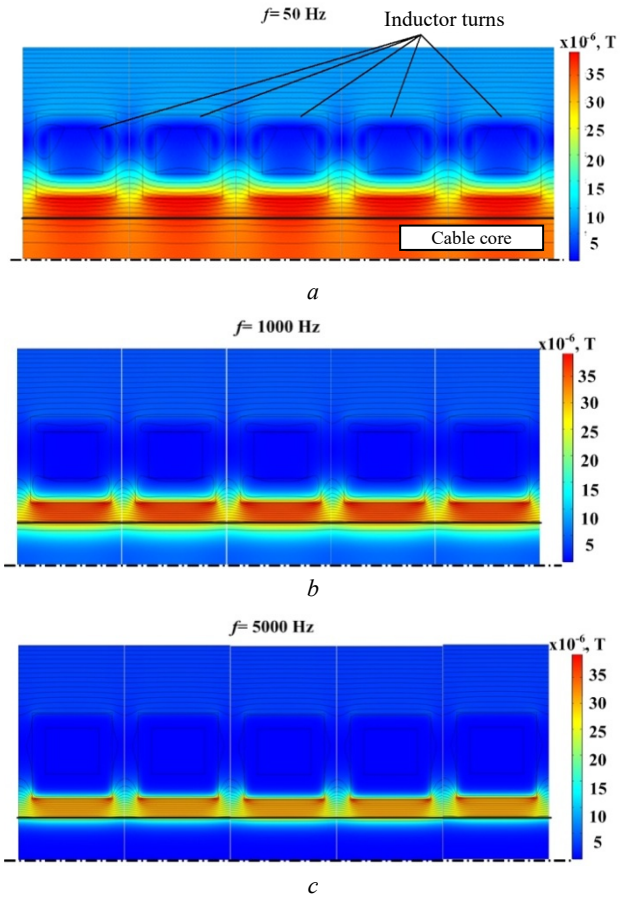

Fig. 6. Magnetic field distributions in inductor of large length at the frequency of electric current: 50 Hz (*a*); 1000 Hz (*b*); 5000 Hz (*c*)

Calculation of equivalent electrical parameters of one turn and multi-turn inductor as a whole. According to the results of the calculation of the electromagnetic field in the area of the elementary cell, the equivalent electrical parameters of one turn of the inductor as an element of this cell should be calculated depending on the frequency of the electric current. Here, the work uses a sequential replacing circuit of the turn (Fig. 7,*a*) and the multi-turn inductor as a whole (Fig. 7,*b*).

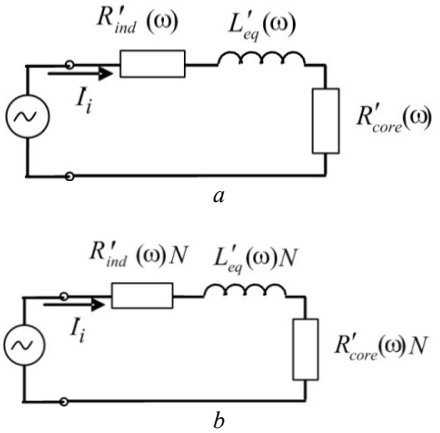

Fig. 7. Serial replacement circuits of: one turn (*a*); multi-turn inductor as a whole (*b*)

The replacing circuit of the multi-turn inductor with the number of turns N_i has the same structure as the circuit for the cell in Fig. 7,*a*, only the values of all parameters are multiplied by this number of turns N_i (Fig. 7,*b*).

These circuits contain the active resistance of the coil $R'_{ind}(\omega)$, the active resistance of the core fragment $R'_{core}(\omega)$ and the equivalent inductance $L'_{eq}(\omega)$, where $\omega = 2\pi f$ is the angular frequency of the electric current. Marking these elements with a dash means that they belong to one turn of the inductor.

The following expressions were used to calculate the frequency dependencies of these parameters:

$$R'_{ind}(\omega) = \frac{1}{I_i^2} \int\limits_{S_{turn}} \frac{\dot{J}\dot{J}^*}{\sigma} 2\pi r \mathrm{d}S\,, \tag{10}$$

$$R'_{core}(\omega) = \frac{1}{I_i^2} \int\limits_{S_{core}} \frac{\dot{J}\dot{J}^*}{\sigma} 2\pi r \mathrm{d}S\,, \tag{11}$$

$$L'_{eq}(\omega) = \frac{1}{I_i^2} \int\limits_{S_{cell}} \dot{B}\dot{H}^* 2\pi r \mathrm{d}S\,, \tag{12}$$

where S_{turn}, S_{core}, S_{cell} are, respectively, the surface of the turn, core and elementary cell.

Figure 8 shows the calculated frequency dependencies of these elementary cell parameters. The following can be concluded from them.

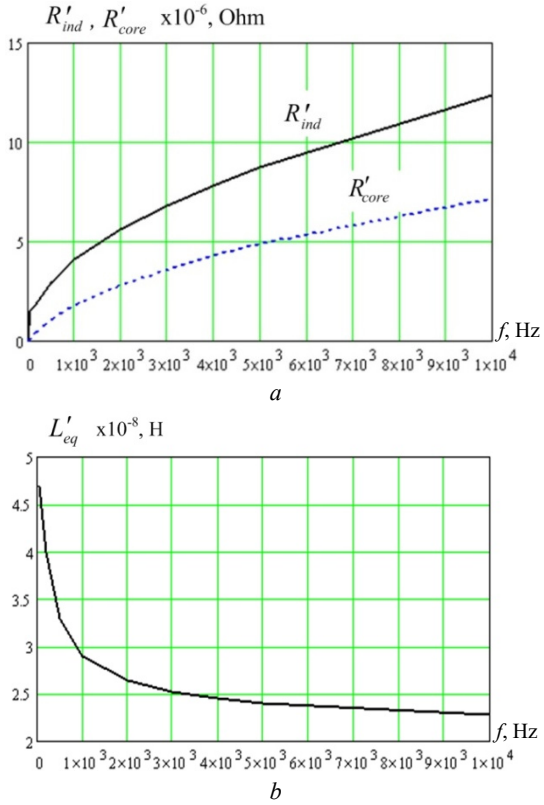

Fig. 8. Frequency dependencies of the parameters of the elementary cell: the active resistance of the turn $R'_{ind}(\omega)$ and the core fragment $R'_{core}(\omega)$ (*a*); the equivalent inductance $L'_{eq}(\omega)$ (*b*)

The equivalent resistance of the core at low frequency (< 50 Hz) approaches a small (zero) value, while the resistance of the winding $R'_{ind}(\omega)$ approaches the resistance at direct current.

Both resistances increase with increasing frequency and allow to calculate the electrical efficiency of the inductor as the ratio of losses in the core to the total losses – in the core and in the inductor.

The equivalent inductance of the cell decreases with the greatest speed in the frequency range of 50 Hz – 1000 Hz, when the magnetic field is intensively displaced into the air gap.

At higher frequencies, the inductance is caused mainly by the magnetic field in this gap and its decrease is significantly slowed down.

The use of the multi-turn inductor replacement circuit (Fig. 7,*b*) allows, using the electrical circuit for the high-frequency power source, to calculate the electrical processes in the installation for induction heating of the core at different power source frequencies.

Knowing the dependence of the equivalent active resistances of the turn and core on the frequency, it is possible to calculate the electrical efficiency of the inductor using the expression

$$\eta_i(\omega) = \frac{R'_{core}(\omega)}{R'_{core}(\omega) + R'_{ind}(\omega)}. \qquad (13)$$

The results of calculating the efficiency of the inductor as a function of the frequency of the power source obtained using the calculated active resistances shown in Fig. 8 are presented in Fig. 9 with a solid curve.

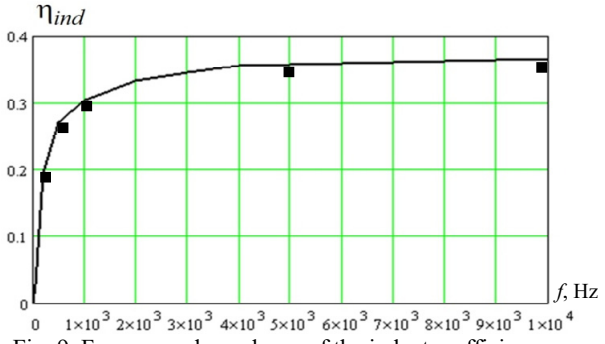

Fig. 9. Frequency dependence of the inductor efficiency as a result of the calculation for the elementary cell (solid curve) and for the inductor as a whole (marks ■)

It can be seen from this figure that the efficiency of heating the core at the power frequency is quite low, the electrical efficiency is equal to $\eta_{ind} = 0.028$. The optimal value of the frequency is 1–2 kHz and at the same time the electrical efficiency is $\eta_{ind} = 0.3$–0.33, respectively.

Although the electrical efficiency increases slightly with further frequency increase, losses in the semiconductor elements of the power source also increase, and therefore recommendations for increasing the frequency $f > 2000$ Hz require additional research.

The results of the calculation of the temperature field in the core at the optimal frequency of 1000 Hz show a uniform temperature distribution along the depth of the core at the exit from the inductor – the coefficient of temperature irregularity $k_T = 2$ %.

To verify the proposed computer model, built on the basis of the multi-scale modeling method, a 2D calculation of the electromagnetic problem was carried out for the entire calculation area, which includes a multi-turn inductor with massive turns, an aluminum core and an air region in a generally accepted way. The resulting distribution of the lines of force of the magnetic field in the calculation area for current frequency of 1000 Hz is shown in Fig. 10.

Fig. 10. Distribution of lines of force of the magnetic field in the cross-section of a multi-turn inductor at frequency of 1000 Hz

According to the results of the calculation, the total losses in the inductor and in the core were determined, and on their basis the electrical efficiency of the inductor $\eta_i(\omega)$ was calculated. The results of these calculations are shown in Fig. 9 with marks ■. A comparison of the results of calculations obtained using the elementary cell (solid curve) and when considering the inductor as a whole (shown by the mark ■) demonstrates the consistency of these results. At the same time, in order for calculation using the generally accepted method of the problem, the results of which are presented in Fig. 10, much more computer resources are required, and this is a feature of the calculation of relatively long inductors used in the technological processes of manufacturing current-conducting cores of power cables.

Table 1 shows the results of an experimental study of the characteristics of aluminum wire used at YUZHCABLE WORKS, PJSC in the manufacture of a conductive core, before and after the annealing process, realized by heating with electrodes in a special chamber with further exposure in a thermostat.

Table 1

Results of an experimental study of the characteristics of aluminum wire

Material – an aluminum core	Tear resistance, N/m^2	Relative elongation, %	Specific electrical resistance at 20 °C, Ω·m
Before annealing	177,9	2,0	$2{,}80 \cdot 10^{-4}$
After annealing	87,6	38	$2{,}77 \cdot 10^{-4}$

Increasing the plasticity of the aluminum core of power cables makes it possible to significantly speed up work on the restoration of PTLs of Ukraine in the war and post-war periods with the use of undamaged cable channels and trays and to increase the reliability of power supply systems of domestic critical infrastructure facilities.

Increasing the specific electrical conductivity of the aluminum core of cables additionally allows either to reduce its cross-section, and accordingly the volume of all active materials in the construction of power cables, or to additionally increase the reliability of power supply systems.

The results obtained in the article substantiate the expediency of creating an experimental model of the installation of high-frequency (1–2 kHz) induction heat treatment of the aluminum core of power cables at voltages up to 110 kV in order to clarify the technological and economic indicators of such heat treatment, in particular, when it is used in industrial lines of continuous application of modern three-layer cross-linked polyethylene insulation on the movable aluminum core of cables, which is serially manufactured by YUZHCABLE WORKS, PJSC, Kharkiv, Ukraine.

Conclusions.

Mathematical and computer models were developed for the analysis of electro-thermal processes in the installation of induction heating of the aluminum core of the power cable to implement the technological process of annealing this core. Taking into account the design features of the inductor for the implementation of such a process (in particular, the long length of the inductor and a significant number of its massive turns), the method of multi-scale modeling was used in the work.

Here, electro-thermal processes in the core were studied at the macro level, and at the micro level (that is, at the level of an elementary cell containing only one inductor turn and a core fragment) the distribution of the electromagnetic field and electric current density in the cross-section of the massive copper turn of the inductor was calculated, taking into account the features of its design. At both levels, the numerical Finite Element Method, implemented in the Comsol computer code, was used in the work.

According to the results of the calculation of the electromagnetic field at the level of the elementary cell, the frequency dependencies of the equivalent R, L parameters of the inductor were obtained, taking into account the skin effect, the proximity effect, and the geometric effect, and the quantitative influence of the electric current frequency on these effects was investigated.

The dependence of the electrical efficiency of the inductor on the frequency of the power source was obtained.

The analysis of the obtained numerical results showed that during the induction heat treatment of a movable aluminum core with diameter of 28 mm and the flow of currents in the inductor with frequency of up to 2 kHz, the efficiency of the heat treatment processes can exceed 30 % and temperature modes sufficient for annealing such a core without the use of a thermal insulation chamber can be realized.

To verify the proposed computer model, built on the basis of the multi-scale modeling method, a 2D calculation of the electromagnetic problem was carried out for the entire calculation area, which includes a multi-turn inductor with massive turns, an aluminum core and the surrounding air region in a generally accepted way. Comparison of the results of the calculations shows the consistency of the obtained results. At the same time, much more computer resources are needed to calculate the problem in a generally accepted way.

The obtained results substantiate the expediency of creating an experimental model of the installation of high-frequency (1–2 kHz) induction thermal annealing of the aluminum core of power cables to clarify the technological and economic indicators of its use in industrial lines of continuous application of modern three-layer cross-linked polyethylene insulation on the moving aluminum core of cables at voltage of up to 110 kV, which are mass-produced by YUZHCABLE WORKS, PJSC, Kharkiv, Ukraine.

Conflict of interest. The authors of the article declare that there is no conflict of interest.

REFERENCES

1. Kyrylenko O.V., Zhuikov V.Y., Denysiuk S.P. Use of dynamic tarification for optimization microgrid technical and economic indicators in local electricity markets. *Technical Electrodynamics*, 2022, no. 3, pp. 37-48. (Ukr). doi: https://doi.org/10.15407/techned2022.03.037.

2. Lezama F., Soares J., Hernandez-Leal P., Kaisers M., Pinto T., Vale Z. Local Energy Markets: Paving the Path Toward Fully Transactive Energy Systems. *IEEE Transactions on Power Systems*, 2019, vol. 34, no. 5, pp. 4081-4088. doi: https://doi.org/10.1109/TPWRS.2018.2833959.

3. Sinha A., Basu A.K., Lahiri R.N., Chowdhury S., Chowdhury S.P., Crossley P.A. Setting of Market Clearing Price (MCP) in Microgrid Power Scenario. *2008 IEEE Power and Energy Society General Meeting - Conversion and Delivery of Electrical Energy in the 21st Century*, 2008, pp. 1-8. doi: https://doi.org/10.1109/PES.2008.4596357.

4. Hirsch A., Parag Y., Guerrero J. Microgrids: A review of technologies, key drivers, and outstanding issues. *Renewable and Sustainable Energy Reviews*, 2018, vol. 90, pp. 402-411. doi: https://doi.org/10.1016/j.rser.2018.03.040.

5. Zolotarev V.M., Shcherba A.A., Karpushenko V.P., Peretiatko Yu.V., Zolotarev V.V., Oboznyi A.L. *Recommendations for the selection of characteristics, designs and application of self-carrying insulated wires produced by PJSC YUZHCABLE WORKS for overhead power lines of increased reliability and safety.* Kharkiv, Maidan Publ., 2008. 62 p. (Ukr).

6. Peschke E., Olshausen R. *Cable Systems for High and Extra-High Voltage*. MCD Verlag, 1999. 296 p.

7. Shydlovsky A.K., Shcherba A.A., Zolotariov V.M., Podoltsev A.D., Kucheriavaia I.N. *Polymer insulated cables for extra high voltage.* Kyiv, Institute of Electrodynamics National Academy of Sciences of Ukraine Publ., 2013. 550 p. (Rus).

8. Bezprozvannych G.V., Pushkar O.A. Increasing noise immunity of cables for fire protection systems. *Electrical Engineering & Electromechanics*, 2020, no. 4, pp. 54-58. doi: https://doi.org/10.20998/2074-272X.2020.4.07.

9. Kyrylenko O.V., Blinov I.V., Parus E.V., Trach I.V. Evaluation of efficiency of use of energy storage system in electric networks. *Technical Electrodynamics*, 2021, no. 4, pp. 44-54. (Ukr). doi: https://doi.org/10.15407/techned2021.04.044.

10. Nijman E., Buchegger B., Böhler E., Rejlek J. Experimental Characterization and Dynamic Modelling of Electrical Cables. *SAE International Journal of Advances and Current Practices in Mobility*, 2023, vol. 5, no. 2, pp. 888-896. doi: https://doi.org/10.4271/2022-01-0952.

11. Baranov M.I., Rudakov S.V. Electrothermal Action of the Pulse of the Current of a Short Artificial-Lightning Stroke on Test Specimens of Wires and Cables of Electric Power Objects. *Journal of Engineering Physics and Thermophysics*, 2018, vol. 91, no. 2, pp. 544-555. doi: https://doi.org/10.1007/s10891-018-1775-2.

12. Shazly J.H., Mostafa M.A., Ibrahim D.K., Abo El Zahab E.E. Thermal analysis of high-voltage cables with several types of insulation for different configurations in the presence of harmonics. *IET Generation, Transmission & Distribution*, 2017, vol. 11, no. 14, pp. 3439-3448. doi: https://doi.org/10.1049/iet-gtd.2016.0862.

13. Shcherba A.A., Suprunovska N.I. Electric energy loss at energy exchange between capacitors as function of their initial voltages and capacitances ratio. *Technical Electrodynamics*, 2016, no. 3, pp. 9-11. doi: https://doi.org/10.15407/techned2016.03.009.

14. Beletsky O.A., Suprunovska N.I., Shcherba A.A. Dependences of power characteristics of circuit at charge of supercapacitors. *Technical Electrodynamics*, 2016, no. 1, pp. 3-10. (Ukr). doi: https://doi.org/10.15407/techned2016.01.003.

15. Ochin P., Gilchuk A.V., Monastyrsky G.E., Koval Y., Shcherba A.A., Zaharchenko S.N. Martensitic Transformation in Spark Plasma Sintered Compacts of Ni-Mn-Ga Powders

Prepared by Spark Erosion Method in Cryogenic Liquids. *Materials Science Forum*, 2013, vol. 738-739, pp. 451-455. doi: https://doi.org/10.4028/www.scientific.net/MSF.738-739.451.
16. Vinnychenko D.V. Influence of electrical parameters of high-voltage electric-discharge systems for synthesis of nanocarbon on their performance and specific power inputs. *Technical Electrodynamics*, 2016, no. 4, pp. 95-97. (Ukr). doi: https://doi.org/10.15407/techned2016.04.095.
17. Ametani A., Xue H., Ohno T., Khalilhezhad H. *Electromagnetic Transients in Large HV Cable Networks: Modeling and calculations*. The Institute of Engineering Technology, 2021. 591 p. doi: https://doi.org/10.1049/PBPO204E.
18. Mokhort A.V., Chumak M.G. *Thermal processing of metals*. Kyiv, Lybid Publ., 2002. 512 p. (Ukr)
19. Rudnev V., Loveless D., Cook R. *Handbook of induction heating.* Boca Raton, CRS Press, 2017. 776 p. doi: https://doi.org/10.1201/9781315117485.
20. Sharma G.K., Pant P., Jain P.K., Kankar P.K., Tandon P. Numerical and experimental analysis of heat transfer in inductive conduction based wire metal deposition process. *Proceedings of the Institution of Mechanical Engineers, Part C: Journal of Mechanical Engineering Science*, 2022, vol. 236, no. 5, pp. 2395-2407. doi: https://doi.org/10.1177/09544062211028267.
21. Bao L., Wang B., You X., Li H., Gu Y., Liu W. Numerical and experimental research on localized induction heating process for hot stamping steel sheets. *International Journal of Heat and Mass Transfer*, 2020, vol. 151, art. no. 119422. doi: https://doi.org/10.1016/j.ijheatmasstransfer.2020.119422.
22. Mortimer J., Rudnev V., Clowes D., Shaw B. Intricacies of Induction Heating of Wires, Rods, Ropes & Cables. *Wire Forming Technology International*, Winter 2019, pp. 46-50.
23. Lope I., Acero J., Carretero C. Analysis and Optimization of the Efficiency of Induction Heating Applications With Litz-Wire Planar and Solenoidal Coils. *IEEE Transactions on Power Electronics*, 2016, vol. 31, no. 7, pp. 5089-5101. doi: https://doi.org/10.1109/TPEL.2015.2478075.
24. Fisk M., Ristinmaa M., Hultkrantz A., Lindgren L.-E. Coupled electromagnetic-thermal solution strategy for induction heating of ferromagnetic materials. *Applied Mathematical Modelling*, 2022, vol. 111, pp. 818-835. doi: https://doi.org/10.1016/j.apm.2022.07.009.
25. Siesing L., Frogner K., Cedell T., Andersson M. Investigation of Thermal Losses in a Soft Magnetic Composite Using Multiphysics Modelling and Coupled Material Properties in an Induction Heating Cell. *Journal of Electromagnetic Analysis and Applications*, 2016, vol. 08, no. 09, pp. 182-196. doi: https://doi.org/10.4236/jemaa.2016.89018.
26. Amarulloh A., Haikal H., Atmoko N.T., Utomo B.R., Setiadhi D., Marchant D., Zhu X., Riyadi T.W.B. Effect of power and diameter on temperature and frequency in induction heating process of AISI 4140 steel. *Mechanical Engineering for Society and Industry*, 2022, vol. 2, no. 1, pp. 26-34. doi: https://doi.org/10.31603/mesi.6782.
27. Shang F., Sekiya E., Nakayama Y. Application of High-Frequency Induction Heating Apparatus to Heat Treatment of 6061 Aluminum Alloy. *Materials Transactions*, 2011, vol. 52, no. 11, pp. 2052-2060. doi: https://doi.org/10.2320/matertrans.L-M2011825.
28. Podoltsev A.D., Kucheriavaia I.N. *Multiscale modeling in electrical engineering.* Kyiv, Institute of Electrodynamics National Academy of Sciences of Ukraine Publ., 2011. 255 p. (Rus).
29. Kovachki N., Liu B., Sun X., Zhou H., Bhattacharya K., Ortiz M., Stuart A. Multiscale modeling of materials: Computing, data science, uncertainty and goal-oriented optimization. *Mechanics of Materials*, 2022, vol. 165, art. no. 104156. doi: https://doi.org/10.1016/j.mechmat.2021.104156.
30. Ryu C.J., Kudeki E., Na D.-Y., Roth T.E., Chew W.C. Fourier Transform, Dirac Commutator, Energy Conservation, and Correspondence Principle for Electrical Engineers. *IEEE Journal on Multiscale and Multiphysics Computational Techniques*, 2022, vol. 7, pp. 69-83. doi: https://doi.org/10.1109/JMMCT.2022.3148215.
31. Available at: https://www.comsol.com (accessed 22 March 2023).

Received 11.04.2023
Accepted 29.06.2023
Published 02.01.2024

A.A. Shcherba[1], *Corresponding Member of the National Academy of Sciences of Ukraine, Doctor of Technical Science,*
O.D. Podoltsev[1], *Doctor of Technical Science*, *Chief Researcher,*
N.I. Suprunovska[1], *Doctor of Technical Science*, *Leading Researcher,*
R.V. Bilianin[2], *PhD*,
T.Yu. Antonets[2], *PhD*,
I.M. Masluchenko[3], *PhD*,
[1] Institute of Electrodynamics National Academy of Sciences of Ukraine,
56, Prospect Beresteiskyi, Kyiv-57, 03057, Ukraine,
e-mail: iednat1@gmail.com (Corresponding Author)
[2] YUZHCABLE WORKS, PJSC,
7, Avtogenna Str., Kharkiv, 61095, Ukraine.
[3] Scientific and Technical Center SE «NNEGC «Energoatom»,
22-24, Gogolivska Str., Kyiv, 01054, Ukraine.

How to cite this article:
Shcherba A.A., Podoltsev O.D., Suprunovska N.I., Bilianin R.V., Antonets T.Yu., Masluchenko I.M. Modeling and analysis of electro-thermal processes in installations for induction heat treatment of aluminum cores of power cables. *Electrical Engineering & Electromechanics*, 2024, no. 1, pp. 51-60. doi: https://doi.org/10.20998/2074-272X.2024.1.07

UDC 621.319 https://doi.org/10.20998/2074-272X.2024.1.08

G.V. Bezprozvannych, M.V. Grynyshyna, Y.S. Moskvitin

Requirements for cables as categories of construction products and thermal resistance of power cables

Introduction. *One of the main driving factors of the demand for cable and conductor products is the modern trend of urbanization, which leads to an increase in cities with significantly increased requirements for electrical networks of transportation and distribution of electrical energy. This requires the development of appropriate infrastructure with significant demand for electricity in the commercial, industrial and residential sectors. The construction industry uses a wide range of cables with an appropriate set of electrical and mechanical properties, resistance to the influence of external climatic factors, and, first of all, must meet fire safety requirements. Increasing construction activity is stimulating the market for fire-resistant cables in the construction industry. According to the Construction Products Regulation, power, telecommunication cables, data cables, control and management, fiber optic refer to construction products in the EU member states. These cables are intended for the supply of electrical energy and communication, which are permanently installed in buildings and other engineering structures. Power, telecommunications, data and control cables are considered construction products, and are the only electrical products classified as construction. Over the next 15 years, Eastern Europe is expected to see increased growth in the construction industry, as the end of the war in Ukraine requires nearly $1 trillion in reconstruction. A strategic task in the reconstruction of the country is the use of cable and conductor products with increased operational properties, including in the construction industry. Significant efforts and investments in innovation and certification of cable and conductor products require manufacturers to create construction products of the «Power, control and communication cables» category with a high level of fire safety in accordance with the Euroclassification of cables in terms of reaction to fire depending on the level of safety.* ***Purpose.*** *Analysis of fire safety requirements for cables as a category of construction products and determination of thermal resistance of power cables based on experimental thermal studies of modern electrical insulating compositions.* ***Methodology.*** *The thermal stability of power cables with a voltage of 0,66/1 kV was determined, depending on the design, based on the conducted experimental studies of the thermal stability of electrical insulation materials, between the core filling and the polymer sheath, removed from the cable samples. On the basis of the conducted correlation analysis between thermal resistance and fire load, which are important parameters for confirming the quality and safety of the entire cable, it has been proven that the efficiency of halogen-free compositions to meet fire safety requirements increases with the increase in the cross-section and number of cores in the cable.* ***Practical value****. Determining the heat load and fire resistance of cables of various designs and areas of application based on the obtained experimental data on the heat of combustion of polymer cable materials is necessary and justified at the stage of mastering and determining the prospects for the production of cables with modern halogen-free electrical insulation compositions in accordance with fire safety requirements.* References 40, figures 6.

Key words: **urbanization, construction industry, cable infrastructure, fire safety, cable classification criteria, halogen-free compositions, power cables, thermal resistance, fire load, certified test base.**

Проаналізовано світові тенденції урбанізації та їх вплив на розвиток кабельної індустрії. Представлено основні тренди розвитку будівельної галузі як рушійної сили сегменту вогнестійких та пожежобезпечних кабелів для забезпечення сучасної силової та інформаційної інфраструктури. Акцентовано на темпах застосування пожежобезпечних кабелів з низьким вмістом диму та безгалогенними композиціями у Європі. Зазначено, що для забезпечення жорстких вимог щодо пожежної безпеки кабельної інфраструктури у будівельному секторі введено узагальнену категорію «Силові, контрольні кабелі та кабелі зв'язку». Представлено класифікацію кабелів за пожежною ознакою відповідно до Регламенту будівельної продукції Європейського Союзу. Наведено критерії класифікації та методи випробувань для визначення вогнестійких характеристик кабелів відповідно до кількості випромінюваного тепла. Визначено теплову стійкість та пожежне навантаження в залежності від застосованих композитних полімерних галогеновмісткіх та безгалогенних композицій і конструктивного виконання силових кабелів низької напруги. Підтверджено ефективність безгалогенних композицій для забезпечення вимог щодо пожежобезпеки для кабелів з більшим діаметром струмопровідної жили та кількістю жил. Наголошено на необхідності створення відповідної сучасної сертифікованої випробувальної бази для визначення пожежної стійкості будівельної продукції категорії «Силові, контрольні кабелі та кабелі зв'язку». Бібл. 40, рис. 6.

Ключові слова: **урбанізація, будівельна промисловість, кабельна інфраструктура, пожежна безпека, критерії класифікації кабелів, безгалогенні композиції, силові кабелі, теплова стійкість, пожежне навантаження, сертифікована випробувальна база**.

Introduction. Three main sectors are crucial for the development of the cable industry: electric power, transport and construction. Investments in these sectors have a direct impact on the demand for cables and wires. The size of the global wire and cable market in 2022 was estimated at USD 202.05 billion. It is predicted that from 2023 to 2030 it will grow by an average of 4.2 % [1-3]. One of the main driving factors in this case is the modern trend of urbanization, which leads to the increase of cities with significantly increased requirements for electrical networks of transportation and distribution of electrical energy. This requires the development of appropriate infrastructure with significant demand for electricity in the commercial, industrial and residential sectors. Increased investments in the intelligent modernization of power transmission and distribution systems and the development of smart networks will contribute to the growth of the cable and conductor products market. So, in particular, the introduction of intelligent network technology satisfies the growing need for system-forming network connections, which leads to an increase in

investments in highly efficient power underground and underwater cables of high and ultra-high voltage, including direct current [1].

According to the UN, about 60 % of the world's population will live in cities by 2030, and 68 % by 2050, which will lead not only to new network needs, but also to the renewal of aging infrastructure. Trends towards greener solutions in the transmission of electrical energy, such as e-mobility (digital), also create additional opportunities for the cable industry. In particular, renewable energy is a sector in which the demand for cable products is growing significantly. Investments in renewable energy sources contribute to growth in the segment of demand for medium voltage power cables [1, 2]. Innovations can significantly change distribution networks: cable technologies offer real solutions that turn the distribution infrastructure into an active player, for example by using the data transmission potential of power cables with integrated optical fibers. The solutions, among other things, will allow monitoring and evaluation of the network, the activity of the Internet of Things [4, 5], as well as providing detailed information about the operation of the network.

According to the mentioned trend of urbanization, the construction segment is expected to grow at the highest rate: 4.8 % in the forecast period. Thanks to the reconstruction of old commercial, residential, industrial buildings and new construction, the market for cable and conductor products is predicted to grow worldwide. This growth is split fairly evenly between civil construction, as well as the non-residential (commercial) and residential construction segments, with the latter expected to have the highest level of investment. Rapid economic development and urbanization, especially in Southeast Asia, is contributing to significant growth in construction investment. In more mature markets, such as in Europe and North America, the dynamics of growth is slower: currently the level of urbanization in Asia is 50 %, in North America is 82 %, in Africa is 43 %. For example, according to Global Construction Perspectives and Oxford Economics (British economists) [6], by 2030 it is expected that the world construction production will increase by 85 % and reach USD 15.5 trillion: China, the US and India is the top three will contribute 57 % of growth. It is expected that the US construction market will grow faster than the Chinese one in the next 15 years [7]. Thus, the growing construction sector will contribute to the global growth of the wire and cable market.

In Europe, it is predicted that the best investment forecasts are related to civil engineering projects (roads, railways, airports and seaports). These are favorable structural trends to increase the growth rate of demand for signal interlock cables and control cables. Thus, construction products of the EU are estimated at approximately EUR 500 billion. In addition, construction is one of the main European industrial sectors: it accounts for 10 % of European GDP. This domain provides 20 million jobs for more than 3 million enterprises [8]. Such a huge business needs to be kept open by the internal market of construction products in accordance with national regulations. The construction industry uses a wide range of cables with an appropriate set of electrical and mechanical properties, resistance to the influence of external climatic factors, and, first of all, must meet fire safety requirements. According to forecasts, the construction segment is projected to be the largest segment in the fire resistant cable market. Increasing construction activity stimulates the market of fire-resistant cables in the construction industry [7]. In any case, the construction sector is a factor that stimulates the growth of the wire and cable market. Trade in construction products within the EU or the European Economic Area is regulated by European rules and regulations [9-11]. The construction industry covers all design and construction activities, regardless of whether it concerns the population and private buildings, transport infrastructure, utility networks, etc. According to the Construction Products Regulation (CPR), power, telecommunication cables, data cables, control and control cables, and fiber optic cables are considered construction products in EU member states. These cables are intended for the supply of electrical energy and communication, which are permanently installed in buildings and other engineering structures [12]. Power, telecommunications, data and control cables are considered construction products, and are the only electrical products classified as construction. Cables designed for connecting appliances or for internal wiring of equipment or electrical appliances, as well as all those cables not used as cables for construction, are not included in the category of construction products. The Construction Products Regulation in the EU is mandatory for cables since July 1, 2017 [12, 13].

Eastern Europe is expected [6] to see increased growth in the construction industry over the next 15 years, as the end of the war in Ukraine requires nearly USD 1 trillion in reconstruction. A strategic task in the reconstruction of the country is the use of cable and conductor products with increased operational properties, including in the construction industry.

The goal of this work is to analyze the fire safety requirements for cables as a category of construction products and to determine the thermal resistance of power cables based on experimental thermal studies of modern electrical insulating compositions.

Problem definition and analysis of literary sources. The Construction Products Regulation establishes the agreed rules for the marketing of construction products in the EU [12]. One of the rules is that manufacturers must provide information about the safety of their products: fire safety; security for users; noise protection. All cables that fall under the category of construction products, regardless of type, are affected only by safety characteristics in case of fire (resistance and reaction to fire) and hazardous substances (emissions and content). Other technical characteristics, including electrical and mechanical, are defined in the relevant standards on the cable [14, 15]. Given that cables provide the fundamental infrastructure of today's construction sector, the strict application of state-of-the-art fire safety requirements for such infrastructure is of paramount importance for safety and reliability. The fire response of construction products in the category «Power, control and

communication cables» is one of the most pressing problems in the cable industry at the moment.

Kilometers of cables laid inside the building must ensure its safety, especially during fires and emergency situations. High requirements for fire safety relate to resistance to the spread of burning when the cable is placed singly and when laid in a bundle (Fig. 1); low smoke and gas emission; low corrosive activity of gases released during cable combustion; fire resistance (preserving the performance of the cable under conditions of exposure to flame).

The fulfillment of fire safety requirements became possible thanks to a new class of materials – halogen-free compositions, which are flame-resistant polymer materials with low smoke and gas emissions that do not contain halogens [16-19]. The global market for cable polymer composites is expected to be valued at USD 13.9 billion in 2023, driven by the growing demand in the automotive, telecommunication, and construction industries [7, 10]. For the production of cables Europe accounted for 16.3 % of the global production of polymer materials in 2019 [8]. By the end of 2023, the use of fire safety cables with low smoke content and halogen-free compositions is expected to be more than 20 %. At the same time, the share of compounds based on polyvinyl chloride plasticate will decrease from 50 % to 35 % [8, 10].

a

b

Fig. 1. Fragments of the arrangement of cables in bundles inside (*a*) and on the roof of the building (*b*, cultural and entertainment center, private house, etc.)

In September 2020, the German international group HEXPOL Technologies launched a comprehensive portfolio of compounds for wires and cables based on high-performance materials, additives, advanced production technologies of organosilicon rubber and thermoplastic elastomers that meet the international cable standards IEC 60811 [20] and EN 50363 [21]. The unique fire safety characteristics of halogen-free compositions include low smoke emission, low toxicity and fire resistance and meet the requirements of RoHS (Restriction of Hazardous Substances – Directive 2002/95/EC, which limits the content of harmful substances, in particular, lead, mercury, cadmium,

The authors of [23] proved the expediency of using fire-resistant compositions for the manufacture of cable products, in which the maximum continuous temperature of the current-conducting core does not exceed 90 °C, and the maximum temperature under short-circuit conditions is 170 °C, and investigated the influence of alloying additives on the electrophysical properties of fire-resistant polymer compositions, which do not contain halogens.

The work [19] presents the composition of a halogen-free composition based on polyethylene with the introduction of flame retardants and other additives into the polymer matrix, which increase the resistance of the material to flame propagation, as well as better dispersion of fillers in the polymer. At the same time, it is emphasized that with an increase in the degree of filling of the polymer with flame retardants, its breaking strength, relative elongation, specific volumetric electrical resistance, and frost resistance decrease.

Cables are complex objects, as they consist of insulation and sheaths of polymeric materials of different chemical composition, thickness, and additives [17, 24].

Thus, on the basis of experimental studies, it was established that the characteristics of the used cable insulation material based on polyvinyl chloride plasticate (PVC) had a significant impact on the toxicity of exhaust gases. The most toxic gases are released during smoldering combustion of a cable with a plasticized PVC sheath [25].

The semi-real scale tests presented in [26] showed that the cable with polyvinyl chloride plasticate demonstrated high fire resistance properties related to heat release, smoke generation and flame propagation.

The complex fire-resistant properties of electric wires and cables are widely studied both theoretically and experimentally [17, 23, 25-27], regarding compliance with the criteria of the European classification of cables for fire safety [11], which indicates the importance of the problem.

Classification of cables by fire rating. The EU has created a single and uniform classification criterion throughout Europe to determine the fire-resistant characteristics of cables. The fire resistance classes of the cables were determined based on the classification criteria according to the amount of radiated heat in the presence of fire.

According to the effectiveness of fire propagation and heat release, 7 classes of cables are defined [28]: Aca, B1ca, B2ca, Cca, Dca, Eca, Fca (Fig. 2,*a*).

Class Aca – cables do not contribute to fire. Classes B1ca – B2ca – minimal contribution to fire. Classes Cca – Dca – Eca – combustible, contribute to fire (the contribution to the fire of cables of class E is higher than that of D). Class Fca – an undefined property contribution [29]. The classification stipulates that the manufacturer does not have requirements related to reaction to fire (the parameter «Indeterminate performance» (Euroclass) is indicated.

An additional classification concerns the release of smoke, burning drops and acidity indicators.

Smoke emission properties: s1, s1a, s1b, s2, s3 (Fig. 2,*b*). This classification provides information about the opacity of emitted smoke (s – smoke) [29]: s1 – small smoke formation and slow smoke spread; s1a – transmission coefficient of more than 80 %; s1b – transmission coefficient in the range from 80 % to 60 %; s2 – average formation and distribution of smoke; s3 – none of the above.

Burning drops/particles: d0, d1, d2 (Fig. 2,*c*). This classification provides information about the dripping of burning material during a fire (d – droplets) [29]: d0 – absence of combustible droplets or particles; d1 – absence of combustible drops or particles lasting more than 10 s; d2 – none of the above.

Acidity indicators: a1, a2, a3 (Fig. 2,*d*), for which the test described in the UNE-EN 50267-2-3 standard is additionally applied. This classification provides information on the release of acid gases under fire time (a – acidity): a1 – conductivity < 2.5 μS/mm and hydrogen pH > 4.3; a2 – conductivity < 10 μS/mm and pH > 4.3; a3 - none of the above.

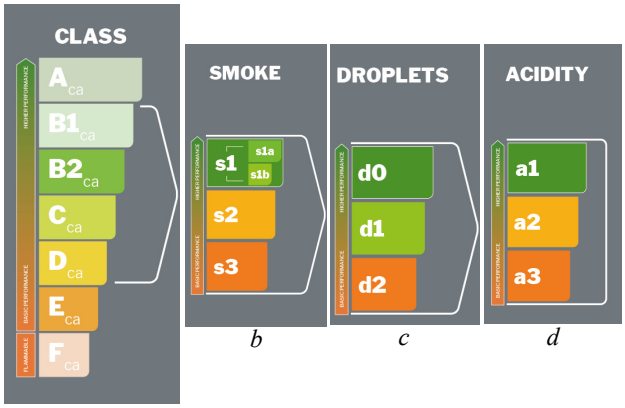

Fig. 2. Euroclassification of cables according to the category of construction products [12]

Class Aca cables are special cables with inorganic insulation tested according to [30] and must have a higher calorific potential (PCS – gross calorific potential) of less than 2 MJ/kg.

Class B1ca cables are tested according to [29] with a 30 kW flame source according to the classification criteria: flame spread FS ≤ 1.75 m, total heat release THR_{1200c} ≤ 10 MJ, peak heat release rate HRR ≤ 20 kW, higher calorific value FIGRA ≤ 120 W/s with additional classification for smoke emission, burning drops and acidity and [31] with flame spread H ≤ 425 mm.

Class B2ca cables are tested according to [29] with a 20.5 kW flame source according to classification criteria: flame spread FS ≤ 1.5 m and total heat release THR_{1200c} ≤ 15 MJ, peak heat release rate HRR ≤ 30 kW and higher calorific value FIGRA ≤ 150 W/s with additional classification for smoke emission, burning drops and acidity and [31] with flame spread H ≤ 425 mm.

Class Cca cables are tested according to [29] with a 20.5 kW flame source according to the classification criteria: flame spread FS ≤ 2 m and total heat release THR_{1200c} ≤ 30 MJ, peak heat release rate HRR ≤ 60 kW and higher calorific value FIGRA ≤ 300 W/s with additional classification by smoke emission, burning drops and acidity and [31] with flame spread H ≤ 425 mm.

Class Dca cables are tested according to [29] with a 20.5 kW flame source according to the classification criteria: total heat release THR_{1200c} ≤ 70 MJ, peak heat release rate HRR ≤ 60 kW and higher heating capacity FIGRA ≤ 300 W/s.

Class Eca cables are tested according to [31] with flame spread H ≤ 425 mm.

Class Fca cables are tested according to [31] with flame spread H > 425 mm.

The duration of the tests is 1-8 min with burner power of 1 kW with air convection [29], 20 min with burner power of 30 kW with a non-flammable shield [29] and 20 kW without a fire shield [29] with an air supply of 8000 l/min (Fig. 3).

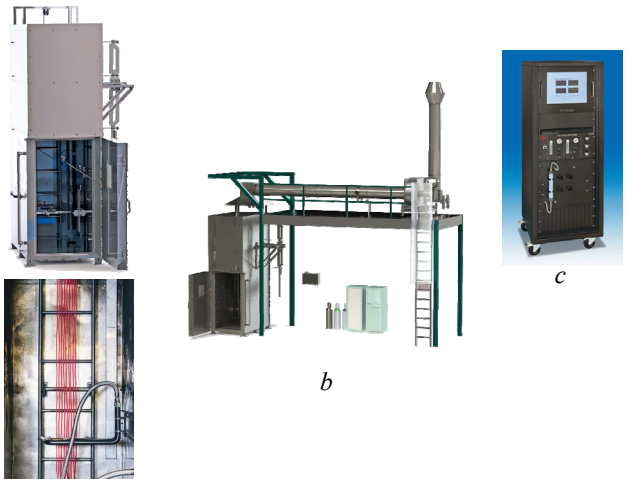

Fig. 3. Test chamber with burner and ladder with cable samples (*a*), test complex (*b*) (length 8.60 m, width 2.50 m, minimum height 4.10 m) and gas analyzer with software (*c*) [29]

Accordingly, [29] is central to cable classification tests as it combines heat release measurements (classes B1ca, B2ca, Cca, Dca), smoke penetration measurements (s1, s2, s3) and burning droplet evaluation (d0, d1, d2).

Each country has its own technical requirements and standards [32] for assessing and reducing the risk of fire consequences. High-quality cable infrastructure is a critical component of the construction industry and must meet fire safety requirements to ensure continuity of power and communication to all critical devices in the event of a fire. The performance of the cables itself during a fire is of crucial importance. The release of cables in the category of construction products requires an understanding by all involved parties of the importance of providing the construction industry of Ukraine with cable and conductor products by domestic manufacturers.

In accordance with the current building regulations of public buildings, it is necessary to take into account the established limit values for the accumulation of combustible materials located directly in public buildings, including cables and wires. There is a need to determine

the thermal resistance of cables and the amount of heat released during their burning, i.e. fire load.

Determination of thermal resistance and fire load of power cables with modern electrical insulating compositions. The cable business is largely focused on the use of modern polymer compositions with the appropriate set of physico-chemical, electrical and thermal properties with cable manufacturing technology adapted to their rheological indicators as a whole. The implementation of fire safety requirements is related to reaching a certain compromise between the level of requirements for fire safety indicators and the main electrical and physical-mechanical characteristics of cables [33-35]. Significant efforts and investments in innovation and certification of cable and conductor products require manufacturers to create construction products of the «Power, control and communication cables» category with a high level of fire safety in accordance with the euroclassification of cables in terms of reaction to fire depending on the level of safety. Fire safety features in cable designs can be implemented individually or in combination.

The degree of realization of fire safety requirements of cables is determined by the scope of their application.

Scientifically based decisions on the fire resistance of cables to confirm the appropriate classification [12, 29] are made on the basis of tests of cable samples in specialized certification centers (laboratories). Such tests are expensive. So, for example, 12 cable samples [33] are needed to confirm the reaction to fire class B2ca, which costs more than EUR 18,000.

Determining the thermal resistance of cables on the basis of the obtained experimental data on the thermal resistance of the actual polymer materials of the cable, depending on the design and field of application, is necessary and justified. Especially – at the stage of mastering and determining the prospects for the production of cables with modern halogen-free electrical insulating materials in accordance with fire safety requirements. For example, cables for internal laying in residential and industrial construction must meet European requirements for electrical safety and load capacity. Instead of 2-core installation wires, 3-core (phase, neutral, grounding) ones are needed for residential buildings, offices, and work spaces. Instead of 4-core cables, which are currently used to supply electricity, for example, to residential buildings from substations, 5-core cables are needed. Of course, such cables must meet fire safety requirements.

The calorific value of cross-linked polyethylene is 48 MJ/kg, self-extinguishing polyethylene is 41.9 MJ/kg. For polyvinyl chloride plastic, this depends on the brand (recipe), MJ/kg: ordinary recipes – 23.7 (insulating) and 25.8 (sheathing); reduced flammability 18.4 – 19.7; reduced fire safety with low smoke and gas emission 10 (for filling) – 17.7 (for sheath) – 18.9 (for insulation) [36-38]. For example, 1 m of cable with polyvinyl chloride insulation in a protective sheath made of polyvinyl chloride plastic (bare) VVG 4×35+1×16 releases during combustion 10.5 MJ of heat; the VVHng cable 4×35+1×16 – 9.9 MJ, and the VVHng-LS cable – 9 MJ [39].

In non-flammable ng (non-flammable) and ng-LS (non-flammable with low smoke) cables, the flammability of the sheaths is reduced due to the introduction of flame retardants (aluminum oxide trihydrate, magnesium hydroxide). And although the flammability of the materials has decreased somewhat, these compositions continue to remain combustible materials and will burn in the event of a fire, releasing smoke and a large amount of heat into the surrounding space [39, 40].

Power cables with copper cores at voltage of 0.6/1 kV and frequency of 50 Hz for the transmission and distribution of electrical energy in stationary installations, insulation, inter-core filling and sheath made on the basis of modern polymer materials, including halogen-free compositions, were considered. Cables provide the transmission of electrical energy, control signals and control of electrical equipment, the operation of which in case of fire is mandatory for rescue operations. They are used at facilities with increased fire safety requirements for single and laid cable bundles in rooms and tunnels.

Figures 4, 5 present, depending on the number of cores of different cross-sections, the determined values of thermal resistance and thermal load of power cables on the basis of conducted experimental studies of the thermal resistance of insulation materials, between the core filling and the polymer sheath, removed from the cable samples.

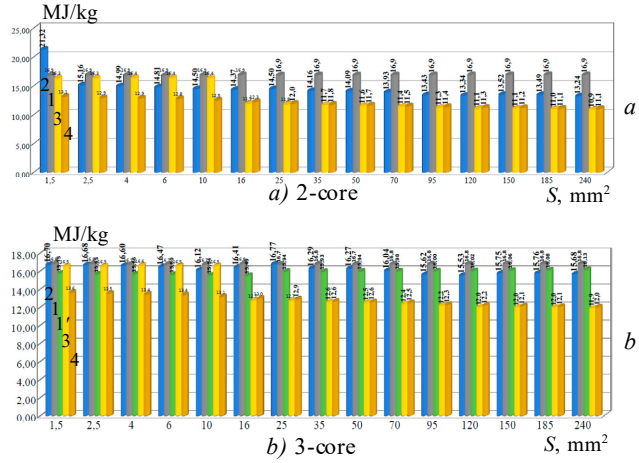

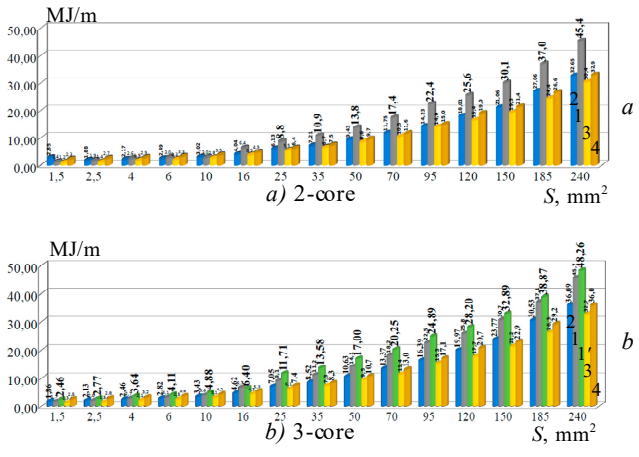

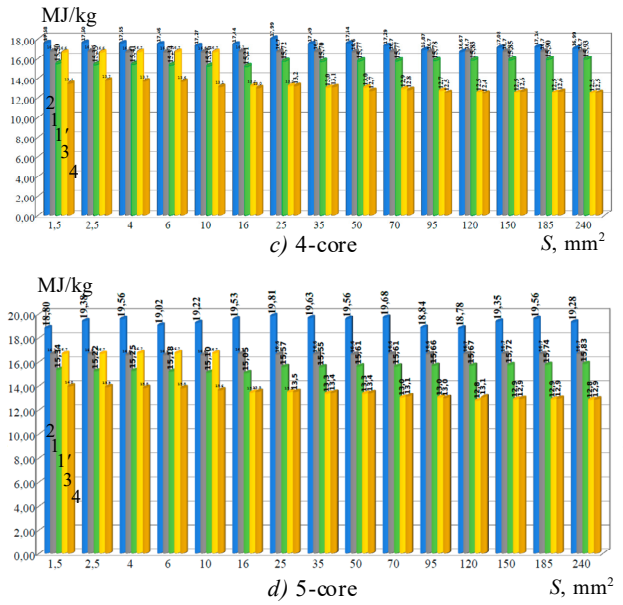

Fig. 4. Thermal resistance of power cables depending on used materials and design

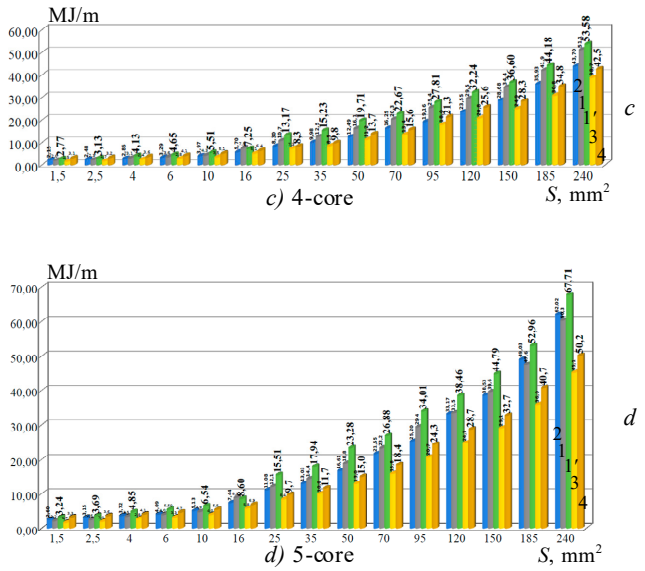

Fig. 5. Fire load of power cables depending on the used materials and design

Figure 6 shows the correlation dependence of the ratio of thermal resistance (p.u.T) and fire load (p.u.F) of 5-core vs 3-core cables with different applied polymer compositions (notation in Fig. 6 is identical to that shown in Fig. 4, 5, respectively).

Curves in Fig. 4–6 correspond to: 1, 1' – compositions containing halogens; 2, 3 and 4 – halogen-free.

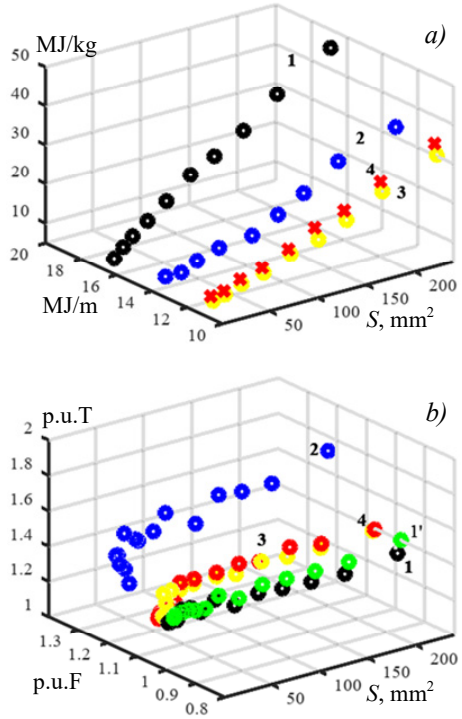

Fig. 6. Correlation between heat resistance and fire load for 2-cores (*a*) and ratio of these parameters of 5-core vs 3-core (*b*) power cables with different applied polymeric materials

When the cross-section of the current-conducting core increases, depending on their number, there is a change in the thermal resistance and fire load of the cables. For example, for a 2-core cable, the thermal resistance and fire load of a halogen-containing polymer composition (curve 1, Fig. 4,*a* and Fig. 5,*a*) is lower compared to a halogen-free one (curve 2, Fig. 4,*a* and Fig. 5,*a*) in the case of smaller values of the cross-section of the current-conducting core. And vice versa, it increases and exceeds these indicators in the case of larger cross-sections of the cable core. Such dynamics are also observed for 3-, 4-, and 5-core cables (compare curves 1 with curves 2, 3 and 4 in Fig. 4–6). In other words, the effectiveness of halogen-free compositions to meet fire safety requirements increases with the increase in cross-section and the number of cores in the cable.

Thus, the fire safety of cables is determined by the applied cable compositions and significantly depends on the design of the cables: the diameter of the current-conducting core and their number, that is, the ratio between the metal and polymer parts in the cable.

Conclusions.

1. Generalized requirements for fire safety of cables in the construction sector according to the category «Power, control cables and communication cables» are defined.

2. The classification of cables according to the fire sign in accordance with the EU Construction Products Regulation with the relevant classification criteria and test methods for determining the fire-resistant characteristics of cables is given.

3. A comparative analysis of fire safety indicators is presented based on the determination of thermal resistance and fire load depending on the applied composite polymer compositions and the design of low-voltage power cables.

4. Based on the correlation analysis between thermal resistance and fire load, which are important parameters for confirming the quality and fire safety of the entire cable, the effectiveness of the use of halogen-free polymer compositions in power cables with a larger cross-section and number of cores has been confirmed.

Conflict of interest. The authors declare no conflict of interest.

REFERENCES

1. *Wires And Cables Market Size, Share & Trend Analysis Report By Voltage (Low, Medium, High, Extra-High), By Installation (Overhead, Underground), By End-Use, And Regional Forecasts, 2023 – 2030*. 2022, 120 p.

2. *Wire and Cable Market – By Product (Coaxial Cables/Electronic Wires, Fiber Optics Cables, Power Cables, Signal & Control Cable, Telecom & Data Cables), By Voltage (Low, Medium, High), By Application & Forecast, 2023-2032*. 2023, 320 p.

3. *Global Wire and Cable Materials Market (2022 to 2030): Industry Analysis, Size, Share, Growth, Trends, and Forecasts*.

4. Maes J., Nuzman C.J. The Past, Present, and Future of Copper Access. *Bell Labs Technical Journal*, 2015, vol. 20, pp. 1-10. doi: https://doi.org/10.15325/BLTJ.2015.2397851.

5. *Harting. Single pair Ethernet. The infrastructure for IioT*. HARTING. 2020, 20 p.

6. *Construction Future. Oxford Economics*. Research Briefing, June, 21, 2023.

7. *Global Building Materials Industry 2023-2027*. Report. 2023, 179 p.

8. *Europe Construction Market Report and Forecast 2023-2028*. Report. 2023, 80 p.

9. *Recommendation for Use adopted by the Cableways Sectoral Group of Notified Bodies, and agreed by the Cableways Expert Group*. 2021. 5 p.

10. *Günter Beyer The Global Cable Industry: Materials, Markets, Products*. 2021, 416 p.

11. *Regulation (EU) No 305/2011 of the European Parliament and of the Council of 9 March 2011 laying down harmonised conditions for the marketing of construction products and repealing Council Directive 89/106/EEC (Text with EEA relevance)* (Consolidated text).

12. *Commission Delegated Regulation (EU) 2016/364 of 1 July 2015 on the classification of the reaction to fire performance of construction products pursuant to Regulation (EU) No 305/2011 of the European Parliament and of the Council*.

13. Pedersen L.L. *Cables for the EU must be CE marked*. 2017.

14. *DSTU EN 60228:2015 Conductors of insulated cables. General technical requirements (EN 60228:2004, AC:2005)*. (Ukr).

15. *IEC 60811-501:2012+AMD1:2018. Electric and optical fibre cables. Test methods for non-metallic materials. Part 501: Mechanical tests. Tests for determining the mechanical properties of insulating and sheathing compounds. Edition 1.1*. IEC TC 20, 2018. 67 p.

16. Mirchuk I.A. Halogen-free compositions for cable and wire products. Advantages, disadvantages and application features. *The Scientific Heritage*, 2018, vol. 1, no. 30, pp. 32-41. (Rus).

17. Bezprozvannych G.V., Mirchuk I.A. *Synthesis of technological modes of cooling and radiation testing of electrical insulation of cables. Monograph*. Kharkiv, Madrid Publ., 2021. 179 p. (Ukr).

18. Xu J., Ou H., Shan X., Liu B., Jiang J., Xu G. Investigation of novel intumescent flame retardant low-density polyethylene based on SiO 2 @MAPP and double pentaerythritol. *Journal of Applied Polymer Science*, 2020, vol. 137, no. 41, art. no. 49242 doi: https://doi.org/10.1002/app.49242.

19. Li Y., Qi L., Liu Y., Qiao J., Wang M., Liu X., Li S. Recent Advances in Halogen-Free Flame Retardants for Polyolefin Cable Sheath Materials. *Polymers*, 2022, vol. 14, no. 14, art. no. 2876. doi: https://doi.org/10.3390/polym14142876.

20. *IEC 60811-100:2012 Electric and optical fibre cables – Test methods for non-metallic materials – Part 100: General*. 21 p.

21. *EN 50363-0:2011 Insulating, sheathing and covering materials for low-voltage energy cables – Part 0: General introduction.* 2023, 10 p.

22. *Restriction of the use of certain hazardous substances (RoHS). Directive 2011/65/EU*.

23. Zolotaryov V.M., Chulieieva O.V., Chulieiev V.L., Kuleshova T.A., Suslin M.S. Influence of doping additive on thermophysical and rheological properties of halogen-free polymer composition for cable insulation and sheaths. *Electrical Engineering & Electromechanics*, 2022, no. 2, pp. 35-40. doi: https://doi.org/10.20998/2074-272X.2022.2.06.

24. Bezprozvannych G.V., Zolotaryov V.M., Antonets Y.A. Effect of the thickness of insulation of protected wires of high-voltage overhead transmission lines to their current carrying capacity. *Electrical Engineering & Electromechanics*, 2018, no. 2, pp. 41-46. doi: https://doi.org/10.20998/2074-272X.2018.2.07.

25. Porowski R., Kowalik R., Ramiączek P., Bąk-Patyna P., Stępień P., Zielecka M., Popielarczyk T., Ludynia A., Chyb A., Gawdzik J. Application Assessment of Electrical Cables during Smoldering and Flaming Combustion. *Applied Sciences*, 2023, vol. 13, no. 6, art. no. 3766. doi: https://doi.org/10.3390/app13063766.

26. Fangrat J., Kaczorek-Chrobak K., Papis B.K. Fire Behavior of Electrical Installations in Buildings. *Energies*, 2020, vol. 13, no. 23, art. no. 6433. doi: https://doi.org/10.3390/en13236433.

27. Wang K., Kong G., Shao M., Yu Q., Yang R. Study on Flame Retardancy of Enamelled Wires Using a Cone Calorimeter. *Journal of Physics: Conference Series*, 2023, vol. 2460, no. 1, art. no. 012014. doi: https://doi.org/10.1088/1742-6596/2460/1/012014.

28. *DSTU EN 13501-6:2019 Fire classification of building products and building structures. Part 6. Classification according to the results of the test for reaction to fire of power, control and communication cables (EN 13501-6:2018, IDT)*. (Ukr).

29. *DSTU EN 50399:2016 General methods of fire tests. Determination of heat release and smoke generation indicators of cables during the flame propagation test. Test equipment. Test procedures and evaluation of results (EN 50399:2011, IDT)*. 2016, 11 p. (Ukr).

30. *DSTU EN ISO 1716:2019 Testing of products for reaction to fire. Determination of the heat of combustion (calorific value) (EN ISO 1716:2018, IDT; ISO 1716:2018, IDT)*. (Ukr).

31. *DSTU EN 60332-1-2:2017 (EN 60332-1-2:2004; A1:2015; A11:2016, IDT; IEC 60332-1-2:2004; A1:2015, IDT) Fire tests of electrical and fiber optic cables. Part 1-2. Test for vertical spread of flame of a single insulated wire or cable. The method of testing with a flame of a premixed type with a capacity of 1 kW*. National standard of Ukraine. Kyiv, SE UkrNDNC Publ., 2017. 12 p. (Ukr).

32. *DSTU 4809:2007. Insulated wires and cables. Fire safety requirements and test methods*. Kyiv, Derzhspozhivstandard of Ukraine, 2007. 14 p. (Ukr).

33. *DSTU IES 60502-1:2009 Power cables with extruded insulation and fittings for them for a nominal voltage from 1 kV (Um = 1.2 kV) to 30 kV (Um = 36 kV). Part 1. Cables for a nominal voltage of 1 kV (Um = 1.2 kV) and 3 kV (Um = 3.6 kV) (IEC 60502-1:2004, IDT)*. National standard of Ukraine. Kyiv, SE UkrNDNC Publ., 2011. 44 p. (Ukr).

34. Bezprozvannych G.V., Grynyshyna M.V., Kyessayev A.G., Grechko O.M. Providing technical parameters of resistive cables of the heating floor system with preservation of thermal resistance of insulation. *Electrical Engineering & Electromechanics*, 2020, no. 3, pp. 43-47. doi: https://doi.org/10.20998/2074-272X.2020.3.07.

35. Bezprozvannych G.V., Mirchuk I.A. Correlation between electrical and mechanical characteristics of cables with radiation-modified insulation on the basis of a halogen-free polymer composition. *Electrical Engineering &*

Electromechanics, 2018, no. 4, pp. 54-57. doi: https://doi.org/10.20998/2074-272X.2018.4.09.
36. Di Nenno P.J. *The SFPE Handbook of Fire Protection Engineering, 4th ed.* National Fire Protection Association, Quincy, MA, USA, 2008. 1604 p.
37. Hirschler M.M. Flame retardants and heat release: review of traditional studies on products and on groups of polymers. *Fire and Materials*, 2015, vol. 39, no. 3, pp. 207-231. doi: https://doi.org/10.1002/fam.2243.
38. Li C., Chen J., Zhang W., Hu L., Cao J., Liu J., Zhu Z., Wu S. Influence of Arc Size on the Ignition and Flame Propagation of Cable Fire. *Energies*, 2021, vol. 14, no. 18, art. no. 5675. doi: https://doi.org/10.3390/en14185675.
39. Meinier R., Fellah M., Sonnier R., Zavaleta P., Suard S., Ferry L. Ignition and Charring of PVC-Based Electric Cables. *Fire Technology*, 2022, vol. 58, no. 2, pp. 689-707. doi: https://doi.org/10.1007/s10694-021-01168-0.
40. Bezprozvannych G.V., Mirchuk I.A. The evaluation of possibility of normal operation of cables based on twisted pairs with pvc jacket under the conditions of high humidity and temperature. *Electrical Engineering & Electromechanics*, 2017, no. 5, pp. 51-54. doi: https://doi.org/10.20998/2074-272X.2017.5.08.

Received 10.06.2023
Accepted 01.08.2023
Published 02.01.2024

G.V. Bezprozvannych[1], *Doctor of Technical Science, Professor*
M.V. Grynyshyna[2], *Postgraduate Student*, *Tech. Director*,
Y.S. Moskvitin[1], *PhD,*
[1] National Technical University «Kharkiv Polytechnic Institute»,
2, Kyrpychova Str., Kharkiv, 61002, Ukraine,
e-mail: Hanna.Bezprozvannukh@khpi.edu.ua (Corresponding Author);
yevhen.moskvitin@khpi.edu.ua
[2] LLC Interkabel Kyiv,
5, Dachnaya Str., Kapitanovka village,
Kyiv-Svyatoshyn district, Kyiv region, 08112, Ukraine,
e-mail: m.grynyshyna@interkabel.ua

How to cite this article:
Bezprozvannych G.V., Grynyshyna M.V., Moskvitin Y.S. Requirements for cables as categories of construction products and thermal resistance of power cables. *Electrical Engineering & Electromechanics*, 2024, no. 1, pp. 61-68. doi: https://doi.org/10.20998/2074-272X.2024.1.08

UDC 621.315.61 https://doi.org/10.20998/2074-272X.2024.1.09

O.O. Palchykov

Determination of the maximum mechanical stresses in the insulating material around a defect with a high dielectric permittivity in an electrostatic field

Introduction. *All insulating macrohomogeneous solid materials change shape under the influence of an electric field.* ***Problem.*** *The presence of minor defects changes the distribution of an electric field and causes a significant concentration of mechanical stresses in a given section of the material, which, under certain circumstances, can cause partial or complete destruction of this material.* ***Goal.*** *The purpose of the work is to determine maximum mechanical stresses according to the von Mises criterion in insulating materials around defects with ionized air and water in an electrostatic field. Also, to analyze the influence of the following parameters on the indicated stresses: the location of the defect, the orientation angle of the semi-major axis of the defect cross-section, the ratio of semi-major and semi-minor axes, elastic and dielectric properties of the insulating material and the defect.* ***Methodology.*** *The study is based on the interrelated equations of electrostatics and structural mechanics for an isotropic piecewise homogeneous medium. The solution of these equations is obtained by the finite element method.* ***Results.*** *Graphs of dependences of maximum mechanical stresses on the ratio of semi-major and semi-minor axes of the ellipsoidal cross-section of the defect have been obtained. The minimum ratio of the greatest stresses in the insulating materials around the surface cracks and pores for ionized air has been 9.3 times for the maximum ratio of major and minor semi-axes of the cross-section of the defect considered in the work, which is 10. For a water defect, the similar ratio has been 2...5.6 times, increasing when the relative dielectric permittivity of the insulating material changes from 7 to 2. When Young's modulus of the insulating material increases from 1 MPa to 100 GPa, the angles of the inclination of the linearized dependences of maximum mechanical stresses around bounded pores with ionized air (water) to the axis of the ratio of major and minor semi-axes of the defect cross-section have been increased by 35.9° (58.0°) and 18.6° (20.1°) at orientations of major semi-axes at angles of 0° and 45°, respectively.* ***Originality.*** *The numerical-field mathematical two-dimensional model has been developed for the first time, which consists of sequentially solved equations of electrostatics and structural mechanics, for the determination of the distribution of mechanical stresses in an insulating material with a liquid or gaseous defect. It has been established for the first time that the ratio of the elastic properties of the insulating material and the defect determines the angle of the inclination of the linearized dependence of the maximum mechanical stress to the axis of the ratio of major and minor semi-axes of the defect cross-section.* ***Practical value.*** *The types of defects that contribute to the aging of insulation materials under the combined action of an electric field and a stress field to the greatest extent have been established.* References 28, table 1, figures 10.

Key words: **insulating material, internal and surface defect, electrostatics, structural mechanics, von Mises stress, finite element method.**

В роботі методом скінченних елементів розроблено двовимірну математичну модель розрахунку розподілу механічних напружень під дією електростатичного поля в ізоляційному матеріалі з дефектом. Модель являє собою послідовно розв'язувані задачі електростатики та структурної механіки. У якості матеріалу дефекту виступали іонізоване повітря і вода. Розглядалися варіанти з внутрішніми та поверхневими дефектами, з врахуванням і без пружних властивостей дефекту. Поле механічних напружень розраховувалось на основі критерію фон Мізеса. Встановлено, що мінімальне відношення найбільших напружень в ізоляційних матеріалах з поверхневими тріщинами і порами для іонізованого повітря склало 9,3 рази для максимального співвідношення півосей поперечного перерізу дефекту 10. Для водного дефекту аналогічне відношення склало 2…5,6 разів, збільшуючись при зміні відносної діелектричної проникності ізоляційного матеріалу від 7 до 2. Визначено, що при збільшенні модуля Юнга ізоляційного матеріалу від 1 МПа до 100 ГПа кути нахилу до вісі лінеаризованих залежностей максимальних механічних напружень навколо обмежених пор з іонізованим повітрям (водою) збільшуються на 35,9° (58,0°) і 18,6° (20,1°) при орієнтаціях великих півосей під кутами 0° і 45° відповідно. Бібл. 28, табл. 1, рис. 10.

Ключові слова: **ізоляційний матеріал, внутрішній і поверхневий дефект, електростатика, структурна механіка, механічні напруження за фон Мізесом, метод скінченних елементів.**

Introduction. Solid, technically clean insulating materials have imperfections, a defective structure. Defects may have a technological or operational nature of origin. Structural micro-heterogeneity of solid insulating materials is confirmed by effective methods [1-4]. All insulating materials at the micro level change shape under the influence of an electric field. The presence of minor defects changes the distribution of electric field strength and creates a significant concentration of mechanical stresses in a given area of the material, which under certain circumstances can cause its partial or complete destruction. The most significant mechanical stresses are detected when the dielectric permittivity of the insulating material and the material defect differ sharply, for example, when the volume of the defect is filled with water or ionized air, for example, as a result of a partial discharge caused by high electric field strength.

Analysis of publications. The regularities of the distribution of the electrostatic field in insulating materials were considered in [5-10]. When covering the topic in [5], it would be worthwhile to reveal other shapes of defects, for example, with an ellipsoidal cross section, as well as to investigate the effect on the detection of dielectric breakdown of the inhomogeneity of the location of pores. The drawback in [6] is the lack of determination of the correlation between the increase in the electric field strength concentration and the experimental decrease in the breakdown voltage, as was done in [5]. Also, the shortcomings of this work include the failure to take into account air defects in the model, which are replaced by water coming from the environment. In [7], when studying the effect of defects on the linear capacity of the insulation, the compensatory effect of defects of different

nature is not taken into account, for example, a combination of local thinning and an internal defect with a lower dielectric permittivity than in the insulating material. With this effect, the linear capacity may not change much, although the concentration of the electric field will be significantly different from the average. The disadvantages of the work [8] are insufficient justification of the choice of shape and placement of air and water inclusions, which can affect the results of the work. Also, in [8], the volume of insulating material before and after seepage and after was taken unchanged, which is evident, in my opinion, not entirely correct. The results in [9] may be affected by the failure to take into account other orientations of the defect with a triangular cross section. The disadvantage in [10] is that the accuracy of the calculation of the electric field based on the neural network decreases when the parameters sought are far from the parameters of the numerical finite element model that participated in the training. The classic approach to considering the influence of the ionized region on the mechanical strength of the insulating material is based on Griffith criteria [11, 12]. The results of work [11] refer only to metal inclusion, the probability of which in modern insulation is rather insignificant. The shortcomings of the work [11] can also include the neglect of the elastic properties of the defect, as well as the lack of the consideration of the issue of the orientation of the defect at an angle of 45° to the area of the electrodes. Horovyts [12] considered surface cracks perpendicular to the electrode area in a 2D and axisymmetric formulation. The disadvantages in [12] are the lack of calculation of the field of mechanical stresses, that is, there is no understanding of the size of the area of stress concentration, and all the possible options for the orientation of the surface crack are not considered.

Stark and Garton made additions to the theory of mechanical stresses taking into account the plastic deformations of the dielectric to explain its destruction [13]. The failure criterion obtained by them corresponds to the minimum deformation when the collapse of the dielectric thickness occurs. A more general model for considering plastic deformation in polymers is presented in [14]. The common drawback of these models, in my opinion, is their one-dimensionality, which does not allow taking into account the Poisson effect. The work [15] presents a model of the formation of a nucleus and the growth of a conductive channel based on the energy principle, taking into account electric and mechanical fields, as well as the chemical potential at the interface between a conductive defect and a dielectric. However, the phenomenological parameter for determining the minimum possible size of a conductive nucleus, obtained from the study of the energy surface, is not supported by a physical assessment of its boundary (for example, how this parameter depends on the mechanical stresses at the boundary of the two-phase distribution).

In [16, 17], the possibilities of the formation of defects and dendrites under the action of electromechanical and mechanical forces, respectively, were investigated. In the model [16] there are parameters that cannot be directly determined, and therefore their value is determined only by the need to match the theoretical and experimental durability times of polyethylene insulation. In [17], there is no numerical assessment of the size of the defect and the electric field in it, which may affect the validity of the dendrite growth mechanism proposed in the work. In [18, 19], the growth patterns of dendrites under the influence of electric voltage were considered with the involvement of the concepts of Maxwell's stress tensor and fracture mechanics. In [18] it was established that the pre-channel structures are not caused by partial discharges, but an explanation of their occurrence by electromechanical stresses and shock ionization is proposed. The last mechanism is not considered in the work. Minor shortcomings in [18] when determining the field of mechanical stresses are the lack of consideration of the change in the density of the dendrite material (which was established experimentally in the work), as well as the arbitrary choice of the conductivity of the dendrite walls. The disadvantage of the work [19] is that the electromechanical forces are not calculated during the growth of the dendrite, but are only estimated by the rate of energy release.

The work [20] developed a model for determining mechanical stresses in polyethylene insulation with an ellipsoidal defect, the minor axis of which is parallel to the plane of the electrodes. The publication [21] developed a mathematical model for calculating the electric field, associated forces and mechanical stresses in the area of microdefects of polyethylene insulation in an axisymmetric formulation. A multiphysics 3D model that takes into account electric, thermal, and mechanical fields in the area of water treeings is presented in [22]. The common shortcomings of the works [20-22] are the consideration of only one orientation of the defect (which, in turn, is not the most likely), failure to take into account the elastic properties of the defect, insufficient justification of the choice of electrical properties of the defect, partiality of the study (only polyethylene is considered).

An experimental study of the influence of the level of irradiation by accelerated electrons with energy of 0.5 MeV as a result of technological manufacturing on the mechanical and electrical characteristics of cable insulation was carried out in [23]. Despite the high level of research, there is no theoretical explanation of the strong correlation between the mechanical and electrical characteristics of radiation cross-linked insulation in [23]. In [24], a model for calculating the electric field in three-component insulation, modeled as a two-layer tape, is proposed. It would be worth comparing this model with the numerical field model, which consists of a fiberglass base, an impregnation composition, and a mica paper tape. The authors of the work [25] justified the effectiveness of detecting technological defects in high-voltage insulation based on the characteristics of partial discharges in gas inclusions. In [25] there is no comparison of the proposed chain model with the numerical field model, and there is also a question about the shape of the defect.

In [26], various criteria for the destruction of polymers (and in the general case of porous materials, including composite materials, wood, metals) were

analyzed and it was shown that all criteria can be reduced to the von Mises criterion with some error. The disadvantage is that the introduction of new failure criteria, in addition to the von Mises and Tresca criteria, requires additional parameters that are determined experimentally for a specific material, which reduces their universality.

Thus, at the moment, the existing mathematical models do not allow to calculate the maximum mechanical stresses for solid insulation with a liquid or gaseous defect in a 2D formulation and to determine them depending on the ratio of the semi-axes of the cross section of the defect, the orientation of the defect, as well as when changing the elastic and dielectric properties of the insulation material and defect within wide limits.

General characteristics of work. The goal of the work is to determine the maximum mechanical stresses according to the von Mises criterion in insulating materials around defects with ionized air and water in an electrostatic field. To analyze the influence of the following parameters on the indicated stresses: the location of the defect, the orientation angle of the semi-major axis of the cross-section of the defect and its relation to the minor semi-axis, elastic and dielectric properties of the insulating material and the defect.

The relevance of the work is related to the theoretical explanation of the heterogeneity of the microstructure of insulating materials, as well as the identification of the features and reasons for the development of micro-sized air/water cavities and treeing formations in such materials.

Object of study. In the work, the pore in the volume of the dielectric is modeled in cross-section as an ellipse, and the crack on the surface of the dielectric is modeled as half an ellipse. The computational domain in the case of a pore is a rectangle with sides $10a$ and $14a$, where a is the semimajor axis of the ellipse. The minor semi-axis of the ellipse is defined as $b = a/k$, where k is the parameter that lies within $k \in [1...10]$. The computational domain in the case of a crack is a rectangle with sides $10a$ and $7a$. The distance between the electrodes in the first case is the larger side of the rectangle, in the second case it is the smaller side. The dimensions of the computational domain are chosen so that on its boundaries the modulus of the electric field strength vector approaches the values of the modulus of the strength vector in the insulating material without a defect. Three cases of ellipse and semi-ellipse arrangement were considered in the work: at angles of 0°, 45°, and 90° between the semi-minor axis and the plane of the electrode. Options of through and limited pore were also considered. In the first case, the elastic properties of the material of the defect can be neglected. In the second case, we mean a rather long cylindrical volume in the direction perpendicular to the computational domain, bounded on both sides by parallel planes. The elastic properties of the material of this volume should affect the distribution of mechanical stresses in the insulating material.

Mathematical model. The calculation of electromechanical forces is based on the coupled solution of the equations of electrostatics and structural mechanics developed for an isotropic piecewise homogeneous medium with linear properties in a 2D formulation [27, 28]:

$$\nabla^2\varphi = 0;$$

$$\boldsymbol{E} = -\nabla\varphi;$$

$$\boldsymbol{D} = \varepsilon_0\varepsilon_{ri(d)}\boldsymbol{E};$$

$$\nabla\boldsymbol{\sigma} = 0; \quad (1)$$

$$\boldsymbol{\varepsilon} = 0{,}5[(\nabla\boldsymbol{u})^{\mathrm{T}} + \nabla\boldsymbol{u}]; \quad (2)$$

$$(\sigma_{xx}\ \sigma_{yy}\ \sigma_{zz}\ \sigma_{xy})^T = C_M(\varepsilon_{xx}\ \varepsilon_{yy}\ \varepsilon_{zz}\ \varepsilon_{xy})^T, \quad (3)$$

where φ is the scalar electrostatic potential; $\boldsymbol{E}$ is the electric field strength vector; $\boldsymbol{D}$ is the electric induction vector; ε_0 is the electrical constant ($8.854\cdot10^{-12}$ F/m); $\varepsilon_{ri(d)}$ is the relative dielectric permittivity of the insulating material (defect); $\boldsymbol{\sigma}$ is the tensor of mechanical stresses; $\boldsymbol{\varepsilon}$ is the strain tensor; $\boldsymbol{u}$ is the vector of displacements of the body (the difference between the coordinates of the final and initial position of each point); σ_{ij}, ε_{ij} are the components of mechanical stress and strain tensors, respectively; C_M is the elasticity matrix, which is written through Young modulus E_M and Poisson ratio ν for an isotropic material in the form:

$$C_M = \frac{E_M}{(1+\nu)\cdot(1-2\nu)}\begin{pmatrix} 1-\nu & \nu & \nu & 0 \\ \nu & 1-\nu & \nu & 0 \\ \nu & \nu & 1-\nu & 0 \\ 0 & 0 & 0 & 0{,}5(1-2\nu) \end{pmatrix}.$$

It is convenient to write the elasticity matrix for gas and liquid inclusion in terms of the shear modulus G and the volumetric modulus of elasticity K:

$$C_M = \begin{pmatrix} K+\frac{4G}{3} & K-\frac{2G}{3} & K-\frac{2G}{3} & 0 \\ K-\frac{2G}{3} & K+\frac{4G}{3} & K-\frac{2G}{3} & 0 \\ K-\frac{2G}{3} & K-\frac{2G}{3} & K+\frac{4G}{3} & 0 \\ 0 & 0 & 0 & G \end{pmatrix}.$$

According to [27], all volume forces are reduced to surface forces and are taken into account due to boundary conditions.

The specific force per unit surface area of the insulating material f_s is calculated on the basis of the Maxwell stress tensor [28] as

$$f_s = (\boldsymbol{D}_2\cdot\boldsymbol{n}\cdot\boldsymbol{E}_2 - \boldsymbol{D}_1\cdot\boldsymbol{n}\cdot\boldsymbol{E}_1) - 0{,}5(\boldsymbol{D}_2\cdot\boldsymbol{E}_2 - \boldsymbol{D}_1\cdot\boldsymbol{E}_1)\cdot\boldsymbol{n}, \quad (4)$$

where $\boldsymbol{n}$ is the external normal vector.

For liquids and gases, the shear modulus is zero, but for numerical implementation, $G = 0.2$ Pa was assumed. The volumetric elastic modulus of the defect in the case of a limited pore was taken as $K = 2.2$ GPa for water, and $K = 0.101$ MPa for ionized air.

Equations of structural mechanics (1)–(3) are written in the plane strain approximation [28], i.e. $\varepsilon_{xz} = \varepsilon_{yz} = \varepsilon_{zz} = 0$. Therefore, $\sigma_{xz} = \sigma_{yz} = 0$ and the elasticity matrix changes its dimension from 6×6 to 4×4.

Boundary conditions of the problem of electrostatics:

- for the lower plane $\varphi_1 = |\boldsymbol{E}_\infty|\cdot d$;
- for the upper plane $\varphi_2 = 0$;
- for the side surface $\boldsymbol{n}\cdot\boldsymbol{D} = 0$,

where $\boldsymbol{E}_\infty$ is the electric field strength vector in the insulating material in the absence of a defect; d is the distance between the upper and lower planes.

Boundary conditions of the structural mechanics problem:

- for the lower plane $\boldsymbol{u} = 0$;
- for the upper plane $\boldsymbol{\sigma}\cdot\boldsymbol{n} = f_s$.

At the interface of two media, the following are accepted: for the problem of structural mechanics, the equality of the displacement vectors, for the problem of electrostatics, Neumann boundary conditions.

The main assumptions made in the model are: the insulating material has no conductivity; charges at the interface of dielectric media are absent, as well as volume charges; there are no mechanical stress components caused by thermal and gravitational fields; when the volume changes, the physical properties of the materials do not change and there is no associated polarization; small deformations of the studied sample (for example, the maximum deformation was calculated for rubber in pre-breakthrough fields, which was 2.4 %; for polyimide film – 0.049 %). The latter involves considering the model only within the limits of the theory of linear elasticity, and also allows the coupled system of equations to be divided into two subproblems that are solved sequentially: the electrostatics problem for calculating the specific force, which is then used as a boundary condition for the structural mechanics problem. As a result of the linearity of the separately taken problems of electrostatics and structural mechanics, when the dimensions of the sample are changed in compliance with the above-mentioned boundary conditions, the values of the electric and mechanical fields change proportionally.

The distribution of mechanical stresses was calculated according to the von Mises criterion [28]

$$\sigma = 0{,}5^{0{,}5}\cdot[(\sigma_{xx} - \sigma_{yy})^2 + (\sigma_{yy} - \sigma_{zz})^2 + (\sigma_{zz} - \sigma_{xx})^2 + 6(\sigma_{xy})^2]^{0.5}.$$

Among such stresses the maximum value $\sigma_{\max}$ was founded, which was further presented in relative units:

$$\sigma^*_{\max} = \sigma_{\max}/[0{,}5\varepsilon_0\varepsilon_{ri}(\boldsymbol{E}_\infty)^2].$$

Therefore, without a defect, the relative mechanical stress according to von Mises is $\sigma^*_{\max} = 1$. The similarity of the forces (4) created by the electrostatic field based on Maxwell's stress tensor serves as a justification for the presentation of mechanical stresses in relative units.

The model is also characterized by the similarity of electrostatic fields when the permittivity of the insulating material changes, which is true when the condition $\varepsilon_{ri} << \varepsilon_{rd}$ is fulfilled. Mechanical stresses were studied at the relative dielectric permittivity of the insulating material within $\varepsilon_{ri} \in [2\ldots7]$, of the defect with water $\varepsilon_{rd} = 80.2$. Strongly ionized regions arising in the case of a partial breakdown were modeled by a material with a relative dielectric permittivity $\varepsilon_{rd} = 16000$ to adjust the numerical model [5]. This value was chosen for the purpose of practical implementation in the problem of electrostatics of the model of an ideal conductor with $\varepsilon_{rd} \to \infty$, as several times the value of the maximum dielectric permittivity of the materials in the model. The given model is numerically implemented using the finite element method in the COMSOL code. For a more general approach to the problem of mechanical stresses caused by an electric field, the problem is formulated in such a way as to take into account the mechanical and electrical properties of most electrical insulating materials (and even hypothetical values such as $E_M = 10^5$ MPa). The physical properties of some electrical insulating materials are given in Table 1. That is, based on the analysis of the properties of electrical insulating materials, the following ranges of parameter changes were chosen: relative dielectric permittivity $\varepsilon_{ri} = 2$–7; Poisson ratio $\nu = 0.1$–0.499; Young modulus $E_M = 1$–10^5 MPa.

Table 1

Physical properties of some electrical insulating materials

Material	Young's modulus E_M, MPa	Poisson ratio ν	Dielectric permittivity ε_{ri}
Rubber	0,5…8	0,47	2,6
Polyvinyl chloride	$(2{,}7\ldots4)\cdot10^3$	0,35…0,38	3,2
Polyimide film	$3\cdot10^3$	0,499	3,5
Cellulose	$(2{,}7\ldots6{,}5)\cdot10^3$	0,38…0,46	6,5
Electro-porcelain	$6\cdot10^4$	0,23	6…7

Research results. Examples of electric fields and mechanical stress fields in insulating materials ($\varepsilon_{ri} = 2$) at $|\boldsymbol{E}_\infty| = 40$ MV/m with variants of the water defect are shown in Fig. 1–3. The maximum concentration of mechanical stresses for the defect shown in Fig. 1,*b*, is located at some angle to the semi-major axis, which tends to decrease with an increase in the geometric ratio of the defect section. According to Fig. 1, the orientation of the areas of concentration of mechanical stresses promotes the growth of surface cracks with angles of 0°...45° between the minor semi-axis and the surface of the electrodes in the direction of the opposite electrode in the event that the mechanical stress exceeds the compressive strength limit of the insulating material. As can be seen from Fig. 2, 3, when changing the Young modulus of insulating materials, the maximum mechanical stress shifts. In the case presented in Fig. 2, the concentration of mechanical stresses decreases along the extension of the major semi-axis and increases along the minor axis. In the case of Fig. 3, the concentration of mechanical stresses with an increase in the Young modulus moves from a position above the semi-major axis to below it. For a limited water pore with a semi-major axis parallel to the plane of the electrodes and a circular limited pore, the zone of concentration of mechanical stresses with an increase in Young modulus turns by a jump of 90°.

For air ionized through pores, the zones of concentration of mechanical stresses are located: as rotated at a small angle clockwise relative to the major semi-axis for the defect region, similar to the image in Fig. 3,*d*; on an axis parallel to the plane of the electrodes for other cases of orientation of pores.

Figure 4 presents the results of calculating the maximum mechanical stresses depending on the orientation of the surface defect filled with ionized air, its geometric ratio and Poisson ratios of insulating materials. For variants of cracks with 0° and 45° orientation, the effect of Poisson ratio of the insulating material on the stress concentration around the defect is minimal. For the specified options, the dependencies for the material with $\nu = 0.1$ are presented. The difference in dependencies for defects in the insulating material with $\nu = 0.499$ is up to –3.5 %. Here, the specified models for determining the stress field are invariant to a change in Young modulus.

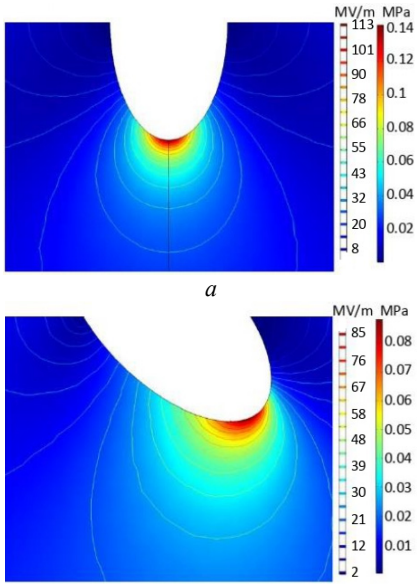

Fig. 1. Mechanical and electric fields around a surface water crack, the minor semi-axis of the cross-section of which is oriented at an angle of 0° (*a*) and 45° (*b*) to the plane of the electrodes in insulating materials with $\nu = 0.1$ regardless of Young modulus

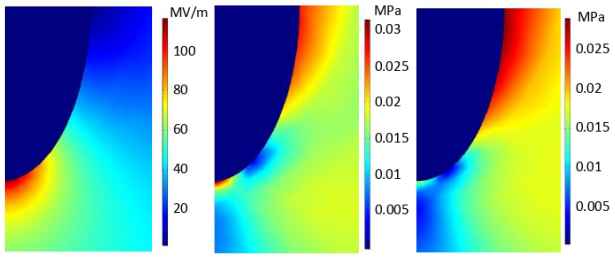

Fig. 2. Distribution of the modulus of the electric strength vector (a) and von Mises stresses for the cases of water limited pores in insulating materials with $\nu = 0.1$: $E_M = 1$ MPa (*b*), $E_M = 10^5$ MPa (*c*)

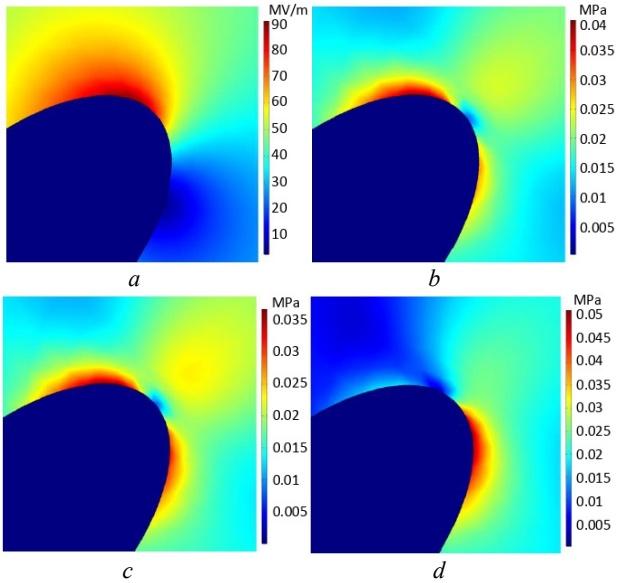

Fig. 3. Distribution of the electric strength vector modulus (*a*) and von Mises stresses for the cases of water limited pores in insulating materials with $\nu = 0.1$: $E_M = 1$ MPa (*b*), $E_M = 10^3$ MPa (*c*), $E_M = 10^5$ MPa (*d*)

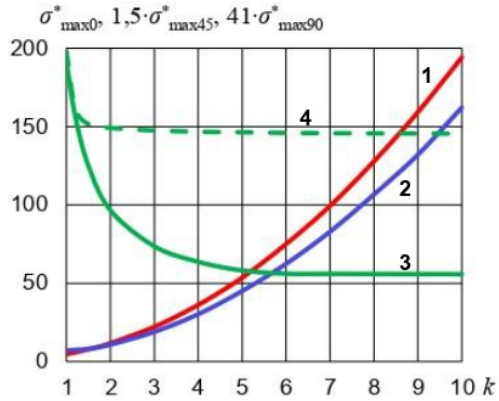

Fig. 4. Dependencies of the maximum mechanical stresses around surface cracks with ionized air, the minor semi-axis of which is oriented to the plane of the electrodes at angles of 0° (curve 1), 45° (curve 2), and 90° (curves 3 and 4 for materials with $\nu = 0.1$ and with $\nu = 0.499$, respectively), on the geometric ratio

Figures 5, 6 present the results of calculating the maximum mechanical stresses depending on the orientation of the cross-section of the pore filled with ionized air, its geometric ratio and the elastic properties of the insulating material.

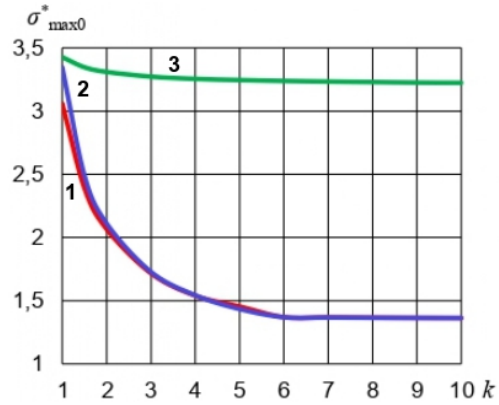

Fig. 5. Dependencies of the maximum mechanical stresses around pores with ionized air, the minor axis of which oriented to the plane of the electrodes at an angle of 0°, on geometric ratio for the cases of: a limited pore in a material with $\nu = 0.1$ and $E_M = 1$ MPa (curve 1); through pores in materials with $\nu = 0.1$ (curve 2) and with $\nu = 0.499$ (curve 3)

In Fig. 5, the stress graph in the material with $\nu = 0.1$ and $E_M = 10^5$ MPa coincides with the graph for the through pore in the material with the corresponding Poisson ratio. Also in Fig. 5 graph of stresses in materials with $\nu = 0.499$ and Young modulus in the range $[1...10^5]$ MPa coincides with the graph for a through pore in the material with the corresponding Poisson ratio. The maximum discrepancy by module in these cases was 1.1 %. Figure 6 for limited pores with an orientation of 45° in insulating materials with $E_M = 1$ MPa and Poisson ratio in the range [0.1...0.499] presents a graph constructed according to the data of the model with $\nu = 0.1$. The maximum differences in the modulus of stress mapping for the model with $\nu = 0.499$ amounted to 1.4 % and 10.9 % for $k \in [2…10]$ and $k = 1$, respectively. In Fig. 6 graphs of stresses in materials with $E_M = 10^5$ MPa and Poisson ratios $\nu = 0.1$ and $\nu = 0.499$ coincide with the graphs for through pores

in materials with the corresponding Poisson ratio and the position of the defect with a maximum discrepancy of –0.54 %.

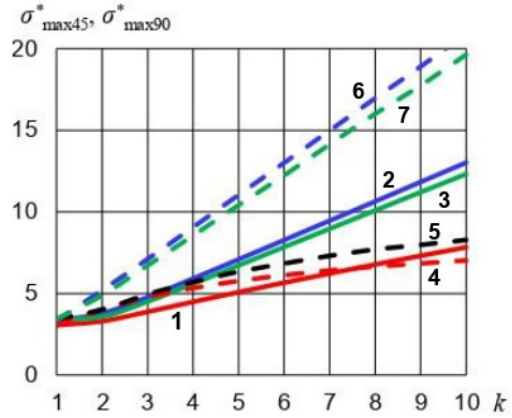

Fig. 6. Dependencies of the maximum mechanical stresses around pores with ionized air, the minor semi-axis of which oriented to the plane of the electrodes at angles of 45° (solid lines), 90° (dashed lines), on the geometric ratio for the cases: in materials with E_M = 1 MPa and ν = 0.1...0.499 (curve 1); in the material with E_M = 1 MPa and ν = 0.1 (curve 4); in the material with E_M = 1 MPa and ν = 0.499 (curve 5); for through pores in materials with ν = 0.1 (curves 2 and 6) and with ν = 0.499 (curves 3 and 7)

Figures 7, 8 present the results of calculating the maximum mechanical stresses depending on the orientation of the cross-section of the water pore, its geometric ratio and the elastic properties of insulating materials. Figure 7 does not show stress graphs in materials with ν = 0.1 and $E_M = 10^5$ MPa; ν = 0.499 and E_M = 1 MPa; ν = 0.499 and $E_M = 10^5$ MPa. These, as in the case of pores with ionized air, coincide with the graphs for through pores. The maximum discrepancy is 2.3 %. The dependences for materials with $E_M = 10^5$ MPa and ν = 0.499 when defects are oriented at angles of 45° and 90° coincide with those shown in Fig. 8 dependencies for the material with $E_M = 10^5$ MPa and ν = 0.1. The difference of dependencies for the range of change of the parameter $k \in [2...10]$, which determines the size of the defect, is modulo [4.9...1.2] %.

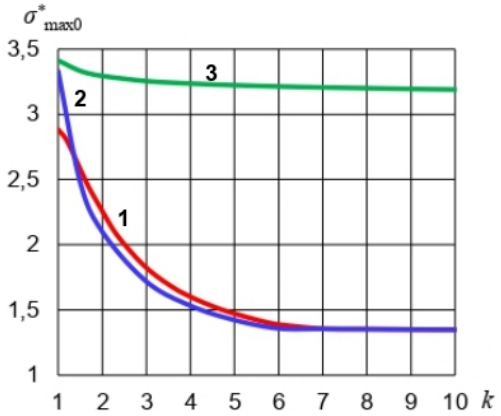

Fig. 7. Dependencies of the maximum mechanical stresses around water pores, the semi-minor axis of which is oriented to the plane of the electrodes at an angle of 0°, on the geometric ratio for the cases of: a limited pore in a material with ν = 0.1 and E_M = 1 MPa (curve 1); through pores in materials with ν = 0.1 (curve 2) and with ν = 0.499 (curve 3)

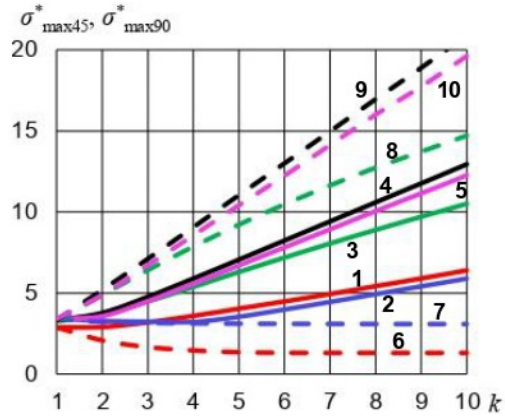

Fig. 8. Dependencies of maximum mechanical stresses around water pores, the minor semi-axis of which is oriented to electrode planes at 45° angles (solid lines), 90° (dashed lines), on the geometric ratio for the cases: in the material with E_M = 1 MPa and ν = 0.1 (curves 1 and 6); in the material with E_M = 1 MPa and ν = 0.499 (curves 2 and 7); in the material with $E_M = 10^5$ MPa and ν = 0.1 (curves 3 and 8); for through pores in materials with ν = 0.1 (curves 4 and 9) and with ν = 0.499 (curves 5 and 10)

For all considered through pores, changing the Young modulus of the insulating material has no effect on the pattern of stress distribution. It can be asserted about the practical identity of the dependencies of the maximum mechanical stresses in the region of defects with ionized air and water when their major semi-axis is oriented at the angle of 90° to the plane of the electrodes, as well as about the identity of stresses around through pores with ionized air and water at other angles. When the ratio of the major and minor semi-axes of the defect cross-section k increases from 1 to 10, the maximum mechanical stresses around limited and through pores with ionized air (water) when their major semi-axes are oriented to the plane of the electrodes at angles of 0° and 45° increase by 2.3...6.3 (0.5...6.3) and 2.6...3.9 (2.2...3.9) times, respectively.

During the study of the surface water defect, the lack of proportionality of the mechanical stresses with a change in the relative dielectric permittivity was revealed. This can be explained by the presence of a small electric field in the defect, which will change when the dielectric permittivity of the insulating material changes. And therefore the graphs shown in Fig. 9, 10, are constructed with defined relative mechanical stresses as follows: $\sigma^*_{maxw} = \sigma^*_{max}\varepsilon_{ri}$.

The graphs presented in Fig. 9, 10 are valid for insulating materials whose elastic properties vary widely. The average discrepancy of the dependences in Fig. 9 when the Poisson ratio changes in the range [0.1...0.499] is 3 %. According to Fig. 9 when the relative dielectric permittivity of the insulating material increases from 2 to 7 for the range of the ratio of the major and minor semi-axes of the defect section $k \in [1…10]$, the maximum mechanical stresses around the surface water cracks with the orientation of the minor semi-axes to the plane of the electrodes at angles of 0° and 45° decrease 1.1...3 times.

So, despite the identity of the distribution of the electric field for identical regions of the variants with external and internal defects, the distribution of the mechanical stress field is not the same, but depends on the

ratio of the elastic properties of the insulating material and the defect, the location of the defect.

Verification of the obtained results. The model was tested according to the numerical study of the work [20]. In the model given in [20], the problem was solved in an axisymmetric formulation, taking into account the direct current conductivity. For the adequacy of the comparison, the axisymmetricity of the problem and the complex dielectric permittivity were taken into account in the model developed in this work. The error for the maximum value of the mechanical stress in comparison with the result obtained in [20] was 0.12 %, which confirms the correctness of the numerical results of this work. In addition, according to the order of electrical and electromechanical quantities, the numerical results of this work and works [21, 22] coincide.

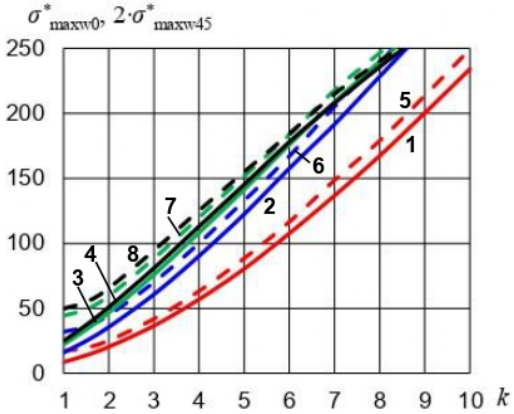

Fig. 9. Dependencies of the maximum mechanical stresses around surface water cracks, the minor semi-axis of which is oriented to the plane of the electrodes at angles of 0° (solid lines), 45° (dashed lines), on the geometric ratio for cases: $\varepsilon_{ri} = 2$ (curves 1 and 5), $\varepsilon_{ri} = 4$ (curves 2 and 6), $\varepsilon_{ri} = 6$ (curves 3 and 7), $\varepsilon_{ri} = 7$ (curves 4 and 8)

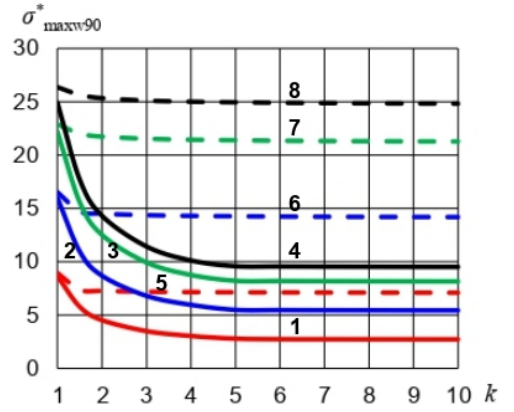

Fig. 10. Dependencies of the maximum mechanical stresses around surface water cracks, the minor semi-axis of which is oriented to the plane of the electrodes at an angle of 90°, on the geometric ratio in materials with $\nu = 0.1$ (solid lines) and with $\nu = 0.499$ (dashed lines) for the cases: $\varepsilon_{ri} = 2$ (curves 1 and 5), $\varepsilon_{ri} = 4$ (curves 2 and 6), $\varepsilon_{ri} = 6$ (curves 3 and 7), $\varepsilon_{ri} = 7$ (curves 4 and 8)

Conclusions.

1. A numerical field mathematical 2D model was developed, which consists of sequentially solved equations of electrostatics and structural mechanics for determining the distribution of mechanical stresses in an insulating material with a liquid or gaseous defect and implemented in COMSOL. The adequacy of the model is confirmed by comparison with results known in the literature.

2. The minimum ratio of the maximum stresses in the insulating materials around the surface cracks and pores for ionized air was 9.3 times for the maximum ratio of the major and minor semi-axes of the cross-section of the defect $k = 10$ considered in the work. For the water defect, the similar ratio was 2...5 .6 times, increasing when the relative dielectric permittivity of the insulating material changes from 7 to 2.

3. When the Young modulus of the insulating material increases from 1 MPa to 100 GPa, the angles of inclination to the axis of the ratio of the major and minor semi-axes of the defect cross-section of the linearized dependencies of the maximum mechanical stresses around the limited pores with ionized air (water) increase by 35.9° (58.0 °) and 18.6° (20.1°) at orientations of major semi-axes at angles of 0° and 45°, respectively.

4. The further direction of research consists in establishing the dependencies of the distribution of mechanical stresses in insulating materials with defects based on an improved mathematical model, taking into account the additional spatial coordinate and anisotropy of the physical properties of the materials of the model.

Conflict of interest. The author of the article declares no conflict of interest.

REFERENCES

1. Zhou T., Zhu X., Yang H., Yan X., Jin X., Wan Q. Identification of XLPE cable insulation defects based on deep learning. *Global Energy Interconnection*, 2023, no. vol. 6, no. 1, pp. 36-49. doi: https://doi.org/10.1016/j.gloei.2023.02.004.

2. Qu Z., Zhang G., Fu Y., An Y., Chen C., Shan X. Defect detection for the insulation layer of bent aircraft cables based on ultrasonic guided waves. *IEEE Transactions on Instrumentation and Measurement*, 2023, vol. 72, pp. 1-8. doi: https://doi.org/10.1109/TIM.2023.3241040.

3. Zhou X., Tian T., Li X., Chen K., Luo Y., He N., Liu W., Ma Y., Bai J., Zhang X. and Zhang G. Study on insulation defect discharge features of dry-type reactor based on audible acoustic. *AIP Advances*, 2022, vol. 12, no. 2, art. no. 025210. doi: https://doi.org/10.1063/5.0078735.

4. Wang Y., Nie Y., Qi P., Zhang N., Ye C. Inspection of defect under thick insulation based on magnetic imaging with TMR array sensors. *IEEE Transactions on Magnetics*, 2021, vol. 58, no. 3, art. no. 6200510. doi: https://doi.org/10.1109/TMAG.2021.3138587.

5. Palchykov O.O. Breakdown voltage of micron range air inclusions in capacitor paper. *Electrical Engineering & Electromechanics*, 2020, no. 6, pp. 30-34. doi: https://doi.org/10.20998/2074-272X.2020.6.05.

6. Li G., Liang X., Zhang J., Li X., Wei Y., Hao C. Insulation properties and interface defect simulation of distribution network cable accessories under moisture condition. *IEEE Transactions on Dielectrics and Electrical Insulation*, 2022, vol. 29, no. 2, pp. 403-411. doi: https://doi.org/10.1109/TDEI.2022.3157902.

7. Vavilova G., Yurchenko V., Keyan L. Influence of the insulation defects size on the value of the wire capacitance. *Progress in Material Science and Engineering, Part of the Studies in Systems, Decision and Control book series* (SSDC), 2021, no. 351, pp. 113-123. doi: https://doi.org/10.1007/978-3-030-68103-6_11.

8. Ndama A.T., Ndong E.O., Boussougou Y.C.M., Tsoumou G.J., Blampain E.J.J. Theoretical Study of Potential Manufacturing Insulation Defects in Medium–Voltage Traction Motors. *International Journal of Emerging Technology and Advanced Engineering*, 2022, vol. 12, no. 1, pp. 83-98. doi: https://doi.org/10.46338/ijetae0122_09.
9. Uydur C.C., Arikan J., Kalenderli Ö. The effect of insulation defects on electric and magnetic field distributions in power cables. *Tehnicki Vjesnik*, 2021, vol. 28, no. 4, pp. 1152-1160. doi: https://doi.org/10.17559/TV-20200205084232.
10. Han W., Yang G., Hao C., Wang Z., Kong D. and Dong Y. A data-driven model of cable insulation defect based on convolutional neural networks. *Applied Sciences*, 2022, vol. 12, no. 16, art. no. 8374. doi: https://doi.org/10.3390/app12168374.
11. Zeller H.R., Schneider W.R. Electrofracture mechanics of dielectric aging. *Journal of Applied Physics*, 1984, vol. 56, no. 2, pp. 455-459. doi: https://doi.org/10.1063/1.333931.
12. Scanavi G.I. *Physics of dielectrics (region of strong fields)*. Moscow, GIFML Publ., 1958. 909 p. (Rus).
13. Blythe T., Bloor D. *Electrical properties of polymers.* Cambridge University Press, 2008. 496 p.
14. Zhou X., Zhao X., Suo Z., Zou C. Electrical breakdown and ultrahigh electrical energy density in poly (vinylidene fluoride-hexafluoropropylene) copolymer. *Applied Physics Letters*, 2009, vol. 94, no. 16, art. no. 162901. doi: https://doi.org/10.1063/1.3123001.
15. Karpov V.G., Kryukov Y.A., Karpov I.V., Mitra M. Field-induced nucleation in phase change memory. *Physical Review B*, 2008, vol. 78, no. 5, art. no. 052201. doi: https://doi.org/10.1103/PhysRevB.78.052201.
16. Montanari G.C., Seri P., Dissado L.A. Aging mechanisms of polymeric materials under DC electrical stress: A new approach and similarities to mechanical aging. *IEEE Transactions on Dielectrics and Electrical Insulation*, 2019, vol. 26, no. 2, pp. 634-641. doi: https://doi.org/10.1109/TDEI.2018.007829.
17. Ding H.-Z., Varlow B.R. Thermodynamic model for electrical tree propagation kinetics in combined electrical and mechanical stresses. *IEEE Transactions on Dielectrics and Electrical Insulation*, 2005, vol. 12, no. 1, pp. 81-89. doi: https://doi.org/10.1109/TDEI.2005.1394018.
18. Pallon L.K.H., Nilsson F., Yu S., Liu D., Diaz A., Holler M., Chen X.R., Gubanski S., Hedenqvist M.S., Olsson R.T., Gedde U.W. Three-Dimensional Nanometer Features of Direct Current Electrical Trees in Low-Density Polyethylene. *Nano Letters*, 2017, vol. 17, no. 3, pp. 1402-1408. doi: https://doi.org/10.1021/acs.nanolett.6b04303.
19. Kitani R., Iwata S., Imatani S. Energy-Release Rate in Electrically Deteriorated Materials Introduced by Using Maxwell Stress Tensor at Crack Tip. *IEEE Transactions on Dielectrics and Electrical Insulation*, 2021, vol. 28, no. 6, pp. 1925-1932. doi; https://doi.org/10.1109/TDEI.2021.009692.
20. Zuoqian Wang, Marcolongo P., Lemberg J.A., Panganiban B., Evans J.W., Ritchie R.O., Wright P.K. Mechanical fatigue as a mechanism of water tree propagation in TR-XLPE. *IEEE Transactions on Dielectrics and Electrical Insulation*, 2012, vol. 19, no. 1, pp. 321-330. doi: https://doi.org/10.1109/TDEI.2012.6148534.
21. Kucheriava I.M. Computer analysis of electromechanical stress in polyethylene insulation of power cable at available micro-inclusion. *Technical Electrodynamics*, 2012, no. 5, pp. 10-16. (Rus).
22. Podoltsev O.D., Kucheriava I.M. Multiphysics processes in the region of inclusion in polyethylene insulation of power cable (three-dimensional modeling and experiment). *Technical Electrodynamics*, 2015, no. 3, pp. 3-9. (Rus).
23. Bezprozvannych G.V., Mirchuk I.A. Correlation between electrical and mechanical characteristics of cables with radiation-modified insulation on the basis of a halogen-free polymer composition. *Electrical Engineering & Electromechanics*, 2018, no. 4, pp. 54-57. doi: https://doi.org/10.20998/2074-272X.2018.4.09.
24. Bezprozvannych G.V., Boyko A.N., Roginskiy A.V. Effect of a dielectric barrier on the electric field distribution in high-voltage composite insulation of electric machines. *Electrical Engineering & Electromechanics*, 2018, no. 6, pp. 63-67. doi: https://doi.org/10.20998/2074-272X.2018.6.09.
25. Bezprozvannych G.V., Kyessayev A.G., Mirchuk I.A., Roginskiy A.V. Identification of technological defects in high-voltage solid insulation of electrical insulation structures on the characteristics of partial discharges. *Electrical Engineering & Electromechanics*, 2019, no. 4, pp. 53-58. doi: https://doi.org/10.20998/2074-272X.2019.4.08
26. Abrate S. Criteria for Yielding or Failure of Cellular Materials. *Journal of Sandwich Structures & Materials*, 2008, vol. 10, no. 1, pp. 5-51. doi: https://doi.org/10.1177/1099636207070997.
27. Stratton J.A. *Electromagnetic Theory*. Hoboken, IEEE Press, 2007. 630 p.
28. Lurie A. I. *Theory of Elasticity*. Heidelberg, Springer-Verlag Berlin, 2005. 1050 p.

Received 24.04.2023
Accepted 02.08.2023
Published 02.01.2024

O.O. Palchykov[1]*, PhD,*
[1] Admiral Makarov National University of Shipbuilding,
9, Heroyiv Ukraine Ave, Mykolaiv, 54025, Ukraine,
e-mail: ole2012hulk@gmail.com

How to cite this article:
Palchykov O.O. Determination of the maximum mechanical stresses in the insulating material around a defect with a high dielectric permittivity in an electrostatic field. *Electrical Engineering & Electromechanics*, 2024, no. 1, pp. 69-76. doi: https://doi.org/10.20998/2074-272X.2024.1.09

UDC 621.3 https://doi.org/10.20998/2074-272X.2024.1.10

V. Paquianadin, K. Navin Sam, G. Koperundevi

Maximizing solar photovoltaic system efficiency by multivariate linear regression based maximum power point tracking using machine learning

Introduction. *In recent times, there has been a growing popularity of photovoltaic (PV) systems, primarily due to their numerous advantages in the field of renewable energy. One crucial and challenging task in PV systems is tracking the maximum power point (MPP), which is essential for enhancing their efficiency.* ***Aim.*** *PV systems face two main challenges. Firstly, they exhibit low efficiency in generating electric power, particularly in situations of low irradiation. Secondly, there is a strong connection between the power output of solar arrays and the constantly changing weather conditions. This interdependence can lead to load mismatch, where the maximum power is not effectively extracted and delivered to the load. This problem is commonly referred to as the maximum power point tracking (MPPT) problem various control methods for MPPT have been suggested to optimize the peak power output and overall generation efficiency of PV systems.* ***Methodology.*** *This article presents a novel approach to maximize the efficiency of solar PV systems by tracking the MPP and dynamic response of the system is investigated.* ***Originality.*** *The technique involves a multivariate linear regression (MLR) machine learning algorithm to predict the MPP for any value of irradiance level and temperature, based on data collected from the solar PV generator specifications. This information is then used to calculate the duty ratio for the boost converter.* ***Results.*** *MATLAB/Simulink simulations and experimental results demonstrate that this approach consistently achieves a mean efficiency of over 96 % in the steady-state operation of the PV system, even under variable irradiance level and temperature.* ***Practical value.*** *The improved efficiency of 96 % of the proposed MLR based MPP in the steady-state operation extracting maximum from PV system, adds more value. The same is evidently proved by the hardware results.* References 24, table 4, figures 14.

Key words: **machine learning, maximum power point trackers, solar photovoltaic systems.**

Вступ. *Останнім часом зростає популярність фотоелектричних (ФЕ) систем, насамперед через їх численні переваги в галузі відновлюваної енергетики. Однією з найважливіших і складних завдань у ФЕ системах є відстеження точки максимальної потужності (MPP), яка необхідна для підвищення їх ефективності.* ***Мета***. *ФЕ системи стикаються із двома основними проблемами. По-перше, вони демонструють низьку ефективність вироблення електроенергії, особливо в умовах низького випромінювання. По-друге, існує сильний зв'язок між вихідною потужністю сонячних батарей і погодними умовами, що постійно змінюються. Ця взаємозалежність може призвести до невідповідності навантаження, коли максимальна потужність не ефективно відбиратиметься і передаватиметься в навантаження. Цю проблему зазвичай називають проблемою відстеження точки максимальної потужності (MPPT). Для оптимізації пікової вихідної потужності та загальної ефективності генерації ФЕ систем було запропоновано різні методи керування MPPT.* ***Методологія***. *У цій статті представлено новий підхід до максимізації ефективності сонячних ФЕ систем шляхом відстеження MPP та дослідження динамічної реакції системи.* ***Оригінальність***. *Цей метод включає алгоритм машинного навчання багатовимірної лінійної регресії (MLR) для прогнозування MPP для будь-якого рівня освітленості і температури на основі даних, зібраних зі специфікацій сонячних ФЕ генераторів. Ця інформація потім використовується для розрахунку коефіцієнта заповнення перетворювача, що підвищує.* ***Результати***. *Моделювання MATLAB/Simulink та експериментальні результати показують, що цей підхід послідовно забезпечує середню ефективність понад 96 % в режимі роботи ФЕ системи, що встановився, навіть при змінних рівнях освітленості і температурі.* ***Практична цінність***. *Підвищена ефективність 96 % пропонованого MPP на основі MLR в режимі роботи, що вистачає максимум з ФЕ системи, підвищує цінність. Те саме, очевидно, підтверджують і апаратні результати.* Бібл. 24, табл. 4, рис. 14.

Ключові слова: **машинне навчання, відстежувачі максимальної потужності, сонячні фотоелектричні системи.**

Introduction. Solar photovoltaic (PV) generator energy systems have become increasingly popular as a source of renewable energy. However, one of the main challenges is, achieving maximum power extraction from the PV generator as it is typically not operated at its optimal point for specific levels of irradiance (I_r) and temperature (T). To address this challenge, various techniques have been developed for tracking the maximum power point (MPP) known as MPP tracking (MPPT) techniques, which aim to improve the efficiency of PV generator. The most common conventional methods for MPPT of a PV generator are Perturb & Observe (P&O) and Incremental Conductance (IC) algorithms. These methods involve adjusting the voltage of the PV generator [1-3] to calculate the required change in voltage for maximum power extraction. Other methods include mathematical-based approaches like the curve-fitting algorithm, which indirectly tracks the MPP using the power-voltage curve of the panel. Constant-parameter algorithms like fractional open-circuit voltage require periodic measurement of the open-circuit voltage, while the fractional short-circuit current algorithm requires periodic measurement of the short-circuit current. Trial-and-error-based methods like gradient descent calculate the adjacent local MPP using the gradient function. Intelligent prediction algorithms like fuzzy logic control (FLC) and artificial neural networks (ANN) can predict MPP by adjusting the weights of different layers through a training process [4, 5]. Optimization methods like ant colony optimization, firefly algorithm, genetic algorithm, and grey wolf optimization attempt to optimize functions or variables to achieve maximum power extraction from the PV generator.

These algorithms are designed to operate the PV generator at the MPP to extract the maximum available power for delivery to the load.

Machine learning (ML) algorithms can predict unknown data with a high degree of accuracy by learning from known data. By training a ML algorithm [6] with existing data and testing it with new data, a ML model is created. Typically, 75 % of the data is used for training, and the remaining 25 % for testing the model. Image-based ML and reinforcement learning algorithms have been used for MPPT in PV generator. To operate the PV generator at the MPP, a converter is required.

The literature reports the use of various types of converters, including DC-DC buck converters, boost converters, buck-boost converters, single-ended primary inductor converters, and controlled inverters.

Although the conventional P&O and IC methods are simple and require fewer sensing elements, they have a low MPPT speed for rapid changes in irradiances. Intelligent prediction algorithms like ANN and FLC can address this issue. The performance of the ANN model depends on the correlation between the training and validation data, the number of iterations used for training, and the number of layers and neurons. The accuracy of the FLC is dependent on the rule-based design, which requires human expertise and experience. The Cuckoo Search (CS) technique is considered one of the fastest and most reliable optimization techniques but has a high failure rate and high oscillations in the steady state.

Achieving fast-tracking of the MPP is crucial for efficient solar PV generator, as irradiance and temperature change rapidly. ML algorithms offer a promising solution to improve MPPT speed without requiring an iterative approach or controller. To evaluate this approach, a new multivariate linear regression (MLR) algorithm is proposed in this study, and its performance is compared to conventional techniques like P&O and IC, intelligent methods like ANN and FLC, and optimization algorithms.

The block diagram shown in Fig. 1 for a complete system, where P_{mp} is maximum power available at MPP, V_{mp} is the voltage of the solar PV generator at MPP, I_{mp} is the current through the solar PV generator at MPP, D is duty cycle, R_{mp} is the resistance at MPP and R_0 is the load resistance. The mean efficiency is calculated under different irradiance level (IL) and temperature T to validate the effectiveness of the MLR method.

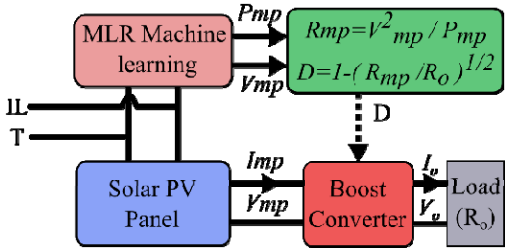

Fig. 1. System block diagram

System description. Characteristics of PV generator and DC-DC boost converter. Solar PV generator convert sunlight into electricity, and several cells are connected to form a PV generator. The one-diode equivalent circuit [7-11] of a PV generator is depicted in Fig. 2 and represented mathematically in (1). The number of solar PV generator in a panel determines the specifications for voltage, current, and power.

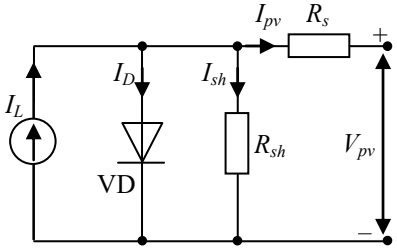

Fig. 2. The one-diode equivalent circuit of a PV generator

$$I_{pv} = I_L - I_D\left(e^{\frac{V+IR_s}{nV_T}} - 1\right) - \frac{V + I_{pv}R_S}{R_{sh}}, \qquad (1)$$

where I_{pv} is the solar PV generator current; I_L is the photocurrent as a function of IL and T; I_D is the diode saturation current; V is the solar PV generator voltage; R_s is the series resistance; n is the diode ideal factor ($1 \le n \le 2$); V_T is the thermal voltage equivalent; R_{sh} is the shunt resistance.

Figure 3 illustrates a boost converter with pulse width modulation control, which is powered by a solar PV generator. The MOSFET switch and duty cycle (D) is responsible for controlling the amount of power that is delivered to the load from the solar PV generator. The inductor L present in the circuit boosts the solar PV generator voltage to the required output voltage level. Additionally, the load current I_o flow through the load and input and output capacitors C_i and C_o are utilized to minimize the ripple content in the voltages [8-10].

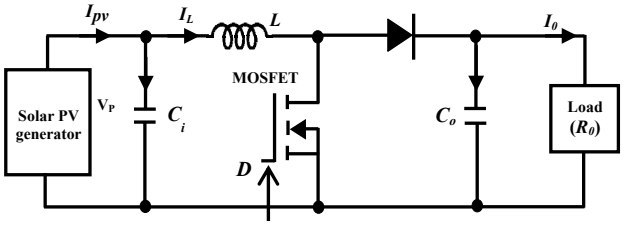

Fig. 3. Boost converter with solar PV generator

The solar panel specifications used for the simulation include a maximum power of 250 W, short-circuit current of 9.38 A, open-circuit voltage of 36 V, voltage at MPP of 28.8 V, and current at MPP of 8.68 A. The current-voltage and power-voltage characteristics of the solar PV generator under different temperature and irradiances are illustrated in Fig. 4.

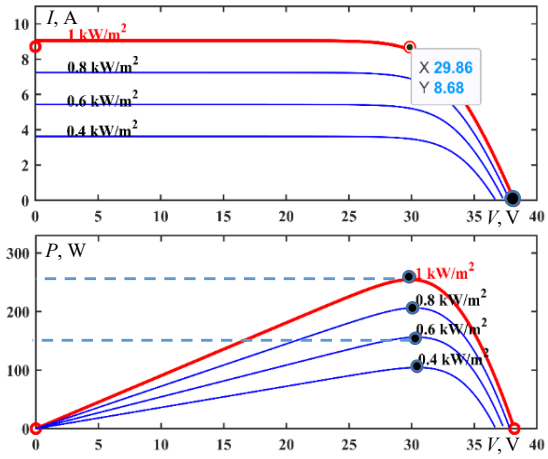

Fig. 4. The current-voltage and power-voltage characteristic curves of solar PV generator

Multivariate linear regression. The linear regression method is a simple ML technique that is suitable for predicting real numbers from available data. It works by predicting unknown data, which is also known as dependent data, from the features, which are referred to as independent data [12, 13]. If the data has a single feature, then the univariate linear regression algorithm gives a straight line that predicts the data in a two-dimensional space. On the other hand, if there are multiple features, the MLR algorithm provides a plane in multidimensional

space. The general form of the multiple linear regression planes [12] can be expressed as:

$$y = \beta_0 + \beta_0 \cdot x_1 + ... + \beta_{n-1} \cdot x_{n-1} + \beta_n \cdot x_n, \quad (2)$$

where y is the data to be predicted in a n-dimensional space $x_1, x_2, ..., x_{n-1}, x_n$ are the feature with $\beta_0, \beta_0, ..., \beta_{n-1}, \beta_{n-1}$ as regression coefficients.

ANN-based MPP [14-18] is shown in Fig. 5 for an example of finding the duty at MPP (D_{mpp}) based on the training provided for the ANN. The results of D_{mpp} are taken as output and are used for comparisons.

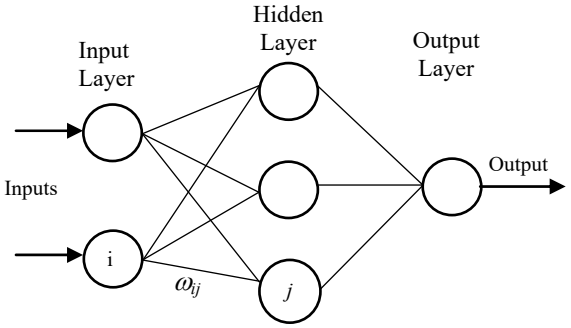

Fig. 5. Neural network example

Data in linear regression. ML algorithms acquire knowledge by analyzing data, allowing them to identify patterns, make informed decisions, and assess their level of certainty based on the information provided. The quality of the training data plays a critical role in determining the effectiveness of the model. Figure 6 indicates the learning model. Three-dimensional MLR model is shown in Fig. 7.

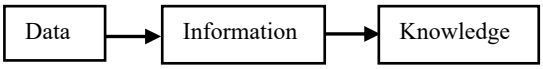

Fig. 6. Learning model

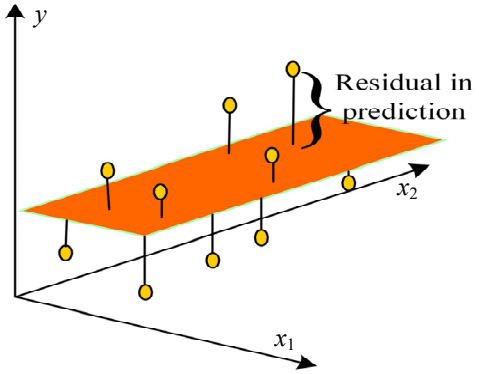

Fig. 7. MLR model in a three-dimensional space

Learning is data refers to raw and unprocessed facts, values, texts, sounds, or images that are yet to be analyzed. It is a crucial component in the fields of ML and artificial intelligence, and without it, cannot train any models. Information, on the other hand, is data that has been interpreted and manipulated to provide final results. Knowledge is a combination of inferred information, experiences, learning, and insights that result in awareness.

Data preprocessing. Training data. The part of data used to train the model. This is the data that the MLR model sees (both input and output) and learns from this data. In the proposed work, 70 % of data is given for training purpose and the records were chosen randomly (Fig. 8).

Validation data. The part of data that is used to do a frequent evaluation of the model, fits on the training dataset along with improving involved hyper parameters (initially set parameters before the model begins learning). This data plays its part when the model is training. For validation of data, only 20 % of the data is given and the records were random.

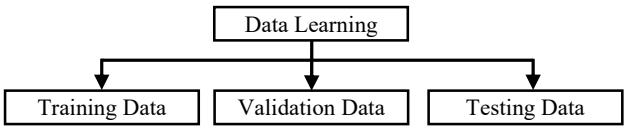

Fig. 8. Data preprocessing

Testing data. Once the model is completely trained, testing data provides an unbiased evaluation. When the inputs of testing data are fed, the trained model will predict some values (without seeing actual output). After prediction, to evaluate the model by comparing it with the actual output present in the testing data.

This is how the evaluation and performance model has learned from the experiences feed in as training data, set at the time of training. The remaining data i.e., 10 % of data is fed to the trained and validated model to evaluate performance.

Methodology. The methodology used in this study is divided into 4 stages, as the flowchart shown in Fig. 9. The first stage involves collecting and processing raw data from the solar PV generator specifications using MATLAB/Simulink. After collecting the data, an analysis is performed to remove any outliers. The second stage focuses on developing the MLR model through training, validation, and testing using the prepared data. The performance of the model is evaluated using metrics such as sum squared error (SSE), R^2, and root mean square error (RMSE). The formula to calculate these measures are provided below.

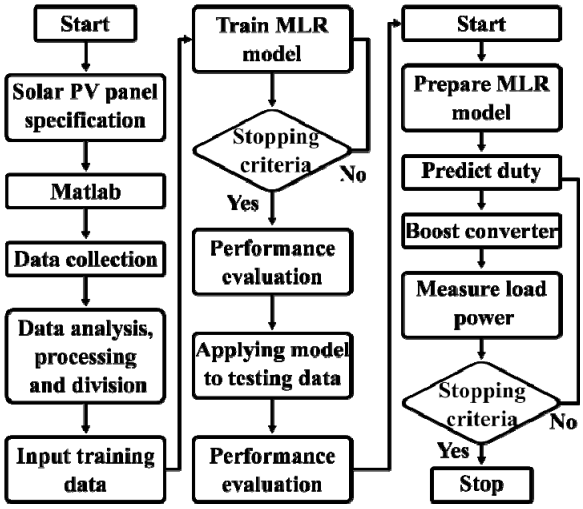

Fig. 9. Flowchart for the proposed MMPT using MLR

$$SSE = \sum_{K=1}^{n_s} \left(Y_{A,K} - Y_{P,K}\right)^2; \quad (3)$$

$$R^2 = 1 - \frac{\sum_{K=1}^{n_s} \left(Y_{A,K} - Y_{P,K}\right)^2}{\sum_{K=1}^{n_s} \left(Y_{A,K} - Y_{P,Avg}\right)^2}; \quad (4)$$

$$RMSE = \sqrt{\left[\frac{1}{n_s} \sum_{K=1}^{n_s} \left(Y_{A,K} - Y_{P,K}\right)^2\right]}, \quad (5)$$

where Y_A represents the actual data; Y_P is the predicted data; n_s is the number of samples; Y_{Avg} is the average

values of Y_A. The value of $R^2 \in [0, 1]$ specifies the prediction strength of models, and an R^2 value closer to 1 ensures the best fit of the model. Likewise, the SSE and RMSE values measure the residual or error among Y_A and Y_P. Therefore, SSE and RMSE values closer to 0 represent the models' superior prediction.

In the proposed methodology, the third stage involved using the MLR model to perform MPPT. The MLR model predicted the maximum power available at MPP (P_{mp}) and the voltage of the solar PV generator at MPP (V_{mp}) for a given IL and temperature T. The predictions were used to determine the required D for the boost converter to operate the PV generator at MPP. The corresponding resistance at MPP (R_{mp}) was computed using these predicted values as in (6). The R_{mp} was reflected between nodes of boost converter by controlling the D of the boost converter. The D in terms of R_{mp} and load resistance R_0 is given in (7):

$$R_{mp} = V_{mp}^2 / P_{mp}\ ; \qquad (6)$$

$$D = 1 - \sqrt{\left(R_{mp} / R_0\right)}. \qquad (7)$$

The maximum and minimum values of the load resistance were determined using the method proposed in [8]. The boost converter is designed using the procedure explained in [7]. The required boost converter inductance L and capacitance C are as follows:

$$L = V_{inp} \cdot \left(V_{out} - V_{inp}\right) / f_{sw} \cdot \Delta I \cdot V_{out}\ ; \qquad (8)$$

$$C = I_{out} \cdot \left(V_{out} - V_{inp}\right) / f_{sw} \cdot \Delta V \cdot V_{out}\ , \qquad (9)$$

where V_{inp} is the input voltage; V_{out} is the output voltage; f_{sw} is the switching frequency; ΔI is the current ripple; I_{out} is the output current; ΔV is the voltage ripple.

The fourth stage of the methodology involved a comparative analysis of the MLR methodology with existing conventional, intelligent, and optimization MPPT methods.

Simulation results and discussion. Data collection. The simulated dynamic result for the IL changed from 900 to 500 W/m^2 is shown in Fig. 10. In that corresponding solar power, voltage, and current were demonstrated that the maximum power can track using the proposed method.

The data collected for this study includes four variables: I_r, T, P_{mp} and V_{mp}. The values of P_{mp} and V_{mp} depend on I_r and T.

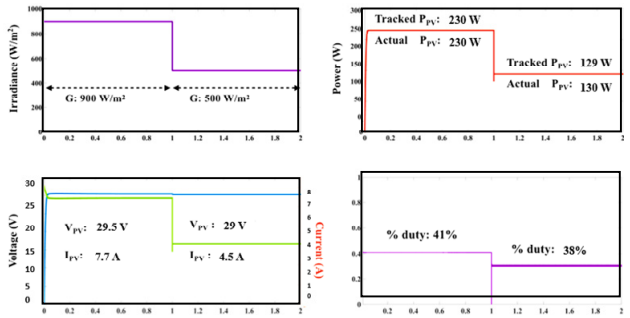

Fig. 10. Simulation results of V_{pv}, I_{pv}, P_{pv} and D for change in I_r from 900 to 500 W/m^2, T = 25 °C

To predict P_{mp} and V_{mp}, I_r and T are used as features. The MPP of changes in variables for the installed roof solar PV generator and its specification of 250 W Zy-TECH 250P [19-21] are given in Table 1.

Table 1

Specification of solar PV generator

Specification	Value
Rated power, W	250
Voltage at maximum power, V	28.8
Current at maximum power, A	8.68
Open circuit voltage, V	36
Short-circuit current, A	9.38
Voltage temperature coefficient	–0.36901
Current temperature coefficient	0.086988

Performance of the proposed MLR model. The MLR machine learning models created using MATLAB/Simulink involves two independent and one dependent variable. These models can predict the values of P_{mp} and V_{mp} based on specific values of I_r and T. The data were collected as described earlier, based on the specification of the PV generator. The MLR model developed is presented mathematically in (10) and (11):

$$P_{mp} = 0.8994 + 0.01001 \cdot I_r - 0.03685 \cdot T; \qquad (10)$$

$$V_{mp} = 19.21 + 0.0007073 \cdot I_r - 0.08946 \cdot T. \qquad (11)$$

The developed MATLAB MLR machine learning technique consists of two input variables and one output variable. These techniques can predict P_{mp} and V_{mp} at various irradiance I_r and temperature T.

The regression coefficients of (10) define a plane in I_r, T and P_{mp} as shown in Fig. 11,*a*. The residuals in the prediction for these parameters are shown in Fig. 11,*b*. The numerical analysis of SSE, R^2, and RMSE are 0.0197, 0.9999 and 0.0405, respectively. The SSE and RMSE values are close to 0, and the R^2 value is close to 1, indicating the best prediction of the models and the results given in Table 2, 3.

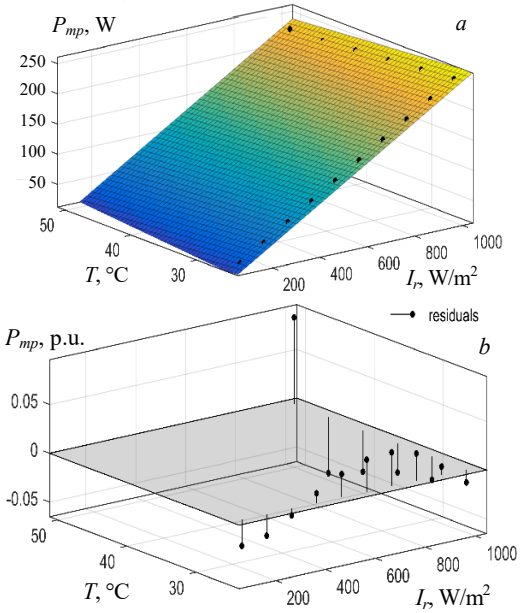

Fig. 11. *a* – P_{mp} plane defined by regression coefficients; *b* – residuals in prediction

Table 2

Training results

Metric	Value
RMSE	$1.0347 \cdot 10^{-14}$
R^2	1
MSE	$1.0762 \cdot 10^{-28}$
Prediction speed	9800 obs/s*
Training time	4.9252 s

*obs/s – refers to number of observations processed per second.

Table 3

Testing results

Metric	Value
RMSE	$3.6016 \cdot 10^{-14}$
R^2	1
MSE	$1.2972 \cdot 10^{-27}$

Performance comparison of various methods. The performance of the MLR model was compared to other models, and the results were summarized in Table 4 for the time range of 0 to 0.5 s. The comparison indicated that the P&O and IC methods exhibited oscillations in steady-state, while the other models did not [22-24]. According to Table 4 the MLR model settled in less than half the time with a high steady-state value of 230 W and almost zero overshoot compared to the P&O method. Similarly, the MLR model settled in less than half the time with a high steady-state value and nearly zero overshoot compared to the IC method. Overall, the MLR model outperformed the P&O and IC algorithms in terms of settling time, steady-state value, and overshoot.

Table 4

Comparison of the MPPT response characteristics for various methods

Parameter	MLR	P&O	IC	ANN
Rise time, s	0.1409	0.0463	0.0352	0.1314
Settling time, s	0.2410	0.5000	0.4994	0.2144
Overshoot, %	0.0023	9.2364	39.294	0
Peak time, s	0.4999	0.0829	0.2300	0.5

According to the power response numerical values, the MLR model's performance is comparable to that of the intelligent methods, such as ANN and FLC, while the CS method exhibits an undesirable undershoot. Moreover, the MLR model outperforms the CS optimization method in terms of rise time and overshoot. Based on this analysis, it can be concluded that the MLR control method is suitable for MPPT in PV generator, as it can track the MPP under varying I_r and T conditions in a stable state and ensure that the PV generator operate at the MPP.

Experimental results and discussion. To further substantiate the dynamic performance, the experiments have been conducted using the solar PV generator of 250 W Zy-TECH 250P where considered for this work shown in Fig. 12. Under standard test conditions of I_r = 1000 W/m^2 and T = 25 °C solar PV generator produce power of 250 W. MLR algorithm tested for solar PV generator under various algorithm is tested for solar PV generator under various I_r and T profiles.

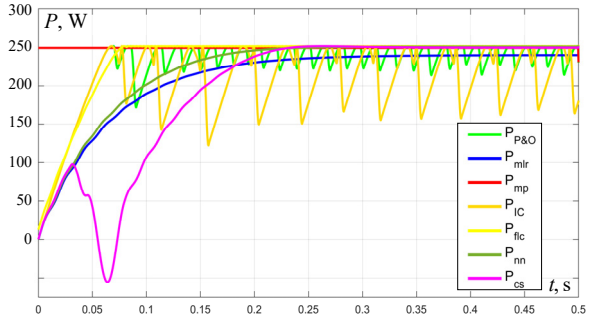

Fig. 12. Solar PV panel power comparison for various methods

The experimental setup shown in Fig. 13 consists of a solar PV panel, a designed boost converter and a program kit ESP-32. The IL is changed from 900 W/m^2 to 500 W/m^2 at t_{IL} result shown in Fig. 14.

Fig. 13. Experimental setup

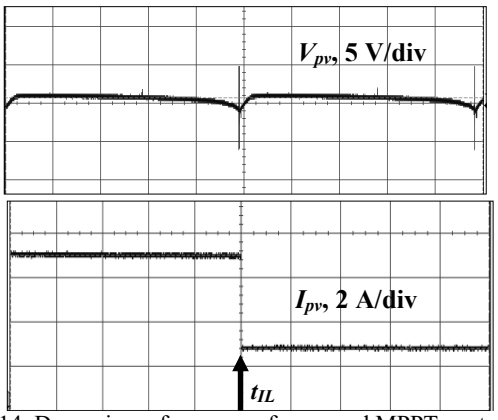

Fig. 14. Dynamic performance of proposed MPPT controller. IL changed from 900 W/m^2 to 500 W/m^2

Note. T = 25 °C, V_{pv} = 29 V, time axis: 20 ms/div, and t_{IL} is the instant at which step change in I_r of solar PV generator initiated

Conclusions. A new approach based on multivariate linear regression machine learning was implemented in this study to achieve high accuracy in tracking the maximum power point of a solar photovoltaic generator using a pulse width modulation control boost converter. The mean efficiency was found to be over 96.18 % in steady-state, which validates the effectiveness of the multivariate linear regression algorithm. Simulation with experimental hardware results showed that the multivariate linear regression algorithm had a high level of accuracy in maximum power point tracking in steady-state compared to conventional perturb & observe, incremental conductance algorithms, intelligent prediction artificial neural networks algorithm, and cuckoo search optimization method. Moreover, the multivariate linear regression algorithm proved to be effective even in the presence of varying irradiance and temperature.

As a part of future work, the effect of partial shading on photovoltaic generator will be analyzed with the help of hardware implementation.

Acknowledgment. The authors would like to thank Charitesh Raja K., Sameer S., Sravankumar Reddy K. and Senthamizh Selvan S. for their support in the preparation of this work.

Conflict of interest. The authors declare that they have no conflicts of interest.

REFERENCES

1. Khodair D., Salem M.S., Shaker A., El Munim H.E.A., Abouelatta M. Application of Modified MPPT Algorithms: A Comparative Study between Different Types of Solar Cells.

Applied Solar Energy, 2020, vol. 56, no. 5, pp. 309-323. doi: https://doi.org/10.3103/S0003701X20050084.
2. El Telbany M.E., Youssef A., Zekry A.A. Intelligent Techniques for MPPT Control in Photovoltaic Systems: A Comprehensive Review. *2014 4th International Conference on Artificial Intelligence with Applications in Engineering and Technology*, 2014, pp. 17-22. doi: https://doi.org/10.1109/ICAIET.2014.13.
3. Karanjkar D.S., Chatterji S., Shimi S.L., Kumar A. Real time simulation and analysis of maximum power point tracking (MPPT) techniques for solar photo-voltaic system. *2014 Recent Advances in Engineering and Computational Sciences (RAECS)*, 2014, pp. 1-6. doi: https://doi.org/10.1109/RAECS.2014.6799656.
4. Hessad M.A., Bouchama Z., Benaggoune S., Behih K. Cascade sliding mode maximum power point tracking controller for photovoltaic systems. *Electrical Engineering & Electromechanics*, 2023, no. 1, pp. 51-56. doi: https://doi.org/10.20998/2074-272X.2023.1.07.
5. Saeed H., Mehmood T., Khan F.A., Shah M.S., Ullah M.F., Ali H. An improved search ability of particle swarm optimization algorithm for tracking maximum power point under shading conditions. *Electrical Engineering & Electromechanics*, 2022, no. 2, pp. 23-28. doi: https://doi.org/10.20998/2074-272X.2022.2.04.
6. Carballo J.A., Bonilla J., Berenguel M., Fernández-Reche J., García G. Machine learning for solar trackers. *AIP Conference Proceedings*, 2019, vol. 2126, no. 1, p. 030012. doi: https://doi.org/10.1063/1.5117524.
7. Rashid M.H. *Power Electronics: Circuits, Devices, and Applications. 4th ed.* London, UK, Pearson Publ., 2013. 1024 p.
8. Ayop R., Tan C.W. Design of boost converter based on maximum power point resistance for photovoltaic applications. *Solar Energy*, 2018, vol. 160, pp. 322-335. doi: https://doi.org/10.1016/j.solener.2017.12.016.
9. Balakishan P., Chidambaram I.A., Manikandan M. Improvement of power quality in grid-connected hybrid system with power monitoring and control based on internet of things approach. *Electrical Engineering & Electromechanics*, 2022, no. 4, pp. 44-50. doi: https://doi.org/10.20998/2074-272X.2022.4.06.
10. Chandramouli B., Vijayaprabhu A., Arun Prasad D., Kathiravan K., Udhayaraj N., Vijayasanthi M. Design of single switch-boosted voltage current suppressor converter for uninterrupted power supply using green resources integration. *Electrical Engineering & Electromechanics*, 2022, no. 5, pp. 31-35. doi: https://doi.org/10.20998/2074-272X.2022.5.05.
11. Hashim N., Salam Z., Johari D., Nik Ismail N.F. DC-DC Boost Converter Design for Fast and Accurate MPPT Algorithms in Stand-Alone Photovoltaic System. *International Journal of Power Electronics and Drive Systems (IJPEDS)*, 2018, vol. 9, no. 3, pp. 1038-1050. doi: https://doi.org/10.11591/ijpeds.v9.i3.pp1038-1050.
12. Mahesh P.V., Meyyappan S., Alla R.K.R. A New Multivariate Linear Regression MPPT Algorithm for Solar PV System with Boost Converter. *ECTI Transactions on Electrical Engineering, Electronics, and Communications*, 2022, vol. 20, no. 2, pp. 269-281. doi: https://doi.org/10.3793/ecti-eec.2022202.246909.
13. Kim K., Timm N. *Univariate and Multivariate General Linear Models: Theory and Applications with SAS. 2nd ed*. New York, USA, Chapman and Hall/CRC Press, 2007. 549 p.
14. Sahraoui H., Mellah H., Drid S., Chrifi-Alaoui L. Adaptive maximum power point tracking using neural networks for a photovoltaic systems according grid. *Electrical Engineering & Electromechanics*, 2021, no. 5, pp. 57-66. doi: https://doi.org/10.20998/2074-272X.2021.5.08.
15. Younis M.A., Khatib T., Najeeb M., Mohd Ariffin A. An Improved Maximum Power Point Tracking Controller for PV Systems using Artificial Neural Network, *Przeglad Elektrotechniczny*, 2012, vol. 88, no. 3B, pp. 116-121.
16. Muthubalaji S., Devadasu G., Srinivasan S., Soundiraraj N. Development and validation of enhanced fuzzy logic controller and boost converter topologies for a single phase grid system. *Electrical Engineering & Electromechanics*, 2022, no. 5, pp. 60-66. doi: https://doi.org/10.20998/2074-272X.2022.5.10.
17. Dzung P.Q., Le Dinh Khoa Hong Hee Lee, Le Minh Phuong, Nguyen Truong Dan Vu. The new MPPT algorithm using ANN-based PV. *International Forum on Strategic Technology 2010*, 2010, pp. 402-407. doi: https://doi.org/10.1109/IFOST.2010.5668004.
18. Nebti K., Lebied R. Fuzzy maximum power point tracking compared to sliding mode technique for photovoltaic systems based on DC-DC boost converter. *Electrical Engineering & Electromechanics*, 2021, no. 1, pp. 67-73. doi: https://doi.org/10.20998/2074-272X.2021.1.10.
19. Praveen Kumar B., Prince Winston D., Cynthia Christabel S., Venkatanarayanan S. Implementation of a switched PV technique for rooftop 2 kW solar PV to enhance power during unavoidable partial shading conditions. *Journal of Power Electronics*, 2017, vol. 17, no. 6, pp. 1600-1610. doi: https://doi.org/10.6113/JPE.2017.17.6.1600.
20. Shavelkin A.A., Gerlici J., Shvedchykova I.O., Kravchenko K., Kruhliak H.V. Management of power consumption in a photovoltaic system with a storage battery connected to the network with multi-zone electricity pricing to supply the local facility own needs. *Electrical Engineering & Electromechanics*, 2021, no. 2, pp. 36-42. doi: https://doi.org/10.20998/2074-272X.2021.2.06.
21. Yuvarajan S., Shoeb J. A fast and accurate maximum power point tracker for PV systems. *2008 Twenty-Third Annual IEEE Applied Power Electronics Conference and Exposition*, 2008, pp. 167-172. doi: https://doi.org/10.1109/APEC.2008.4522717.
22. Kumar R.S., Reddy C.S.R., Chandra B.M. Optimal performance assessment of intelligent controllers used in solar-powered electric vehicle. *Electrical Engineering & Electromechanics*, 2023, no. 2, pp. 20-26. doi: https://doi.org/10.20998/2074-272X.2023.2.04.
23. Janardhan G., Surendra Babu N.N.V., Srinivas G.N. Single phase transformerless inverter for grid connected photovoltaic system with reduced leakage current. *Electrical Engineering & Electromechanics*, 2022, no. 5, pp. 36-40. doi: https://doi.org/10.20998/2074-272X.2022.5.06.
24. Louarem S., Kebbab F.Z., Salhi H., Nouri H. A comparative study of maximum power point tracking techniques for a photovoltaic grid-connected system. *Electrical Engineering & Electromechanics*, 2022, no. 4, pp. 27-33. https://doi.org/10.20998/2074-272X.2022.4.04.

Received 03.06.2023
Accepted 04.08.2023
Published 02.01.2024

V. Paquianadin [1], *Research Scholar,*
K. Navin Sam [1], *PhD, Assistant Professor,*
G. Koperundevi [1], *PhD, Associate Professor,*
[1] Department of Electrical and Electronics Engineering, National Institute of Technology Puducherry, Karaikal, India,
e-mail: paquia@rediffmail.com (Corresponding Author), navinsam.k@nitpy.ac.in, koperundevi@nitpy.ac.in

How to cite this article:
Paquianadin V., Navin Sam K., Koperundevi G. Maximizing solar photovoltaic system efficiency by multivariate linear regression based maximum power point tracking using machine learning. *Electrical Engineering & Electromechanics*, 2024, no. 1, pp. 77-82. doi: https://doi.org/10.20998/2074-272X.2024.1.10

Матеріали приймаються за адресою:
Кафедра "Електричні апарати", НТУ "ХПІ", вул. Кирпичева, 2, м. Харків, 61002, Україна
Електронні варіанти матеріалів по e-mail: a.m.grechko@gmail.com

Довідки за телефонами: +38 067 359 46 96 Гречко Олександр Михайлович

Передплатний індекс: 01216